UNIVERSIDAD DE CANTABRIA

Departamento de Ingeniería de Comunicaciones

TESIS DOCTORAL

Low Noise Receivers for Millimetre-wave Bands Radio Astronomy

Receptores de Bajo Ruido para Radioastronomía en Bandas de Ondas Milimétricas

Autor: **José Vicente Terán Collantes**

Directores: **Eduardo Artal Latorre**

Tesis doctoral para la obtención del título de Doctor por la Universidad de Cantabria en Tecnologías de la Información y Comunicaciones en Redes Móviles

Santander, Junio de 2017

Dedicado A la memoria de Carmen Collantes Fernández,
Mi luz en el cielo.

Acknowledgments

To my family, Papa, Mama and Luisja. Their support and love show me the way to be better every day. And for give me the opportunity to have a University education.

I wish to thank people from the Department of Communications Engineering of the University of Cantabria, professors Eduardo Artal and Maria Luisa de la Fuente for being my guide during the PhD and transfer me all their knowledge and experience. To all my colleagues Beatriz Aja, Juan Luis Cano, Eva Cuerno, Ana Rosa Pérez, and Enrique Villa for their assistance with all the work done, from Friday’s brain storming to coffee times. I remember all my University colleagues, from the first year in “Ingeniera Técnica” in 2001. They walked with along my University life. Special mention to Rubén Cavaducas, Jaime James, and David Güelu Bolucas. They converted into my friends and share special moments out the University, enjoying Verbenas parties, music festivals, and the passion for the mountains. In the end, we share Putas risas.

I wish to thank Rome, my lovely city. My work at University of Tor Vergata was so rewarding. The friendship of Xavi, Antonio, Helena, Susana, Carlos with our Sgroppino, Prosecco, and Peroni nights discovering the city and incredible places.

To Emma because you showed me the meaning of real and true love.

Oscarin, Pajarelis, the night fighters. You know your friendship and blessed madness will be with us forever. My Rabucas, Samu, Adri, Sara, Ana, Laura, Fabio, Hugo, Nuri. My friend’s family, lunch times, *aperolos*, weddings, crazy *nocheviejas*.

Since I jointed the *Pezones*, the happiness, dancing, *fiesta* and the Mahou became so different and special. I met there so nice people. Amazing *brujas* nights.

Thank you very much to all of you. You are a part of this win.

Acknowledgments v
Acronyms xi
ABSTRACT xiii
CHAPTER I: INTRODUCTION 15
1.1. Radio astronomy receivers 17
1.1.1. Total power radiometer 17
1.1.2. Switched radiometer 18
1.1.3. Correlation receiver 20
1.1.4. Calibration of radio astronomy receivers 20
1.2. QUIJOTE experiment 21
1.3. Motivation 24
1.4. Outline of the thesis 24
1.5. References 25
CHAPTER II: CRYOGENIC BROADBAND Q-BAND MMIC LOW-NOISE AMPLIFIER 27
2.1. Introduction 27
2.2. Technology 28
2.3. MMIC LNA design 28
2.3.1. Transistor Small-Signal and Noise Models 29
2.3.2. LNA design 34
2.3.3. Yield 37
2.3.3.1. Large signal model yield analysis 38
2.3.3.2. Small signal model yield analysis 40
2.3.4. Connection of the LNA: Bonding wire 42
2.3.5. Manufacturing 43
2.4. LNA measurements and characterisation 43
2.4.1. Measurements on wafer at room temperature 43
2.4.2. Amplifier characterisation at cryogenic temperature 45
2.4.3. Comparing the LNA performance with other published works 47
2.4.4. Gain compression: P_{1dB} 48
2.5. Impact of the LNA in a radiometer 49
2.6. Conclusions 50
2.7. References 51
CHAPTER III: Ka-BAND FULL-HYBRID CRYOGENIC LOW-NOISE AMPLIFIER 55
3.1. Introduction 55
3.2. Technology 55
3.3. MIC LNA design 56

    - 3.3.1. Transistor small signal and noise models 56
    - 3.3.2. Radio frequency (RF) capacitor model 59
    - 3.3.3. Bonding wire in the source of the transistor 61
    - 3.3.4. LNA design 73
- 3.4. LNA performance 74
    - 3.4.1. Room temperature 75
    - 3.4.2. Cryogenic temperature 76
    - 3.4.3. Gain compression: P_{1dB} 77
- 3.5. Conclusions 78
- 3.6. References 79

CHAPTER IV: NOISE ANALYSIS IN DISTRIBUTED AMPLIFIERS WITH FEEDBACK-ACTIVE LOAD 81

- 4.1. Introduction 81
- 4.2. Distributed Amplifiers in radio astronomy receivers 82
- 4.3. Noise figure 82
    - 4.3.1. Noise figure of DA 83
    - 4.3.2. Noise temperature of an active load 85
- 4.4. Design example 88
    - 4.4.1. Two-stage distributed amplifier with resistive terminations 88
    - 4.4.2. Active load 91
    - 4.4.3. Distributed amplifier with active gate line termination 93
- 4.5. Performance of the DA: Fabrication and measured results 94
    - 4.5.1. DA with resistive line terminations 94
    - 4.5.2. DA with active gate line termination 95
    - 4.5.3. Gain compression: P_{1dB} 97
- 4.6. Cascading DAs 98
- 4.7. Conclusions 100
- 4.8. References 100

CHAPTER V: EQUALISING THE GAIN PERFORMANCE 103

- 5.1. Introduction 103
- 5.2. Equaliser methodological design 104
- 5.3. Implementation and experimental results 111
    - 5.3.1. Cryogenic equaliser characterisation 114
- 5.4. Bonding wires 117
    - 5.4.1. BEM equalisers 117
    - 5.4.2. FEM cryogenic equaliser 119
- 5.5. Inside an amplifier: BEM gain module of the FGI instrument 120

5.6. Inside an amplifier: FEM gain module of the FGI instrument 121
5.7. Conclusions.. 122
5.8. References.. 123
CHAPTER VI: FGI RECEIVER TEST BENCH 125
6.1. Receiver Scheme 125
6.2. Principle of operation.. 126
6.2.1. Detected signals in the receiver outputs without Phase Switches 128
6.2.2. Detected signals in the receiver outputs with Phase Switches........................ 129
6.3. Checking the radiometer operation 130
6.4. Subsystems of the FGI receiver 131
6.4.1. FEM subsystems 131
6.4.2. BEM subsystems.. 134
6.5. Test-bench.. 139
6.5.1. BEM test-bench 139
6.5.2. Gain chain test-bench 140
6.5.2.1. Noise performance.. 141
6.5.2.2. Effective bandwidth 143
6.5.3. Instrument operation with the FEM at cryogenics 145
6.5.3.1. Low-frequency spectrum 152
6.5.3.1.1. No switching.. 152
6.5.3.1.2. Switching operation 154
6.6. Conclusions.. 155
6.7. References.. 155
CHAPTER VII: RADIOMETER AT W-BAND 157
7.1. Introduction.. 157
7.2. Radiometer sensitivity principles 158
7.3. Goals of the designed filter 159
7.4. Filter implementation 160
7.4.1. Filter design 160
7.4.2. Adjustment.. 163
7.4.3. Manufacture considerations 165
7.5. Filter characterisation 166
7.6. W-band radiometer scheme 168
7.6.1. W-band low-noise amplifiers 169
7.6.2. W-band band-pass filter.. 170
7.6.3. Sub-harmonic mixer 170

7.6.4. IF amplifier ... 172

7.6.5. Detector and video amplifier ... 172

7.7. Radiometer characterisation ... 173

7.7.1. Total power radiometer ... 174

7.7.2. Dicke radiometer ... 175

7.8. Conclusions ... 177

7.9. References ... 177

CHAPTER VIII: CONCLUSIONS ... 181

8.1. Thesis results ... 181

8.2. Future lines ... 183

8.3. Publications ... 184

8.3.1. Magazines ... 184

8.3.2. International Symposiums ... 184

8.3.3. National Symposiums ... 184

RESUMEN ... 187

CONCLUSIONES ... 189

Resultados de la tesis ... 189

Líneas futuras ... 191

Acronyms

AC: Alternating Current

AIV: Assembly, Integration and Verification laboratory

BCB: Benzocyclobutene

BEM: Back End Module

BPF: Band Pass Filter

BW: Bandwidth

CDM: Correlation and Detection Module

CMB: Cosmic Microwave Background

CTE: Coefficient of Thermal Expansion

DA: Distributed Amplifier

DAS: Data Acquisition System

DC: Direct Current

DICOM: Department of Communications Engineering of University of Cantabria

DUT: Device Under Test

ENR: Excess Noise Ratio

F: Noise Factor

FEM: Front End Module

FFT: Fast Fourier Transform

FGI: Forty Gigahertz Instrument

FOM: Figure Of Merit

G: Gain

GND: Ground

HEMT: High Electron Mobility Transistor

Hz: Hertz

IAC: Astrophysics Institute of Canary Islands

IAF: Fraunhofer Institute for Applied Solid State Physics

IF: Intermediate Frequency

IFCA: Physics Institute of Cantabria

k: Boltzmann constant

K: Kelvin

LNA: Low Noise Amplifier

LO: Local Oscillator

MFI: Multi Frequency Instrument

MIC: Microwave Integrated Circuit

MMIC: Monolithic Microwave Integrated Circuit

MSG: Maximum Stable Gain

NF: Noise Figure

OMT: Ortho Mode Transducer

PCM: Process Control Monitor

QUIJOTE: Q-U-I Joint Tenerife

RADOM: Receptores de Radioastronomía en Ondas Milimétricas

RF: Radio Frequency

RMS: Root Mean Square

SiN: Silicon Nitride

SiO: Silicon Oxide

SMD: Surface Mount Device

TGI: Thirty Gigahertz Instrument

ABSTRACT

The QUIJOTE (Q-U-I JOint TEnerife) experiment is devoted to measure and study the characteristics of the Cosmic Microwave Background (CMB) such intensity and polarisation. The telescope and measurement instruments to carry out the experiment are placed in the Izaña Observatory (Teide, Canary Islands). The instrumentation is composed by a Multi Frequency Instrument (MFI) already working in the observatory, a Thirty Gigahertz Instrument (TGI) under integration work in the telescope, and a Forty Gigahertz (FGI) Instrument under manufacture.

QUIJOTE experiment is a scientific consortium formed by the Astrophysics Institute of Canary Islands (IAC), the Physics Institute of Cantabria (IFCA), the Department of Communications Engineering of University of Cantabria (DICOM), the Jodrell Bank Observatory of Manchester (United Kingdom), the Cavendish Laboratory in Cambridge (United Kingdom), and Spanish company IDOM.

The DICOM group is the responsible of the design and development of the TGI and FGI instruments. The FGI is a radiometer operating in the Q-band (40 GHz) that complements the CMB measurements of the MFI and TGI Instruments of the QUIJOTE experiment.

The goal of this thesis is the design, development, characterisation of cryogenic low noise amplifiers (LNA) in GaAs mHEMT technology aimed to the front-end module of a radiometer. Q-band LNA using Monolithic Microwave Integrated Circuit (MMIC), and Ka-band LNA using hybrid Microwave Integrated Circuit (MIC) technologies have been developed.

The distributed amplifier (DA) topology has been studied to design a prototype amplifier in 1-5 GHz frequency band with a higher output power than the classic low-noise amplifier, using an active load as line termination in order to minimize the low-frequency high noise, typical in distributed topologies.

The design of equalisers using planar microstrip technology has been used to improve the planarity and bandwidth of cryogenic amplifiers and “hot” amplifiers working at room temperature.

Some of the designed circuits has been integrated in the FGI prototype radiometer. A characterisation in terms of effective bandwidth, the noise operation temperature, and the detected output signals has been performed over the FGI full-radiometer.

A new observation window is opened in W-band, in which a W-band radiometer with frequency down-conversion has been proposed. The radiometer is made up by commercial components, except the W-band filter that fixes the radio frequency band of interest (80-99 GHz).

The thesis is divided into next points:

- Introduction about the study of CMB and the instruments to measure it.
- Design and characterisation of cryogenic low-noise amplifiers using mHEMT GaAs technology. MMIC and MIC amplifiers are presented.
- Study and improvement of the low-frequency noise in DA.
- Design microstrip equalisers to compensate negative gain slope in low-noise amplifiers and increase the effective bandwidth.
- Characterisation of a radiometer in terms of effective bandwidth, noise temperature and output signals.
- Proposal of W-band radiometer for a new observation window of the CMB.

CHAPTER I: INTRODUCTION

To the question, where are we come from? Where are we? Where our future goes? The Cosmology, the universe science, tries to answer. Everything started long time ago, about 13,700 million years, with the explosion of the Big Bang (Fig. 1.1). The Big Bang theory explains our universe begin. After the big explosion a soup of particles called quarks filled the energy inflation at a very hot temperature. The universe cools clumping the quarks into neutrons and protons. As the universe was cooling, first light arise through first light nuclei of hydrogen and helium. The electrons started to orbit nuclei creating atoms, the glow of the primitive universe. Past 300 millions of years the cosmic background radiation was the only light. That period was called the dark ages. Dense clouds of gas started to collapse under their own gravity forming first galaxies and stars. After being slowed by the gravity, the cosmic expansion accelerated again (10.000 million years ago). Today the Universe continues expanding becoming less dense; new stars and galaxies born every time.

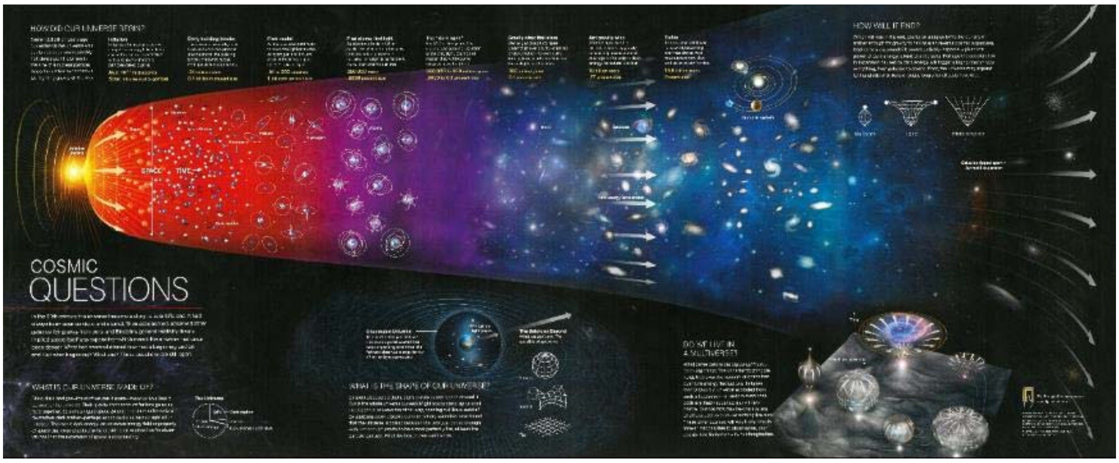

Fig. 1.1. Timeline of the Universe expansion (from National Geographic, April 2014).

The microwave cosmic background (CMB) is the echo of the big explosion of Big Bang. It is a very weak signal that has been travelling over the time. The study of the characteristic of CMB is very important to understand the start point of the universe.

The history of CMB experiments started such a puzzle in the 50's of the XX century. After Einstein, Friedmann and Hubble, the Cosmology tried to fit in the astronomy discoveries with the relativity theory and the effort to explain a coherent universe [1.1].

Fred Hoyle (1915-2001), an astrophysicist from the Trinity College of Cambridge University (England), built the theory of a stable state from the incorrect calculus of Hubble about the Universe age. Hoyle said that the Universe was an eternal body, always existing and creating matter. Hoyle was an enthusiastic transmitter in radios and televisions.

In many appearances, he was strongly discussed by the soviet George Gamow (1904-1968), with the opposite thought about the Universe. Gamow defended the idea a Universe birth, a big explosion. The Universe had a hot radiation at the beginning, and since the Universe is not so old, that radiation remains. But unfortunately at 1950, there were not the suitable technology and instrumentation to measure this radiation and confirm the hypothesis.

When the scientific community was lost in the discussion of the two theories, an evidence, such old as the Universe itself was discovered. This discovery cancelled one the two theories because the Universe was whispering the signal of this birth.

In 1965, Arno Penzias (1933-) and Robert Wilson (1936-) were two scientist working in a communications laboratory for Bell, not in Cosmology. Testing a new communication antenna. They detected a microwave constant signal, independent of the point view of the antenna. The signal was noise similar to the interference of a radio or television. The first hypothesis was they were detecting an excrement of a bird, but after processing the detected signal, that noise remained.

After a few months, a colleague suggested to talk to Robert Dicke (1916-1997), an important American experimental physics from Princeton University. Dicke was searching the signal Gamow postulated. Legend says, the phone call between Wilson and Dicke finished in "we have find either a dove shit or the Universe birth".

Really, what Penzias and Wilson detected was the signal Dicke was searching for, and Gamow was postulated. They discovered the Universe was very hot at the beginning, and cooled down along the timeline. This signal was named the CMB, and it means for the Cosmology the same as the DNA (Deoxyribonucleic acid) for the Genetic.

Wilson and the Princeton team published their work in the Astrophysical Journal in 1965, and Penzias and Wilson obtained de Nobel prize in 1978 for "the discovery of the Cosmic Microwave Background".

1.1. Radio astronomy receivers

The radiometers are the radio astronomy type receivers, aimed to measure the characteristics of CMB such intensity and polarisation. Many experiments studying the intensity and polarisation of the CMB have been developed. The CMB experiments are classified depending the location they are. There are terrestrial instruments, such BiCEPS-2 and Keck Array (South Pole), AMiBA (Hawaii), ABS (Atacama, Chile), CLASS and QUIET (Llano de Chajnantor, Chile), Very Small Array (VSA, Tenerife), VLA (VLA, New Mexico), SKA (the multi-purpose instrument), and MEERKAT as the precursor of SKA (South Africa). VSA, VLA and SKA are interferometer type radio astronomy instruments for multiple radio astronomy experiments. And space missions such WMAP, COBE, and PLANCK. All the instruments cited can measure both intensity and polarisation of the CMB, except COBE, which was the first space mission for CMB observations finished in 1993 and only measured the intensity.

Nowadays, the terrestrial instruments are in observation time. Meanwhile, the space missions are finished and the observation data are under analysis and post-process.

Three architectures have been traditionally adopted in the literature to implement the radio astronomy receivers, the total power, correlation radiometers, and the switched radiometers (used in interferometers) [1.2].

1.1.1. Total power radiometer

The total power radiometer is considered as the basic radio astronomy receiver. Although it is not very used nowadays. The classic scheme of this receiver is shown in Fig. 1.2. The radio frequency (RF) amplifier is often a cooled type, a low-noise cryogenic amplifier. Then a mixer was traditionally used to down-convert the RF to intermediate frequency (IF), so the subsequent detection could be performed. Nowadays, the RF signal is directly detected with detectors working up to 50 GHz. The detector in the radio astronomy receivers is usually a square-law type that provides an output DC voltage directly proportional to the receiver input noise power, and disturbing low-frequency fluctuations. The amplitude of the undesirable fluctuations is softened by a low-pass filter amplifier and an integrator.

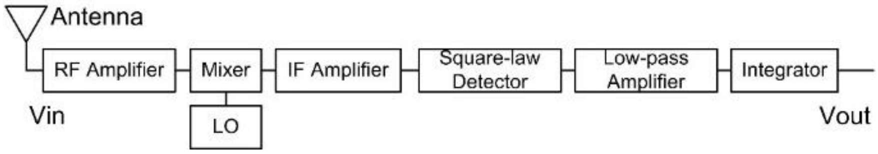

Fig. 1.2. Scheme of the total power radiometer.

The high RF and DC gain in the total power of the receiver requires very stable amplifiers. The gain stability, instead low-frequency fluctuations from receiver noise, determines how small a signal can be detected by the receiver.

1.1.2. Switched radiometer

Dicke was the first to introduce the modulation principle for removing fluctuations induced by receiver instabilities. Fig. 1.3 shows the scheme of the Dicke radiometer. The input of the receiver is switched between the antenna and the reference load with a frequency of f_M. The signal power is modulated at f_M because the signal enters in the receiver through the antenna during half period of the switching frequency. If f_M is high enough in comparison with the gain instability frequencies, it is possible to detect the signal without disturbing effects. The modulation frequency is in practice 10-1000 Hz. Switches are commonly semiconductor diodes.

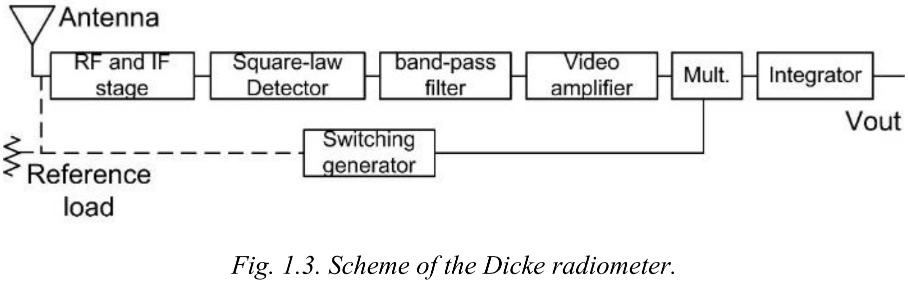

Fig. 1.3. Scheme of the Dicke radiometer.

In the Dicke radiometer the signal is connected to the receiver only half of the time. Hence, the sensitivity is one half of the theoretical sensitivity of the total power radiometer.

One method for obtaining a balanced Dicke radiometer is gain-modulation. Fig. 1.4 shows the scheme of gain-modulation receiver. Two stable passive attenuators are switched in synchronism with the input switch into de RF-IF amplification block.

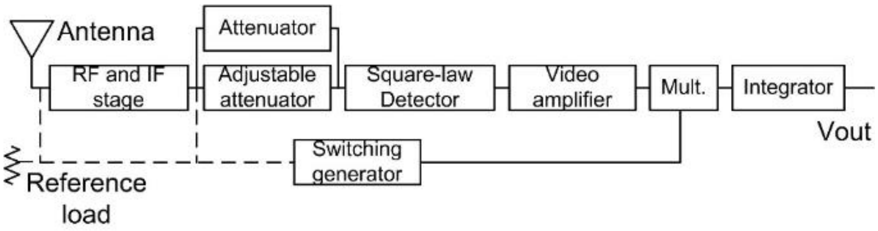

Fig. 1.4. Scheme of the Dicke radiometer with gain-modulation.

All the previous Dicke configurations suffer from gain instabilities when the signal is present, especially when the input signal is strong. The null-balancing Dicke receiver proposed by Machin, Ryle and Vonberg [1.3] assures the balanced condition all the time. The scheme is shown in Fig. 1.5. The comparison load has an adjustable noise source. The output noise power of the source is controlled by the integrator circuit output so that the output is always zero. The output signal of the receiver is then the controlling signal. At very-high (VHF) and ultra-high (UHF) frequencies the comparison source can be a noise diode. At microwave frequencies the comparison source can be a cold load.

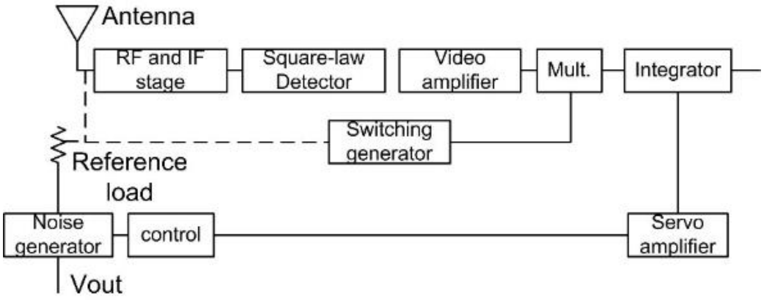

Fig. 1.5. Scheme of the null-balancing Dicke radiometer proposed by Machin, Ryle and Vonberg.

The Dicke configuration only permits the observation of the input signal power half of the time. Full efficiency in the observation time is achieved switching the telescope antenna between two identical receivers. Both receivers can be Dicke radiometers and outputs of both can be added. One implementation was proposed by Graham [1.4] (see Fig. 1.6). Due to the adding of two independent observations the sensitivity is √2 times better than in case of having one receiver.

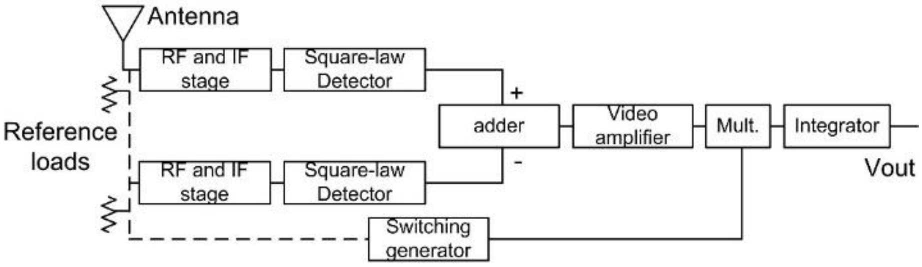

Fig. 1.6. Graham receiver.

1.1.3. Correlation receiver

Two identical receivers can be connected as shown in Fig. 1.7 resulting in a correlation receiver [1.5]-[1.6]. Both receivers are coupled in parallel to the antenna and the IF output signals are multiplied. The multiplier output contains only a correlation sample proportional to the noise power coming from the antenna with is the same for both receivers. The noise powers from the two receivers are uncorrelated, and, hence, will not produce any DC undesirable signal at the output.

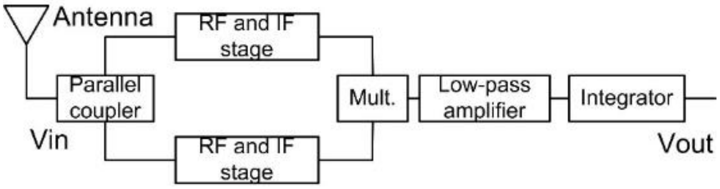

Fig. 1.7. Correlation receiver.

The correlation principle has also been applied by Ryle in the phase switching radiometer used in interferometric applications (Fig. 1.8) [1.7]. Two identical receivers are connected to two antennas of the interferometer. The detector output varies at switching frequency f_M due to the correlated signal.

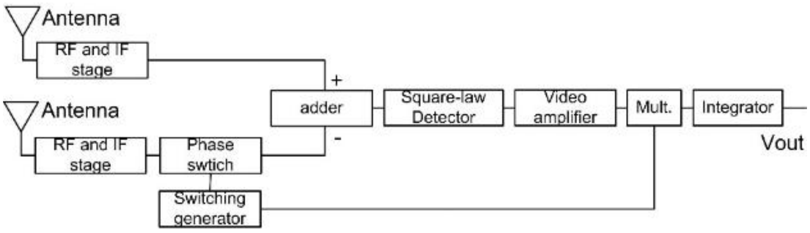

Fig. 1.8. Phase switching receiver.

1.1.4. Calibration of radio astronomy receivers

Radio astronomy receivers must be calibrated in order to measure the signal power. It is common practice to perform the calibration before and after the observation period or use a calibration signal switched automatically and periodically.

1.2. QUIJOTE experiment

The QUIJOTE experiment (Q-U-I JOint TEnerife) is a scientific consortium formed by the Astrophysics Institute of Canary Islands (IAC), the Physics Institute of Cantabria (IFCA), the Department of Communications Engineering of University of Cantabria (DICOM), the Jodrell Bank Observatory of Manchester (United Kingdom), the Cavendish Laboratory in Cambridge (United Kingdom), and Spanish company IDOM. The experiment consists in two telescopes and three instruments aimed to measure the polarisation of the Cosmic Microwave Background (CMB) radiation from the sky. The frequency operation band of the instrument goes from 10 to 47 GHz, in order to characterise the CMB and other processes of galactic and extra-galactic emissions, with big resolution scales (around one degree) [1.8].

First instrument, named the Multi-Frequency Instrument (MFI), has eight channels centred in the frequencies of 11, 13, 17 and 19 GHz. Nowadays the first telescope is working in the Observatory of Teide (Tenerife) with the first instrument.

Second instrument (TGI, Thirty Gigahertz Instrument) has 29 receivers working at 30 GHz. The number of receivers has been optimised to have suitable sensitivity to detect a component of gravitational waves which is related to the CMB through the B-modes. The detection of B-modes opens a new way to understand the physics of the inflation period of Universe. The TGI is in integration and verification stage in the Observatory of Teide.

Second stage of QUIJOTE experiment includes a third instrument (FGI, Forty Gigahertz Instrument) working at 40 GHz. This instrument will be placed in a second telescope already installed at Teide. The number of receivers in the instrument is also 29. Nowadays, the FGI is under manufacture stage.

All the instruments of QUIJOTE are polari-meters, radiometers with the capability to measure the polarisation of the input signal. They are correlation receiver type. The signal is captured by a telescope [1.9], Fig. 1.9, with a Dragon Gregorian scheme, formed by two parabolic reflectors: a primary of 2.25 meters diameter, and a secondary of 1.85 meters diameter. The telescope is designed to have low cross-polarisation and a symmetric radiation beam. The system is sub-illuminated to minimize side-lobes and the Earth radiation.

Fig. 1.9. QUIJOTE telescopes installed at Observatory of Teide (Canary Islands). Photo courtesy from IAC, June 2015.

TGI and FGI receivers are implemented following a similar scheme. In Fig. 1.10, the FGI scheme is presented. There is a front-end module (FEM) cooled down to cryogenic temperatures (20 K) to have the noise as low as possible. Then, there is the back-end module (BEM) working at room temperature (298 K).

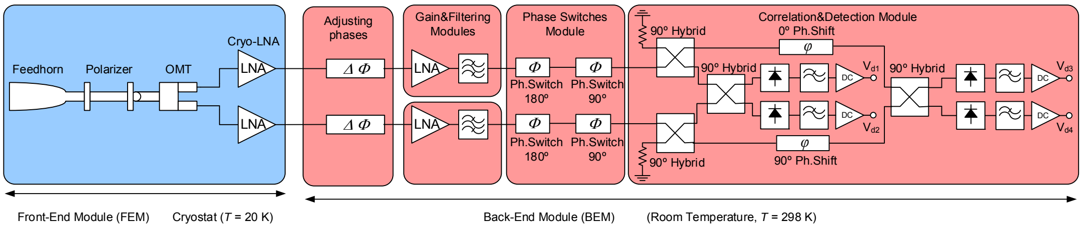

Fig. 1.10. FGI block diagram.

FEM is composed by the feed system followed by the cryogenic low-noise amplifier (cryo-LNA). The cryo-LNA is cooled down in order to have the lowest noise as possible, and the feed system in order to minimize its contribution to the receiver noise because they are at the front of the receiver. Feed system is composed by a feed-horn antenna, a polarizer, and the ortho-mode transducer (OMT).

The assembly polarizer and the OMT provides two components proportional to the left and right circular polarisation waves of the input signal captured by the antenna. The two signals are amplified and filtered in two branches with a theoretical identical amplitude and phase response. Fine adjustment to balance the two branches is made up with an adjusting phase at the input of the BEM (see Fig. 1.10).

The amplification is done in two stages, the cryo-LNA in the FEM and in the BEM. Fig. 1.11 shows a photo of the integration of FEM of TGI inside the cryostat. The TGI will share the cryostat with the FGI instrument so both receivers follow the same architecture in the FEM. Fig. 1.12 shows the integration of 30 pixels in the cryostat at the Assembly, Integration and Verification (AIV) laboratory of IAC.

The correlation and detection of the input signal is done in the BEM. A phase modulation is performed before detection to prevent systematic errors. This modulation is done with a phase-switch module formed by two identical branches with broadband 180º/90º switches. The switching velocity is set to 16 KHz, a frequency much more slow than the radio frequency input signal.

The correlation consists in additions and subtractions of the microwave signal, based on 90º hybrids and a 90º fixed phase shifter in one of the two branches. The DC output of the receiver is proportional to the Stokes parameters (Q, U, I) both the four modulation states (0º, 90º, 180º and 270º). The Stoke parameters define the polarisation level of an electromagnetic wave and they are the magnitudes to extract from the observations.

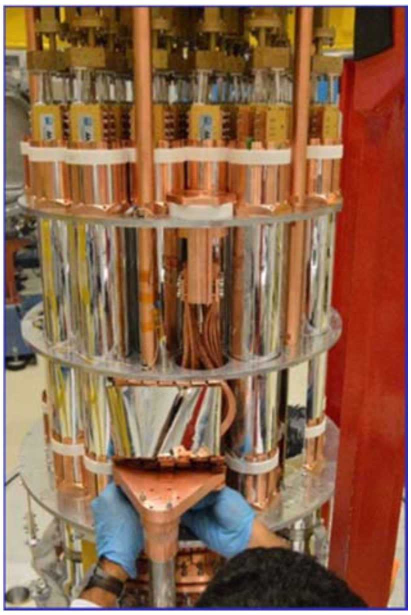

Fig. 1.11. Integration of TGI FEM in the cryostat.

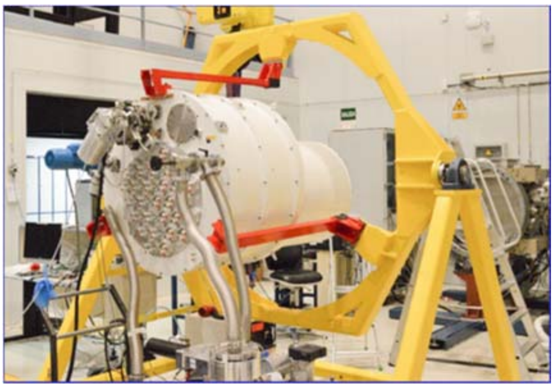

Fig. 1.12. General view of the full TGI/FGI cryostat in the AIV (integration and verification) laboratory at IAC (Canary Islands).

1.3. Motivation

This work deals with the FGI instrument of QUIJOTE. The performance of polarimeter radiometers is mainly improved focusing on the sensitivity. The sensitivity in a radiometer is directly affected by system temperature and effective bandwidth. The lower temperature system temperature, the high sensitive is a radiometer. On the other hand, the broadband is the effective bandwidth, the more sensitive is the radiometer.

As seen before, the FGI radiometer is divided in two parts, front-end (FEM) and back-end (BEM) modules. The heart of temperature in a receiver is in the FEM, where the low-noise amplifier mainly sets the overall noise. Moreover, a high gain in the FEM minimizes the noise temperature contribution of BEM. The effective bandwidth of the receiver is a key to achieve a higher sensitivity minimizing the observation time. The equalization of gain modules minimizes the ripple and flats the gain in order to increase the bandwidth of the receiver.

The level of RF power driven into the correlation and detection modules is very important to guarantee a linear behaviour. Traditionally, the compression point of low-noise amplifiers is poor. Improving the output power level of the low-noise amplifiers is an issue to be considered in the behaviour of a radio astronomy receiver.

1.4. Outline of the thesis

The thesis is divided into eight chapters:

- The present chapter 1 draws a frame and introduces the work done. The motivation of the thesis is also presented.
- The design and implementation of cryogenic amplifiers aimed to FEM of radio astronomy receivers are presented in chapters 2 and 3. The design of low-noise amplifiers with different technologies is the goal.
- Chapter 4 presents and analyses the technique of active load to improve the noise performance in distributed amplifiers. The distributed topology is used in the gain module of a radio astronomy receiver to increase the output power delivered to correlation and detection modules.
- In order to increase the bandwidth of a receiver the design of different equalisers based on microstrip technology is detailed in chapter 5.

- The analysis and characterization of full FGI instrument is presented in chapter 6, from the mathematical analysis of the principle of operation to the validation in laboratory tests.
- A new instrument in W-band is proposed to complement the QUIJOTE experiment in chapter 7. The choice of W-band as a new observation window is discussed. Different configurations of the W-band radiometer made up with commercial components will be performed to validate the feasibility of the future instrument.
- The chapter 8 summarizes and comments the results obtained in the thesis.

1.5. References

[1.1] Daniel Manrique, *Fundamentos de Cosmología, La ciencia del Universo*, Ediciones Guadalmazán, Septiembre 2016.

[1.2] M. E. Tiuri, “Radio Astronomy Receivers”, IEEE Transactions on Military Electronics, July-October 1964, pp. 264-272

[1.3] K. E. Machin, M. Ryle, and D. D. Vonberg, “The design of an equipment for measuring small radio-frequency noise powers”, *Proc. IEE*, vol. 99; pp. 127-134; May, 1952.

[1.4] M. H. Graham, “Radiometer circuits”, *Proc. IRE*, vol. 46, p. 1966; 1958.

[1.5] S. J. Goldstein, Jr., “A comparison of two radiometer circuits”, *Proc. IRE*, vol. 43, pp. 1663-1666; November, 1955.

[1.6] D. G. Tucker, M. H. Graham, and S. J. Goldstein, Jr., “A comparison of two radiometer circuits”, *Proc. IRE*, vol. 45, pp. 365-366; March, 1957.

[1.7] M. Ryle, “A new radio interferometer and its application to the observation of weak radio stars”, *Proc. Roy. Soc. (London) A*, vol. 211, pp. 351-375; 1952.

[1.8] Eduardo Artal Latorre, Beatriz Aja Abelán, Juan Luis Cano de Diego, Luisa de la Fuente Rodríguez, Angel Mediavilla Sánchez, José Vicente Terán Collantes, Enrique Villa Benito, “Radiómetros en ondas milimétricas del experimento QUIJOTE”, Simposium Nacional de la Unión Científica Internacional de Radio, URSI 2016, Madrid, 5-7 Septiembre, 2016.

[1.9] A. Gomez, G. Murga, B. Etxeita, R. Sanquirce, R. Rebolo, et al. "QUIJOTE telescope design and fabrication", Porc. SPIE 7733, Ground-based and Airbone Telescopes III, 77330Z (July 28, 2010); doi: 10.1117/12.857286.

CHAPTER II: CRYOGENIC BROADBAND Q-BAND MMIC LOW-NOISE AMPLIFIER

2.1. Introduction

In the field of radio astronomy, the scientist community demands high sensitivity receivers in order to detect very weak signals from the sky. Cryogenic low-noise amplifiers (LNA) are placed in the front-end of these receivers to amplify these weak input signals with a very low contribution to the overall noise [2.1]-[2.3].

Research activity in new materials has led to the development of HEMT on indium phosphide (InP) semiconductor technology, which allows to have amplifiers with very high gain and ultra-low-noise [2.4]. However a low stability, fragility and limited access to this technology, have pushed the development of metamorphic HEMT (mHEMT) on Gallium Arsenide (GaAs) semiconductor substrates with a high content of InP in the channel, leading to high performance semiconductors. Many works based on mHEMT structures have been presented with excellent results [2.5]-[2.9].

The monolithic technology (MMIC) can be a better option for high frequency designs since the element sizes and their interconnections can be more accurate controlled and higher yield is achieved. However, this technology has the handicap of the costs associated with its production (for low quantities) and sometimes it is not affordable.

Since there are some commercial products like references CGY2122XUH from OMMIC foundry and CHA2194-99F from UMS (United Monolithic Semiconductors), they does not cover the whole Q band. So a custom cryogenic low-noise amplifier must to be designed for specific radio astronomy applications.

The design of a cryogenic MMIC LNA in the 33- 50 GHz (corresponding to the Q frequency band) with very low-noise and DC power consumption is described in next lines [2.10].

2.2. Technology

With the aim of develop European technology, the design of the MMIC LNA is done using the technology from OMMIC foundry (stablished in France).

Transistors are built in a mHEMT technology process with 70 nm gate length called D007IH. The active component is based on a GaInAs-InAlAs-GaInAs-InAlAs hetero-structure and a conductive channel with 52% and 70% of Indium content respectively (Fig. 2.1). It provides a transition extrinsic frequency f_T = 300 GHz and a maximum oscillation frequency f_{max} = 350 GHz. The wafer is thinned down to 100 µm.

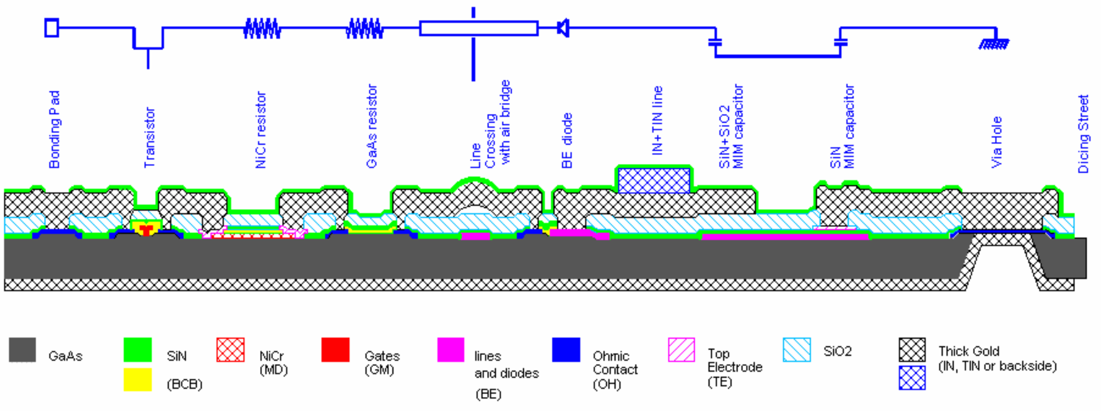

Fig. 2.1. Layers for process D007IH of OMMIC foundry.

For the amplifier design the transistor size is chosen to have a 4 fingers x 15 µm gate periphery for all the stages of the amplifier. Fig. 2.2 shows a picture of this OMMIC mHEMT transistor.

2.3. MMIC LNA design

The design of the amplifier starts modelling the heart of the circuit, the transistor. A schematic level design finds the requirements for linear performance and noise. Finally an electromagnetic optimization completes the LNA, in which layout considerations are taking into account for manufacturing process.

2.3.1. Transistor Small-Signal and Noise Models

Accurate small signal and noise transistor models are very important for a successful LNA design. Using discrete transistors with the same gate periphery and same technology that those used in the amplifier design, DC (Fig. 2.3) and S-parameter measurements have been made to extract the small signal model. In order to get the model, the approach followed in [2.11]-[2.12] is used to get an estimation of the suitable bias point for low-noise. From DC measurements, the minimum of the function (2.1) can be calculated providing the optimum bias point to minimize T_{min}. The bias point chosen for the OMMIC 4x15 gate length mHEMT transistor is V_d = 0.6 V and V_g= -0.125 V (a minimum in Fig. 2.4). The drain current is I_d = 6.7 mA.

$$f(V_{ds}, V_{gs}) \sim \frac{\sqrt{I_{ds}}}{g_m} \tag{2.1}$$

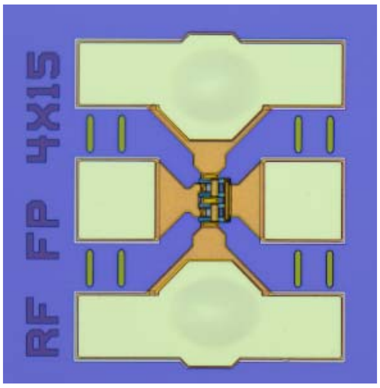

Fig. 2.2. A 4 x 15 µm OMMIC mHEMT transistor.

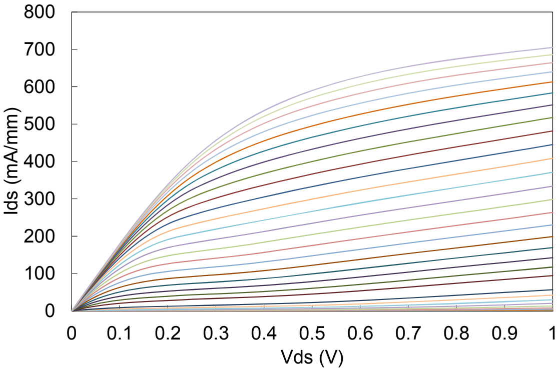

Fig. 2.3. IV curves for a 4x15 µm OMMIC mHEMT transistor. V_{ds}: 0 to 1 V. V_{gs}: -1 to 0.3 V, in steps of 25 mV.

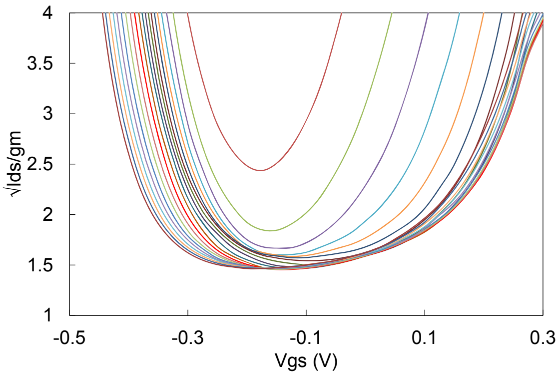

Fig. 2.4. The 4x15 µm OMMIC mHEMT transistor bias approximation for minimum noise (1). V_{gs}*: -0.5 to 0.3 V in steps of 25 mV.* V_{ds}*: 0 to 1 V, in steps of 50 mV.*

Fig. 2.5 shows the small signal model. The numerical values for the bias point chosen, $V_d = 0.6$ V and $I_d = 6.7$ mA are shown in Table 2.1.

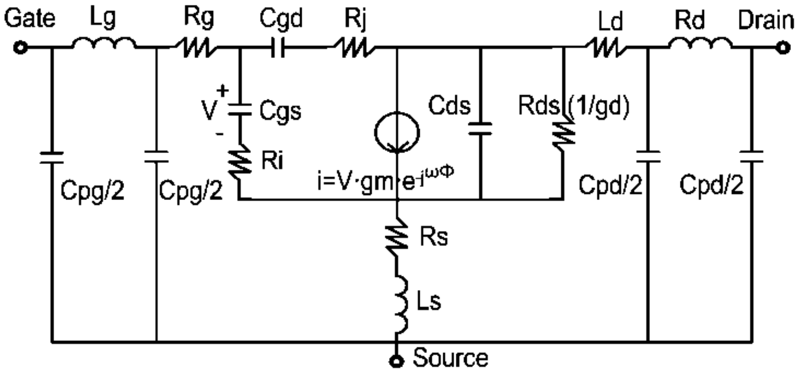

Fig. 2.5. The 4x15 µm mHEMT transistor small signal model.

Table 2.1. Small signal parameters values for a 4 x15 µm OMMIC mHEMT transistor. $V_d = 0.6$ *V,* $I_d = 6.7$ *mA.*

Intrinsic parameter	**Value**	**Extrinsic parameter**	**Value**
Cgs	38 fF	Cpg/2	14.75 fF
Ri	7.5 Ω	Lg	38.31 pH
Cgd	13.7 fF	Rg	0.5 Ω
Rj	19 Ω	Cpd/2	14.75 fF
Gm	71 mS	Ld	40.75 pH
Φ	0 ps	Rd	4.19 Ω
Cds	17.5 fF	Rs	2.75 Ω
Gd	6.9 mS	Ls	4.84 pH

The agreement between the measured S-parameters (blue traces in Fig. 2.6) and the model (red traces in Fig 2.6) is quite good.

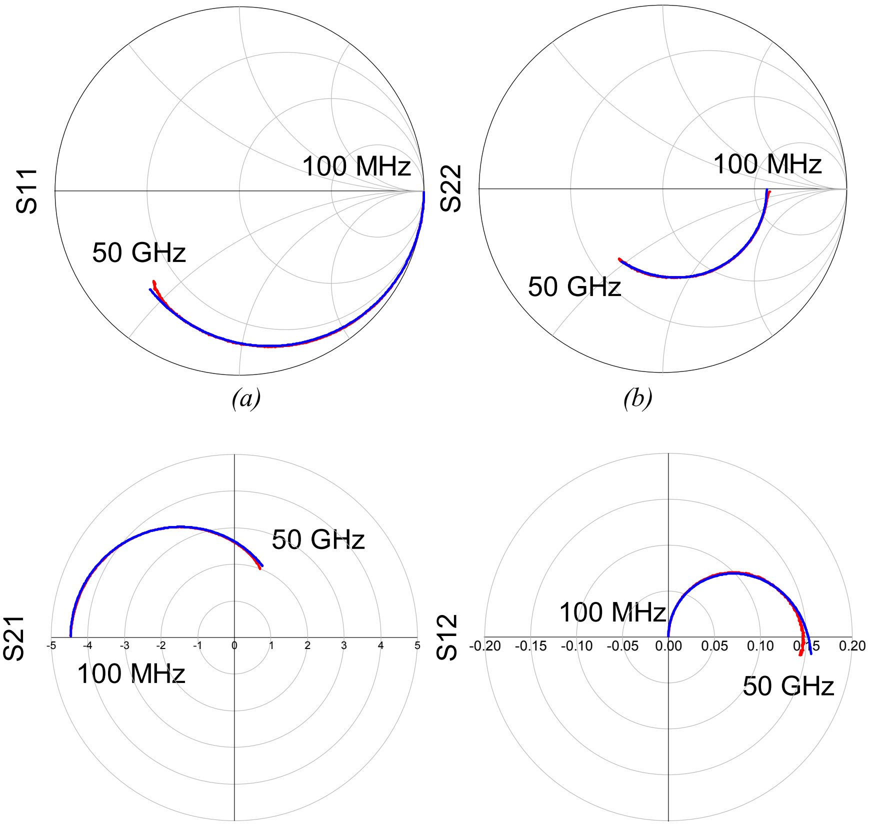

(a) (b)

(c) (d)

Fig. 2.6. Linear performance of the 4x15 µm OMMIC mHEMT transistor. Blue, measurements. Red, simulation of the model (Fig. 5). (a) S_{11}*. (b)* S_{22}*. (c)* S_{21}*. (d)* S_{12}*.*

For the noise model, the Pospieszalski model [2.11] has been used and the two temperatures T_d and T_g have been obtained. T_g is assumed to be equal to the ambient temperature and 50 Ω noise figure measurements of the transistor have been made in order to get T_d. The results of these measurements for $V_d = 0.6$ V and $I_d = 6.7$ mA are shown in Fig. 2.7, where the ripple is due to mismatching between the transistor and the source. The value obtained for T_d is 3200 K, while the remaining resistors of the small signal model are set to an ambient temperature $T_g = 300$ K. Note that noise figure measurements were performed up to 40 GHz (Ka-band) due to the laboratory set-up available. Anyways, the noise model is reasonable extrapolated up to 50 GHz (Q-band).

A 2x15 µm (Fig. 2.8) OMMIC mHEMT was also measured to clarify the best size of the transistor to design the LNA. DC curves (Fig. 2.9) are similar to the 4x15 µm transistor (Fig. 2.3). The bias point for minimum noise (Fig. 2.10) is the same as for the 4x15 µm transistor, $V_d = 0.6$ V, $V_g = -0.125$ V.

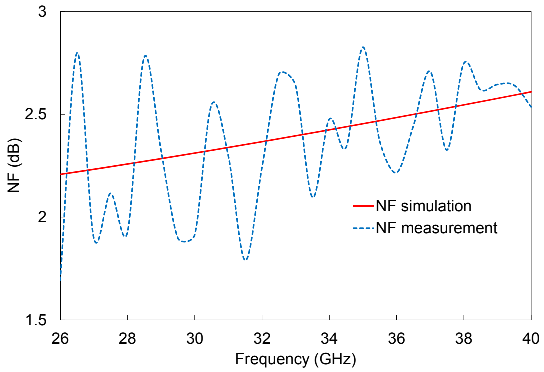

Fig. 2.7. Noise performance over 50 Ω of a 4 x 15 μm OMMIC mHEMT transistor at room temperature for $V_d = 0.6$ V and $I_d = 6.7$ mA.

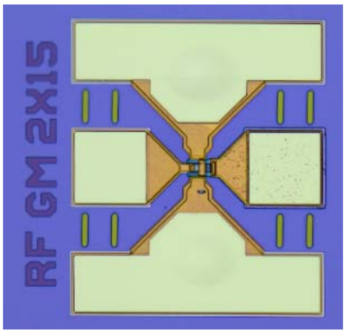

Fig. 2.8. Photo of a 2x15 μm OMMIC mHEMT transistor.

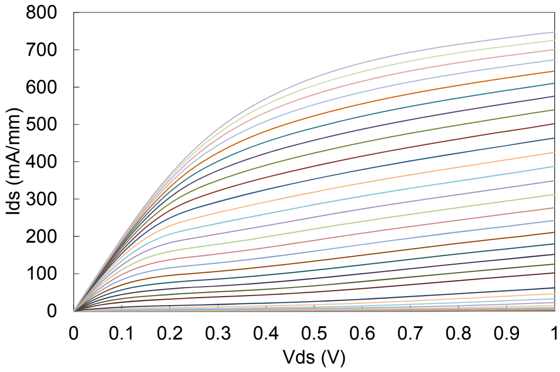

Fig. 2.9. IV curves for a 2x15 μm OMMIC mHEMT transistor. V_{ds}: 0 to 1 V. V_{gs}: -1 to 0.3 V, in steps of 25 mV.

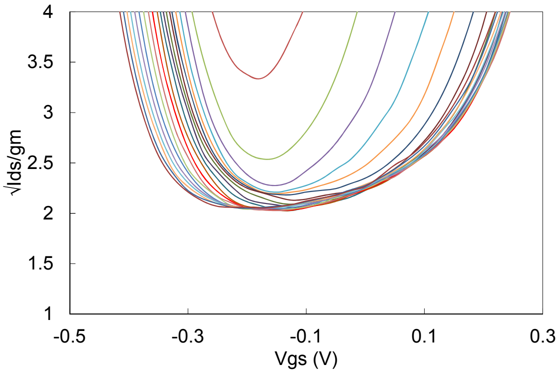

Fig. 2.10. The 2x15 μm OMMIC mHEMT transistor bias approximation for minimum noise (1). V_{gs}: -0.5 to 0.3 V in steps of 25 mV. V_{ds}: 0 to 1 V, in steps of 50 mV.

Noise measurements are performed for different drain current densities (mA/mm). The mean noise figure in 2x15 µm (Fig. 2.11(b)) transistor is 0.5 dB higher than the noise figure of 4x15 µm option (Fig. 2.11(a)). So the 4x15 µm is the best option attending to 50 Ω noise measurements at room temperature.

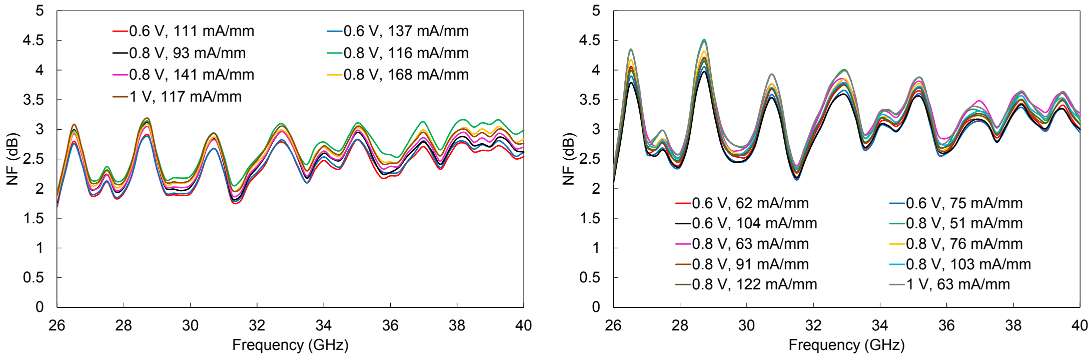

(a) *(b)*

Fig. 2.11. Noise performance versus frequency for different drain current densities (mA/mm). (a) 4x15 µm, (b) 2x15 µm transistor.

To check the goodness of the noise model a parameter called *R* (2.2) is defined following [2.11]. The foundry model (blue) is compared with the homemade model (red) in Fig. 2.12. Both the homemade extracted small signal and foundry models satisfy the condition, *R*<2, in (2.2), from DC to 50 GHz.

$$1 \le R < 2$$
$$R = \frac{4 \cdot N \cdot T_0}{T_{min}} \tag{2.2}$$

where $N = R_{opt} \cdot g_n$, R_{opt} is the real part of optimal noise impedance, and g_n is the noise conductance ($1/R_n$). T_{min} is the minimum noise temperature.

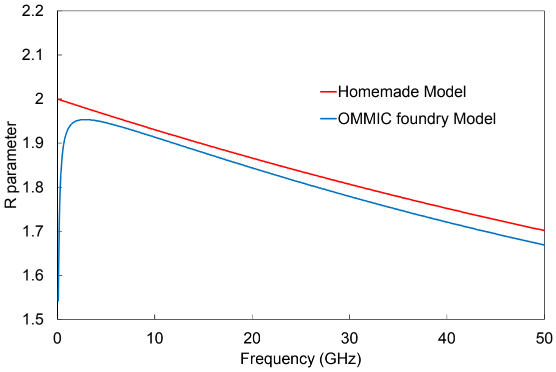

Fig. 2.12. Parameter R. In blue the foundry model. In red the homemade model.

The major difference appears in noise parameters R_n and S_{opt}. The noise resistance R_n (Fig. 2.13(b)) is ten ohms lower in the homemade small signal model. Meanwhile, the S_{opt} (Fig. 2.13(c)) is close to 50 ohms so the homemade small signal model is easy to match the optimum noise coefficient with 50 ohm input reflection coefficient.

The homemade model shows a realistic and higher noise figure over 50 Ω than the foundry model (Fig. 2.13(d)).

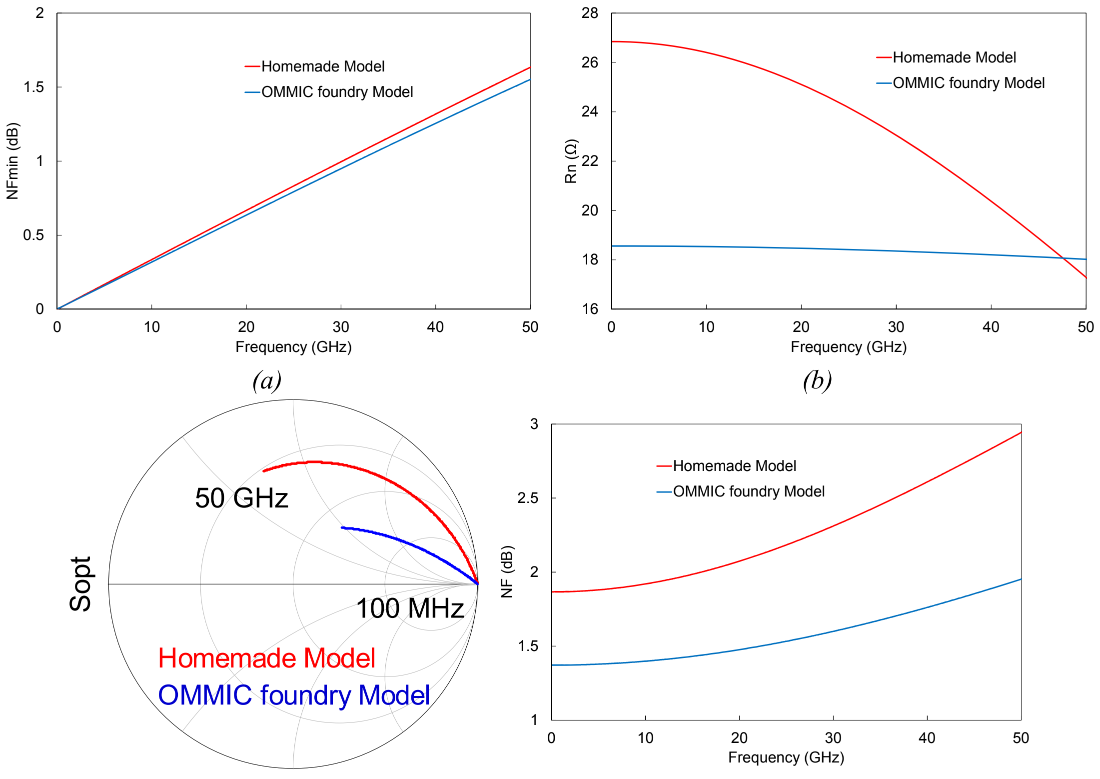

(a) *(b)*

(c) *(d)*

Fig. 2.13. Noise parameters and noise over 50 Ω of the 4x15 μm OMMIC mHEMT transistor. In red the foundry model. In blue the homemade model. (a) NFmin. (b) R_n. (c) S_{opt}. (d) NF over 50 Ω.

2.3.2. LNA design

The MMIC LNA is a classic four stage design with transistors in common source configuration. All the stages have the same transistor size of 4 x 15 μm and the same bias point ($V_d = 0.6$ V, $I_d = 6.7$ mA). Source feedback technique for the two first stages has been used to get good noise performance as well as input matching and stability. J. Engberg [2.13] presented in 1974 an optimisation method for low-noise amplifiers, in which the use of series-shunt configurations match the input conjugate admittance to the optimum noise admittance. Moreover, with the use of lossless networks, it was considered that noise did not vary because feedback was not introducing noise itself. L. Besser [2.14] added one year later the noise variation versus series-shunt source feedback network. In [2.15] the exact noise figure formulation is presented taking into account both series and shunt feedback. In 1985 [2.16] the source feedback technique is introduced in X-band monolithic amplifier (8-12 GHz). In Fig. 2.14 the input conjugate reflection coefficient (blue) and optimum noise coefficient (red) are plotted in a Smith chart before (Fig. 2.14(a)) and after (Fig. 2.14(b)) a series source feedback is added to the transistor. Feedback joins both coefficients and move them to the centre of Smith chart improving matching.

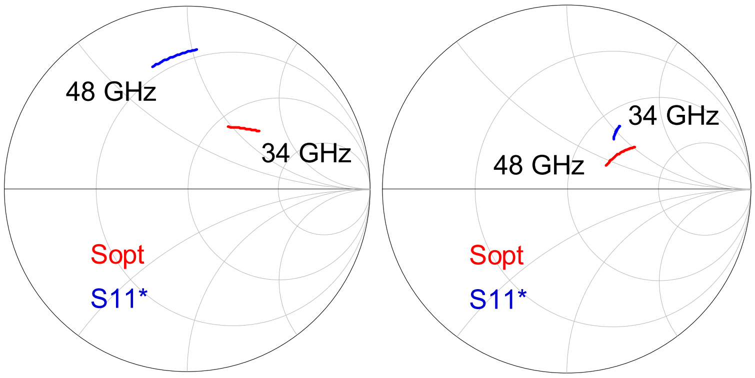

(a) *(b)*

Fig. 2.14. Noise optimum coefficient (red) and conjugate input reflection coefficient (blue). (a) Before and, (b) after the source feedback is introduced in the transistor.

Since the first stage is the most important in terms of noise, the design should rely on simple microstrip lines for the input stage. Matching networks for the last two are designed to achieve flat gain keeping the noise of the amplifier as low as possible. Design and optimization processes are carried out using ADS Momentum simulator from Keysight Technologies. Bias networks are kept independent for each stage and they are made up of a combination of resistors and capacitors providing filtering networks. Fig. 2.15 shows the schematic of the LNA with the bias networks.

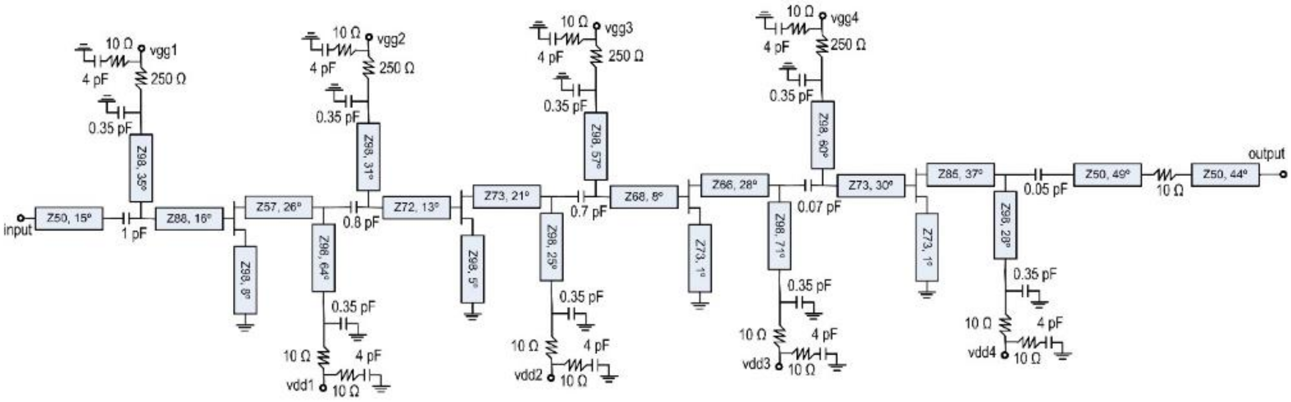

Fig. 2.15. Schematic of the four stage MMIC LNA (impedance and electrical length of microstrip lines are obtained at central frequency of 41 GHz).

The knowledge of the technological process is an important issue to be carefully considered in the electromagnetic optimisation. In Fig. 2.16 the layers map used in the layout of the LNA is presented. Layers go from the most external called FreeSpace to Ground (GND). The detail of each layer of the process D007IH used is described below.

- The most external conductive layers IN and TIN are placed between the first layer of Silicon Nitride (SiN) and the layer of Silicon Oxide (SiO). IN layer is the second interconnection metallic layer of TiPtAu with 1.25 µm of thickness. TIN layer is the first interconnection metallic layer of the same thickness and material than IN layer.
- A via hole is in the Silicon Oxide layer to connect IN, TIN layer to next conductive layer (TE). Via hole is in CO layer made up of a dielectric deposition of Silicon Oxide with 800 µm of thickness.
- Next layer is TE which forms the top electrode of the MIM capacitors. It is also used to protect the gates in TiAl and the gold lines in order to guarantee a high reliable connection. The thickness is 560 µm.
- Below TE it is found the second layer of Silicon Nitride in which via hole is implemented in CG mask. This mask is formed by Silicon Nitride (Si_3N_4) and interconnects metals.
- Next layer is BE. Formed by TiPtAu is a metallisation used as the bottom electrode of MIM capacitors. It is also used in 3 µm diodes. Its thickness is 650 nm.
- A Benzocyclobutene (BCB) layer is deposited on a Silicon Nitride floor of 10 nm. It is used to support the gates of the transistors with a layer of low dielectric constant (2.65) and 800 nm of thickness. So the active parts are protected. Moreover, it is used in diodes and GaAs/NiCr resistors. In this layer there are defined via holes in CG mask to interconnect metals.
- Finally, the resistive layer MD is implemented. It is used in NiCr resistors. It has a 30 nm of thickness and a resistivity of 40 Ω/square.

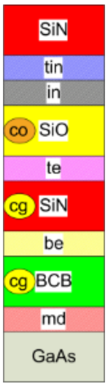

Fig. 2.16. Layers of the process D007IH from OMMIC foundry.

There are a lot of layers defined in the process D007IH but there are referred to the active component, the transistor. Since in the electromagnetic optimisation the microstrip networks are only included, the transistor layers are not defined in this text.

2.3.3. Yield

When a large amount of MMIC chips has to be manufactured it is important to have an estimation of how many chips will achieve the performance requirements. This information is a statistical data about variations in the elements that compose the circuit. For example, all the monolithic processes have tolerances in the resistivity of resistors, gap in capacitors, dimensions of microstrip lines, or the model of the transistors. Measuring own structures of the process (PCM, process control monitor) the probability distribution function that determines how is the variation of the components of the process is obtained. Yield analysis includes the simulation of the circuit many times where different parameters of the design are varied around their nominal value. The simulator registers each iteration like a pass or a fail depending the performance is achieved or not. This a Monte Carlo method of analysis which has the property of the precision is independent of the number of statistical variables and distributions.

The difference between the obtained yield and that expected depends directly on the iterations of the analysis done. If the number of iterations is small, the results probably will not be representative and the statistical error will be high. So it is necessary a big number of iterations in order to have a high confidence level and very low statistical error.

Main results obtained in the simulator after a yield analysis are:

Mean value $$m_x = \frac{\sum_{i=1}^{n} x_i}{n} \tag{2.3}$$

Standard deviation
$$\sigma_x = \sqrt{\frac{\sum_{i=1}^{n}(x_i - m_x)^2}{n-1}} \tag{2.4}$$

Correlation coefficient
$$\rho_{xy} = \frac{\sum_{i=1}^{n}\sum_{j=1}^{n}(x_i - m_x)\cdot\left(y_j - m_y\right)}{(n-1)\cdot\sigma_x\cdot\sigma_y} \tag{2.5}$$

The mean value and the standard deviation are typical indicators. The correlation coefficient denotes the quantitative variations of variable *x* with variable *y* (2.5). Moreover, it explains de variations of *x* and *y* with a third variable that usually is the time.

In next lines a yield analysis of the designed LNA is performed. The variables to be varied are the dimensions of the transmission lines, capacitor values, and some transistor parameters (*gm*, pinch-off, etc.).

2.3.3.1. Large signal model yield analysis

The yield analysis in large signal is necessary to evaluate the variations of the transistor. The analysis is divided into two parts: the first one is focused in Scattering parameters in the frequency band of interest (35-47 GHz) and second covers the frequency band 100 MHz – 80 GHz to analyse the stability of the LNA.

In this analysis the noise performance is not evaluated because the large signal model of the transistor has no information about noise parameters.

The goals of Scattering yield analysis in the 35-47 GHz frequency band are:

- $|S_{21}|^2 > 25$ dB.
- $|S_{11}|^2 < -10$ dB.
- $|S_{22}|^2 < -8$ dB.
- Iterations number for the analysis = 1000.

The results of the Scattering yield analysis are shown in the histograms of Fig. 2.17. These histograms represent the distribution function of the values of the Scattering parameters. The values of the mean and the standard deviation are summarized in Table 2.2.

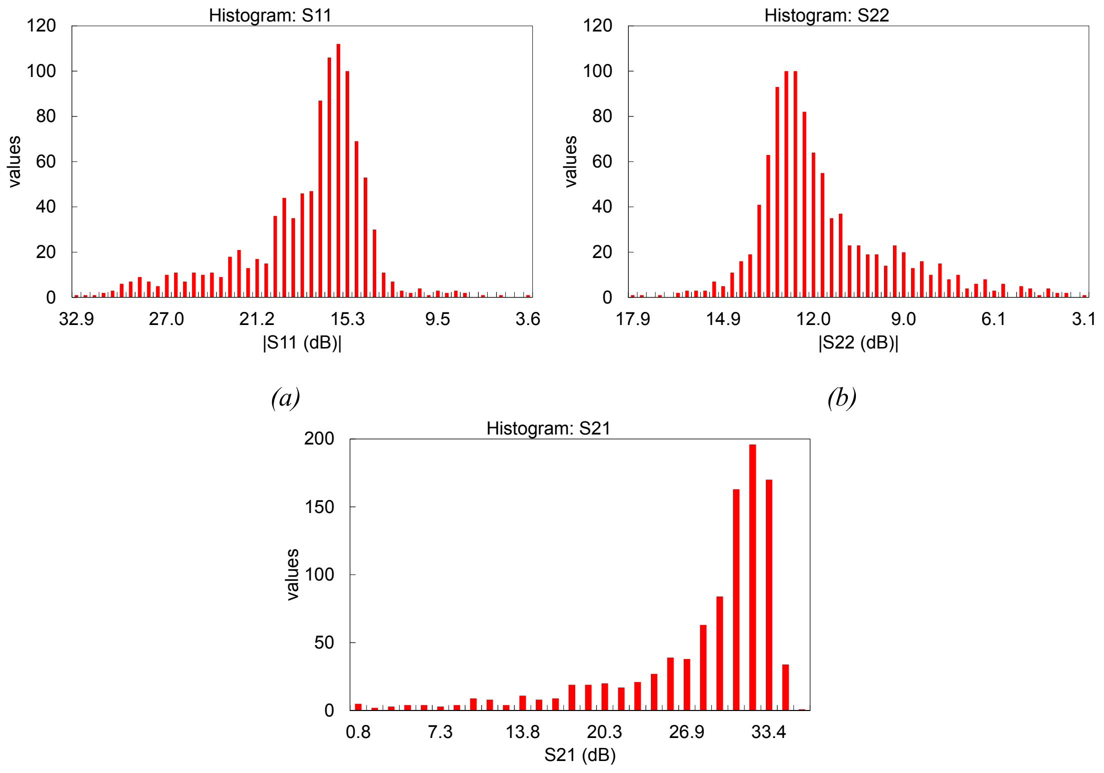

(a) *(b)*

(c)

Fig. 2.17. Histograms of Scattering yield analysis in large signal model for 1000 iterations. (a) S_{11}. (b) S_{22}. (c) S_{21}.

Table 2.2. Mean and standard deviation for Scattering yield analysis of the LNA with transistor large signal model.

Parameter	Mean (dB)	Standard deviation (dB)
S_{11}	-17.8	4.1
S_{22}	-11.7	2.2
S_{21}	27.6	8.1

The percentage of circuits that achieve the performance requirements is 60.4 %. It means, 604 chips will pass the test in a hypothetic amount of 1000 chips manufactured. This value is quite small, so an analysis in small signal will be done to compare the results.

The second analysis with the transistor large signal model is the stability. It is studied through the parameters k and μ, which they have to be greater than 1. Fig. 2.18 shows the histograms and Table 2.3 summarises the mean and deviation of these parameters. In this case the yield is the 100%, it means, all the manufactured circuits will pass the test in terms of stability.

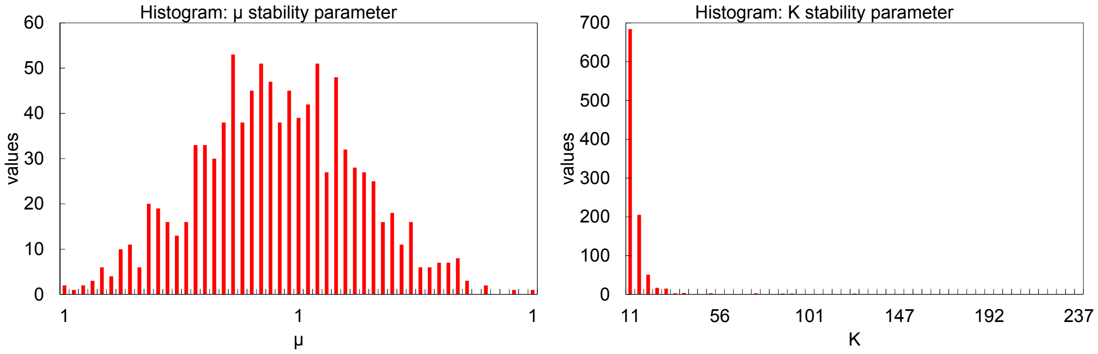

(a) *(b)*

Fig. 2.18. Histograms of stability yield analysis in large signal model for 1000 iterations. Parameters: (a) μ. (b) k.

Table 2.3. Mean and standard deviation for stability yield analysis of the LNA in large signal regimen.

Parameter	Mean	Standard deviation
μ	1	1.2e-6
k	15.1	15.1

2.3.3.2. Small signal model yield analysis

In the yield analysis using the transistor small signal model, the variations are only produced in passive elements. So the transistors are excluded in this analysis. The noise performance is added to the Scattering analysis. The new goals are:

- $|S_{21}|^2 > 25$ dB.
- $|S_{11}|^2 < -10$ dB.
- $|S_{22}|^2 < -10$ dB.
- NF (noise figure) < 1.8 dB.
- Iterations number for the analysis = 750.

In Fig. 2.19, the histograms for Scattering and noise are shown. In Table 2.4 mean and standard deviation simulation results are summarised. Comparing the results with the ones obtained in Table 2.3, it is clear the deviation values are now smaller and the mean values better. So the predicted yield is higher in the small signal analysis. In fact, it is a 100 % compared with 60 % in the case of large signal model. This is due to the higher influence of the active element, the transistor, in the performance of the LNA MMIC.

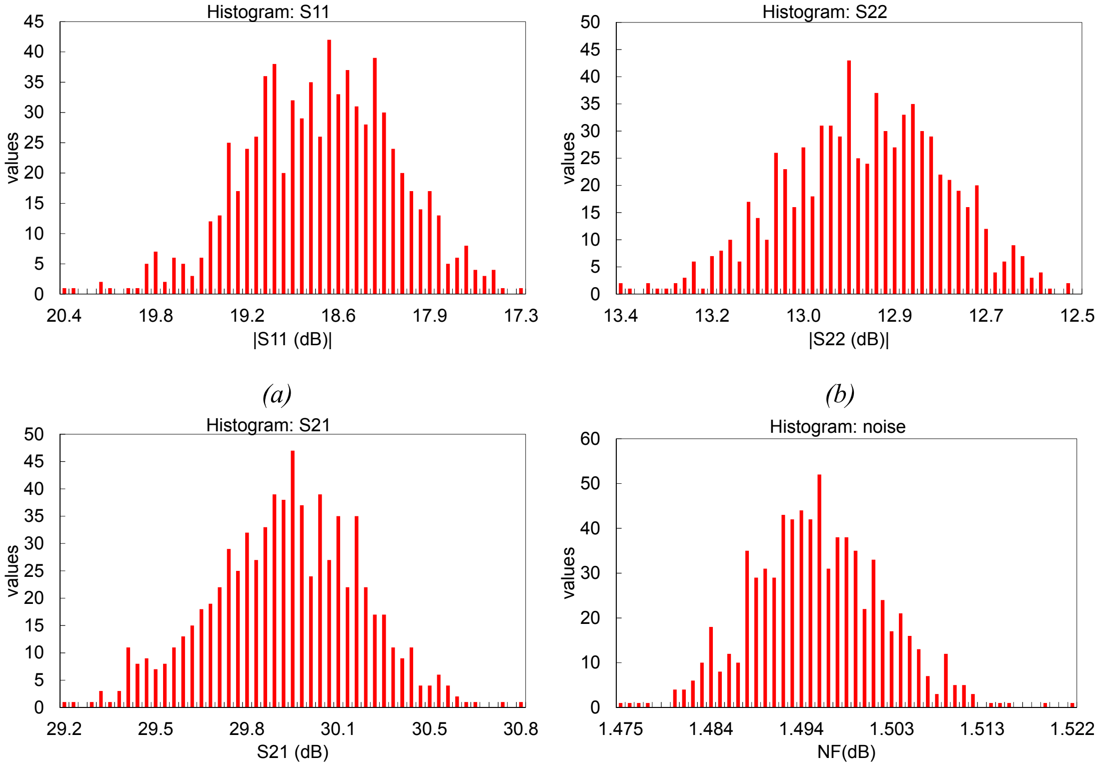

(a) *(b)*

(c) *(d)*

Fig. 2.19. Histograms of Scattering yield analysis in small signal model for 750 iterations. (a) S_{11}. (b) S_{22}. (c) S_{21}. (d) Noise figure.

Table 2.4. Mean and standard deviation for Scattering yield analysis of the LNA in small signal regimen.

Parameter	Mean (dB)	Standard deviation (dB)
S_{11}	-18.6	0.51
S_{22}	-12.9	0.15
S_{21}	29.9	0.26
NF	1.49	0.007

The stability yield analysis with small signal model achieves the same results than in large signal regimen, as expected. In Fig. 2.20 the histograms for parameters k and μ are plotted, and in Table 2.5 the mean and deviation obtained are summarised.

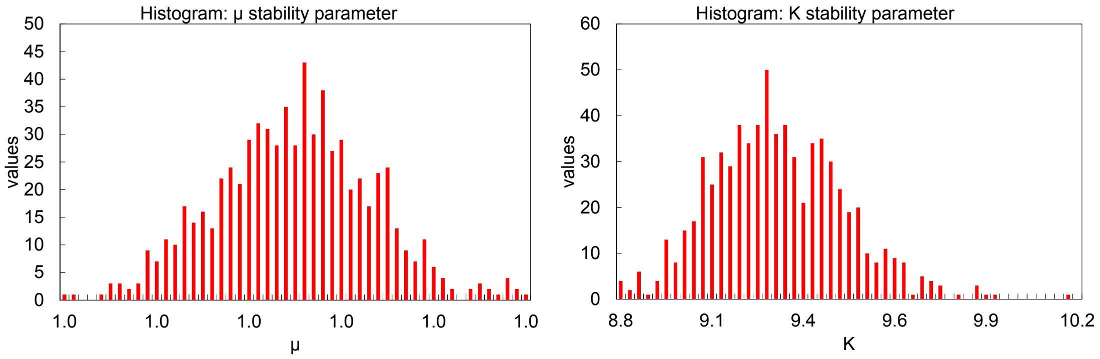

(a) *(b)*

Fig. 2.20. Histograms of stability yield analysis in small signal model for 1000 iterations. Parameters: (a) μ. (b) k.

Table 2.5. Mean and standard deviation for stability yield analysis of the LNA with transistor small signal model.

Parameter	Mean	Standard deviation
µ	1	1.2e-6
k	9.3	0.19

Looking forward at the yield analyses, both large and small signal models, the importance of the active element, the transistor, is significant because the variation of its parameters dominates the global performance of the LNA. The critical performance parameter is the gain due to variations of pinch-off voltage and transconductance *gm* of the transistor.

One of the most important issues in an amplifier is the stability. It has been verified that the LNA is stable under any variation of its components and for both transistor models, small and large signal.

2.3.4. Connection of the LNA: Bonding wire

When the MMIC LNA is integrated in a chassis it is very important its connection with the access lines, both bias and radio frequency (RF). The usual way to do that interconnections, in high frequency designs, is bonding gold wires to MMIC access pads.

In Fig. 2.21 the simulation of the MMIC gain and noise performance is shown for different bonding wire lengths to RF pads, from 0 to 600 µm. The gain decreases as the bonding wire is longer. Meanwhile the noise increases. This effect is more significant in high frequencies due to the inductive behaviour of the wire.

So the connection bonding wires should be shorter than 300 µm in order to not degrade gain and noise performances.

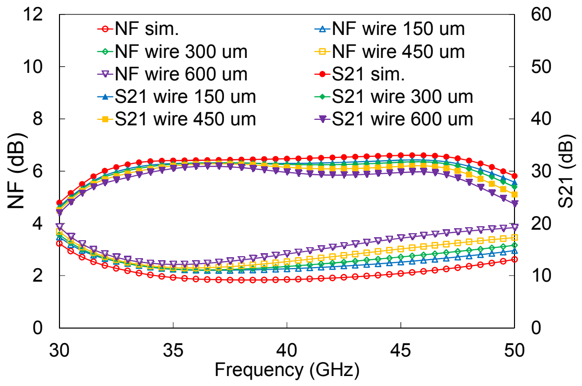

Fig. 2.21. Gain and noise simulation of the MMIC LNA for different bonding wire lengths, from 0 to 600 µm stepped by 150 µm.

2.3.5. Manufacturing

Once all the optimisation stages are finished and the design is validated, the layout is sent to the foundry to be manufactured. The adjusted size 3 x 1 mm^2 for the LNA is a standard used in OMMIC foundry. A picture of the manufactured MMIC LNA is shown in Fig. 2.22.

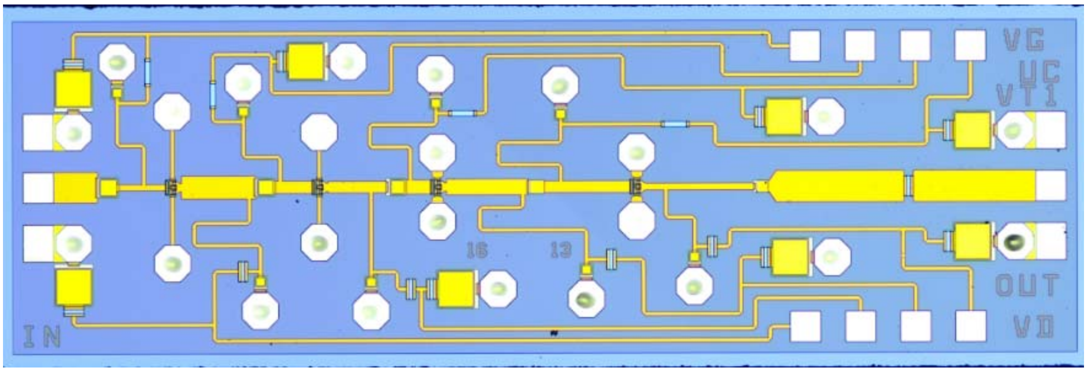

Fig. 2.22. Photograph of the manufactured MMIC LNA (size 3 x 1 mm^2).

2.4. LNA measurements and characterisation

2.4.1. Measurements on wafer at room temperature

Firstly the LNA is characterised on wafer at room temperature. These measurements are made in a coplanar probe station from Cascade Microtech (Fig. 2.23). RF characterisation is performed using a Keysight E8364A network analyser. Noise measurements (Fig. 2.24) are performed using the Y-factor method with a Keysight N8975A noise figure analyser. An external down-converter is used to measure in the 33-50 GHz frequency band because the noise figure analyser only has the capability to measure up to 26.5 GHz. A 6 dB attenuator at the output of the noise source (346C_K01 from Keysight) is used to reduce the excess noise ratio (ENR) in order to improve the noise measurement accuracy [2.17].

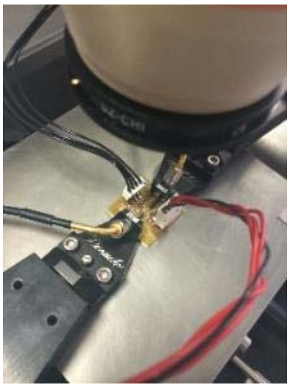

Fig. 2.23. MMIC in the coplanar probe station for S-parameter measurement.

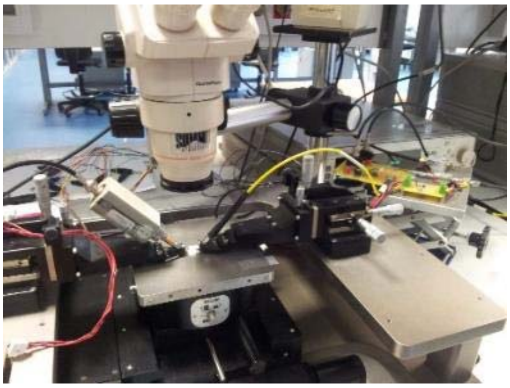

Fig. 2.24. MMIC in the coplanar probe station for noise measurement.

Fig. 2.25(a) shows the linear performance (S-parameters) result, while noise temperature and insertion gain are shown in Fig. 2.25(b). The average gain in the 33-50 GHz frequency band is 28.2 dB. Input return loss is better than 4 dB and output return loss is better than 11 dB within the whole band. The average noise temperature is 145 K in the 33-50 GHz frequency band, and the minimum noise temperature is 101 K near 45 GHz. The gain achieved is quite lower than 30 dB expected (red traces in Fig. 2.25(b)) because the transistors used in the model during the design stage had a higher transconductance compared with the ones used in the manufactured MMIC. Moreover, the measured noise temperature response is quite flat and lower at high frequencies than the simulation approach.

The bias point for getting the lowest noise in the amplifier at room temperature is V_d = 0.61 V and a total current I_d = 24.9 mA for the 4 stages, with a DC power consumption of 15.2 mW. These values are very close to the bias point for lowest noise provided by (2.1), validating this expression for the initial design.

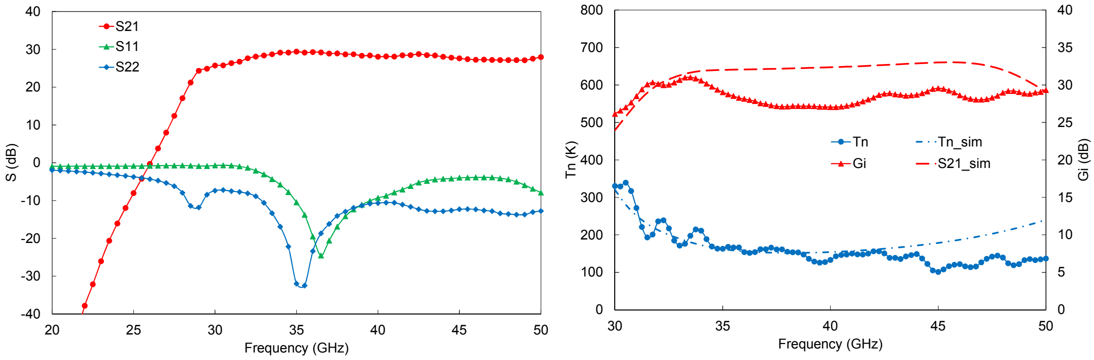

(a) *(b)*

Fig. 2.25. On wafer MMIC LNA measurements at room temperature, V_d = 0.61 V and I_d = 24.9 mA. (a) Scattering parameters. (b) Noise temperature.

2.4.2. Amplifier characterisation at cryogenic temperature

For the characterisation of the MMIC LNA at cryogenic temperatures a suitable module has been machined. This module is made of aluminium in order to improve the thermal conductivity and to reduce the total weight. Afterwards, the chassis is nickel and gold plated.

The chassis has two cavities: one for the chip and the high frequency access lines with 1.2 mm width, whereas the other houses the biasing networks as shown in Fig. 2.26. DC bias accesses are narrow channels in order to avoid resonances in the cavity. The chassis is equipped with 1.85 mm coaxial connectors, and the transition between these connectors and the microstrip lines is made using sliding contacts to allow flexibility in the joints during cryogenic operation. The off-chip bias networks are made up of capacitors, resistors and protection diodes to prevent potential low-frequency instabilities.

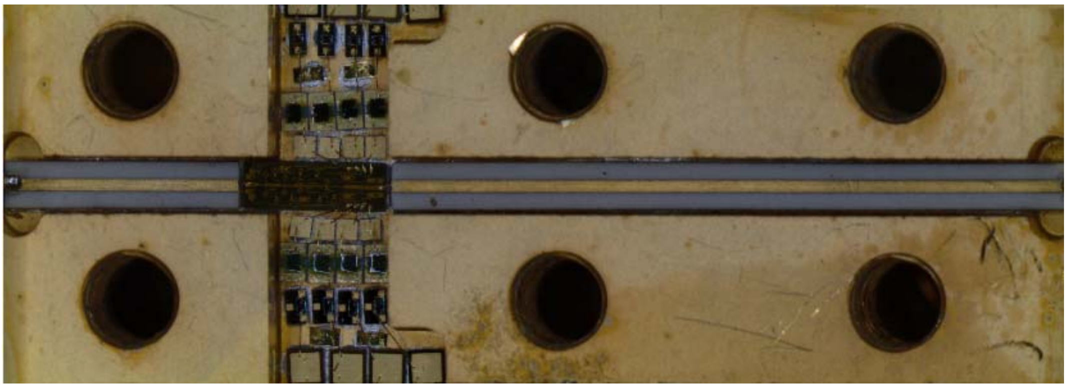

Fig. 2.26. Detail of the MMIC LNA assembly inside the chassis.

At cryogenic temperature the noise measurement was performed using the cold-attenuator technique [2.18] with a 20 dB attenuator module [2.19] inside the cryostat. The noise source is connected directly to the cryostat input line. In Fig. 2.27 the MMIC LNA chassis is presented clamped to the cold base inside the cryostat, just before a cooling cycle.

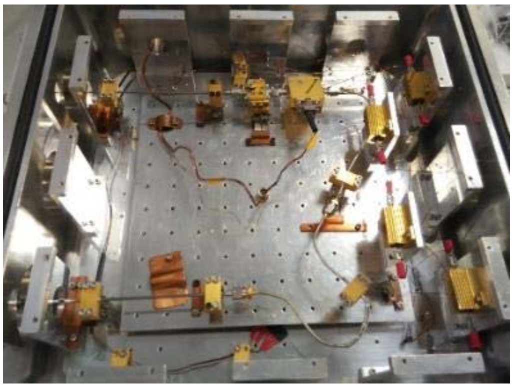

Fig. 2.27. Photo of the MMIC LNA inside the cryostat.

Three units, shown in Fig. 2.28, have been assembled with similar results in terms of noise and gain at cryogenic temperature. Each chassis has a different wire bonding length soldered to the MMIC. Moreover, in the last unit assembled (chassis #03) the MMIC was placed on a Molybdenum pedestal, instead directly on the chassis (on Aluminium). The coefficient of thermal expansion (CTE) of Molybdenum is similar to the Gallium Arsenide substrate of the MMIC (see Table 2.6). This way it is assured the MMIC does not suffer mechanical stress during a cooling cycle.

Table 2.6. Coefficient of thermal expansion (CTE) for different materials used in LNA assemblies.

Material	CTE (ppm/K) @ 20ºC
Molybdenum	4.8
GaAs	5.8
Aluminium	23.1

Fig. 2.28. Three chassis with the MMIC LNA assembled.

Fig. 2.29 shows the measured temperature and associated gain for the three LNA modules at a physical temperature of 15 K. The best results were obtained for unit #03 with 300 µm wire bonding lengths (green trace in Fig. 2.29) and this amplifier achieves an average gain of 27.3 dB and an average noise temperature of 18.4 K in the whole

33-50 GHz frequency band, with a minimum of 13.5 K at 45 GHz. The DC power consumption is only 4.1 mW, $V_d = 0.37$ V and $I_d = 11.2$ mA.

The decrease of gain and increase of noise at 47 GHz seems to be due to the bonding wires and microstrip to coaxial transition effects, since it has not been observed in on wafer measurements. These effects could be minimized using rectangular waveguide to microstrip transitions, because better return loss could be achieved.

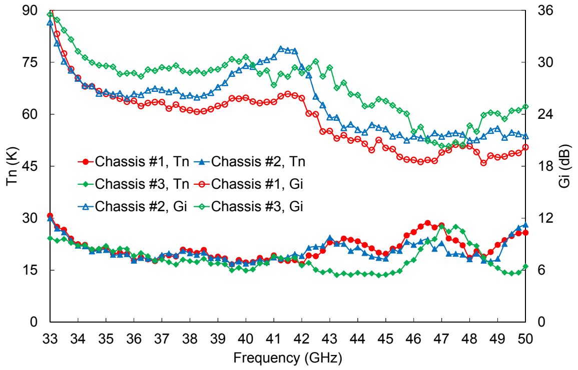

Fig. 2.29. Measured insertion gain and noise temperature for the three assembled LNA modules at physical temperature of 15 K, $V_d = 0.37$ V and $I_d = 11.2$ mA.

2.4.3. Comparing the LNA performance with other published works

The figure of merit (FOM) in (2.6), defined in [2.6], has been used in order to evaluate the performance of the LNA for radio astronomy receivers. This FOM includes linear gain (G), bandwidth (BW (GHz)), noise factor (F), and DC power consumption (P_{DC} (mW)). The results of the MMIC LNA are compared in Table 2.7 with other published works. The noise achieved at cryogenics is close to the one obtained in InP process [2.4] in a similar frequency band. The FOM value at cryogenics is the highest mainly because the very low DC power (4.1 mW, $V_d = 0.37$ V and $I_d = 11.2$ mA). Moreover, the FOM obtained at room temperature is also the highest due to the good noise performance of the presented MMIC LNA.

$$FOM = \frac{G \cdot BW}{(F-1) \cdot P_{DC}} \tag{2.6}$$

Table 2.7. Comparison of previously reported LNA and this work.

Reference	BW (GHz)	G (dB)	NF (dB)	T_n (K)	P_{DC} (mW)	FOM	Process
[2.4]	24-40	28	0.19	13.2 *	10.8	832	130 nm InP HEMT
[2.5]	27.3-50.7	23.1	3.7	390 **	88	2.8	150 nm GaAs mHEMT
	30-50	19.5	0.62	44.8 *	21.4	57.5	
[2.6]	27-45	25	3.1	302 **	9	34	100 nm GaAs pHEMT
[2.7]	30-50	19.8	3.4	345 **	46	3.6	150 nm GaAs mHEMT
		23	0.34	23.4 *	10	347	
[2.8]	37-53.2	32.5	3.2	316 **	152	4.1	150 nm mHEMT
	32-50	29.5	2.8	263 **	140	4.2	
This work	33-50	28.2	1.8	145 **	15.2	55.6	70 nm GaAS mHEMT
		27.3	0.27	18.4 *	4.1	1504	

(*) module. (**) on wafer.

2.4.4. Gain compression: P_{1dB}

The gain compression concludes the LNA characterisation. This measurement is realised at room temperature with the set-up shown in Fig. 2.30. A signal generator (reference 83650B from Hewlett Packard) is used at the input of the LNA to sweep the input power from -50 to -20 dBm, stepped by 0.5 dB. The output power is measured with a power meter (reference E4418B from Hewlett Packard) and a power sensor (also from Hewlett Packard, reference 8487A) which allows to measure a power range from -30 to 20 dBm. The bias point for each LNA module is set to V_d = 0.68V, I_{d1} = 6.7 mA, and I_{d234} = 6.4 mA.

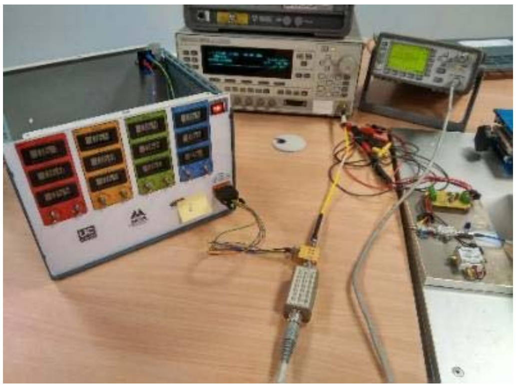

Fig. 2.30. P_{1dB} set-up for the three assembled LNA modules at room temperature.

The measured results for each chassis are plotted in Fig. 2.31 at three representative frequencies, the central point at 41 GHz, and the ends of the band at 33 and 50 GHz. The 1-dB gain compression points referred at the output of the LNA are listed in Table 2.8. The gain compression performance is improved along the frequency band because the maximum P_{1dB} value is obtained at the highest frequency, 50 GHz, where the gain is lower. Best point of -10 dBm output power is achieved in chassis #01.

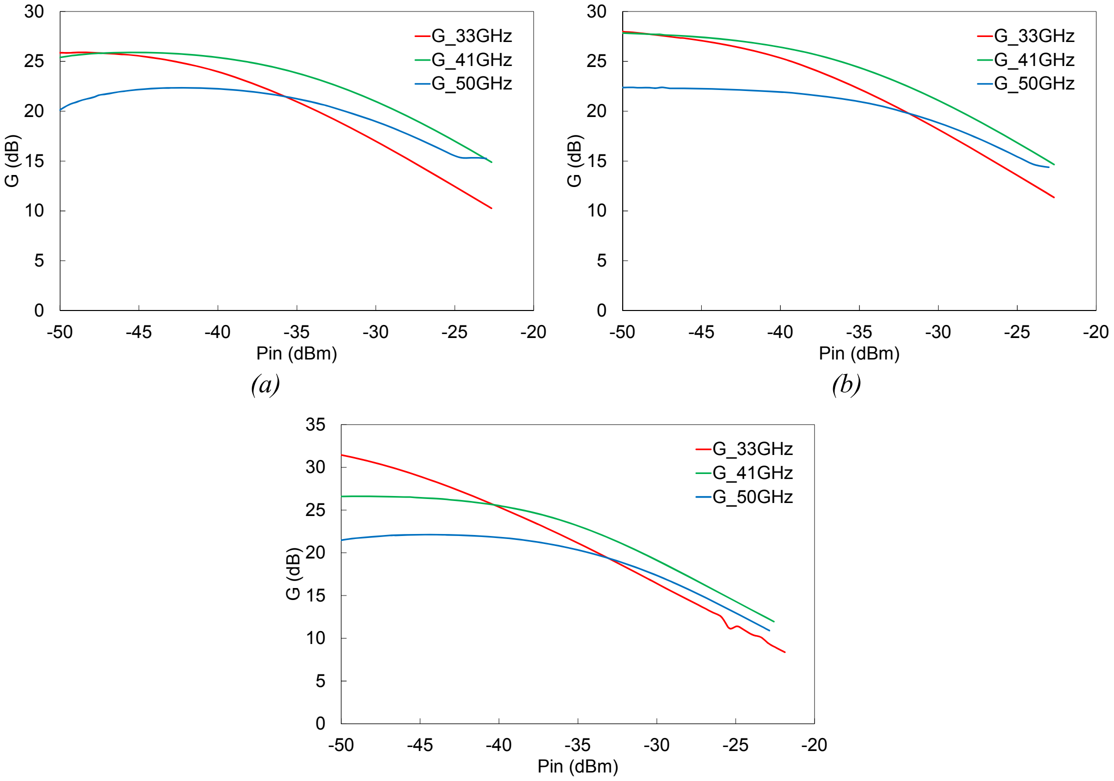

(a) (b)

(c)

Fig. 2.31. Gain compression, P_{1dB}, for the three assembled LNA modules at room temperature. Chassis (a) #01, (b) #02, (c) #03.

Table 2.8. P_{1dB} value (output power) for the three assembled LNA modules at room temperature.

Chassis	33 GHz	41 GHz	50 GHz
#01	-17.7	-12.9	-10.1
#02	-18.8	-15.2	-15.6
#03	-16.4	-13.5	-15.5

2.5. Impact of the LNA in a radiometer

The impact of the cryogenic performance of the MMIC LNA is analysed into a radio astronomy receiver, a radiometer. Considering the scheme of Fig. 2.32, the total receiver equivalent noise temperature (T'_{rec}) can be calculated through (2.7)-(2.10). The contributions of temperature come from the feed system, L_{feed} in (2.8), the back-end module (BEM), T_{BEM} in (2.7) and the LNA, T_{LNA} and G_{LNA} in (2.7).

$$T_{rec} = T_{LNA} + \frac{T_o \cdot (L_{cable} - 1)}{G_{LNA}} + \frac{L_{cable} \cdot T_{BEM}}{G_{LNA}} \tag{2.7}$$

$$T'_{rec} = \left(L_{feed} - 1\right) \cdot T_p + L_{feed} \cdot T_{rec} \tag{2.8}$$

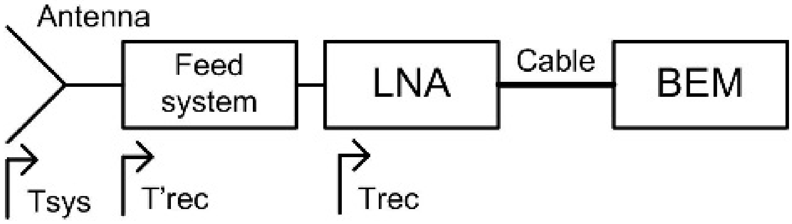

Fig. 2.32. Basic scheme of a radio astronomy receiver.

The system noise temperature including the antenna and the receiver is defined in (2.9). Finally the operation noise temperature of the radiometer includes the sky temperature (2.10).

$$T_{sys} = T_{antenna} + T_{spillover} + T'_{rec} \tag{2.9}$$

$$T_{op} = T_{sky} + T_{sys} \tag{2.10}$$

Taking a BEM noise temperature of 400 K, feed system losses of 0.5 dB (at a physical temperature, Tp, of 15 K), and connection cable losses of 7 dB, the receiver temperature (T'_{rec}) is 29 K. Looking at (2.7), the principal noise contribution comes from the LNA (18 K). The gain of the LNA is not high (27 dB) and the contribution of cables and BEM is considerable (11 K).

Adding to the receiver the contribution of the antenna (6.8 K) the system noise temperature (2.9) of the radiometer is 36 K. And the total operation noise temperature (2.10) taking into account the sky is 51 K.

The LNA minimizes the noise contribution of the back-end but there will be an important contribution in the total noise coming from the components in front of the LNA. Every kelvin improvement in the LNA will reduce in the same quantity the operation temperature of the receiver.

2.6. Conclusions

The design and characterisation of a broadband monolithic cryogenic low-noise amplifier developed for radio astronomy applications in the 33-50 GHz frequency band have been presented in this chapter. The LNA is a four-stage common-source configuration manufactured on 70 nm GaAs metamorphic technology from OMMIC foundry.

The amplifier exhibits a gain of 28 dB and a noise temperature of 145 K in the 33-50 GHz frequency band for on wafer measurements at room temperature. When the amplifier is cooled down to 15 K, the gain is 27.3 dB and the average noise temperature is 18.4 K. The DC power consumption at cryogenics temperatures is only 4.1 mW.

The impact of the LNA performance in the operation noise temperature of a radiometer has been analysed remarking the importance of the LNA as the element who mainly fixes the noise and minimizes the contributions of back-end module in the receiver.

2.7. References

[2.1] Chau-Ching Chiong, Wei-Je Tzeng, Yuh-Jing Hwang, Wei-Ting Wong, Huei Wang, and Ming-Tang Chen "Design and Measurements of Cryogenic MHEMT IF Low Noise Amplifier for Radio Astronomical Receivers," Proceedings of the 4th European Microwave Integrated Circuits Conference, September 2009, pp. 1-4.

[2.2] Christophe Risacher, Erik Sundin, Victor Perez Robles, Miroslav Pantaleev, and Victor Belitsky, "Low Noise and Low Power Consumption Cryogenic Amplifiers for Onsala and Apex Telescopes," 12th GAAS Symposium, Amsterdam 2004.

[2.3] P. Kangaslahti, T. Gaier, M. Seiffert, S. Weinreb, D. Harding, D. Dawnson, M. Soria, C. Lawrence, B. Hooberman, A. Miller, "Planar Polarimetry Receivers for Large Imaging Array at Q-band," in *IEEE 41st European Microwave Conference*, October 2011, pp. 934-937.

[2.4] Joel Schleeh, Niklas Wadefalk, Per-Ake Nilsson, J. Piotr Starski, and Jan Grahn, "Cryogenic Broadband Ultra-Low-Noise MMIC LNAs for Radio Astronomy Applications," *IEEE Transactions on Microwave Theory and Techniques*, 2013, vol. 61, no. 2, pp 871-877.

[2.5] Shou-Hsien Weng, Wei-Chu Wang, Hong-Yeh Chang, Chau-Ching Chiong, and Ming-Tang Chen "A Cryogenic 30-50 GHz Balanced Low Noise Amplifiers Using a 0.15-µm MHEMT Process for Radio Astronomy Applications," *IEEE International Symposium on Radio-Frequency Integration Technology (RFIT)*, 2012, pp. 177-179.

[2.6] Shou-Hsien Weng, Wei-Chu Wang, Hong-Yeh Chang, Chau-Ching Chiong, and Ming-Tang Chen "An Ultra Low-power Q-band LNA with 50% Bandwitdth in WIN GaAs 0.1-µm pHEMT Process," *Asia-Pacific Microwave Conference Proceedings*, 2013, pp. 713-715.

[2.7] Shou-Hsien Weng, *et al.*, “Cryogenic Evaluation of A 30-50 GHz 0.15-µm MHEMT Low Noise Amplifier for Radio Astronomy Applications,” *IEEE MTT-S Int. Microw. Symp. Dig.*, June 2006, pp. 89-92.

[2.8] S.-H. Weng, C.-H. Lin, H.-Y. Chang, C.-C. Chiong, “Q-band low noise amplifiers using a 0.15-µm MHEMT process for broadband communication and radio astronomy applications,” *IEEE MTT-S Int. Microw. Symp. Dig.*, June 2006, pp. 89-92.

[2.9] A.H. Akgiray, New Technologies Driving Decade-Bandwidth Radio Astronomy. Ph.D. dissertation. California Institute of Technology. USA. 2013.

[2.10] J. Vicente Terán Collantes, Luisa de la Fuente, Beatriz Aja, Eduardo Artal, “Cryogenic Broadband Q-Band MMIC Low-Noise Amplifier”, European Microwave Week, October 2016, London (UK).

[2.11] Marian W. Pospieszalski, “Modeling of Noise Parameters of MESFET’s and MODFET’s and Their Frequency and Temperature Dependence,” *IEEE Transactions on Microwave Theory and Techniques*, vol. 37, no. 9, September 1989.

[2.12] J.L. Cano. Cryogenic Technology in the Microwave Engineering: Application to MIC and MMIC Very Low Noise Amplifier Design. Ph.D. Dissertation. University of Cantabria. Spain. 2010.

[2.13] Jakob Engberg, “Simultaneous input power match and noise optimization using feedback,” *4th European Microwave Conference*, 10-13 Sept. 1974, pp. 385-389.

[2.14] Les Besser, “Stability considerations of low-noise transistor amplifiers with simultaneous noise and power match,” *IEEE MTT-S International Microwave Symposium*, 12-14 May 1975, pp. 327-329.

[2.15] Svein Iversen, “The Effect of Feedback on Noise Figure,” *Proceedings of the IEEE*, vol. 63, no. 3, March 1975, pp. 540-542.

[2.16] Randall E. Lehmann, David D. Heston, “X-Band Monolithic Series Feedback LNA,” *IEEE MTT-S International Microwave Symposium Digest*, 4-6 June 1985, pp. 51-54[2.17] J.L. Cano and J.D. Gallego, “Estimation for Uncertainty in Noise Measurements Using Monte Carlo Analysis,” *1st Radionet-FP7 Engineering Forum Workshop*, Gothenburg, Sweden, June 2009.

[2.18] J.E. Fernández, A noise-temperature measurement system using a cryogenic attenuator. Jet Propulsion Lab. (JPL), Pasadena, CA, TMO Progress Rep. 42-135, Nov. 1998.

[2.19] J.L. Cano, N. Waldefalk, and J.D. Gallego-Puyol, "Ultra-Wideband Chip Attenuator for Precise Noise Measurements at Cryogenic Temperatures," *IEEE Trans. Microwave Theory and Tech.*, vol. 58, no. 9, Sept. 2010, pp. 2504-2510.

CHAPTER III: Ka-BAND FULL-HYBRID CRYOGENIC LOW-NOISE AMPLIFIER

3.1. Introduction

Traditionally, Monolithic technology (MMIC) has been used for high frequency designs since it presents fewer parasitic effects and a more repeatable performance [3.1]-[3.5]. However, this technology has the handicap of the costs associated with their production (for low quantities) and sometimes it is not affordable. On the other hand, hybrid technology (MIC), where components are bonded or soldered to the substrate, presents the best noise performance so far and the possibility of post-production adjustments. Moreover, hybrid technology is cheaper than the monolithic technology for low quantities.

This chapter describes the design and characterisation of a cryogenic MIC LNA in the 26-36 GHz frequency band [3.6]. The aimed of this work is to explore the feasibility of design a MIC LNA in a higher frequency band (Q band at 50 GHz). The manufacturers of lumped components provide accurate models up to 30 GHz but not in the Q band.

3.2. Technology

Transistors are built in metamorphic HEMT (mHEMT) technology with 50 nm gate length process from the Fraunhofer Institute (IAF) (Freiburg, Germany). Indium content in the channel is 65 % providing a transition extrinsic frequency f_T = 380 GHz and a maximum oscillation frequency f_{max} = 500 GHz. A view of the transistor layers is shown in Fig. 3.1. The transistor size is chosen to have 4 fingers by 15 μm gate periphery because this size was found the best trade-off between very low noise and gain.

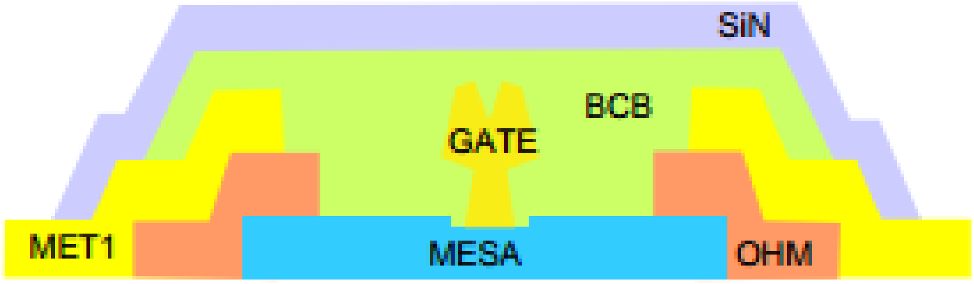

Fig. 3.1. Artist view of the IAF transistor 4x15 µm.

3.3. MIC LNA design

The MIC LNA is a three stage typical design with transistors in common source configuration. In order to achieve the best possible noise performance and increase the design stability, transistors use source feedback technique.

3.3.1. Transistor small signal and noise models

It is necessary to model the transistor in order to have an accurate design, mainly at high frequency designs. First, the DC characterisation through IV curves (Fig. 3.2) is performed to search de minimum noise bias point (Fig. 3.3) as seen in previous chapter 2, section 2.3.1.

Small signal model for the transistor is obtained from different Scattering measurements. First measurement is done at the bias point of minimum noise to extract the intrinsic parameters: V_d = 0.7 V and I_d = 13 mA (217 mA/mm). And two more measurements with V_d = 0 V (cold FET technique) for obtaining the extrinsic parameters; first one with the gate pinched-off and other with the gate forward biased.

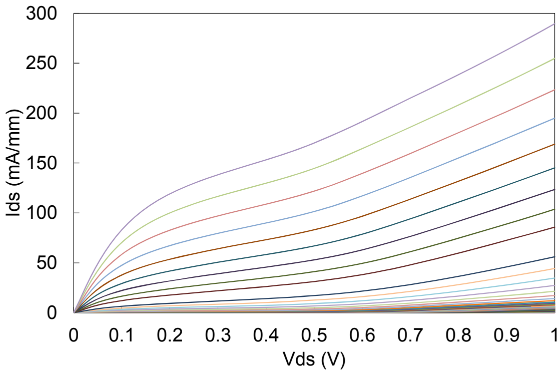

Fig. 3.2. IV curves for IAF transistor. V_{ds}: 0 to 1 V. V_{gs}: -1 to 0 V, in steps of 25 mV.

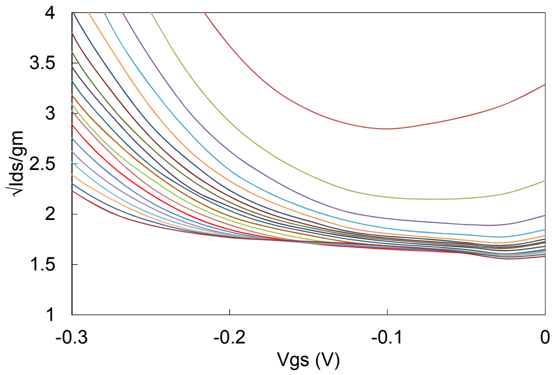

Fig. 3.3. IAF transistor bias approximation for minimum noise. V_{gs}: -0.3 to 0 V. V_{ds}: 0 to 1 V, in steps of 50 mV.

Fig. 3.4 shows the typical small signal model for a transistor following the Pospieszalski approach [3.7]. Table 3.1 presents the model parameters at room temperature for the IAF transistor used in the LNA design.

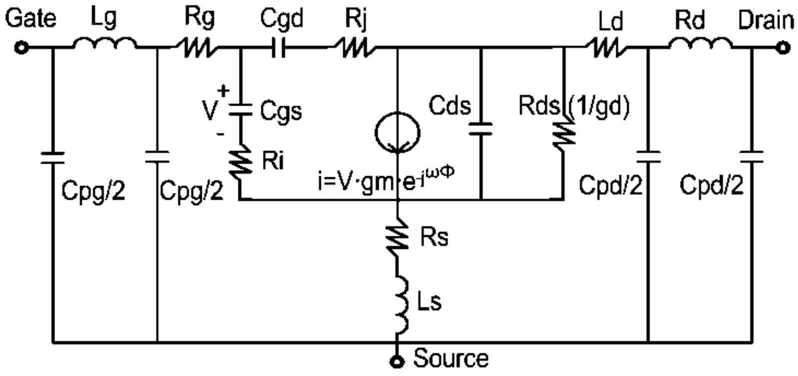

Fig. 3.4. 4 x 15 µm mHEMT transistor small signal model.

Table 3.1. Small signal parameters values for a 4 x15 µm IAF mHEMT transistor. V_d = 0.7 V, I_d = 13 mA.

Intrinsic parameter	**Value**	**Extrinsic parameter**	**Value**
Cgs	34 fF	Cpg/2	7.45 fF
Ri	10 Ω	Lg	39.84 pH
Cgd	15 fF	Rg	0.5 Ω
Rj	10.5 Ω	Cpd/2	7.45 fF
Gm	78.3 mS	Ld	45.11 pH
Φ	0 ps	Rd	2.61 Ω
Cds	17 fF	Rs	1.19 Ω
Gd	9.6 mS	Ls	3.29 pH

Fig. 3.5 shows a picture of the 4 x 15 µm IAF transistor.

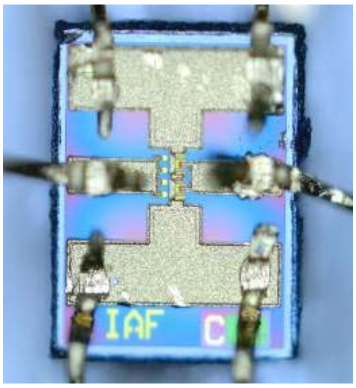

Fig. 3.5. IAF transistor 4x15 µm.

The agreement between the measured Scattering parameters (blue traces in Fig. 3.6) and the model (red traces in Fig 3.6) is quite good.

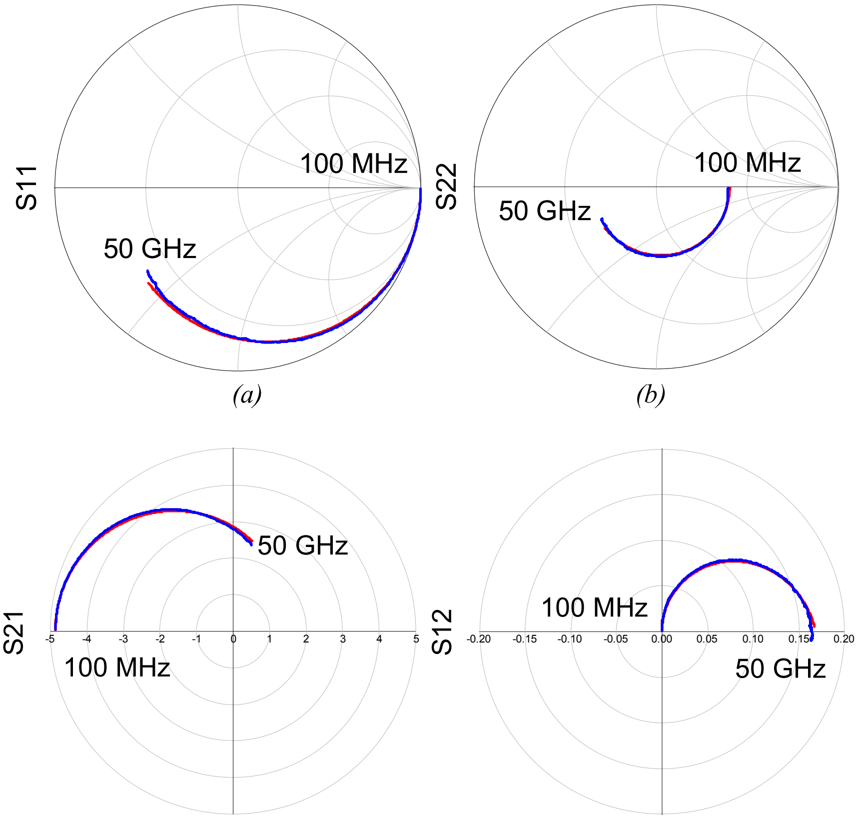

(a) (b)

(c) (d)

Fig. 3.6. Scattering parameters performance of the IAF transistor 4x15 µm. Blue, measurements. Red, simulation of the model (Fig. 3). (a) S_{11}. (b) S_{22}. (c) S_{21}. (d) S_{12}.

A noise model is also required to the design the amplifier. Fig. 3.7 shows the noise figure measurement of the IAF transistor at room temperature (red line) from 24 to 40 GHz. The ripple observed is due to the poor matching of a discrete transistor. The simulated noise figure modelled is traced in green colour in Fig. 3.7. Average noise figure estimation in the 26-36 GHz frequency band is 2.6 dB. This noise performance is included in the small signal model proposed by Pospieszalski (Fig. 3.4) setting up the temperature of the drain to source resistor to $T_d = 4200$ K and the remaining resistors to ambient temperature $T_g = 300$ K.

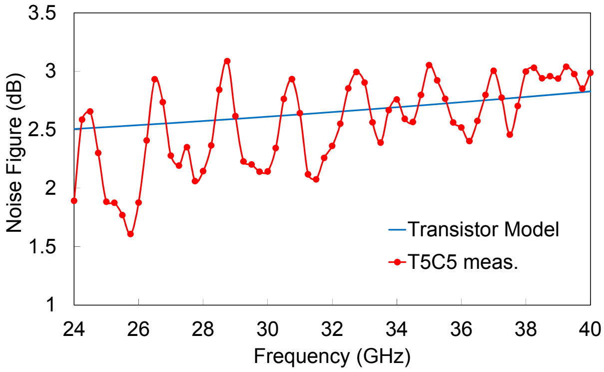

Fig. 3.7. Noise Figure performance of the 4 x15 μm IAF transistor for $V_d = 0.7$ V, $I_d = 13$ mA.

3.3.2. Radio frequency (RF) capacitor model

The surface mount device (SMD) capacitors are key components for DC decoupling. Unfortunately the model supplied by the manufacturers often does not work properly at these high frequency bands (above 20 GHz).

A 0.3 pF capacitor (from ATC) is modelled using the set-up of Fig. 3.8. This includes a 50 ohm microstrip transmission line where the capacitor is mounted, and coplanar-to-microstrip adapters (from JMicro Technology, model PP1003) to land the coplanar probes. Proper calibration eliminates the contribution of the adapters in the measurement.

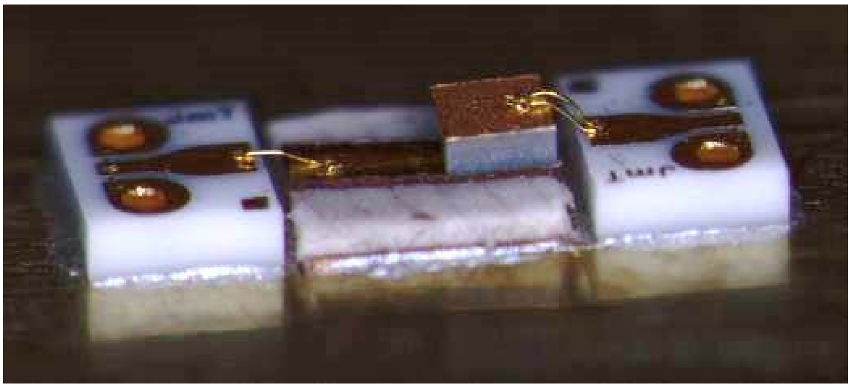

Fig. 3.8. Scattering measurement set-up for a 0.3 pF capacitor with JMicro adapters.

The proposed electrical model for the capacitor is presented in Fig. 3.9, in which all the associated parasitic effects and the bonding wires are included (Table 3.2).

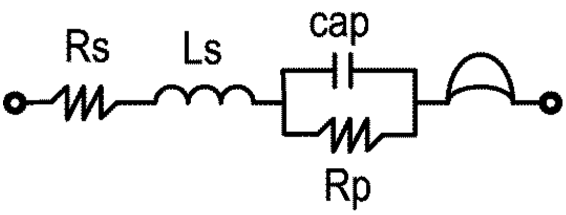

Fig 3.9. Model of a capacitor from ATC Ceramics including the bonding wires at the right-hand.

Table 3.2. Parameters for the ATC capacitor model.

Parameter	Value
cap	0.3 pF
Rs	1 Ω
Ls	20 pH
Rp	100 KΩ
Bonding wire	300 µm

The Scattering parameters performance of the 0.3 pF capacitor is shown in Fig. 3.10, by comparison of the simulation (red trace) versus the measurement (blue trace). A quite good agreement between model and measurement can be observed in the 2-50 GHz frequency band.

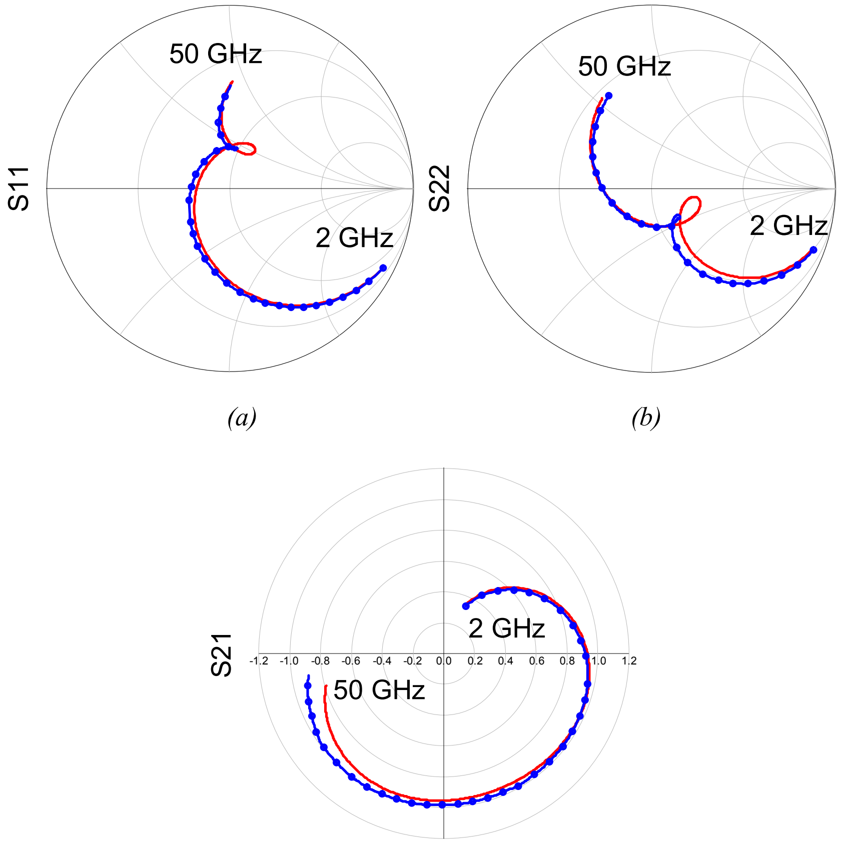

(a) *(b)*

(c)

Fig. 3.10. Scattering parameters performance for the 0.3 pF capacitor in the 2-50 GHz frequency band. Blue, measurement; red, simulation. (a) S_{11}. (b) S_{22}. (c) S_{21}.

3.3.3. Bonding wire in the source of the transistor

The transistor has four source pads in which wires can be bonded. The bonding wire from the source of the transistor to the ground is important in terms of noise. The source feedback implemented with the inductive characteristic of the bonding wires sets the noise performance of the transistor.

First test was done with two short bonding wires, each one in the centre of the source pad as in Fig 3.11. There is a bad fitting in the Scattering parameters performance (Fig. 3.12) above 30 GHz between the measurement (blue) and simulation including the bonding wires (red). The rectangular edges in the source pads have a strong open circuit effect that degrades the simulated performance, mainly in the phase, at high frequencies.

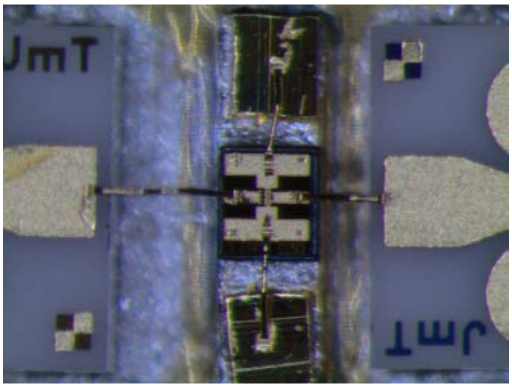

Fig. 3.11. Photo of IAF transistor (unit T1c30) with two bonding wires centred in the source pad.

The bonding wires diameter is set to 17 μm due to the gate and drain pad sizes. The lengths do not exceed the 400 μm because the inductive effect of the wire is harmful to the transistor performance, especially at high frequencies. The gate bonding wire is a bit longer to compensate the effect of DC-to-RF decoupling capacitor that is placed at the input of the transistor in the amplifier design. The lengths are summarised in Table 3.3.

Table 3.3. Bonding wires lengths for IAF transistor (unit T1c30) with two bonding wires centred in the source pad.

Wire	ℓ (μm)
Gate pad	443
Drain pad	283
Up source pad	280
Down source pad	304

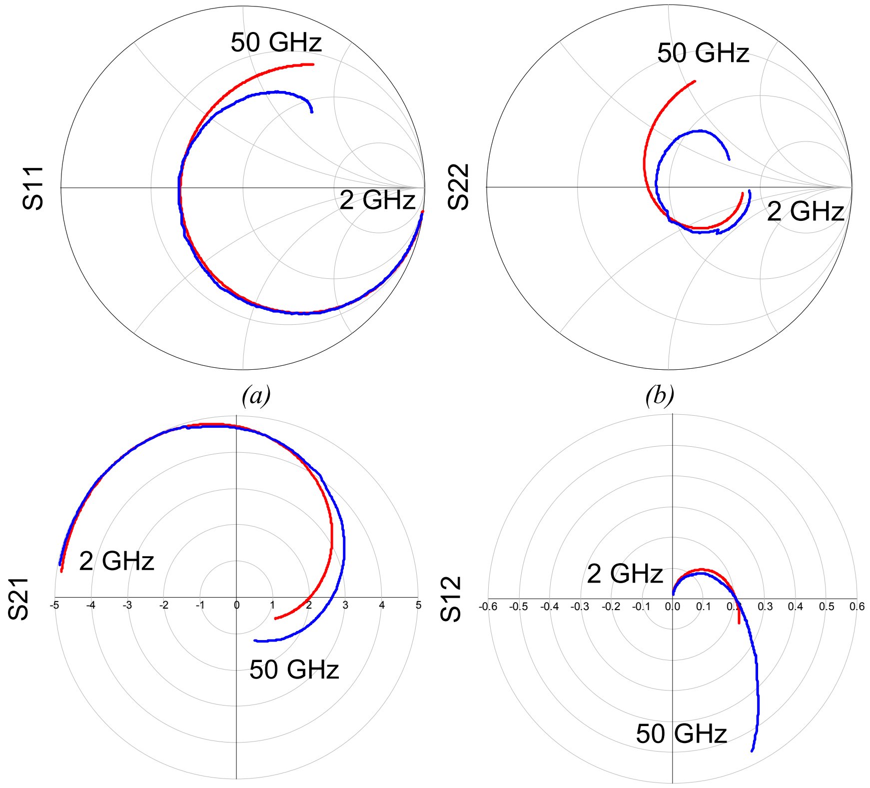

(a) *(b)*

(c) *(d)*

Fig. 3.12. Scattering parameters performance of IAF transistor (unit T1c30) with two bonding wires centred in the source pad. Blue measurement, red simulation. (a) S_{11}. *(b)* S_{22}. *(c)* S_{21}. *(d)* S_{12}.

When the two bonding wires are placed in diagonal in the corners of the source pad (Fig. 3.13), the simulated linear response is even worse. Both amplitude and phase are shifted comparing with measurements (Fig. 3.14). In Table 3.4, the lengths of the bonding wires are listed.

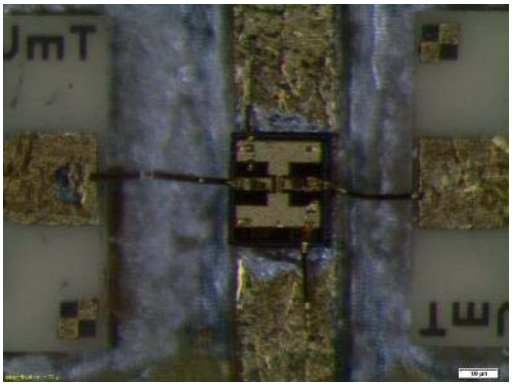

Fig. 3.13. Photo of IAF transistor (unit T1c34) with two diagonal bonding wires in the source pad.

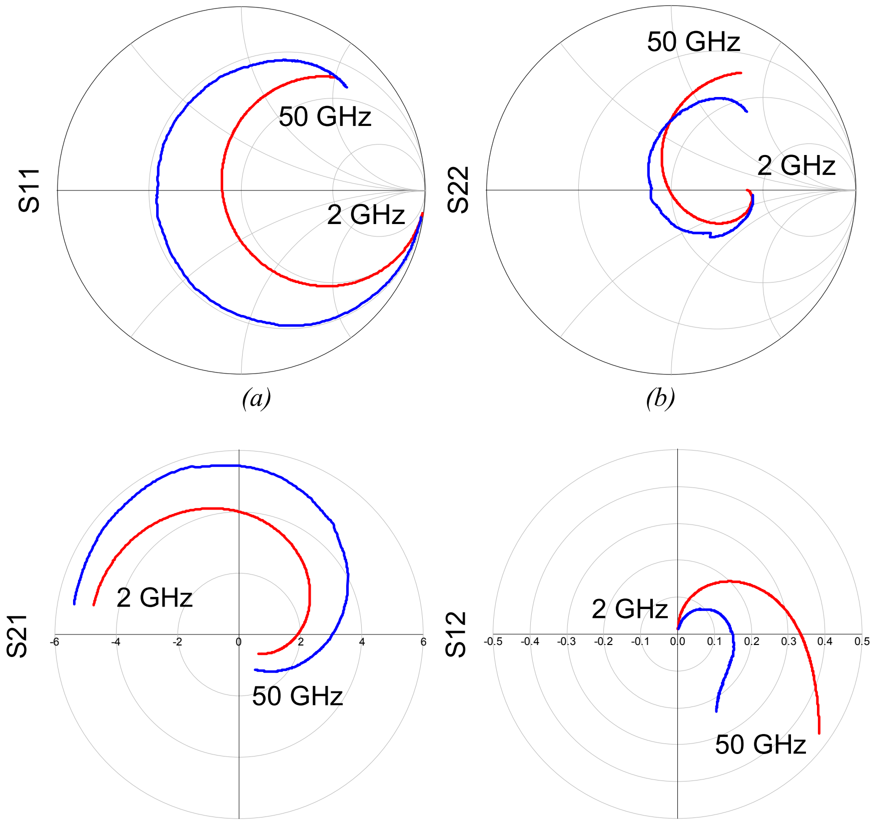

(a) *(b)*

(c) *(d)*

Fig. 3.14. Scattering parameters performance of IAF transistor (unit T1c34) two diagonal bonding wires in the source pad. Blue measurement, red simulation. (a) S_{11}. (b) S_{22}. (c) S_{21}. (d) S_{12}.

Table 3.4. Bonding wires lengths for IAF transistor (unit T1c34) two diagonal bonding wires in the source pad.

Wire	**ℓ (µm)**
Gate pad	540
Drain pad	357
Up source pad	331
Down source pad	364

Rejecting the option of soldering just two bonding wires in the source pad, two more wires are soldered resulting four short bonding wires, soldered to the four corners of the source pad of the transistor (Fig. 3.15). The lengths of the new bonding wires are named “right up source pad” and “left down source pad” in Table 3.5.

Table 3.5. Bonding wires lengths for IAF transistor (unit T1c34) with four bonding wires in the source pad.

Wire	**ℓ (µm)**
Gate pad	540
Drain pad	357
Left up source pad	331
Right up source pad	190
Left down source pad	369
Right down source pad	364

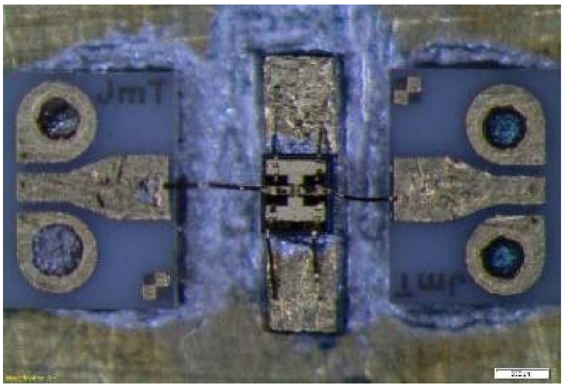

Fig. 3.15. Photo of IAF transistor (unit T1c34) with four bonding wires in the source pad.

In this case, high agreement between the simulation and the measurement of the Scattering parameters performance (Fig. 3.16) is achieved. In Fig. 3.17 the maximum stable gain (MSG) and the K stability factor are plotted. The simulation predicts a lower gain (red trace in Fig. 3.17(a)) and consequently the stability is higher (red trace in Fig. 3.17(b)). However, the simulation is not so far away from the measurement.

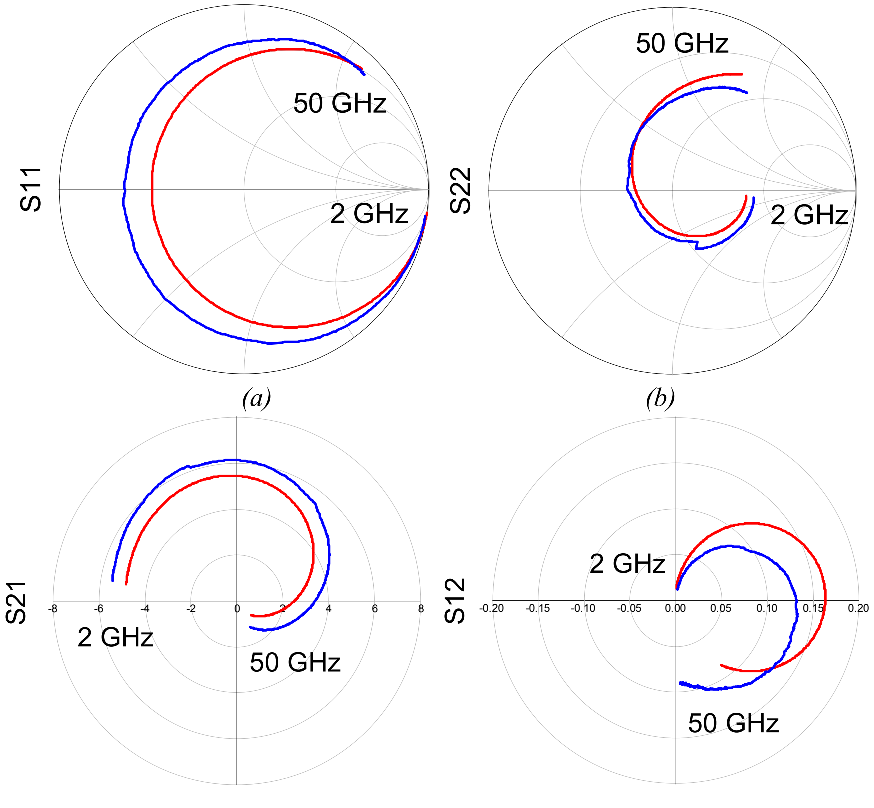

(a) *(b)*

(c) *(d)*

Fig. 3.16. Scattering parameters performance of IAF transistor (unit T1c34) with four bonding wires in the source pad with JMicro calibration. Blue measurement, red simulation. (a) S_{11}. (b) S_{22}. (c) S_{21}. (d) S_{12}.

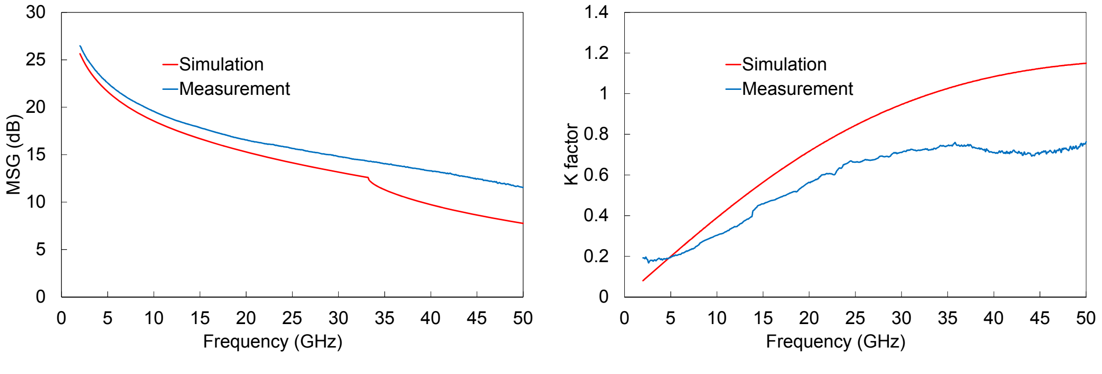

(a) *(b)*

Fig. 3.17. Unit T1c34 with four bonding wires in the source pad with JMicro calibration. Blue measurement, red simulation. (a) MSG. (b) K stability factor.

A new transistor is mounted (Fig. 3.18) but with four long bonding wires in the source pad. So the length effect of wires can be analysed. The lengths grow up above 400 µm as shown in Table 3.6.

Table 3.6. Bonding wires lengths for IAF transistor (unit T1c37) with four long bonding wires in the source pad.

Wire	ℓ (µm)
Gate pad	457
Drain pad	316
Left up source pad	423
Right up source pad	462
Left down source pad	430
Right down source pad	405

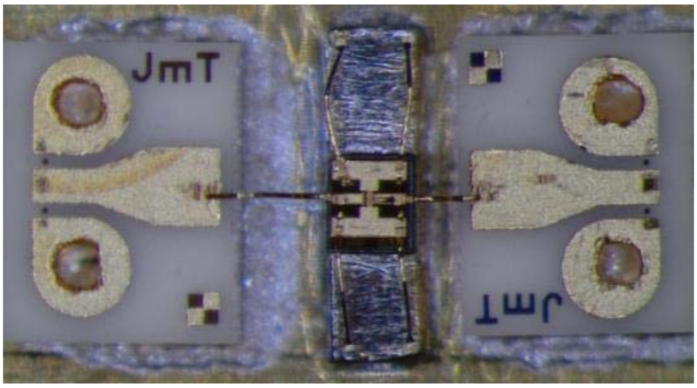

Fig. 3.18. Photo of IAF transistor (unit T1c37) with four long bonding wires in the source pad.

The transmission coefficient S_{21} in Fig. 3.19(c) shows a good agreement but the input/output matching, S_{11} (Fig. 3.19(a)) and S_{22} (Fig. 3.19(b)) respectively, have a significant shift. Moreover, the MSG and K factor simulation and measurement (Fig. 3.20) are closer than the case of short source bonding wires (Fig. 3.17).

But the length of the source bonding wires is important to have an accurate design. It is better to choose not so long wires because the inductive value of a long bonding wire is difficult and critical to model, especially at high frequency.

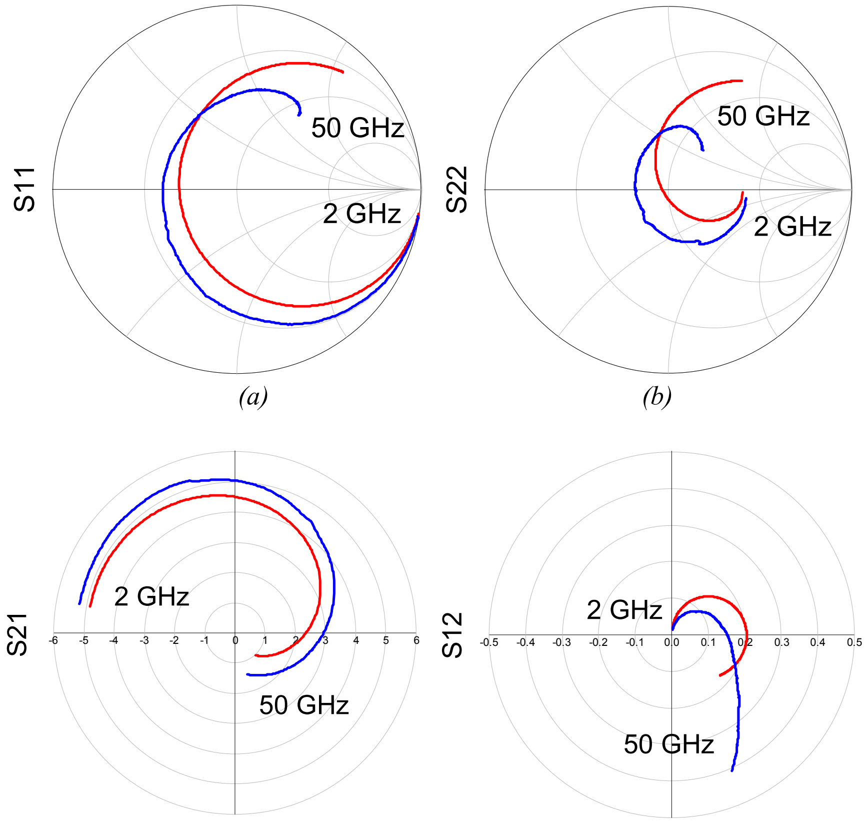

(a) *(b)*

(c) *(d)*

Fig. 3.19. Scattering parameters performance of IAF transistor (unit T1c37) with four long bonding wires in the source pad with JMicro calibration. Blue measurement, red simulation. (a) S_{11}. (b) S_{22}. (c) S_{21}. (d) S_{12}.

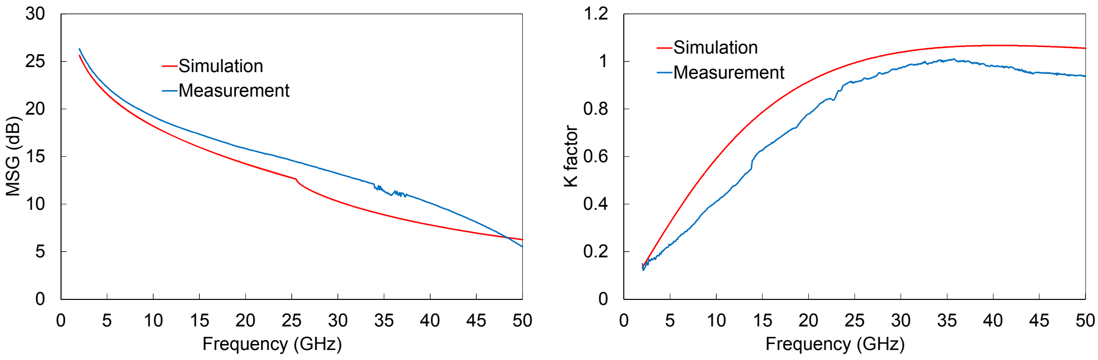

(a) *(b)*

Fig. 3.20. Unit T1c37 with four long bonding wires in the source pad with JMicro calibration. Blue measurement, red simulation. (a) MSG. (b) K stability factor.

Another measurement was performed including the transistor, bonding wires and the JMicro adapters. The JMicro adapter performance from two calibration kits (referenced CM10 and CM12) was measured and compared. The substrate of the

JMicro calibration kit is Alumina with a height of 10 mils. The thru standard was used in the measurement so two adapters were measured for each kit: one at the left-hand and one the right-hand (suffix _O will be used later for this adapter). The calibration procedure of this measurement was done in a probe station with the CS-5 calibration kit from Picoprobe. Attending the response measured (Fig. 3.21 and Fig. 3.22), both calibration kits are quite similar.

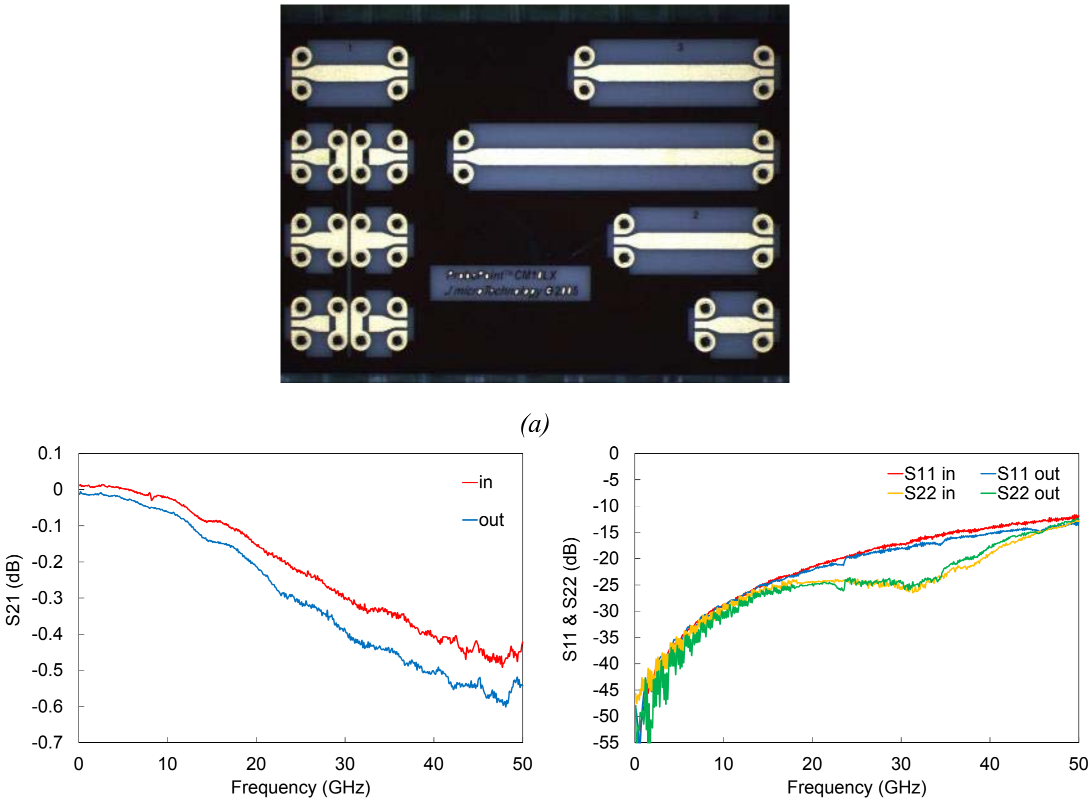

(a)

(b) *(c)*

Fig. 3.21. CM10 calibration kit. (a) Photo of the kit. Scattering parameters performance: (b) S_{21} and S_{12}, (c) S_{11} and S_{22}.

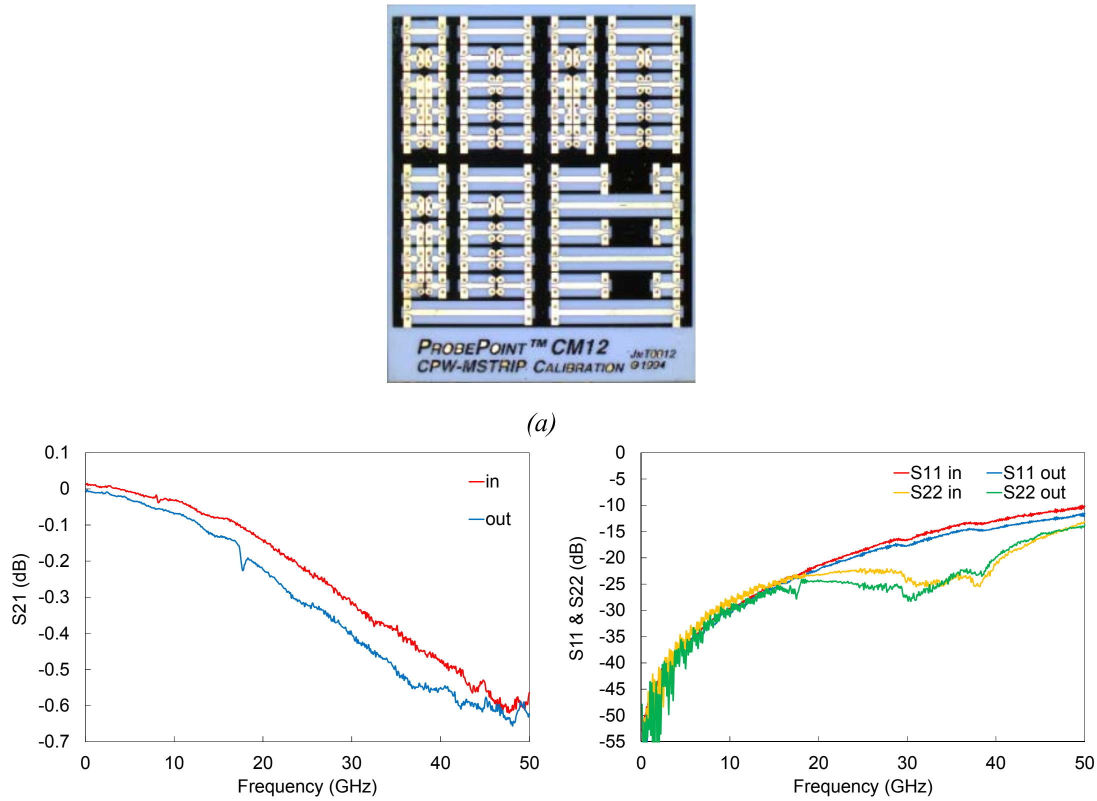

(b) (c)

Fig. 3.22. CM12 calibration kit. (a) Photo of the kit. Scattering parameters performance: (b) S_{21} and S_{12}, (c) S_{11} and S_{22}.

Fig. 3.23 and Fig. 3.24 show the Scattering parameters performance for the transistor with four short bonding wires and different JMicro adapters. In blue the measurements of the whole set-up are plotted, it means the adapters, the bonding wires and the transistor. In red, pink, cyan and purple the simulation for transistor with the four adapter models are represented. The difference between the different adapters is negligible. Although in the simulation is not predicted, the MSG measured has a strange valley centred in 40 GHz (Fig. 3.23). This anomalous behaviour is not so confident. So the use of the adapter as a part of the device under test (DUT) seems not to be the best option.

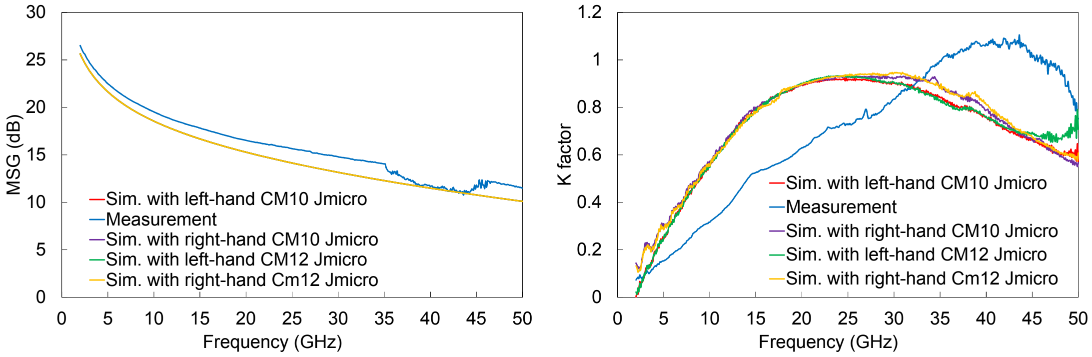

(a) *(b)*

Fig. 3.23. Unit T1c34 with four bonding wires in the source pad without JMicro calibration. Blue measurement, red simulation of left-hand CM10 adapter, pink simulation of right-hand CM10 adapter, cyan simulation of left-hand CM12 adapter, purple simulation of right-hand CM12 adapter. (a) MSG. (b) K stability factor.

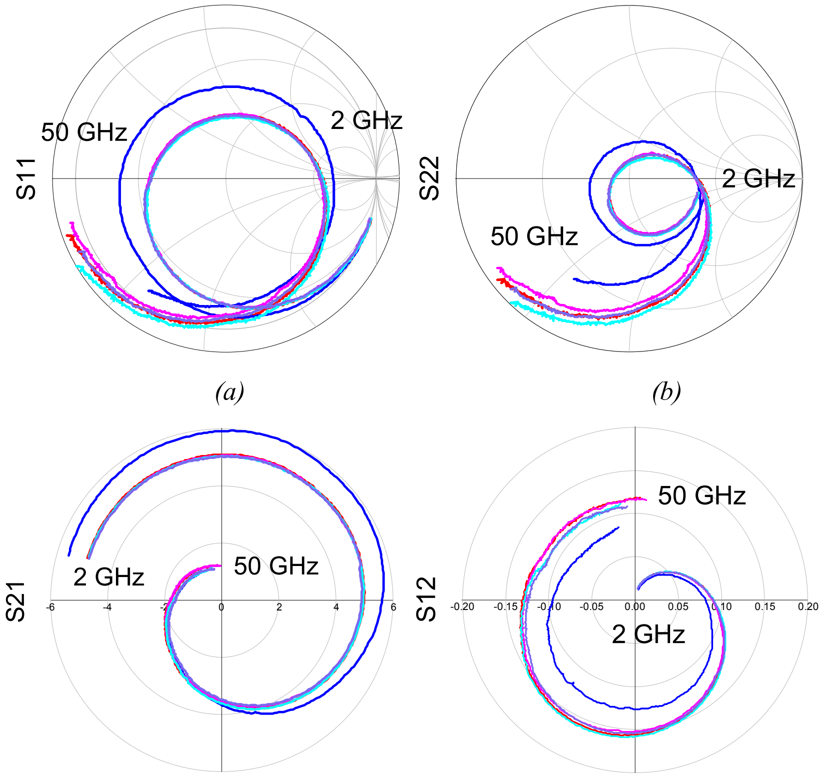

(c) *(d)*

Fig. 3.24. Scattering parameters performance of IAF transistor (unit T1c34) with four bonding wires in the source pad without JMicro calibration. Blue measurement, red simulation of left-hand CM10 adapter, pink simulation of right-hand CM10 adapter, cyan simulation of left-hand CM12 adapter, purple simulation of right-hand CM12 adapter. (a) S_{11}. (b) S_{22}. (c) S_{21}. (d) S_{12}.

When the transistor has a long source bonding wires the Scattering parameters performance (Fig. 3.25) follows the same trend as with short bonding wires (Fig. 3.24). However, the anomalous behaviour in the MSG disappears (Fig. 3.26) resulting the simulation more credible.

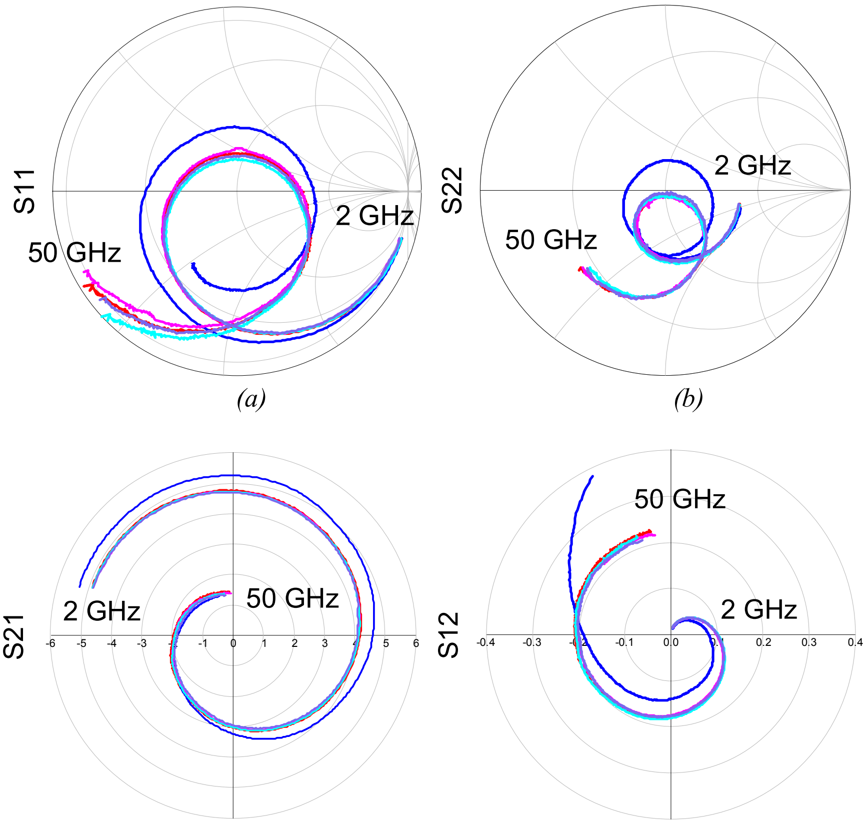

(a) *(b)*

(c) *(d)*

Fig. 3.25. Scattering parameters performance of IAF transistor (unit T1c37) with four long bonding wires in the source pad without JMicro calibration. Blue measurement, red simulation of left-hand CM10 adapter, pink simulation of right-hand CM10 adapter, cyan simulation of left-hand CM12 adapter, purple simulation of right-hand CM12 adapter. (a) S_{11}. (b) S_{22}. (c) S_{21}. (d) S_{12}.

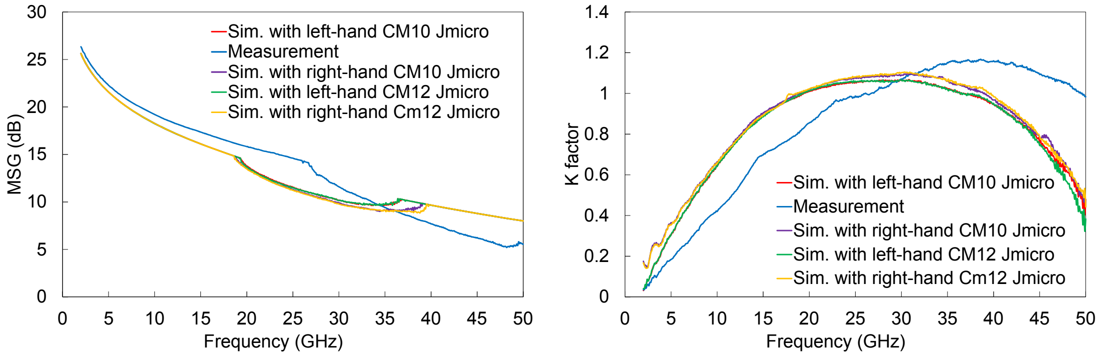

(a) *(b)*

Fig. 3.26. Unit T1c37 with four long bonding wires in the source pad without JMicro calibration. Blue measurement, red simulation of left-hand CM10 adapter, pink simulation of right-hand CM10 adapter, cyan simulation of left-hand CM12 adapter, purple simulation of right-hand CM12 adapter. (a) MSG. (b) K stability factor.

A comparison between the two reference measurement planes is analysed with the CM10 adapters because both CM10 and CM12 adapter performances are quite close. The planes involve removing or not the JMicro adapters during the calibration process for the Scattering parameters measurement. Fig. 3.27 to Fig. 3.30 compare the measurements including the adapters (blue), transistor plus adapters measured separately (red) and the simulation of the transistor with the adapters (pink). Attending the results obtained, the complexity of measuring the transistor with the adapters and after include them to the model is not useful.

So the best way to characterise the transistor with its bonding wires is to remove the JMicro adapters during the calibration process. Moreover, the bonding wires should not be too long in order to extract an accurate design model for the transistor.

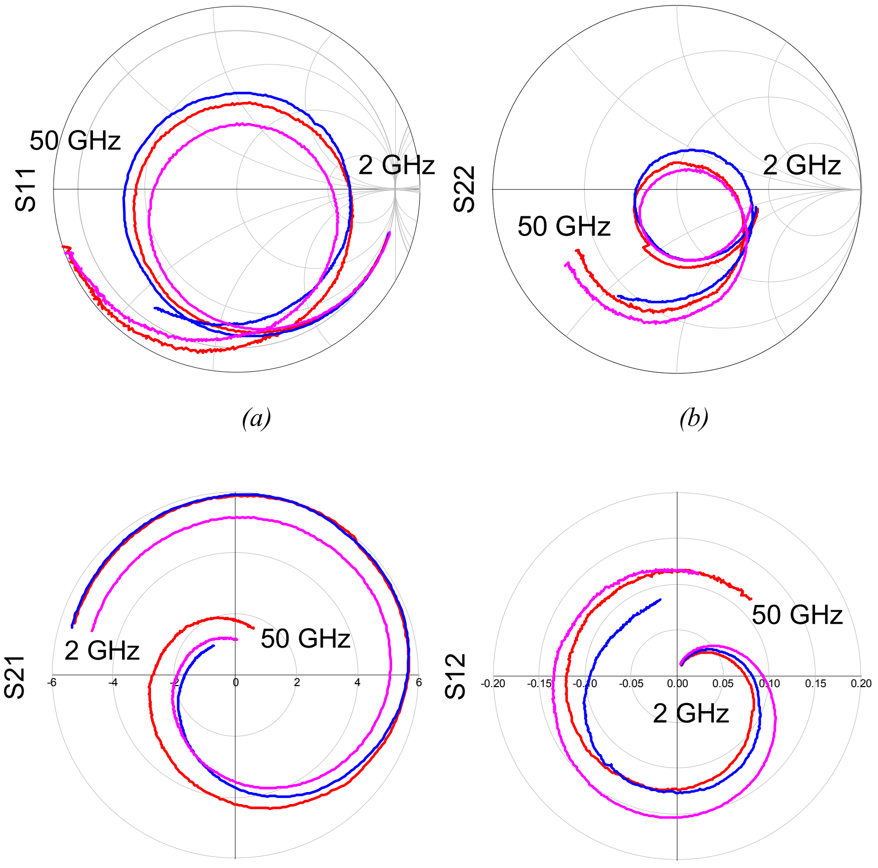

(a) *(b)*

(c) *(d)*

Fig. 3.27. Scattering parameters performance of IAF transistor (unit T1c34)with four bonding wires in the source pad. Blue measurement without JMicro calibration, red measurement with JMicro calibration plus JMicro CM10 adapter measurement, pink simulation with JMicro CM10 adapters. (a) S_{11}. (b) S_{22}. (c) S_{21}. (d) S_{12}.

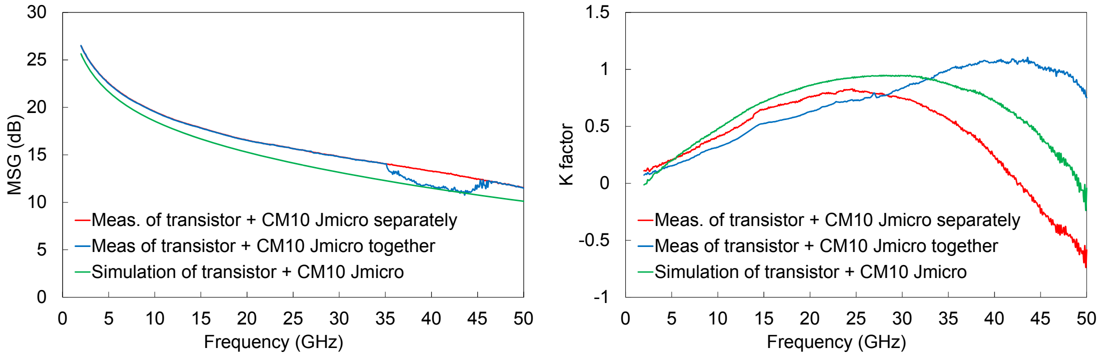

(a) *(b)*

Fig. 3.28. Unit T1c34 with four bonding wires in the source pad. Blue measurement without JMicro calibration, red measurement with JMicro calibration plus JMicro CM10 adapter measurement, pink simulation with JMicro CM10 adapters. (a) MSG. (b) K stability factor.

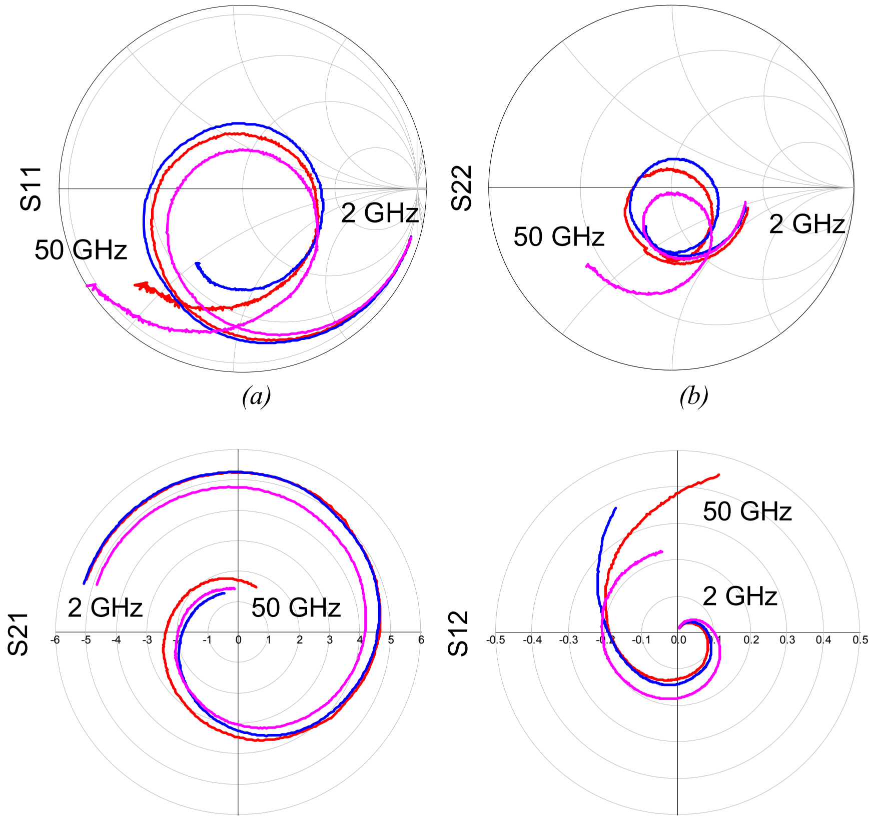

(c) *(d)*

Fig. 3.29. Scattering parameters performance of IAF transistor (unit T1c37) with four long bonding wires in the source pad. Blue measurement without JMicro calibration, red measurement with JMicro calibration plus JMicro CM10 adapter measurement, pink simulation with JMicro CM10 adapters. (a) S_{11}. (b) S_{22}. (c) S_{21}. (d) S_{12}.

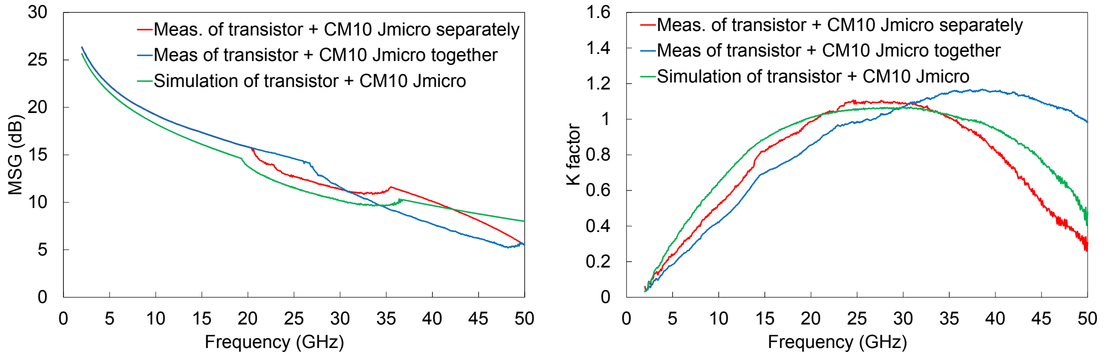

(a) *(b)*

Fig. 3.30. Unit T1c37 with four long bonding wires in the source pad. Blue measurement without JMicro calibration, red measurement with JMicro calibration plus JMicro CM10 adapter measurement, pink simulation with JMicro CM10 adapters. (a) MSG. (b) K stability factor.

3.3.4. LNA design

The most important part for the noise performance of the LNA is the first stage. Therefore, the design should rely on simple microstrip lines at the input. Matching networks between transistors and the output network are designed to achieve flat gain keeping the noise as low as possible, and to compensate the negative gain slope of first stage. Input and output ports are 50 ohm impedance characteristic microstrip lines while inter-stage networks are made by high impedance microstrip lines.

Design and optimisation process is carried out using ADS Momentum simulator from Keysight Technologies. The substrate used for the microstrip lines is CLTE-XT from Arlon (ε_r = 2.79, h = 5 mils) due to its good performance stability with temperature. Fig. 3.31 shows the circuit diagram of the LNA. Bias networks are individual for each gate and drain and they are formed by a combination of resistors and capacitors providing filtering networks for unwanted signals and low-frequency stability.

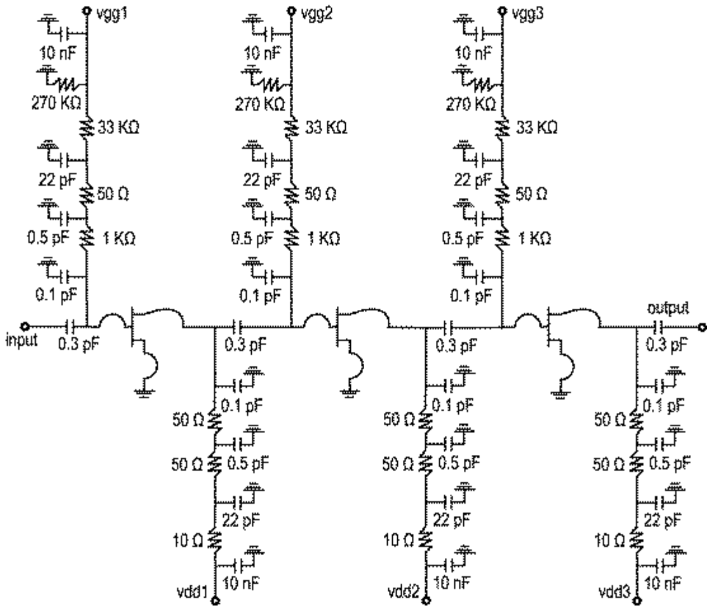

Fig. 3.31. Electrical scheme of the three- stage MIC LNA.

A chassis is manufactured to host the MIC. It consists in a central RF channel to host the transistors and the matching networks, and DC bias ports are narrow channels perpendiculars to RF channel in order to avoid resonances in the cavity. A detailed inner view of the LNA is shown in Fig. 3.32. The chassis is equipped with 2.4 mm female coaxial connectors (Fig. 3.33).

Fig. 3.32. Internal photo of the MIC LNA manufactured.

3.4. LNA performance

Measurements of MIC LNA Scattering parameters were taken with a network analyser E8364A from Keysight Technologies.

The measurement of noise figure in Ka-Band requires a frequency down conversion stage in combination with the available N8975A noise figure analyser and noise source (model 346C_K01 from Keysight Technologies). A 6 dB attenuator is placed after the noise source for two reasons; first the attenuator reduces the excess noise ratio (ENR) of the noise source and approximates it to the expected noise of the device under test (DUT) reducing the uncertainty of the measurement [3.8]. And second, the difference between reflection coefficient of the noise source in the ON and OFF states is smaller, minimizing the ripple in the measurements.

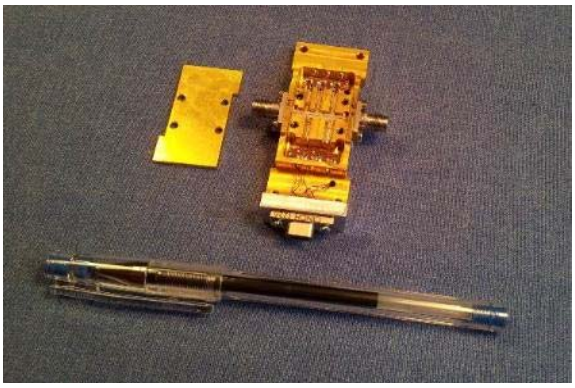

Fig. 3.33. LNA assembly with 2.4 mm female coaxial connectors.

3.4.1. Room temperature

Bias point is tuned in order to achieve the best trade-off between gain and noise. Finally the bias point I_{d1}=15 mA, V_{d1}=2.3 V and I_{d23}=16 mA, V_{d23}=2.5 V was selected. So DC power consumption is 114.5 mW.

Fig. 3.34 shows the measurement of Scattering parameters, the small signal gain, S_{21}, and the input and output matching. Average gain in the 26-36 GHz frequency band is 22.5 dB with a ripple ±2.2 dB. Matching average values are -9.2 dB at the input and -14.7 dB at the output.

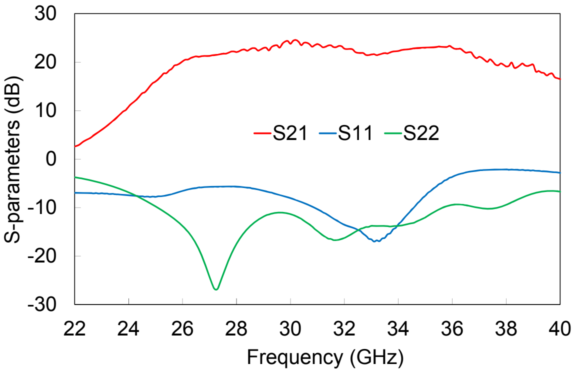

Fig. 3.34. LNA Scattering parameters performance. Small signal gain, S_{21} (blue), input matching S_{11} (pink), and output matching S_{22} (green).

Fig. 3.35 shows noise performance. Average noise temperature in the 26-36 GHz frequency band is T_n =175 K (2.05 dB noise figure) with a minimum noise temperature of 145 K at 36 GHz.

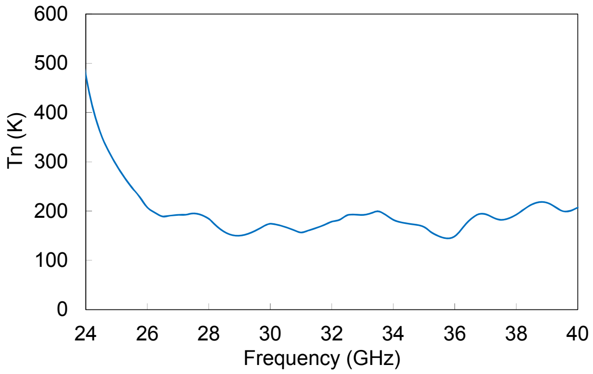

Fig. 3.35. Measured noise temperature T_n at room temperature (300 K).

3.4.2. Cryogenic temperature

LNA measurements under cryogenic conditions were taken using the cold-attenuator technique. It consists in cooling an attenuator placed at the input of the LNA, the DUT, to reduce the noise power injected from the noise source outside the cryostat [3.9] (see Fig. 3.36).

Calibration is performed following the same procedure as at room temperature measurement. Meanwhile the noise source is directly connected to the cryostat input during the measurement, removing the 6 dB attenuator used at room temperature, because of the existing 20 dB attenuator inside the cryostat [3.10].

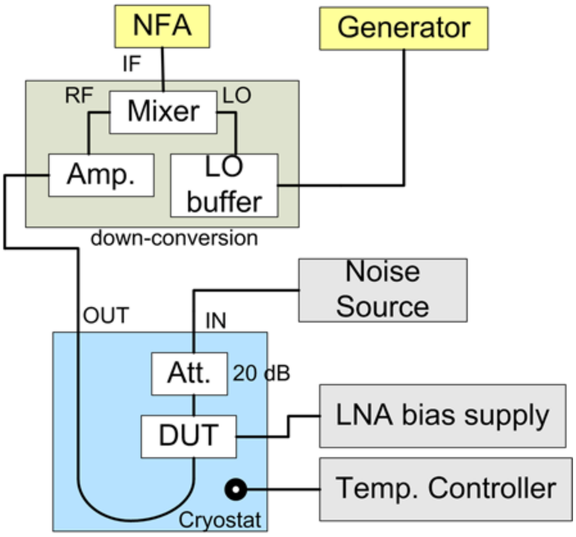

Fig. 3.36. Noise measurement set-up at cryogenic temperature.

In Fig. 3.37 the MIC LNA is presented clamped to the cold base inside the cryostat, just before a cooling cycle [3.11].

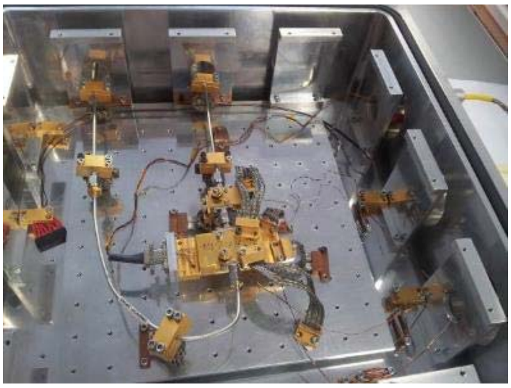

Fig. 3.37. Picture of the MIC LNA inside the cryostat.

The result of the cryogenic measurement is plotted in Fig. 3.38. The average noise temperature in the 26-36 GHz frequency band is 26 K with a minimum noise temperature of 19.5 K at 29 GHz, whereas the associated gain 23.8 ± 2.2 dB. The bias point is I_{d1}=2.5 mA, V_{d1}=0.8 V, I_{d2}=3.5 mA, V_{d2}=0.61 V, I_{d3}=2.2 mA, and V_{d3}=0.7 V. So the DC power consumption is only 5.7 mW.

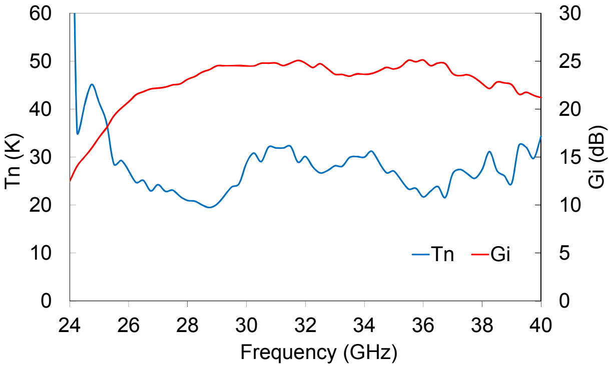

Fig. 3.38. Cryogenic performance: associated gain, G_i (blue), and noise temperature (pink) at physical temperature T_p=13 K.

3.4.3. Gain compression: P_{1dB}

Finally the MIC gain compression is measured at room temperature. The bias point is chosen to V_d =1.5 V and I_d =15 mA. The set-up is shown in Fig. 3.39 and it is identical to the one used in the Q-band MMIC LNA characterisation (see section 2.4.3).

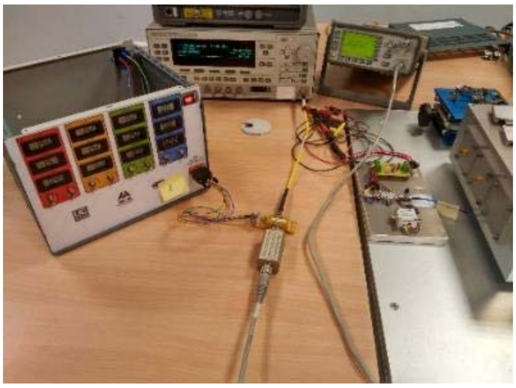

Fig. 3.39. P_{1dB} set-up for the MIC LNA at room temperature.

The obtained P_{1dB} is plotted in Fig. 3.40 at three representative frequencies, the central one at 31 GHz, and the ends of the band at 31 and 36 GHz respectively. The 1-dB gain compression points referred at the output of the MIC LNA are listed in Table 3.7. The gain compression is quite constant along the low frequencies, -3 dBm at 26 and 31 GHz. However, there is a maximum value of -1.4 dBm output power achieved at the highest frequency of 36 GHz. It means the MIC design has a higher compression gain than the value obtained in the MMIC design, -10 dBm (see section 2.4.3), for similar technology processes.

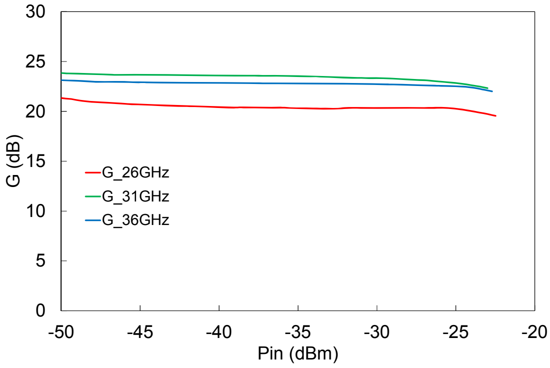

Fig. 3.40. Gain compression, P_{1dB}, of the MIC LNA at three representative frequencies and at room temperature.

Table 3.7. Gain compression values of the MIC LNA at three representative frequencies.

Frequency (GHz)	Output power (dBm)
26	-2.9
31	-3
36	-1.4

3.5. Conclusions

In this chapter, the design and characterisation of a full-hybrid low-noise cryogenic amplifier developed for radio astronomy applications in the 26-36 GHz frequency band has been presented.

The amplifier topology consists in a three stage common source configuration with transistors manufactured on GaAs metamorphic HEMT technology from the Fraunhofer Institute.

The amplifier exhibits 22.4 dB of gain and 175 K of noise temperature in the 26-36 GHz frequency band at room temperature. When the amplifier is cooled down 13 K, the gain achieved is 23.8 dB and the average noise temperature is 26 K. The DC power consumption at cryogenic temperatures is extremely low, only 5.7 mW.

3.6. References

[3.1] Danielle Kettle, Neil Roddis, Rob Sloan, “A Lattice Matched InP Chip Set for a Ka Band Radiometer”, 2005 IEEE.

[3.2] Yu-Lung Tang; Wadelfalk N.; Morgan, M.A.; Weinreb, S. “Full Ka-Band High Performance InP MMIC LNA Module”. Microwave Symposium Digest, 2006. IEEE MTT-S International.

[3.3] B. Aja, M. Seelmann-Eggbert, A. Leuther, H. Massler, M. Schlechtweg, J.D. Gallego, I. López-Fernándz, C. Diez, I. Malo, E. Villa, E. Artal, “4-12 GHz and 25-34 GHz Cryogenic MHEMT MMIC Low Noise Amplifiers for Radio Astronomy”. 2012 IEEE MTT-S Int. Microwave Symp. Dig. June 2012.

[3.4] Wu Chia-Song, Chang Chien-Huang, Liu Hsing-Chung, Lin Tah-Yeong, and Wu Hsien-Ming, “A Ka-band low-noise amplifier with a coplanar waveguide (CPW) structure with 0.15-μm Ga-As pHEMT technology”, Journal of Semiconductors, vol.31, no. 1, January 2010. Chinese Institute of Electronics.

[3.5] Qian Ma1, D. Leenaerts1,2, R. Mahmoudi1, “A 30GHz 2dB NF Low Noise Amplifier for Ka-band Applications”, 2012 IEEE. Radio Frequency Integrated Circuits Symposium.

[3.6] Vicente Terán Collantes, Luisa de la Fuente, Juan Luis Cano, Eduardo Artal, “Ka-Band Full-Hybrid Cryogenic Low-Noise Amplifier”, XXIX Simposium Nacional de la Unión Científica Internacional de Radio, URSI 2014, Valencia, 3-6 Septiembre, 2014.

[3.7] Marian W. Pospiezalsky, “Modeling of Noise Parameters of MESFET’s and MODFET’s and Their Frequency and Temperature Dependence”, IEEE Transactions on Microwave Theory and Techniques, vol. 37, no. 9, September 1989.

[3.8] J.L. Cano and J.D. Gallego, “Estimation for Uncertainty in Noise Measurements Using Monte Carlo Analysis” 1st Radionet-FP7 Engineering Forum Workshop, Gothenburg, Sweden, June 2009.

[3.9] J.E. Fernández, “ A noise-temperature measurement system using a cryogenic attenuator”, Jet Propulsion Lab. (JPL), Pasadena, CA, TMO Progress Rep. 42-135, Nov. 1998.

[3.10] J.L. Cano, N. Waldefalk, and J.D. Gallego-Puyol, “Ultra-Wideband Chip Attenuator for Precise Noise Measurements at Cryogenic Temperatures”, IEEE Trans. Microwave Theory and Tech., vol. 58, no. 9, Sept. 2010, pp. 2504-2510.

[3.11] Juan Luis Cano, Luisa de la Fuente, Eduardo Artal, “Amplificador de Bajo Ruido basado en Tecnología mHEMT para Receptores de Radio Astronomía”, XXVII Simposium Nacional de la Unión Científica Internacional de Radio 2012.

CHAPTER IV: NOISE ANALYSIS IN DISTRIBUTED AMPLIFIERS WITH FEEDBACK-ACTIVE LOAD

4.1. Introduction

Distributed amplifiers (DA) are usually designed to provide flat gain response over wide bandwidths. Resulting noise performance is typically poor, especially at low frequencies [4.1]-[4.3], where the noise introduced by the line termination dominates the noise of the active devices composing the amplifier. As long as the frequency increases, the noise of the active devices begins to be more important than the line termination contribution. One possible technique to minimize noise involves a change in the temperature of line termination. Previous works have adopted active loads as line terminations in order to improve the noise performance [4.4]-[4.6], although only simulations results have been presented and the influence of the active load in the overall amplifier, in terms of noise, is not completely explained. In [4.7]-[4.8], active load terminations are used in order to extend the low-frequency gain, but noise performance is not evaluated.

This chapter provides an extra overview over the noise reduction in a distributed amplifier when using feedback-active loads as line terminations, and a mathematical analysis is proposed to explain such noise reduction phenomena [4.9]. A small-signal analysis of a feedback transistor including noise sources demonstrates the resulting lower noise temperature of such arrangement, as compared to a conventional resistive load. Moreover, the effect of the temperature in the line loads of the distributed amplifier is discussed and the major contributions to the noise temperature are underlined.

Based on the mathematical analysis, a simple two-stage distributed amplifier is designed in two configurations, namely a reference resistively terminated one and an actively terminated amplifier as a test vehicle of the study. The frequency band of the amplifier spans from 1 to 5 GHz, as a prototype to expand up to high frequency bands.

Finally, fabrication and measured results are presented for both amplifiers, demonstrating the improvement achieved in terms of noise performance when an active terminating load is used. The impact of cascading the amplifiers is also analysed from the measurements, showing the increase of gain and keeping the noise performance of the first amplifier of the cascade.

4.2. Distributed Amplifiers in radio astronomy receivers

Since the noise performance of a distributed amplifier is not the best, compared with classic common-source low-noise topology, distributed amplifiers are used in gain modules of low-noise radio astronomy receivers. They are mainly placed as the second amplifier in back-end gain modules. However, they are not suitable to work in cryo-cooled front-end modules due to the high DC power consumption they require.

The distributed topology provides a high 1-dB compression point compared with low-noise topologies because the power of each active device is added sequentially in the drain line (output of the DA). Typically in a radio astronomy receiver, a suitable power is necessary to deliver from gain chain to subsequent stages.

The improvement of noise in the distributed amplifier, keeping its linear performance, is important in order not to spoil the previous low-noise amplification stages.

4.3. Noise figure

In this section, the noise figure of a conventional distributed amplifier is analysed. Noise contributions of drain and gate line terminations are evaluated. Then the noise temperature of an active load considered as a one port device and implemented with a feedback transistor, is obtained.

4.3.1. Noise figure of DA

Noise in distributed amplifiers has been previously discussed by several authors [4.1], [4.2]. The noise factor of the amplifier is defined as

$$F = 1 + \frac{N_a}{k \cdot T_o \cdot B \cdot G_f} \tag{4.1}$$

where N_a is the added noise from the amplifier to its output, G_f is the distributed amplifier forward gain from the input to the output, k is the Boltzmann's constant, T_o is 290 K and B is the bandwidth where noise is measured (1 Hz will be assumed). Added noise can be decomposed in three terms as follows,

$$N_a = N(Z_d) + N(Z_g) + N_{FET} \tag{4.2}$$

where $N(Z_d)$ is the noise power contribution of the drain line termination Z_d and $N(Z_g)$ is the noise power contribution of the gate line termination Z_g. N_{FET} is the overall noise associated to the transistors composing the amplifier. The contributions of the line loads are defined as,

$$N(Z_d) = k \cdot T_o \cdot B \tag{4.3}$$

$$N(Z_g) = k \cdot T_o \cdot B \cdot G_r \tag{4.4}$$

where G_r is the gain of the distributed amplifier in reverse configuration, which corresponds to the available gain from the input to the drain line termination.

Takin into account expressions (4.2), (4.3) and (4.4) and assuming noiseless transistors (N_{FET} =0), the noise factor due to contributions from line termination only can be rewritten as

$$F = 1 + \frac{1}{G_f} + \frac{G_r}{G_f} \tag{4.5}$$

where the forward and reverse gains of the amplifier are explicitly indicated [4.1] in (4.6) and (4.7) under the assumption that drain and gate transmission lines exhibit the same phase constant and are lossless.

$$G_f = \frac{n^2 \cdot g_m^2 \cdot Z_g \cdot Z_d}{4} \tag{4.6}$$

$$G_f = \frac{g_m^2 \cdot Z_g \cdot Z_d}{4} \cdot \left(\frac{\sin n\beta}{\sin \beta}\right)^2 \tag{4.7}$$

As already defined, Z_g and Z_d are gate and drain lines terminating impedances respectively (usually 50 Ω), n is the number of stages of the DA (number of transistors), β is the phase propagation constant of the transmission line, and g_m is the trans-conductance of each transistor (identical transistors are assumed). The function $(\sin n\beta / \sin \beta)^2$ can be approximated by n^2 when $n\beta$ is close to 0 or π. In this case $G_f = G_r$.

In order to improve noise performance, the impact of the temperatures of the loads in the global noise figure of the amplifier is analysed. If a temperature T_g ($\neq T_o$) is assumed in the gate line termination keeping $T_d = T_o$ in drain line termination, its noise contribution $N(Z_g)$ is

$$N(Z_g) = k \cdot T_g \cdot B \cdot G_r \tag{4.8}$$

The resulting amplifier noise factor, F, from (4.5), is,

$$F = 1 + \frac{1}{G_f} + \frac{G_r}{G_f} \cdot \frac{T_g}{T_o} \tag{4.9}$$

On the other hand, if a temperature T_d ($\neq T_o$) is assumed for the drain line termination keeping $T_g = T_o$ in gate line termination, its noise contribution $N(Z_d)$ is,

$$N(Z_d) = k \cdot T_d \cdot B \tag{4.10}$$

The noise factor of the distributed amplifier in (4.5) results in (4.11).

$$F = 1 + \frac{1}{G_f} \cdot \frac{T_d}{T_o} + \frac{G_r}{G_f} \tag{4.11}$$

The effect in the overall noise figure of a temperature change in line loads can be evaluated separately, considering expressions (4.9) and (4.11). Fig. 4.1 shows how the noise figure (10·log(F)) changes with each load temperature when the other is kept constant for a distributed amplifier with $G_f = G_r = 10$ dB. The impact of the gate line termination temperature is significantly higher if compared to the drain one as it can be expected since T_g only is affected by the amplifier forward gain. From this result, it can be concluded that temperature changes in drain line termination will produce a negligible effect in the amplifier noise figure.

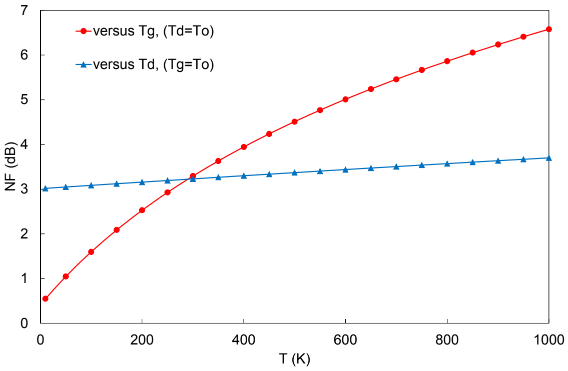

Fig. 4.1. Noise figure of a distributed amplifier in (9) and (11) versus line termination temperature.

4.3.2. Noise temperature of an active load

An active load can be implemented using a feedback transistor [4.10]-[4.12]. The noise temperature of such active load can be analysed through a simplified small-signal model (Fig. 4.2) of the high electron mobility transistor (HEMT).

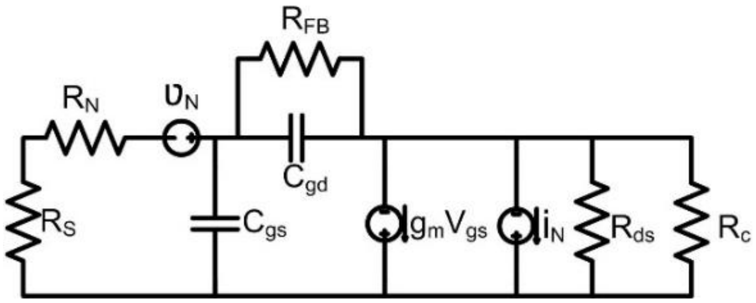

Fig. 4.2. Small-signal model for noise temperature analysis in a HEMT.

Noise sources v_N and i_N can be obtained from transistor noise parameters (measured or provided by device manufacturer). A possible noise model for the transistor is suggested by Pucel et al. [4.13]. On the other hand, those noise voltage source and noise current source can be expressed by the equivalent noise resistance R_n and equivalent noise conductance G_n, which are defined in [4.14], as (4.12)-(4.13), where T is the physical temperature.

$$\overline{v_N^2} = 4 \cdot k \cdot T \cdot B \cdot R_n \tag{4.12}$$

$$\overline{i_N^2} = 4 \cdot k \cdot T \cdot B \cdot G_n \tag{4.13}$$

Applying superposition in the circuit of Fig. 4.2, noise currents can be obtained. The root mean square (RMS) value for the input current, i_i, due to drain noise current source is,

$$\overline{i_i^2} = |-i_N \cdot H_i|^2 = \overline{i_N^2} \cdot |H_i|^2 \tag{4.14}$$

where the transfer function H_i is,

$$|H_i|^2 = \left| \frac{Z_{ds} \cdot Z_{gs}}{(Z_{gs}+R_s+R_n) \cdot \left(Z_{ds} + \frac{R_{FB} \cdot Z_{gd}}{R_{FB}+Z_{gd}} \right) + (R_s+R_n) \cdot Z_{gs} + g_m \cdot (R_s+R_n) \cdot Z_{ds} \cdot Z_{gs}} \right|^2 \tag{4.15}$$

R_{FB} is the gate to drain feedback resistance, Z_{ds}, Z_{gd}, and Z_{gs} are

$$Z_{ds} = R_{ds} // R_c \quad Z_{gd} = \frac{1}{j \cdot \omega \cdot C_{gd}} \quad Z_{gs} = \frac{1}{j \cdot \omega \cdot C_{gs}} \tag{4.16}$$

The RMS value for the input current, i_v, due to gate noise voltage source is

$$\overline{i_v^2} = |v_N \cdot H_v|^2 = \overline{v_N^2} \cdot |H_v|^2 \tag{4.17}$$

where the transfer function H_v is,

$$|H_v|^2 = \left| \frac{1}{R_s+R_n} - \frac{1}{(R_s+R_n) + \frac{(R_s+R_n)^2}{Z_{gs}} + (R_s+R_n)^2 \cdot (1+g_m \cdot Z_{ds}) \cdot \frac{1}{Z_{ds} + \frac{R_{FB} \cdot Z_{gd}}{R_{FB}+Z_{gd}}}} \right|^2 \tag{4.18}$$

The noise current at the input impedance (R_s) is:

$$\overline{i_T^2} = \overline{i_N^2} \cdot |H_i|^2 + \overline{v_N^2} \cdot |H_v|^2 \tag{4.19}$$

The noise temperature can be computed at the input of the transistor (R_s) as

$$T_n = \overline{i_T^2} \cdot \frac{R_s}{k \cdot B} \tag{4.20}$$

Considering (4.20) it is clear than the lower the noise current, the lower the noise temperature. Taking the small-signal model parameters (Fig. 4.2) for the HEMT transistor used in the amplifier design (more details in section 4.4), the effect of feedback can be evaluated. The values for the small-signal parameters of the enhancement-mode transistor (pHEMT) reference ATF551M4 provided by AVAGO Technologies manufacturer, at the frequency of 3 GHz, are summarised in Table 4.1.

Table 4.1. Small-signal parameters at 3 GHz for the ATF551M4 pHEMT transistor from AVAGO Technologies.

R_{ds} (Ω)	R_c (Ω)	R_n (Ω)	R_s (Ω)	C_{gd} (pF)	C_{gs} (pF)	g_m (mS)
3507	260	6.97	50	0.17	0.32	44

The noise current contributions for each noise source, i_i (4.14) and i_v (4.17), versus the feedback resistance (R_{FB}) at three representative frequencies in the band of interest are compared in Fig. 4.3. The noise voltage source contribution is clearly predominant over the noise current one. Therefore, the effect of feedback in the transfer function H_v (4.18) only is analysed.

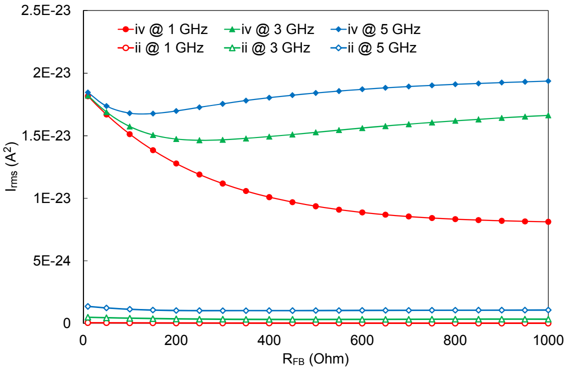

Fig. 4.3. Noise current contribution for the active load due to noise sources versus feedback resistance (R_{FB}) at three frequencies: noise voltage i_v and current i_i source contributions.

Fig. 4.4 shows the influence of the feedback resistance in the transfer function H_v (4.18) at three representative frequencies in the band of interest. H_v magnitude has been magnified by 1000 for easier discrimination. As frequency increases, the required value of the optimum feedback resistance becomes smaller. For example, at 3 GHz the behaviour exhibits a minimum close to 200 Ω. Such value represents therefore the optimum feedback value to minimize noise temperature.

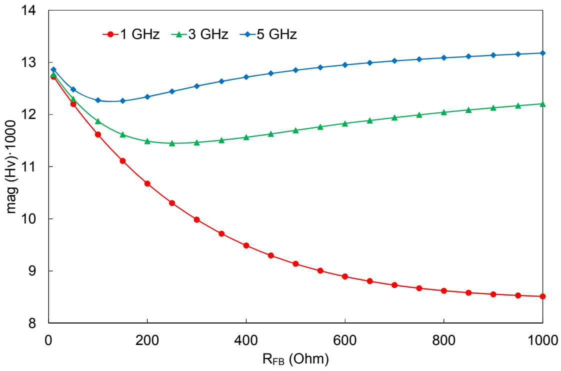

Fig. 4.4. Magnitude of transfer function due to noise voltage source versus feedback resistance (R_{FB}) at three frequencies.

Despite the feedback effect in H_v is small, its influence in the overall noise temperature of the active load is important as depicted in Fig. 4.5(a).

In Fig. 4.5(b), equivalent noise temperature of the active load is plotted versus frequency for different feedback resistances. The active load noise performance is better without feedback only for frequencies below 1 GHz. As feedback resistance decreases (from 1000 to 120 Ω) the noise temperature improvement is remarkable at higher frequencies, and minor at lower ones. As a consequence, the feedback effect provides a much lower noise temperature than 300 K of a passive 50 Ω termination.

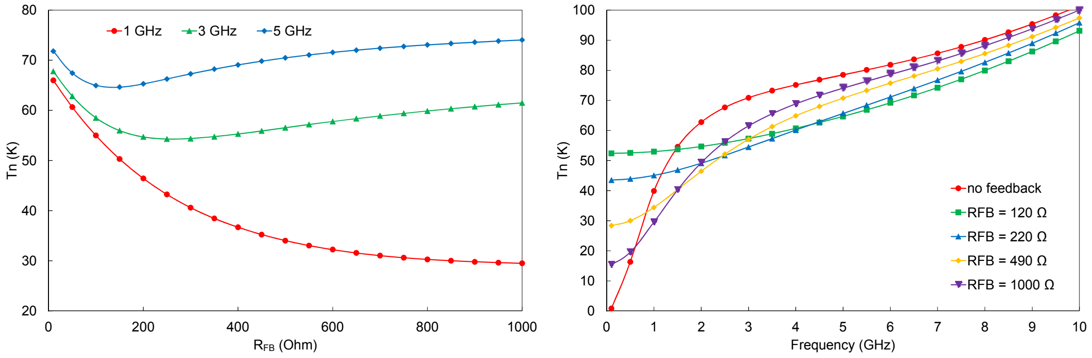

(a) *(b)*

Fig. 4.5. Overall noise temperature of the active load. (a) Versus feedback impedance at three frequencies. (b) Versus frequency for different feedback impedances.

The analysis developed in this section demonstrates that the active load represents an excellent solution to minimize low-frequency noise in a distributed amplifier. Introduction of feedback in the active load improves its noise performance in medium-high frequencies while providing a trade-off with a terminating impedance close to 50 Ω, necessary for a good distributed amplifier behaviour. A lower temperature in gate termination is more important in terms of noise figure than in the drain one, as is demonstrated in section 4.3.1. The active load will therefore be adopted as gate line termination.

4.4. Design example

Let see an example to validate the above analysis.

4.4.1. Two-stage distributed amplifier with resistive terminations

A simple two-stage distributed amplifier is designed in the 1-5 GHz frequency band. Both gate and drain lines are terminated with 50 Ω loads. The transistor is the same as the one used in previous section 4.3.2. The selected bias for each transistor is v_{ds} = 3 V, i_d = 10 mA. The transconductance for such bias point is gm = 44 mS. Fig. 4.6 shows the electrical schematic of the amplifier. Passive elements have been implemented using lumped components.

Pi-networks at the amplifier's input and output were designed to improve return loss. Part of the drain line is made up of microstrip lines in order to get the necessary inductive behaviour. The linear and noise performance simulations of the two cell distributed amplifier are plotted in Fig. 4.7(a) and Fig. 4.7(b) respectively.

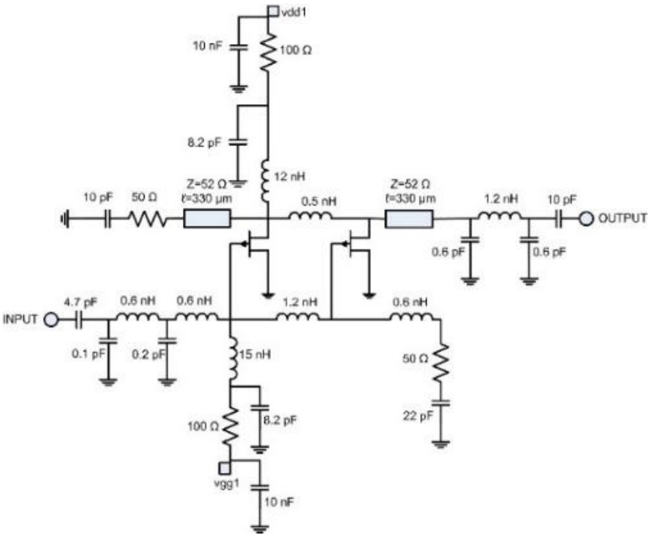

Fig. 4.6. Two cell distributed amplifier.

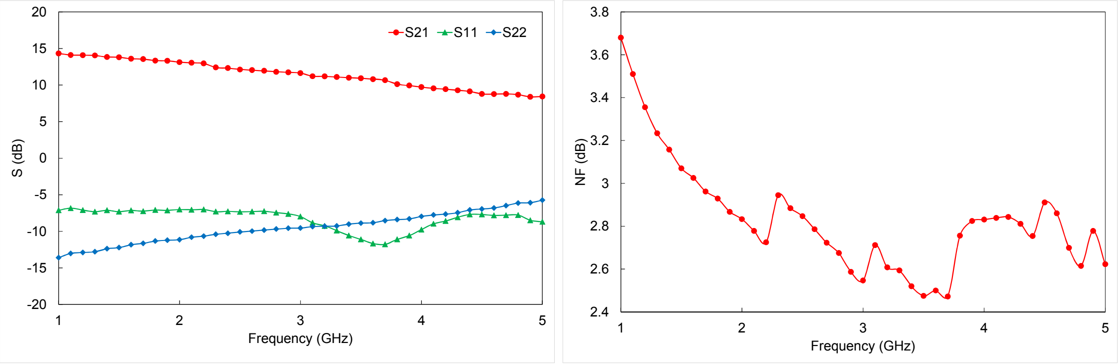

(a) *(b)*

Fig. 4.7. Simulated performance of two cell distributed amplifier. (a) Scattering parameters. (b) Noise figure.

Average values of simulated performance for the two cell distributed amplifier in the 1-5 GHz frequency band are summarized in the first row of Table 4.2. This table includes measurement results. Tests are detailed in next section 4.5.

Table 4.2. Simulation and measurement results for DA with resistive and active gate line termination. Average values from 1 to 5 GHz.

	Average S_{21} (dB)	**Slope S_{21} (dB)**	**Max. S_{11} (dB)**	**Max. S_{22} (dB)**	**Average NF (dB)**	**Max. NF (dB)**	**Min. NF (dB)**	**Slope NF (dB)**
Simulation – 50 Ω line term.	11.4	5.9	-6.8	-5.7	2.8	3.7	2.5	1.2
Measurement – 50 Ω line term.	11.1	3.1	-5.4	-11.1	2.4	3.5	1.6	1.9
Simulation – Active gate line term.	11.7	4.8	-6.3	-6.4	2.1	2.4	1.6	0.8
Measurement – Active gate line term.	10.9	2.5	-6.5	-10.4	2.1	2.8	1.5	1.3

The effect of gate and drain line terminations is analysed in Scattering and noise performance. Load resistances, R_g and R_d, are varied separately from 10 up to 100 Ω. Fig. 4.8 shows the Scattering and noise figure performance when the gate load is swept keeping the drain load fixed to 50 Ω. There is a loss of flatness for small gate load resistance at 1 GHz, see Fig. 4.8(a). Moreover, large resistances are better in terms of noise (see Fig. 4.8(c)) below 2 GHz, but the effect is the opposite for higher frequencies.

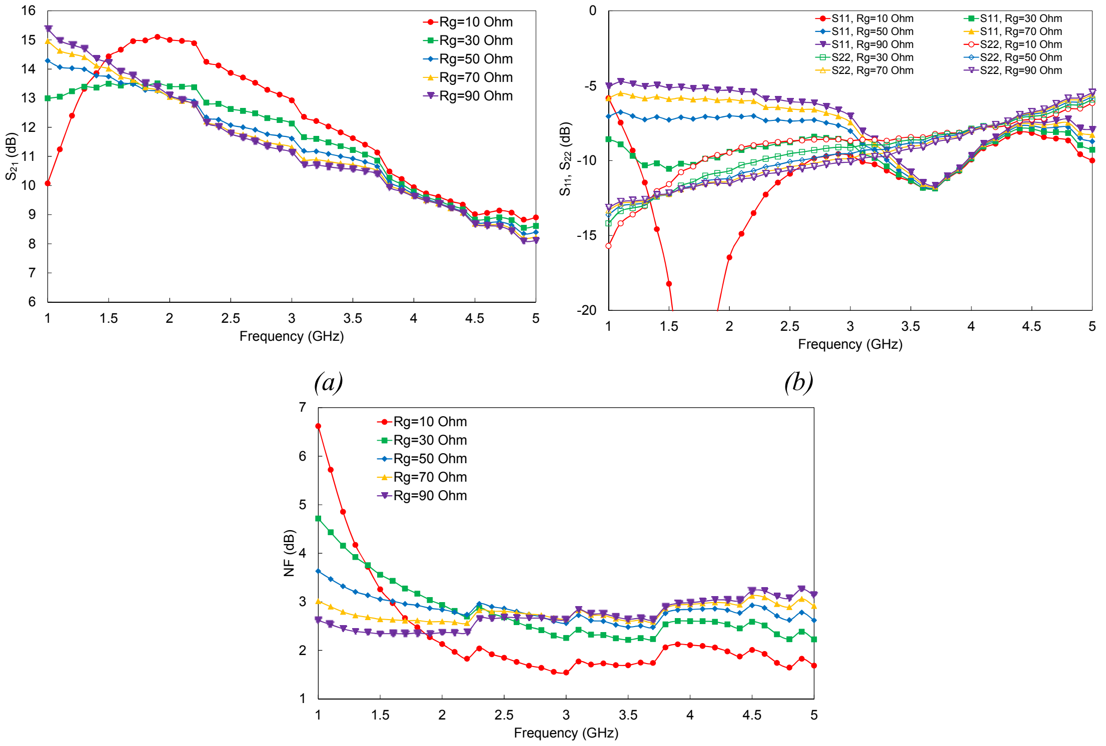

(a) (b)

(c)

Fig. 4.8. Simulated performance versus frequency and gate load for the distributed amplifier with resistive line terminations. Drain load 50 Ω. (a) S_{21}. (b) S_{11} and S_{22}. (c) Noise figure.

Fig. 4.9 shows the Scattering and noise figure performance when the drain load is swept keeping gate load fixed to 50 **Ω**. Very low drain resistance does not allow good results in terms of gain, Fig. 4.9(a), and output matching, Fig. 4.9(b). Noise figure increases at high frequencies for small drain load resistances (see Fig. 4.9(c)).

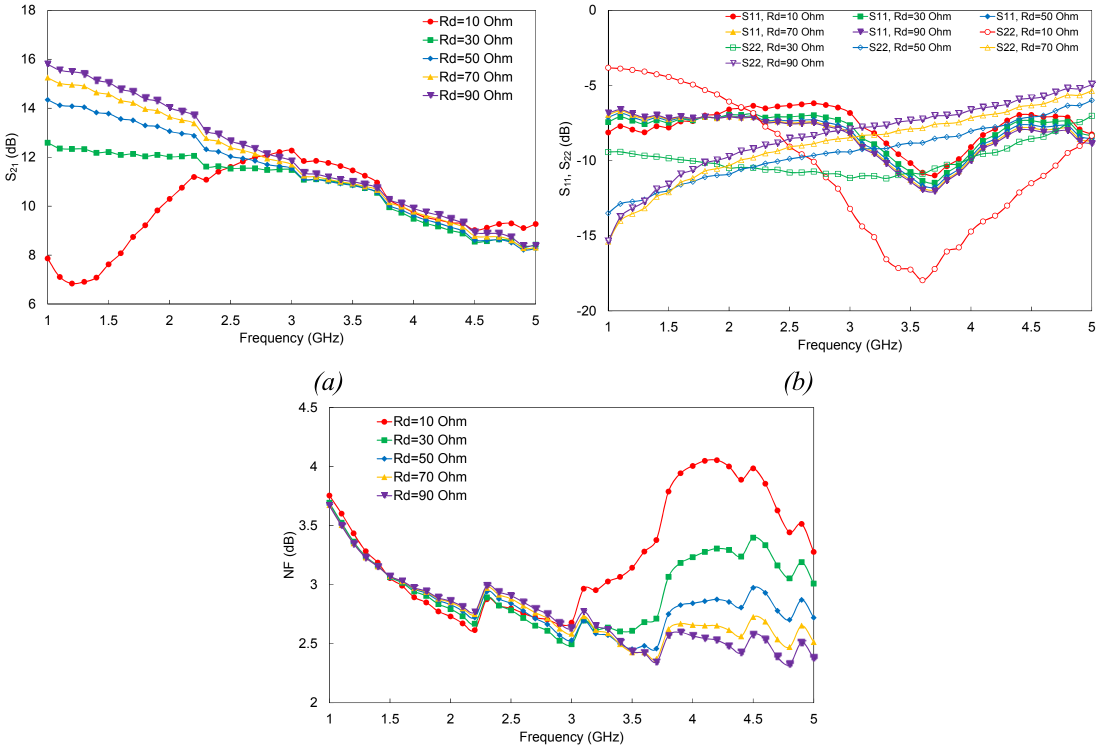

(a) *(b)*

(c)

Fig. 4.9. Simulated performance versus frequency and drain load for the distributed amplifier with resistive line terminations. Gate load 50 Ω. (a) S_{21}. (b) S_{11} and S_{22}. (c) Noise figure.

As a consequence, there is a noticeable effect in noise performance when terminating impedances are changed. For gate termination impedances lower than 50 Ω, noise figure is lower at high frequencies, but higher at low frequencies. A 50 Ω impedance in gate termination is the best trade-off between noise figure and Scattering parameters in the whole frequency range. Regarding variations in drain termination, higher impedances provide a lower noise figure at high frequencies, but there is no influence at low frequencies.

4.4.2. Active load

In order to reduce the noise temperature of the loads of the distributed amplifier, active loads have been used taking into account the results obtained in section 4.3.2. A simple active load is implemented using a feedback transistor (the one used in section 4.3.2). The selected bias point is v_{ds} = 3 V, i_d = 649 µA. The transistor configuration shown in Fig. 4.10(a) without feedback is adopted. Noise power and temperature are obtained through expressions (4.21) and (4.22), where v_n is the simulated noise voltage and R_{in} the simulated input resistance for the transistor. Fig. 4.10(b) shows a schematic of the active load with feedback resistor.

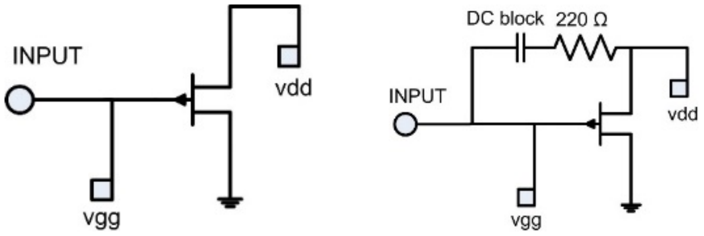

(a) *(b)*

Fig. 4.10. Schematic of a transistor. (a) Common source. (b) Common source with gate to drain feedback.

$$\overline{v_N^2} = 4 \cdot k \cdot T \cdot B \cdot R_n \tag{4.21}$$

$$\overline{\iota_N^2} = 4 \cdot k \cdot T \cdot B \cdot G_n \tag{4.22}$$

The noise temperature presented at the input of the transistor, and the simulated noise temperature of the common source transistor with gate to drain feedback are compared with that introduced by a 50 Ω resistor load in Fig. 4.11. As obtained in section 4.3.2, noise temperature in a feedback transistor is strongly dependent on frequency and feedback resistance. Since a higher feedback resistance is better in terms of noise (section 4.3.2), a 220 Ω was selected as the optimum value for central frequency in the band of interest, 3 GHz.

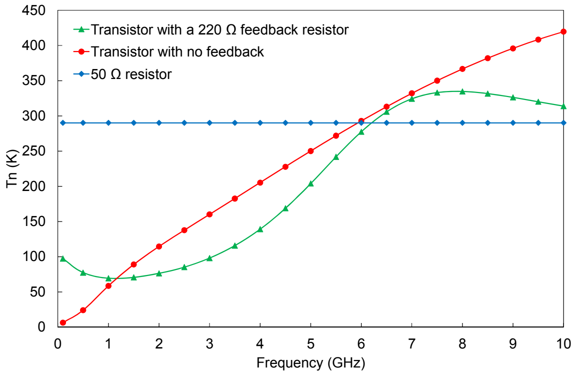

Fig. 4.11. Noise temperature versus frequency for a 50 Ω resistor and the transistor, with no feedback and with a 220 Ω feedback resistor.

The improvement in noise temperature when the transistor is feedback evidences the need of resistive gate line termination replacement by an active one in the amplifier. Moreover, the impedance of the active load remains close to 50 Ω thanks to the feedback (Fig. 4.12) mainly at low frequencies, improving both linear and noise performance, as shown in previous section 4.4.1. The influence in the amplifier noise of the active load will be mainly due to its noise temperature and the real part of its impedance, since its imaginary part (capacitive or inductive) has a negligible effect.

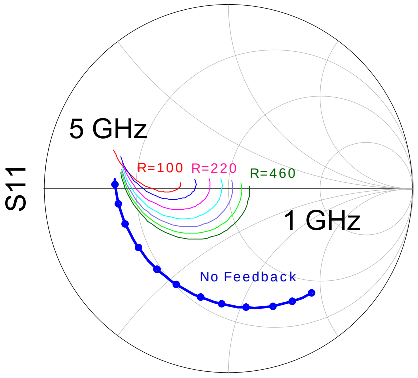

Fig. 4.12. Input reflection coefficient of the active load without feedback and for different feedback resistances from 100 to 460 Ω, in steps of 60 Ω.

4.4.3. Distributed amplifier with active gate line termination

The active load previously designed is hence used as gate line termination of the DA. Since the improvement in noise performance due to a drain active load is small (section 4.3.1), no active load is considered for drain line avoiding the resulting increase in complexity.

Full schematic of the DA is shown in Fig. 4.13. Feedback resistor was adjusted to 150 Ω to account for the influence of parasitic resistance of DC blocks and connection pads. Moreover, a bias network for the active load was implemented through a 2.7 kΩ resistor.

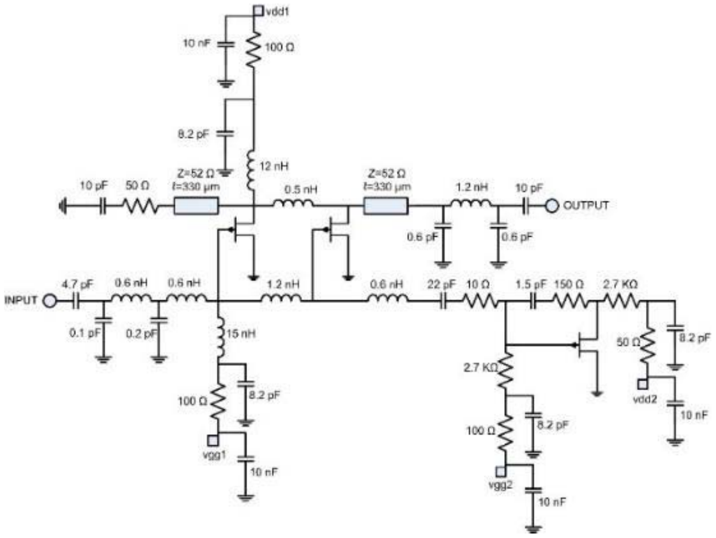

Fig. 4.13. Schematic of DA with active gate line termination.

Simulated results of new configuration for the DA are plotted in Fig. 4.14, the Scattering parameters performance in Fig. 4.14(a), and the noise figure performance in Fig. 4.14(b). Average values in the frequency band of interest, 1-5 GHz, are summarized in the third row of Table 4.2. The Scattering parameters performance is similar to the obtained with the traditional DA, but there is 1 dB improvement in noise figure performance (Fig. 4.14(b)). Mean noise is 2.1 dB and the slope between the maximum and the minimum noise figure in the frequency band of interest is 0.8 dB only. The improvement is higher below 2 GHz because the influence of the gate line termination noise temperature is higher at low frequencies, while the noise of the active devices becomes more significant at high frequencies.

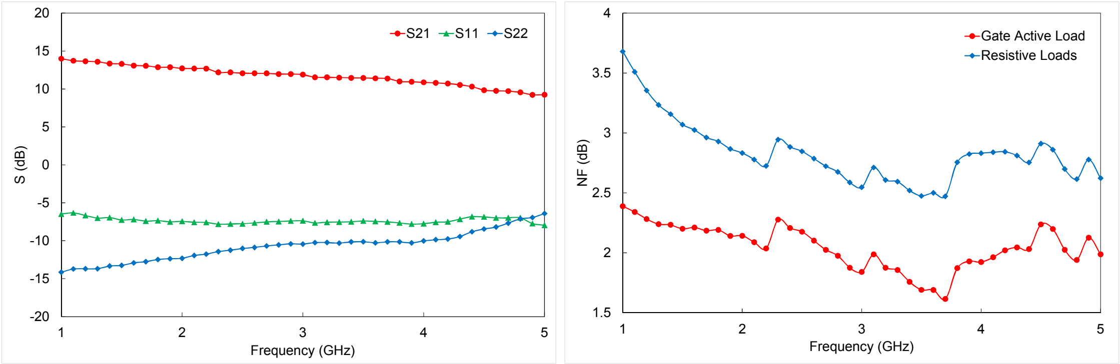

(a) *(b)*

Fig. 4.14. Simulated performance of DA with active gate line termination. (a) Scattering parameters. (b) Noise figure, comparing with the DA with resistive loads.

4.5. Performance of the DA: Fabrication and measured results

One DA is manufactured with the capability of both proposed configurations, the resistive loads and the active gate load.

4.5.1. DA with resistive line terminations

All the components for the implementation of the distributed amplifier are mounted on a 30 mils substrate from Arlon (CUCLAD 250, with dielectric constant 2.5). Capacitors and inductances are carefully selected, from ATC (size 1.397x1.397 mm^2) and Johanson Technology (size 1.524x0.762 mm^2) respectively.

Network analyser PNA E8364A from Keysight Technologies is used as Scattering parameters measurement set-up. Noise test set-up includes a noise figure analyser N8975A and a noise source N4002A, both from Keysight Technologies (Fig. 4.15). Measurement results are presented in Fig. 4.16, linear performance in Fig. 4.16(a) and noise performance in Fig. 4.16(b). The bias point for the transistors has been adjusted for better performance: i_d =20 mA and v_{ds} =4.05 V. Average results are summarized in the second row of Table 4.2 in the frequency band from 1 to 5 GHz. The amplifier achieves an average gain 11.1 dB and an average noise figure of 2.4 dB. Simulation and measurements have a good agreement in terms of linear performance, especially in gain.

However, the noise simulation predicted a higher noise than the measured, especially above 3 GHz.

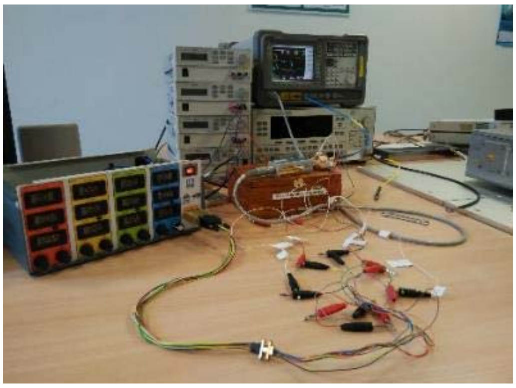

Fig. 4.15. Noise measurement test set-up for the DA.

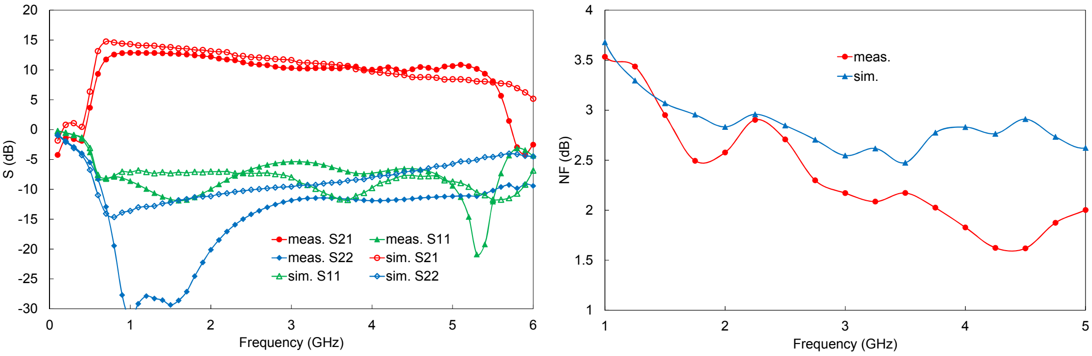

(a) *(b)*

Fig. 4.16. Measured and simulated performance versus frequency for the DA with resistive line terminations. (a) Scattering parameters. (b) Noise figure.

4.5.2. DA with active gate line termination

The designed amplifier was reconfigured by replacing the resistive load termination with an active gate load. Fig. 4.17 shows the full manufactured DA with the active gate line termination. The bias point for the transistors in the two stages of the amplifier is i_d =20mA and v_{ds} =4.05 V; the best bias point for the transistor for the active load is v_{ds} =5.8 V and i_d =2 mA. Both linear and noise performance of the amplifier are shown in Fig. 4.18, linear performance in Fig. 4.18(a) and noise in Fig. 4.18(b).

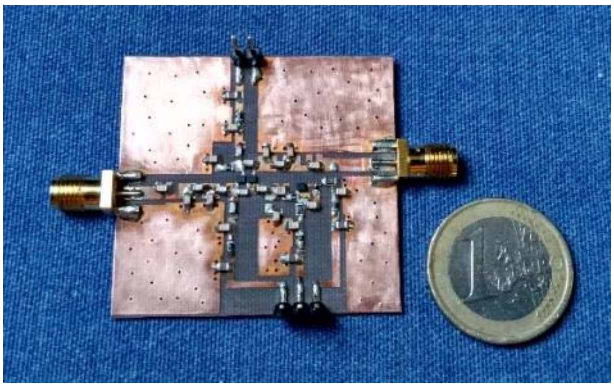

Fig. 4.17. Photo of the full DA with gate line active termination (size 42.3x44.7 mm^2).

Average results in the frequency band of interest, from 1 to 5 GHz, are summarized in the fourth row of Table 4.2. The amplifier exhibits an average gain of 10.9 dB and an average noise figure of 2.1 dB. Scattering performance does not change significantly (see Fig. 4.18(a)), but there is an average reduction of 0.3 dB in terms of noise figure in the band (see Fig. 4.18(b)), and noise flatness is also improved. Fig. 4.18(c) shows a comparison between the noise figure of the DA with the active gate line termination and with resistive ones. The higher noise reduction is evident for frequencies below 2 GHz where the improvement is 0.6 dB. This result agrees with the simulation of the amplifier in section 4.4.3. This improvement at low-frequency is clearly caused by the lower noise contribution of the active load, compared with the resistive one. On the other hand, the noise performance is nearly the same at higher frequencies when the major contribution to the total noise figure comes from the active devices who make up the amplifier.

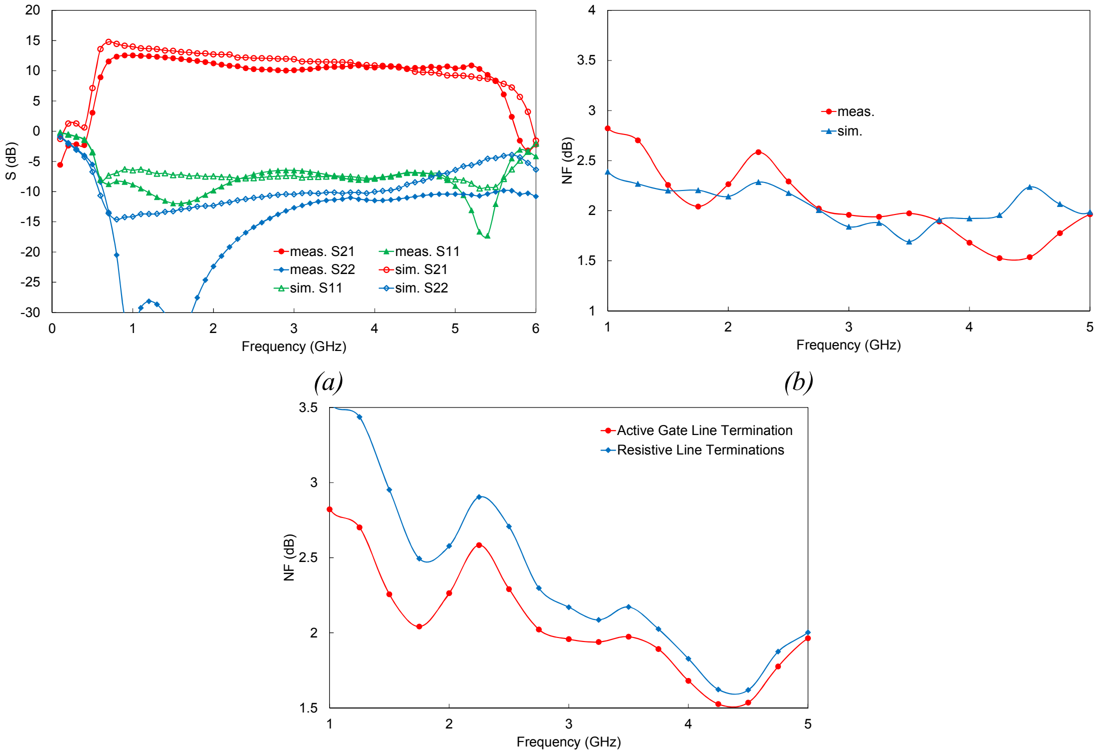

(a) *(b)*

(c)

Fig. 4.18. Measured and simulated performance versus frequency for the DA with active gate line termination. (a) Scattering parameters. (b) Noise figure. (c) Comparison of noise figure of the DA with the active gate line termination and with resistive ones.

4.5.3. Gain compression: P_{1dB}

The gain compression test of the DA with the active load as gate line termination is performed at room temperature. The measurement set-up (Fig. 4.19) is the same used in previous LNA designs (see section 2.4.3 and 3.4.3), but the input power range goes from -25 to 0 dBm, instead the range -50 to -20 dBm, because a higher gain compression point is expected. The bias point for the cell transistors is i_d =20mA, v_{ds} =4.05 V, and the active load is set to v_{ds} =5.8 V and i_d =2 mA.

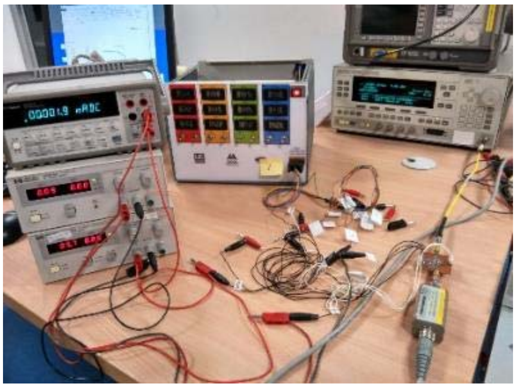

Fig. 4.19. P_{1dB} set-up for the DA.

The obtained P_{1dB} is plotted in Fig. 4.20 at three representative frequencies, the central one at 3 GHz, and the ends of the band at 1 and 5 GHz respectively. The 1-dB gain compression points referred at the output of the DA are listed in Table 4.3. The gain compression increases along the frequency band in a ratio of 1 dB per GHz. It means, the P_{1dB} at 1 GHz is 4 dBm output power and 8 dBm at 5 GHz. In spite of the frequency band (3 GHz) of the DA is lower than the designed (40 and 50 GHz) LNA (see chapter 2 and 3), the output power delivered by the distributed topology is greater than the low-noise topologies. So the DA seems to be a good option as the last amplification stage in back-ends modules of radio astronomy receivers in which the output power needs to be higher.

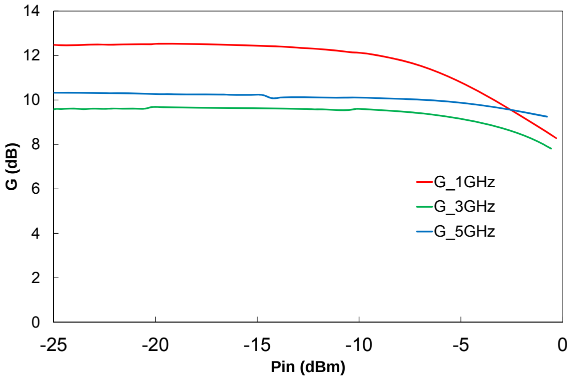

Fig. 4.20. Measured P_{1dB} for the DA with active gate line termination at three representative frequencies, 1 GHz (red), 3GHz (green), and 5 GHz (blue).

Table 4.3. P_{1dB} (output power) for the DA with active gate line termination at three representative frequencies, 1, 3, and 5 GHz.

Frequency (GHz)	P_{1dB} (dBm)
1	4.7
3	6
5	8.1

4.6. Cascading DAs

Since the DA achieves 11 dB of gain, a cascade topology of three DA cells is proposed to increase the gain more than 30 dB keeping the noise and return losses as a single DA cell. Cascading a distributed amplifier cell is easy because the good input and output return losses minimize the inter-stage mismatching. It is not necessary to design matching inter-stage networks and the cascading implementation is full-modular, so the gain can be increased adding stages in cascade without losses because mismatching.

On the other hand, the full-cascaded circuit is relatively sensitive to tolerances due to the high amount of active devices. Moreover, it requires complicated biasing networks, as each stage has to be isolated and biased individually. When the design is focused in high gain levels the cascaded DA is very sensitive and prone to oscillations due to coupling between the adjacent stages. That is the reason, the basic DA cell was designed to be simple and have a reasonable gain of 10 dB.

First stage is the DA with active gate line termination (named AL in Fig. 4.21) because it achieves the best overall noise performance. Third stage is the DA with resistive line terminations (named RL in Fig. 4.21). After two stages, 20 dB of expected gain, the contribution of noise is negligible so the active load configuration only introduces complexity in the circuit (bias network of the active load). The second stage still contributes to the noise so it is important to evaluate which DA configuration is the best, active or resistive.

The simulation of three DA in cascade with different configurations is plotted in Fig. 4.21, the linear performance in Fig. 4.21(a), and the noise figure in Fig. 4.21(b). When cascading three amplifiers the gain grows up to 33 dB both the second stage is resistive or active line termination. And input return losses are equal to one single DA cell (Fig. 4.21(a)). Meanwhile, noise figure is 2.2 dB when cascading, it means 0.1 dB higher than in one single DA cell (Fig. 4.21(b)). So the contribution of the second stage, both in resistive or active line termination configuration, is very small since its noise minimize by the gain of first stage and each DA cell has a low noise itself.

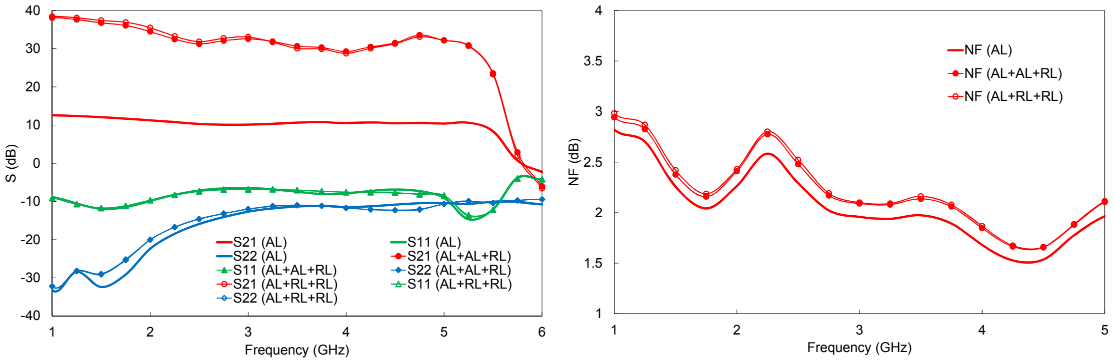

(a) *(b)*

Fig. 4.21. Simulated performance versus frequency cascading the measured DA with different configurations, resistive or active gate line terminations. (a) Scattering parameters. (b) Noise figure.

4.7. Conclusions

A methodology for the improvement of noise performance in a DA at low frequencies has been investigated making use of an active feedback termination of the gate line. To this goal, the influence of temperature changes in DA line termination has been analysed, demonstrating the major influence of gate line termination noise temperature as compared to the drain one. A mathematical formulation of noise temperature for an active load has been also presented. Noise figure expressions in a DA based on the active device small-signal and noise parameters have been derived.

In order to verify the simulations experimentally, a hybrid two-stage distributed amplifier has been designed and fabricated both with resistive and active loads. Measured data result in broadband amplifier performance from 1 to 5.2 GHz with 10.9 dB flat gain. A 0.6 dB noise figure improvement below 2 GHz has been achieved when the active load is adopted as the gate line termination.

Once the DA cell is three times cascaded the gain achieved is 33 dB keeping the noise and the return losses as one DA cell.

4.8. References

[4.1] Colin S. Aitchison: 'The Intrinsic Noise Figure of the MESFET Distributed Amplifier', IEEE Transactions on Microwave Theory and Techniques, 1985, **33**, (6), pp. 460–466

[4.2] K. B. Niclas, “On Noise in distributed Amplifiers at Microwave Frequencies”, IEEE Transactions on Microwave Theory and Techniques, 1983, **31**, (8), pp. 661–668

[4.3] Kambiz Moez and Mohamed I. Elmasry, “A Low-Noise CMOS Distributed Amplifier for Ultra-Wide-Band Applications”, IEEE Transactions on Circuits and Systems, 2008, **55**, (2), pp. 2076–2082

[4.4] P. K. Ikalainen, “Low-Noise Distributed Amplifier with Active Load”, IEEE Microwave and Guided Wave Letters, 1996, **6**, (1), pp. 7–9

[4.5] Kobayashi, K.W.; Denninghoff, D.; Miller, D. "A Novel 100 MHz-45 GHz GaN HEMT Low Noise Non-Gate-Terminated Distributed Amplifier Based on a 6-Inch 0.15µm GaN-SiC mm-Wave Process Technology", Compound Semiconductor Integrated Circuit Symposium (CSICS), 2015, pp. 1–4

[4.6] Shunji Kimura and Yuhki Imai, “0-40 GHz GaAs MESFET Distributed Baseband Amplifier IC’s for High-Speed Optical Transmission”, IEEE Transactions on Microwave Theory and Techniques, 1996, **44**, (11), pp. 2076–2082

[4.7] K. W. Kobayashi, J. Cowles, L. T. Tran, A. Gutierrez-Aitken, T. R. Block, A. K. Oki, and D. C. Streit, “A 50-MHz–55-GHz Multidecade InP-Based HBT Distributed Amplifier”, IEEE Microwave and Guided Wave Letters, 1997, **7**, (10), pp. 353–355

[4.8] Jinho Jeong and Youngwoo Kwon, “Monolithic Distributed Amplifier With Active Control Schemes for Optimum Gain and Group-Delar Flatness, Bandwidth, and Stability”, IEEE Transactions on Microwave Theory and Techniques, 2004, **52**, (4), pp. 1101–1110

[4.9] J. Vicente Terán, Mª Luisa de la Fuente, Ernesto Limiti, Beatriz Aja, Eduardo Artal, “Noise Analysis in Distributed Amplifiers with Feedback-Active Load”, IET Microwaves, Antennas and Propagation, pp. 1-9. June, 2016, ISSN 1751-8725

[4.10] Buhles, P.M.; Lardizabal, S.M. "Design and characterization of MMIC active cold loads", Microwave Symposium Digest. 2000 IEEE MTT-S International, June 2000, **1**, pp. 29–32

[4.11] K. B. Niclas, “Noise in Broad-Band GaAs MESFET Amplifiers with Parallel Feedback”, IEEE Transactions on Microwave Theory and Techniques, 1982, **30**, (1), pp. 63–70

[4.12] K. B. Niclas, “The Exact Noise Figure of Amplifiers with Parallel Feedback and Lossy Matching Circuits”, IEEE Transactions on Microwave Theory and Techniques, 1982, **30**, (5), pp. 832–835

[4.13] Robert A. Pucel, Hermann A. Haus, and Hermann Statz: 'Signal and Noise Properties of Gallium Arsenide Microwave Field-Effect Transistors', Advances in Electronics and Electron Physics, 1975, **38**, pp. 195–265

[4.14] H. Rothe, and W. Dahlke: 'Theory of Noisy Fourpoles', Proceedings if the IRE, 1956, **44**, (6), pp. 811–818

CHAPTER V: EQUALISING THE GAIN PERFORMANCE

5.1. Introduction

Several wideband communication systems require a flat gain or response over a frequency band in order to properly operate. Nevertheless, many subsystems involved in the whole system, such as the amplification stages, cables or transmission lines, do not enable to fulfil this requirement within the bandwidth, showing a negative gain slope versus frequency. Hence, the need of designing positive linear gain equalisers in order to compensate the overall transmission response. One of the main issues in a radiometer polarimeter is to have a big bandwidth of the signal detected in order to increase the sensitivity of the receiver. A flat response is a solution to increase the effective bandwidth of a receiver.

Several equalisation techniques have been proposed [5.1]-[5.6]. Surface mount (SMD) resistors have been implemented in T- or π–type networks [5.1]-[5.2] to achieve positive equalisation slopes at lower frequencies, including microstrip lines to provide the expected performance. Stepped impedance resonators (SIR) have been also used to provide significant equalisation results over a broadband [5.3]-[5.4]. Moreover, additional resonator solutions have been also developed as equalisers, with open loop microstrip rings [5.5] or waveguide solutions [5.6].

In this chapter, a method to design broadband equalisers using a lossy transmission line π–network is described, in which the positive gain slope can be adjusted to fulfil the system requirements. Well-known models of lossy transmission lines in electrical simulators, acting as resistors, provide a precise design procedure in order to obtain the circuit performance. Moreover, the use of SMD resistors at high frequency bands involves additional parasitic effects at assembly stage, which is overcome when substituted for lossy lines. To validate the method, several equalisers working in the Q-band are presented to flatten the gain of cascaded low-noise amplifiers.

5.2. Equaliser methodological design

The equaliser is based on a pi network. The basic equalisation cell is shown in Fig. 5.1. A lossy transmission line resistor is used in the series path, with a characteristic admittance Y_0 and electrical length Φ_0. Lossy-line resistors of characteristic impedance Y_1 and electrical length Φ_1, with a cascaded open-ended quarter-wavelength stub $f_{u/2}$ (half of the highest frequency of interest) with characteristic admittance Y_2 and electrical length Φ_2, are placed in each shunt section of the pi network.

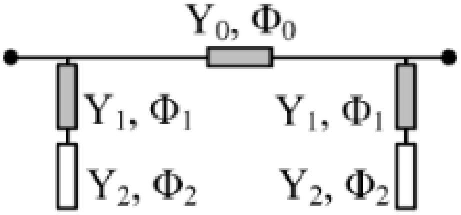

Fig. 5.1. Simplified scheme of the pi network equaliser: lossy transmission lines in grey colour, lossless transmission lines in white.

The admittance matrix of the simplified schematic is expressed as

$$[Y] = \begin{bmatrix} Y_P + \dfrac{Y_0}{\tanh(\Phi_0)} & \dfrac{-Y_0}{\sinh(\Phi_0)} \\ \dfrac{-Y_0}{\sinh(\Phi_0)} & Y_P + \dfrac{Y_0}{\tanh(\Phi_0)} \end{bmatrix} \tag{5.1}$$

Where Y_P is the shunt admittance of the pi network defined as

$$Y_P = \frac{\dfrac{\tanh(\Phi_1)}{Y_2} + j \cdot \dfrac{\tan(\Phi_2)}{Y_1}}{\dfrac{1}{Y_1 \cdot Y_2} + j \cdot \dfrac{\tan(\Phi_2) \cdot \tanh(\Phi_1)}{Y_1^2}} \tag{5.2}$$

Three parameters are used in order to obtain the desired equalisation performance within the bandwidth: input/output return loss, slope of the equalisation gain and minimum insertion loss at the highest frequency point (f_u). Initially in a theoretical calculus (Fig. 5.2), single lumped resistors substitute the lossy lines, R_0 the series one (Y_0) and R_1 the shunt subnetworks (Y_1).

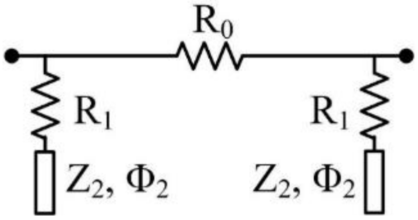

Fig. 5.2. Simplified scheme of the pi network equaliser with single lumped resistors.

The open-ended quarter-wavelength stubs at the connection point with the shunt lossy lines behave as a virtual open circuit at f_u. Therefore, the series resistor R_0 is calculated for the desired input reflection coefficient $|S_{11}|$ as

$$R_0 = \frac{2 \cdot Z_0 \cdot |S_{11}|_{fu}}{1 - |S_{11}|_{fu}} \tag{5.3}$$

where Z_0 is chosen as 50 Ω characteristic impedance, since this avoids discontinuities with the access transmission lines. The transmission coefficient (S_{21}) is related to the specified input return loss, which in terms of R_0 can be expressed as

$$|S_{21}|_{fu} = \frac{2}{2 + \frac{R_0}{Z_0}} \tag{5.4}$$

Afterwards, R_1 is calculated at $f_{u/2}$, since at this frequency the quarter-wavelength stubs create a short-circuit effect at the end if the shunt lossy lines. Consequently, a pi network with R_0 in the series path and R_1 in the shunt ones is formed. Then, R_1 is obtained from the expression which relates the S-parameters of the network at $f_{u/2}$, as follows:

$$\frac{|S_{11}|}{|S_{21}|}_{fu/2} = \left| \frac{R_0}{2 \cdot Z_0} - \frac{Z_0}{R_1} - \frac{Z_0 \cdot R_0}{2 \cdot R_1^2} \right| \tag{5.5}$$

where $|S_{11}|$ is the desired input matching and $|S_{21}|$ is the transmission coefficient at $f_{u/2}$, which is defined by the goal gain slope (M) and the $|S_{21}|$ at f_u in (5.4), expressed by

$$|S_{21}|_{fu/2} = |S_{21}|_{fu} - M \cdot \frac{f_u}{2} \tag{5.6}$$

Furthermore, the transfer gain, G_T, at the centre frequency (f_c) within the band of interest, is used to calculate the characteristic impedance of the shunt open-ended stub ($Z_2=1/Y_2$) using the previous calculated values of R_0 and R_1. The G_T is given by

$$G_T = \frac{4 \cdot \frac{|Y_{21}|^2}{Z_0^2}}{\left|\left(\frac{1}{Z_0} + Y_{11}\right)^2 - Y_{21}^2\right|^2} \tag{5.7}$$

where Y_{21} and Y_{11} are the Y-parameters in (5.1) when the lossy lines are substituted for single resistors, R_0 and R_1, expressed as

$$Y_{21} = \frac{-1}{R_0} \tag{5.8}$$

$$Y_{11} = \frac{1}{R_0} + \left(\frac{R_1}{R_1^2 + (Z_2 \cdot \cot(\Phi_2))^2} + j \cdot \frac{Z_2 \cdot \cot(\Phi_2)}{R_1^2 + (Z_2 \cdot \cot(\Phi_2))^2}\right) \tag{5.9}$$

and the phase of the shunt open- ended stub (Φ_2) is calculated as follows

$$\Phi_2 = \frac{\pi}{2} \cdot \frac{f_c}{f_{u/2}} \tag{5.10}$$

The resistor R_0 fixes the matching and losses at the end of the frequency band. Meanwhile, the open-ended stub gets the slope required of the equaliser. An analysis of the pair resistor R_1 and impedance Z_2 solution in the shunt open-ended stub versus the goal gain slope M, value in dB, has been performed. Considering an equaliser at $f_u = 47$ GHz with an input matching of 15 dB, and a frequency band of 12 GHz, the obtained series resistor R_0 is 21.6 Ω. The obtained pairs of shunt resistor R_1 and impedance Z_2 of the open-ended stub for different gain slopes are plotted in Fig. 5.3.

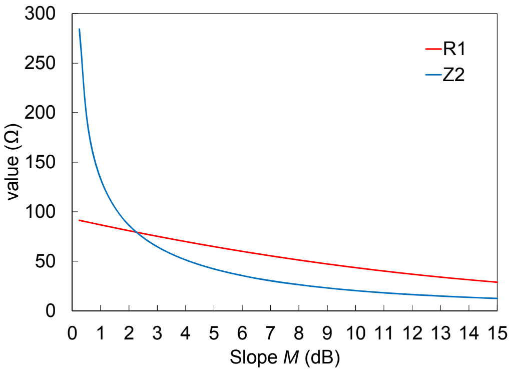

Fig. 5.3. Resistor R_1 and shunt open-ended stub impedance Z_2, versus gain slope M of the equaliser with f_u = 47 GHz and BW = 12 GHz.

Both the resistor R_1 and shunt open-ended stub impedance Z_2, can be obtained as a function of the target gain slope, M.

For the analysed equaliser, the resistor R_1 can be expressed as a polynomial function, given by

$$R_1 = p_1 \cdot M^2 + p_2 \cdot M + p_3 \tag{5.11}$$

where the values of the coefficients are $p_1 = 0.1358$, $p_2 = -6.298$ and $p_3 = 92.94$.

And the impedance Z_2 satisfies the power function expressed as

$$Z_2 = a \cdot M^b + c \tag{5.12}$$

where the coefficients are $a = 169.9$, $b = -0.4637$ and $c = -37.62$.

The influence of resistor R_0 in the matching and insertion losses at f_u is evaluated in Fig. 5.4. As long as the value of R_0 increases the mismatching and insertion losses become higher so fast. So the best performance at f_u implies a value of R_0 below 100 Ω.

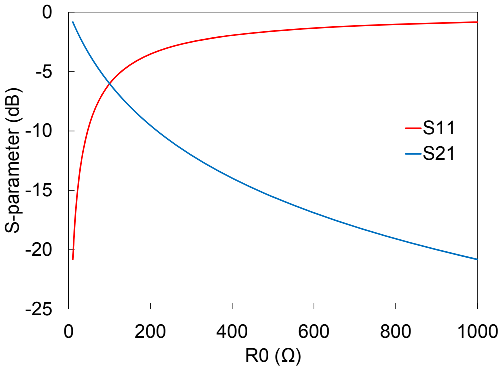

Fig. 5.4. Evolution of S-parameters versus R_0 of the equaliser with f_u = 47 GHz and BW = 12 GHz.

The developed procedure provides the initial values for the equalisation network. Then, the single lumped resistor are replaced by lossy lines, considering for the series lossy line the width that provides Z_0 characteristic impedance. On the other hand, the shunt lossy lines can have the width of the characteristic impedance Z_2 of the open-ended quarter-wavelength stub. Additionally, the electrical length of the lossless transmission lines are corrected due to the phase introduced by the shunt lossy line Φ_1 and the open-end effect of the stub $\Delta\Phi$ [5.7], defining the corrected electrical length of the shunt stubs as (5.13).

$$\Phi_2' = \Phi_2 - \Phi_1 - \Delta\Phi \tag{5.13}$$

The described design procedure is used for designing an equaliser intended to cover the 35 to 47 GHz frequency band, with a gain slope of around 6.5 dB and return loss better than 15 dB at both ports. The values provided by the analysis are the following $R_0 = 21.6\ \Omega$, $R_1 = 57.7\ \Omega$ and $Z_2 = 32.8\ \Omega$. The S-parameters magnitudes of this preliminary design are shown in Fig. 5.5. Note the simulated equalisation is only 5.6 dB. Optimization steps should be introduced to improve the transmission response.

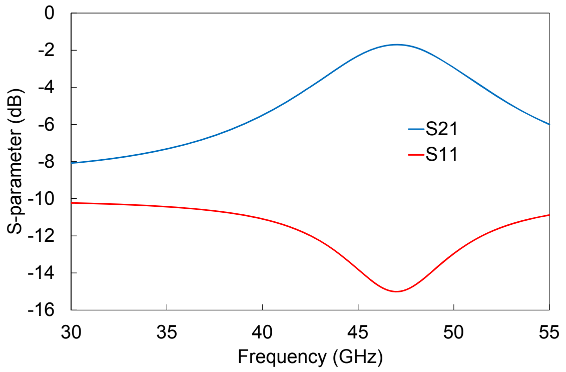

Fig. 5.5. Simulation results for the ideal pi-network obtained with the proposed analysis.

Then the single resistors are made with a 50 Ω/square sheet resistance, and the lossless stubs with microstrip lines. The width of Y_0 is like transmission line of $Z_0 = 50\ \Omega$. Y_2 has the width of a microstrip line of characteristic impedance $Z_2 = 32.8\ \Omega$. The resistor R_1 consists of a lossy transmission line (Y_1), which can be set with different lengths. A correction of the phase introduced by this lossy transmission line Y_1 (Φ_1) in the electrical length of the shunt transmission line Y_2 (Φ_2), is needed, since it has a significant effect in the slope of the equaliser. Consequently it has been analysed and considered in the electromagnetic design. A lossy transmission line has a complex propagation constant which depends on the attenuation per length unit and the wave velocity. Moreover, depending on the lossy transmission line length, its phase has a different behaviour versus frequency. Therefore, the length of the transmission line must be carefully considered in order to properly correct the whole phase of the shunt subnetwork. The phase of the shunt lossy transmission line (Φ_1) to be corrected is calculated at $f_{u/2}$, but the longer that line is, the more inaccurate the correction of electrical length at f_u is, and the goal gain slope cannot be achieved increasing the losses at the higher frequency of the band. For the designed equaliser, the evolution of the transmission coefficient (Fig. 5.6(a)) at the higher frequency ($f_u = 47$ GHz) and the gain slope (Fig. 5.6(b)), are presented in Fig. 5.6, versus the length of the lossy transmission line, when its phase at $f_{u/2}$ is corrected.

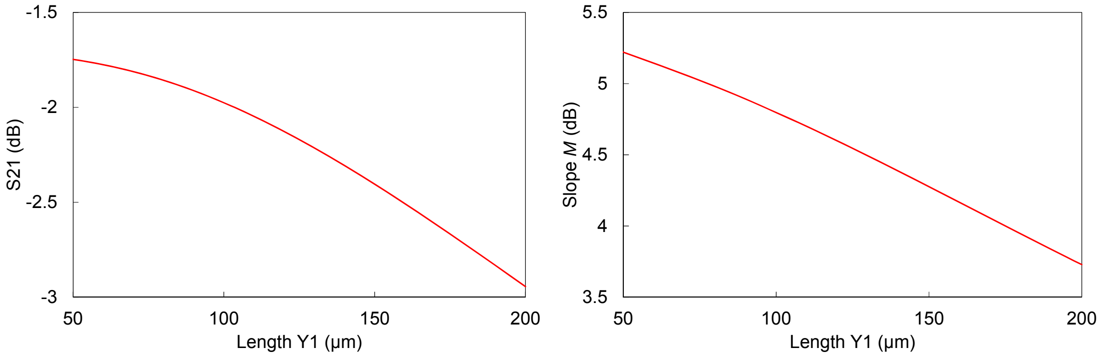

(a) *(b)*

Fig. 5.6. Simulated transmission coefficient and gain slope, M, of the designed equaliser versus the length of the shunt lossy transmission line (Y_1). (a) S_{21}. (b) Gain slope.

The shunt transmission line stub has a λ/4 effect at $f_{u/2}$ and the correction of the lossy transmission line phase at that frequency is expected to provide an open-end effect of the shunt subnetwork at f_u. The obtained results show that the phase difference in the lossy transmission line between $f_{u/2}$ and f_u depends on its length. The longer the length is, the greater the dispersive effect in the phase shown, which produces that the open-end effect in shunt transmission line, expected at f_u, is shifted to higher frequencies. Therefore, the phase correction at $f_{u/2}$ of a long lossy transmission line moves the open-end effect to higher frequencies than f_u and the obtained gain slope decreases. Fig. 5.7 and Table 5.1 show the obtained gain slopes for different lengths of the lossy transmission line (Y_1), of the designed equaliser with 5.6 dB of gain slope from 35 to 47 GHz. In order to obtain lower error in the correction of the lossy transmission line phase, a short length must be set for it.

Table 5.1. Simulated gain slope values obtained for different lengths of Y_1, for the designed equaliser.

ℓ (Y_1) (µm)	***M* (dB)**
50	5.2
100	4.8
150	4.3
200	3.7

The lossy transmission line Y_1 in the designed equaliser has been realised with the width of the Z_2 impedance transmission line, in order to avoid discontinuities and to have a feasible implementation. In this case, the electrical lengths of the microstrip open-ended stubs (Φ_2) are shortened by the phase of this shunt lossy transmission line (Φ_1) and the stub open-end effect ($\Delta\Phi$), which are 5.7^0 and 0.15^0 at $f_{u/2}$ respectively. Since the introduction of real elements in the design process decreases the goal gain slope, an electromagnetic optimization is performed.

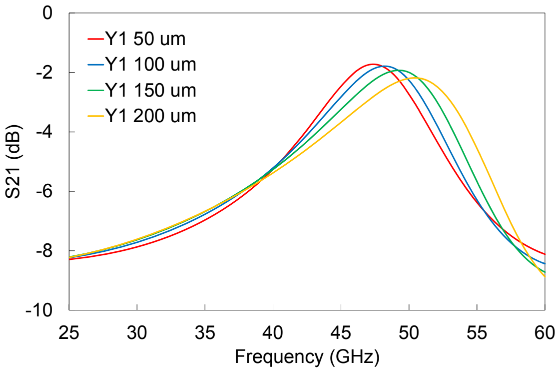

Fig 5.7. Simulated transmission coefficient versus frequency for different lengths of Y_1, for the designed equaliser.

The above equaliser is designed to have minimum insertion losses at the highest point of the frequency band. But the MMIC LNA module, which carries the equaliser, belongs to a receiver with many subsystems involved and with a narrow detection power window. So the RF signal should be controlled to keep appropriate levels at the input of subsequent subsystems. The best way to control the signal is adding attenuation to the equaliser. It means, increasing the attenuation at f_u keeping the slope gain over the bandwidth. A simulation of the S-parameters versus frequency for different values of R_0 is shown in Fig. 5.8. As long as R_0 increases, the insertion losses (Fig. 5.8(a)) at f_u (47 GHz) and the gain slope (Table 5.2) are higher. Meanwhile, the matching (Fig. 5.8(b)) is extremely poor (< 5 dB) at f_u when R_0 is large.

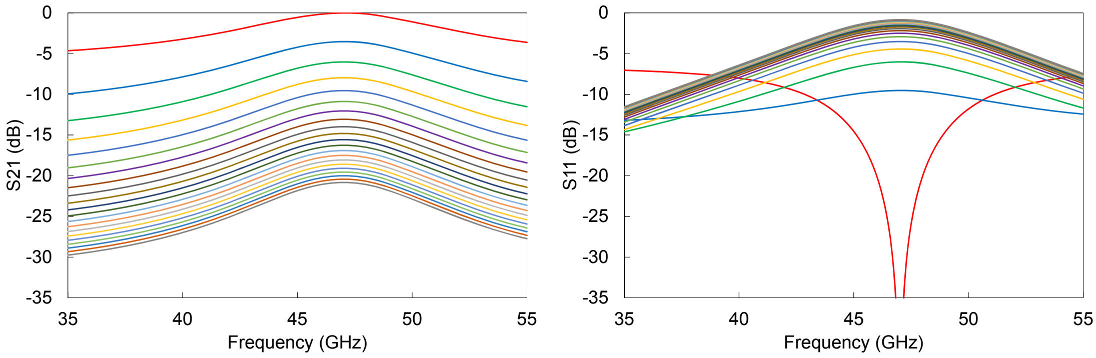

(a) *(b)*

Fig 5.8. Simulated S-parameters of the designed equaliser versus frequency for different values of series resistor (R0). (a) S_{21}. (b) S_{11}.

Table 5.2. Simulated gain slope values obtained for different lengths of Y_1, for the designed equaliser.

R_0 (Ω)	M (dB)	S_{21} (dB) @ f_u (47 GHz)	S_{11} (dB) @ f_u (47 GHz)
0.1	4.6	0	-60
100	7.2	-6	-6
200	8	-9.5	-3.5
300	8.3	-12	-2.5
400	8.5	-14	-1.9
500	8.6	-15.6	-1.6
600	8.7	-16.9	-1.3
700	8.8	-18	-1.2
800	8.9	-19	-1
900	8.9	-20	-0.9
1000	8.9	-20.8	-0.8

When a high attenuation in the equaliser is required a basic equaliser is not enough due to its bad impedance matching performance. So a set of several basic cells are cascaded (Fig. 5.9) in order to have more attenuation keeping the slope with a good matching over the whole bandwidth. The total series resistor, R_0, is divided in each cell by the number of cascaded stages. Meanwhile, the shunt stubs provide the desired equalisation.

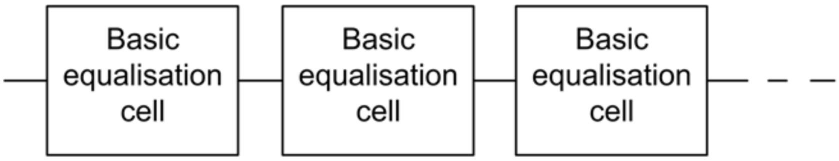

Fig. 5.9. Cascade connection of basic equalisation cells in order to have the required gain slope, attenuation, achieving a good impedance matching.

5.3. Implementation and experimental results

Three different open-ended stub circuits has been implemented in the 35 – 47 GHz frequency band with different attenuation levels, a low attenuation equaliser formed by the basic designed cell, a medium attenuation equaliser formed by two cells, and a high attenuation equaliser formed by three cells. Each circuit is designed on Alumina substrate (εr = 9.9, h = 254 µm) using the initial dimensions from the proposed design methodology. The Alumina substrate provides a resistive layer with a 50 Ω/square sheet underneath the metallisation gold layer. This layer enables the directly etching of thin film resistors over the substrate, which are the lossy transmission lines considered in the circuit design.

All the circuits to be manufactured have been optimised in order to get the goal performance. Besides, 50 Ω microstrip lines at both circuit ports and microstrip T-junctions are included for fabrication purposes and interconnecting the elements of the pi-network. The final schematic of the low attenuation equaliser is shown in Fig. 5.10, in which are described the different lengths and widths of the microstrip lines. The values of lengths and widths for the three manufactured equalisers are listed in Table 5.3.

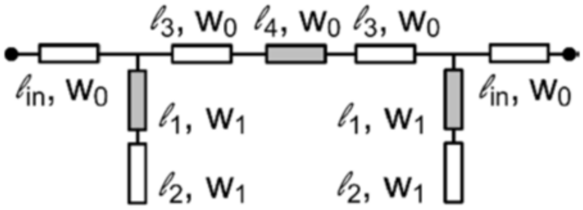

Fig. 5.10. Schematic of the low attenuation equaliser (lossy lines in grey colour).

Table 5.3. Full lengths and widths (in µm) of the microstrip lines and the lossy transmission lines of the three manufactured circuits.

Circuit attenuation	ℓ_{in}	ℓ_1	ℓ_2	ℓ_3	ℓ_4	w_0	w_1
Low	3460	120	710	200	158	263	200
Medium	3229	200	760	200	105	263	200
High	2976	236	690	200	116	263	200

A picture of the manufactured circuits is shown in Fig. 5.11, in which the lossy transmission lines are the dark parts of each circuit. The size of all the manufactured circuits is set to 7.5 x 2.4 mm^2.

The measurements are performed in a coplanar probe station in the frequency range from 30 to 50 GHz using commercial coplanar-to-microstrip transitions, whose effect is de-embedded using a TRL calibration process. A comparison between the electromagnetic simulation of the circuits and the measurements is shown in Fig. 5.12. Each equaliser covers the 35 to 47 GHz frequency band. The measured S-parameters values are summarized in Table 5.4. The gain slope is around 6.5 dB, goes from 6.4 dB in the low attenuation equaliser to 6.8 dB in the high attenuation version. On the other hand, the minimum input matching in the whole bandwidth is better when the equaliser has a big attenuation. This input return losses go from 9 to 15 dB, in the low and high attenuation versions respectively. Measured results fit well with simulation values, validating the proposed design method. The deviation in the transmission data ($|S_{21}|$) is due to the tolerance in the sheet resistance of the resistive layer (±10%).

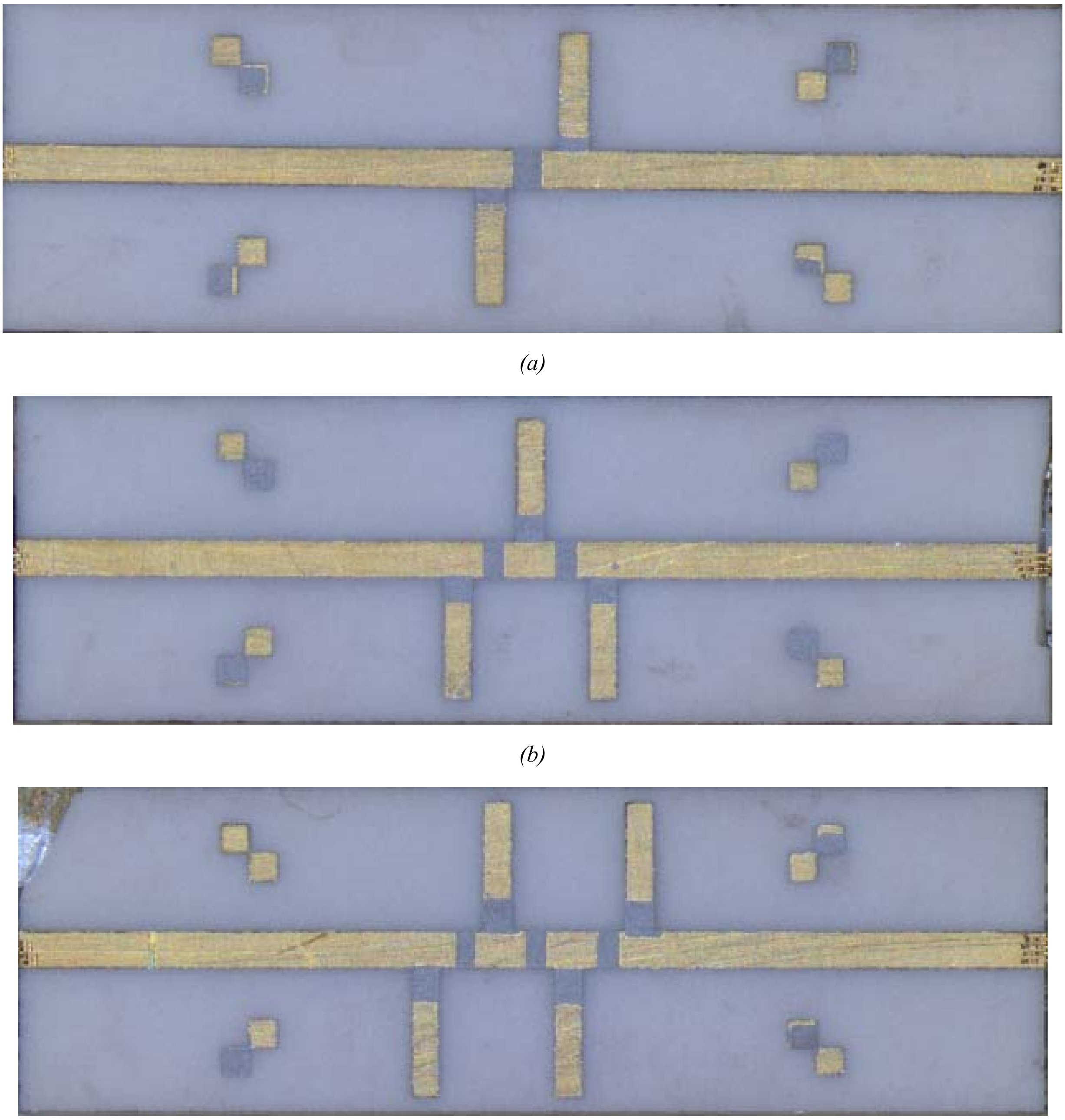

(a)

(b)

(c)

Fig. 5.11. Manufactured Q-band equalisers on Alumina substrate (R_s = 50 Ω/square). Size: 7.5 x 2.4 mm^2. (a) Low, (b) Medium, (c) High attenuation equalisers.

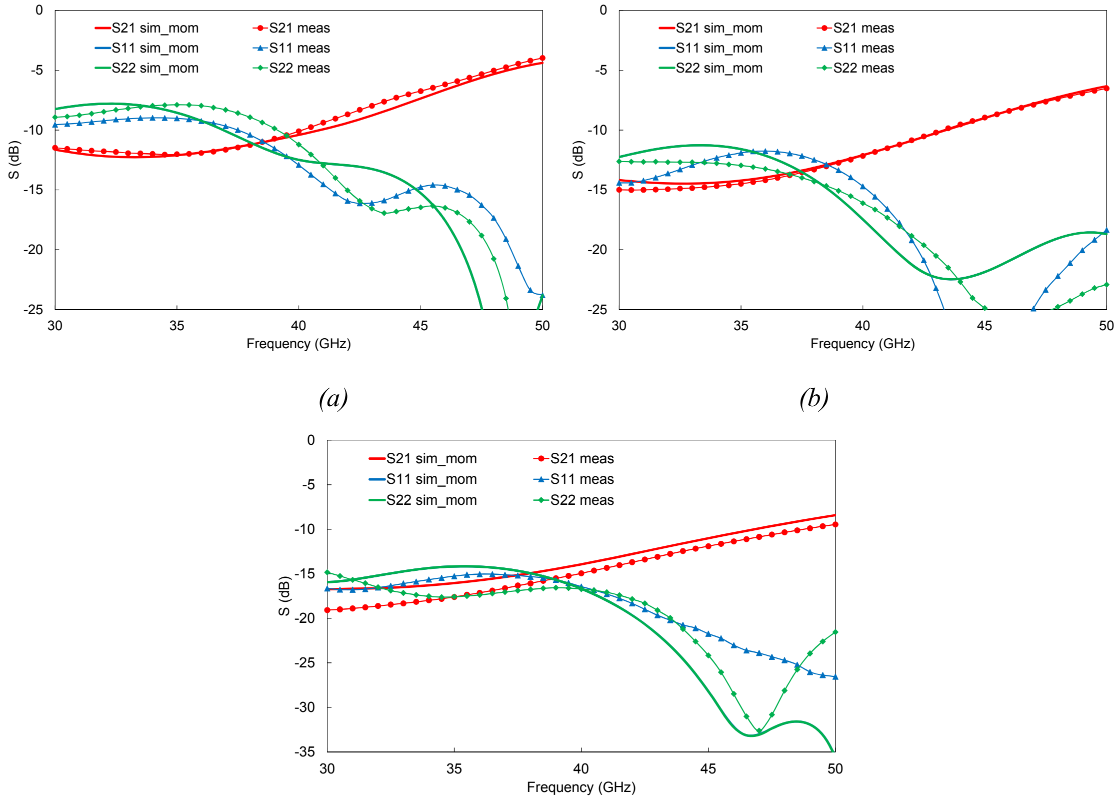

(a) *(b)*

(c)

Fig. 5.12. Q-band equaliser performance: comparison between simulations and measurements results. (a) Low, (b) Medium, (c) High attenuation equalisers.

Table 5.4. Performance values for the three manufactured Q-band equalisers.

Circuit attenuation	***M*** **(dB)**	**$|S_{21}|$(dB) @ f_u (47 GHz)**	**$|S_{21}|$(dB) @ 35 GHz**	**Max. $|S_{11}|$ (dB)**
Low	6.4	-5.6	-12	-9
Medium	6.6	-7.9	-14.5	-11.8
High	6.8	-10.8	-17.6	-15

5.3.1. Cryogenic equaliser characterisation

A new equaliser has been manufactured for a Q-band cryogenic amplifier. It has been designed for low attenuation at the highest frequency of interest and using a new topology to have the open-ended effect in the shunt stubs. The way to implement it is through a $\lambda/4$ line plus via hole (ℓ_3 line plus via hole in Fig. 5.13). The frequency band is also 35-47 GHz and the circuit is designed on the same Alumina substrate as previous equalisers. But in this case, the resistive layer sheet is 20 Ω/square.

The final schematic of the low attenuation equaliser is shown in Fig. 5.13, in which are described the different lengths and widths of the microstrip lines. The values of lengths and widths for the manufactured equaliser are listed in Table 5.5.

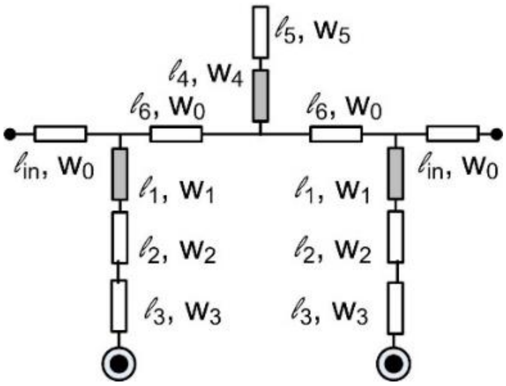

Fig. 5.13. Schematic of the cryogenic equaliser (lossy lines in grey colour).

Table 5.5. Full lengths and widths (in µm) of the microstrip lines and the lossy transmission lines of the cryogenic equaliser.

ℓ_{in}	ℓ_1	ℓ_2	ℓ_3	ℓ_4	ℓ_5	ℓ_6	w_0	w_1	w_2	w_3	w_4	w_5
3560	290	438	856	207	467	500	260	70	250	90	70	260

Since the via hole is always critical in electromagnetic simulations at microwave frequencies, because it is not easy to have an accurate model, the equaliser is simulated with different via hole diameters, from 50 to 250 µm. As long as the diameter increases the gain slope (Fig. 5.14(c)) also increases. There is a tuning margin around 1 dB, from 2.66 to 3.83 dB, as seen in Table 5.6. Looking at Fig. 5.14(a) and Fig. 5.14(b), the return losses degrade with small via hole diameter, below 100 µm. The value is chosen to be 150 µm (red traces in Fig. 5.14).

Table 5.6. Gain slope (dB) values for the cryogenic Q-band equaliser and for different via hole diameters, from 50 to 250 µm, step by 50 µm.

Via hole diameter (µm)	***M* (dB)**
50	2.66
100	3.37
150	3.60
200	3.74
250	3.83

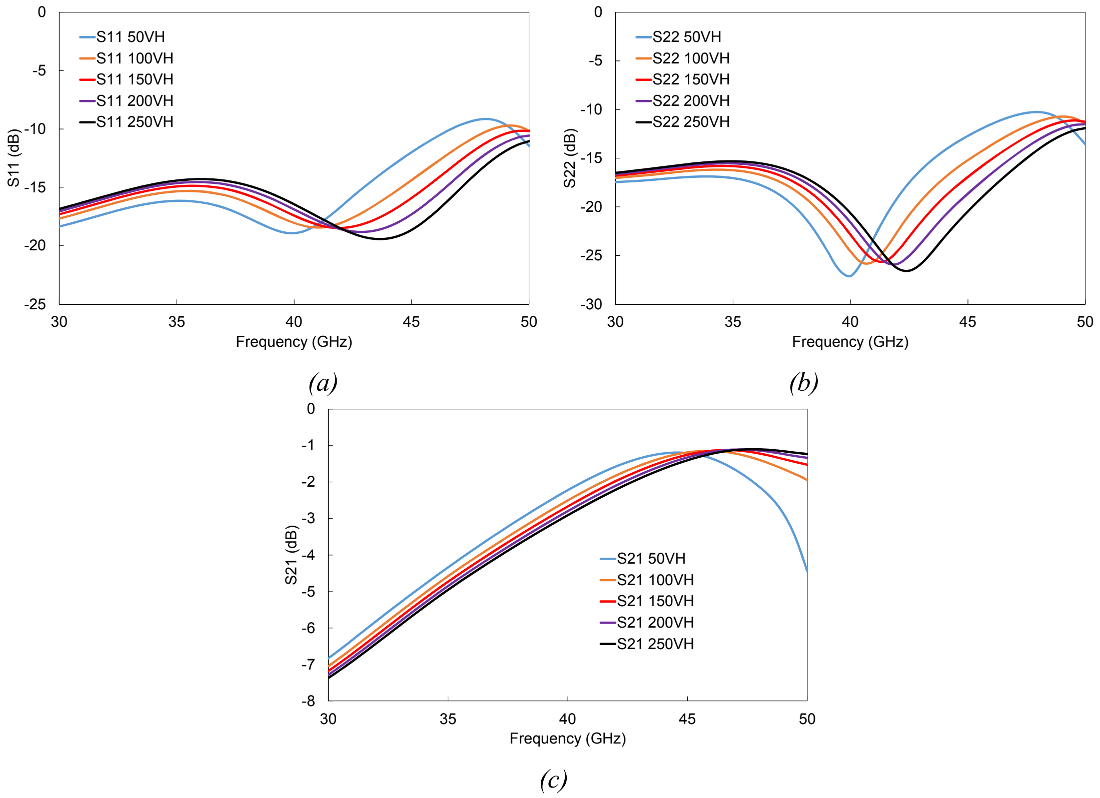

Fig. 5.14. Scattering parameters performance simulation of Cryogenic Q-band equaliser for different via hole diameters, from 50 to 250 µm, step by 50 µm. (a) S_{11}. (b) S_{22}. (c) S_{21}.

A picture of the cryogenic equaliser manufactured in Thin Film Products (France) is shown in Fig. 5.15, in which the lossy transmission lines are the dark parts. The size of the circuit is set to 8.9x1.6 mm^2.

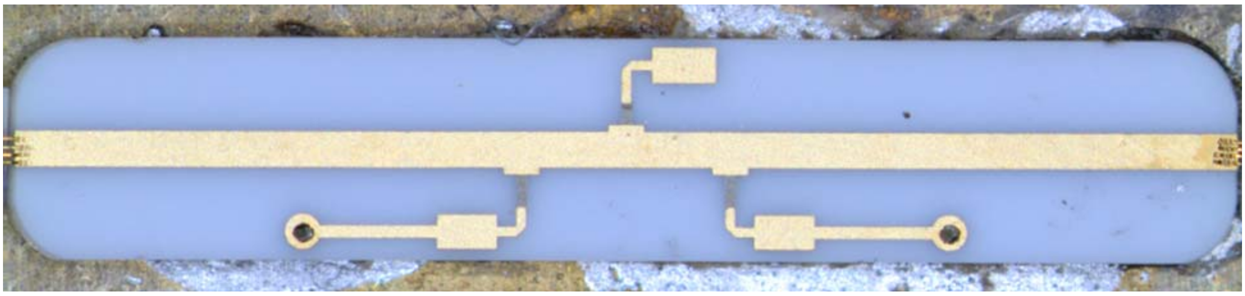

Fig. 5.15. Cryogenic equaliser manufactured in Thin Film Products. Size: 8.9 x 1.6 mm^2.

A comparison between the electromagnetic simulation of the circuit and the measurements is shown in Fig. 5.16. The equaliser covers the 35 to 47 GHz frequency band. The measured S-parameters values are summarized in Table 5.6. The gain slope is around 4.7 dB. The minimum input return loss in the whole bandwidth is better than 9 dB. Measured results fit well with simulation values, validating the proposed new topology for the open-ended effect in the shunt stub through via holes.

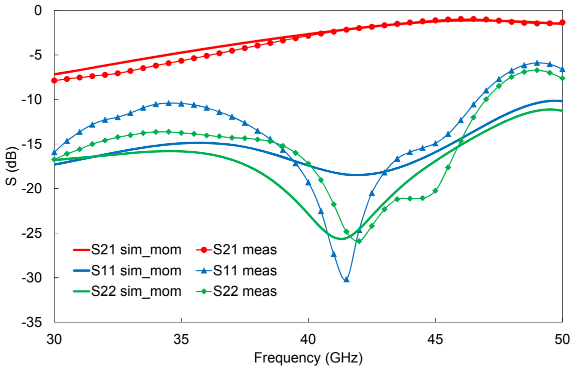

Fig. 5.16. Cryogenic Q-band equaliser performance: comparison between simulations and measurements results.

Table 5.6. Performance values for the cryogenic Q-band equaliser.

M (dB)	$\|S_{21}\|$(dB) @ f_u (47 GHz)	$\|S_{21}\|$(dB) @ 35 GHz	Max. $\|S_{11}\|$ (dB)
4.7	-1	-5.7	-9

5.4. Bonding wires

The measurements of the equalisers have been performed with bonding wires at the input and output microstrip to coplanar line adapters. Four wires are soldered in each port of the equaliser. However, the connection of the equaliser with a MMIC, in which the access pads are small, only allows two bonding wires in the best case scenario.

The effect of bonding wires in the equaliser measurements can be considered negligible since four wires were soldered in parallel minimizing the inductive nature of the bonding.

5.4.1. BEM equalisers

The three BEM equalisers with low (Fig. 5.17), optimum (Fig. 5.18), and high (Fig. 5.19) attenuation levels are simulated with different bonding wire lengths, from 150 to 500 µm. As long as the wire becomes longer the attenuation increases and the input and output return losses are worse. Moreover, the gain slope losses the linearity appearing a smooth ripple in the transmission response.

The bonding wire length should not exceed 250 µm if only one wire can be connected. More wires in parallel means the linear performance of the connected equaliser is close to the alone equaliser.

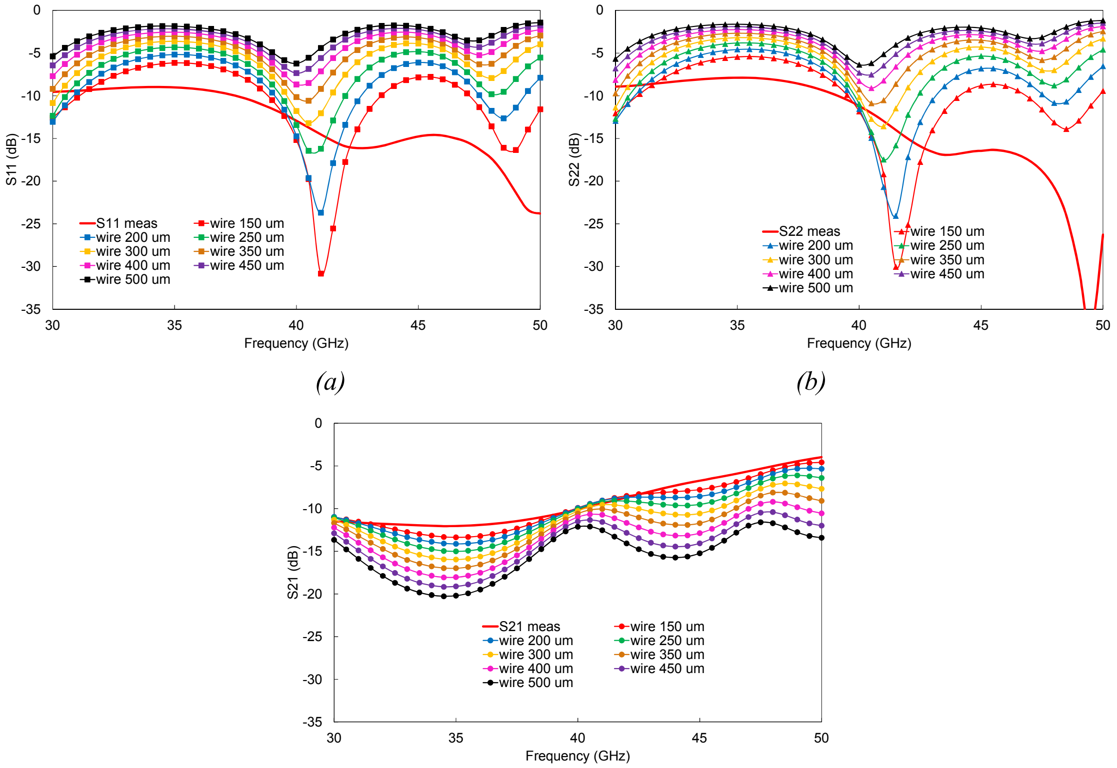

(a) *(b)*

(c)

Fig. 5.17. Scattering parameters performance simulation of the low attenuation equaliser versus bonding wire lengths, from 150 to 500 µm, step by 50 µm. (a) S_{11}. (b) S_{22}. (c) S_{21}.

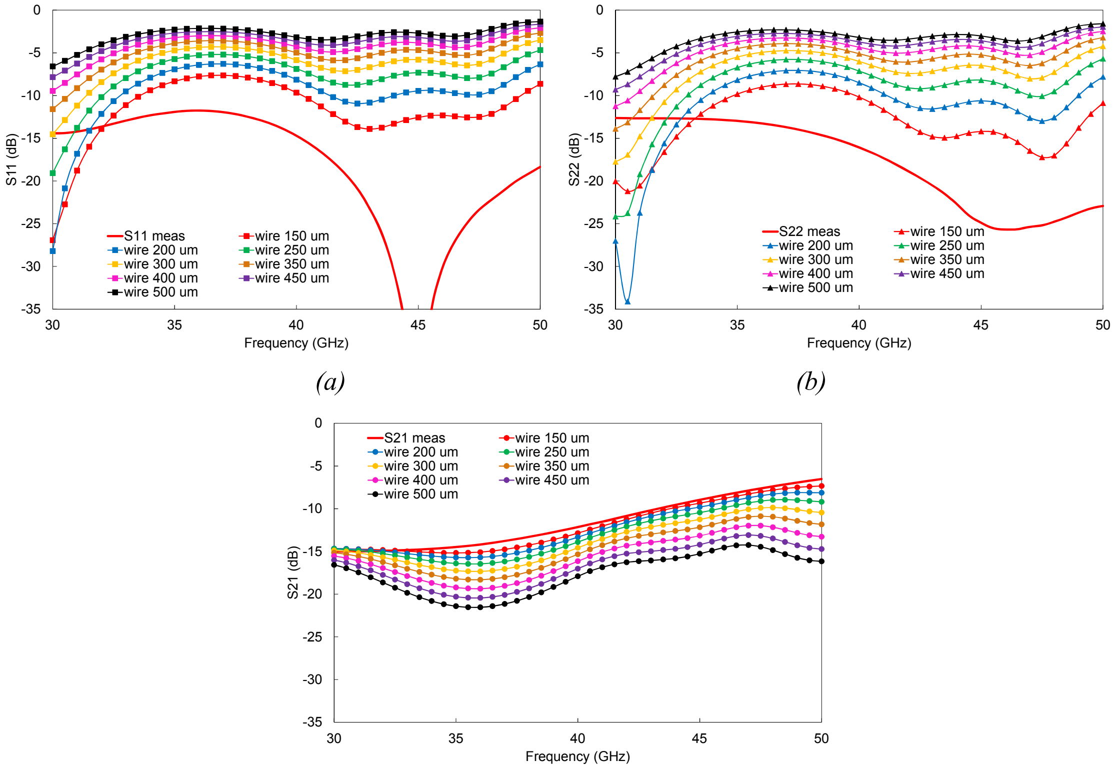

(a) *(b)*

(c)

Fig. 5.18. Scattering parameters performance simulation of the optimum attenuation equaliser versus bonding wire lengths, from 150 to 500 µm, step by 50 µm. (a) S_{11}. (b) S_{22}. (c) S_{21}.

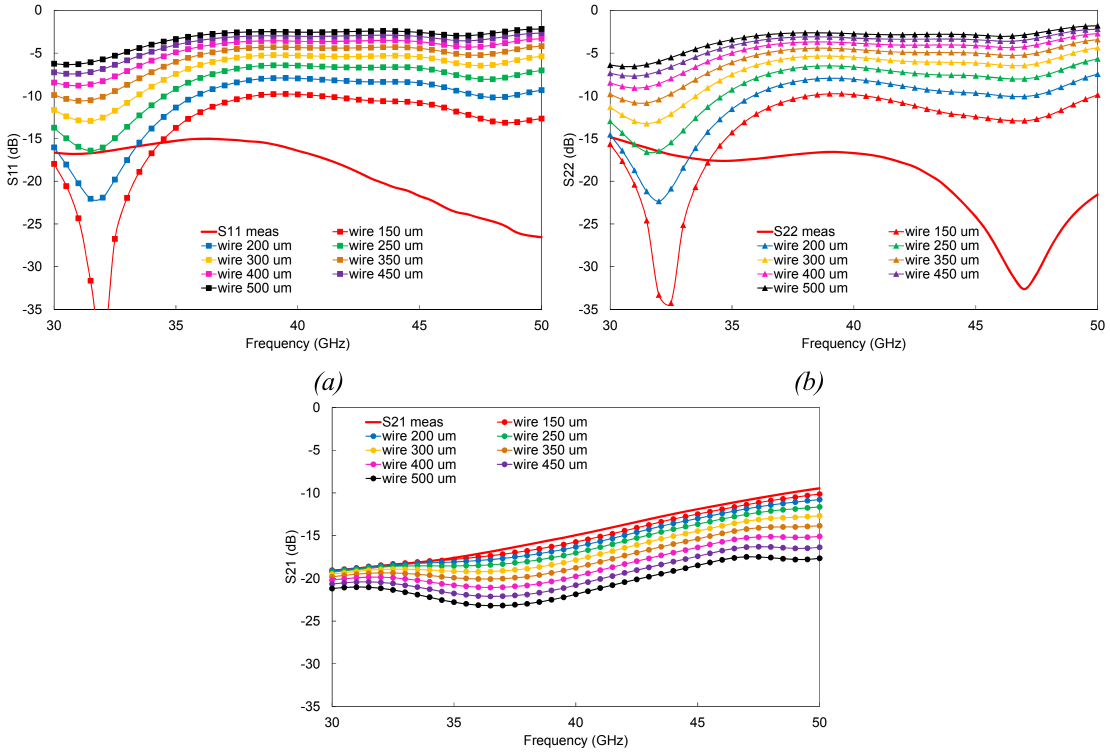

(a) *(b)*

(c)

Fig. 5.19. Scattering parameters performance simulation of the high attenuation equaliser versus bonding wire lengths, from 150 to 500 µm, step by 50 µm. (a) S_{11}. (b) S_{22}. (c) S_{21}.

5.4.2. FEM cryogenic equaliser

The effect of bonding wires (Fig. 5.20) in the cryogenic equaliser is stronger due to the attenuation level is smaller than the BEM equalisers. The ripple in the gain slope is noteworthy, so the wire should not be longer than 200 µm. Since, this length is rather short, the best option to connect the equaliser with other circuits is to solder two bonding wires in each port in order to minimize the equivalent wire inductance.

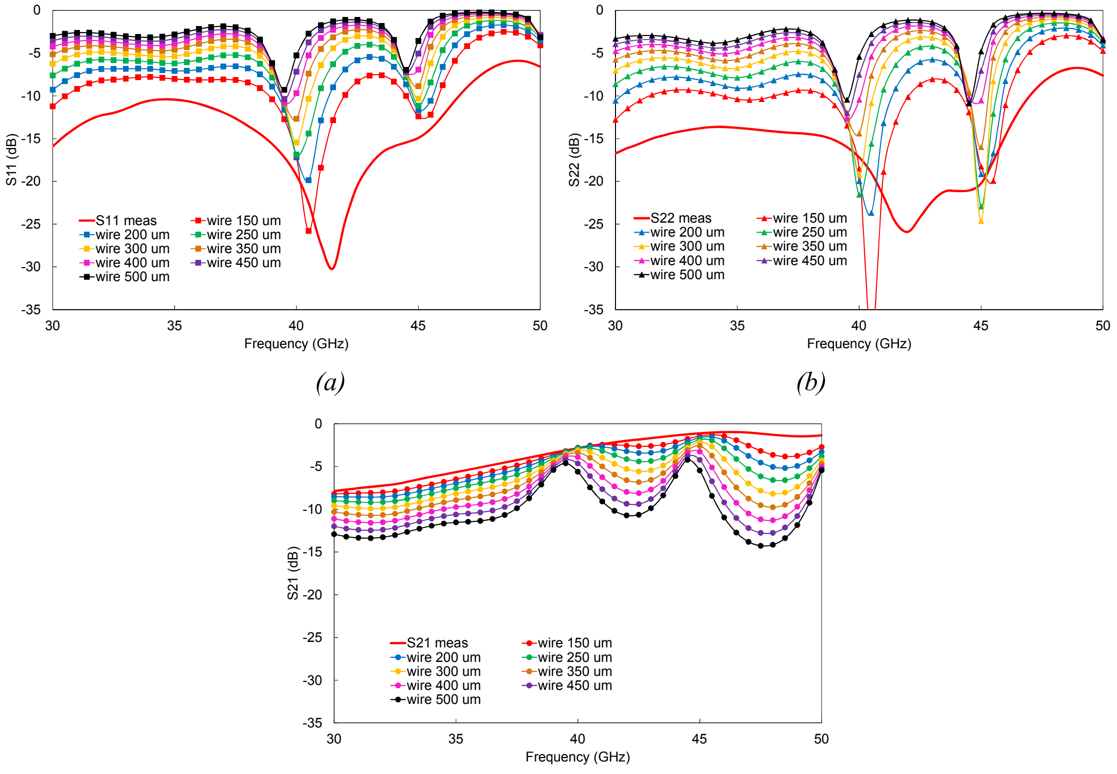

(a) *(b)*

(c)

Fig. 5.20. Scattering parameters performance simulation of the cryogenic equaliser versus bonding wire lengths, from 150 to 500 µm, step by 50 µm. (a) S_{11}. (b) S_{22}. (c) S_{21}.

5.5. Inside an amplifier: BEM gain module of the FGI instrument

The low attenuation version of the manufactured equaliser is chosen to be placed in the BEM gain module of the FGI receiver. A total amount of sixty equalisers are manufactured by Thin Film Products to be assembled in the amplifiers needed for the back-end module (BEM) of the forty gigahertz instrument (FGI) of QUIJOTE experiment. A picture of the equaliser manufactured by Thin Film Products is presented in Fig. 5.21.

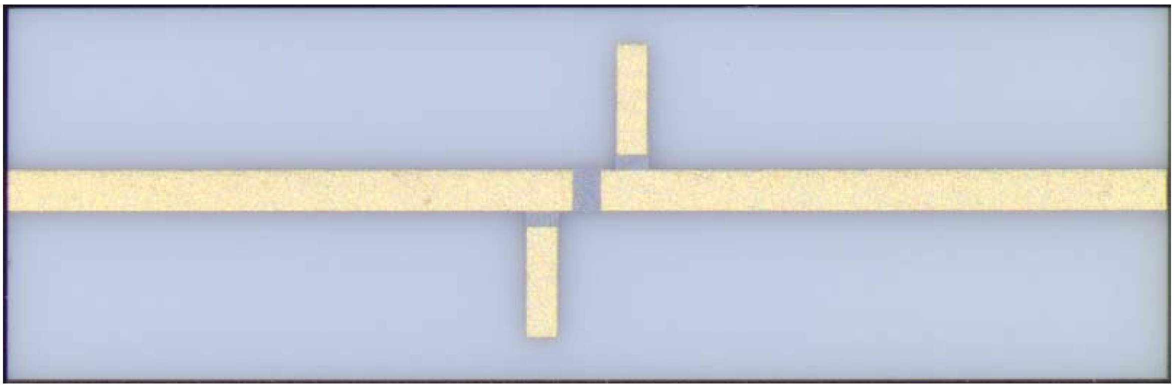

Fig. 5.21. Low attenuation equaliser manufactured in Thin Film Products. Size: 7.5 x 2.4 mm^2.

In Fig. 5.22, a view of the gain module microstrip circuitry is shown. The equaliser is placed between the two MMIC amplifiers. A band pass filter and waveguide-to-microstrip transitions are also included.

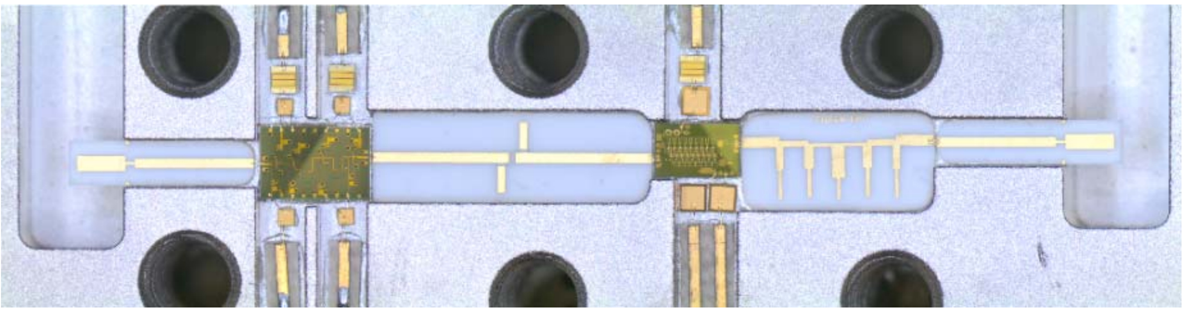

Fig. 5.22. Photo of BEM gain module.

The performance of the full gain module is presented in Fig. 5.23, the equaliser provides a positive slope in the gain against the simulated flat response of the gain module without it. Input and output return losses achieve values around 10 dB. The simulation exhibits a better matching because the transitions are not included.

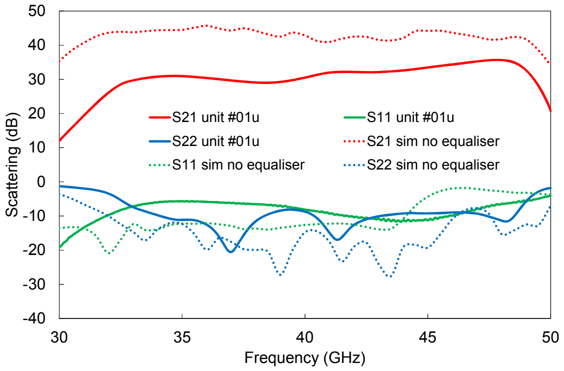

Fig. 5.23. Simulation of the BEM gain module without an equaliser, and measurements of the BEM gain module with the equaliser.

5.6. Inside an amplifier: FEM gain module of the FGI instrument

The cryogenic equaliser is placed in the FEM gain module of the FGI receiver. A total amount of sixty equalisers have been manufactured to be assembled in the cryogenic amplifiers of the front-end module (FEM) of the FGI instrument of QUIJOTE experiment. In Fig. 5.24, a view of the cryogenic amplifier is shown. The equaliser is placed between two identical low-noise MMIC amplifiers. Waveguide-to-microstrip transitions are also included in the radio frequency ports of the chassis. The performance of the full cryogenic amplifier is plotted in Fig. 5.25, the equaliser compensates the negative gain slope of the MMIC reducing it from 6.6 to 4.1 dB. More equalisation could be performed, however high attenuation shoots the noise and the cryogenic amplifier would loss low noise behaviour. Input and output return losses achieve values around 10 dB.

Fig. 5.24. FEM gain module internal view.

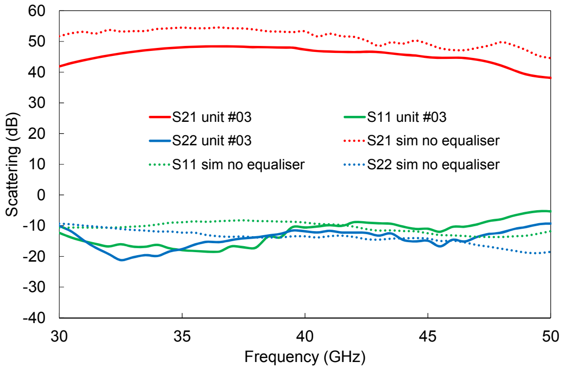

Fig. 5.25. Simulation of the FEM gain module without an equaliser, and measurements of the FEM gain module with the equaliser.

5.7. Conclusions

In this chapter, the design methodology of an equaliser composed of a lossy pi-network that provides positive slope response over a frequency range has been described. In addition, a Q-band equaliser on microstrip technology based on the proposed design methodology, has been presented. The design procedure objective is to achieve required insertion loss at the highest frequency of the desired frequency band, with simultaneously good return loss over the whole bandwidth. The design method enables to adjust the equalisation slope of the equaliser, according to the requirements. The method has been validated by the manufacturing of three equalisers which cover the 35-47 GHz frequency band, providing around 6.5 dB gain slope, with return losses better than 10 dB within the band. Moreover an equaliser with an open-ended effect topology for the shunt stubs based on via holes has been manufactured aimed to a cryogenic amplifier. This cryogenic equaliser provides a 4.7 dB gain slope in the 35-47 GHz frequency band, with return losses better than 10 dB within the band.

Finally, the equalisers have been integrated in gain modules, the cryogenic equaliser compensates the negative gain slope in a cryogenic amplifier, and the other equaliser provides a positive slope in the linear performance of gain module working at room temperature.

5.8. References

[5.1] Wu, S.M., Huang, S.H., Wang, H.Y., Chiu, C.T., Hung, C.P., Kuo, C.W., Wang, C.C.: 'Enhanced passive equaliser using open-stub structure', Electronics Letters, 2013, 49, (24), pp. 1528–1529. Available at http://dx.doi.org/10.1049/el.2013.3139

[5.2] Morgan, M., Newton, T., Hayward, B., Boyd, T.: 'Non-reflective transmission-line filters for gain slope equalization', IEEE/MTT-S International Microwave Symposium, Honolulu, United States, June 2007, pp. 545-548. Available at http://dx.doi.org/10.1109/MWSYM.2007.380547

[5.3] Wang, H., Yan, B., Wang, Z., Xu, R.: 'A broadband microwave gain equalizer', Progress in Electromagnetics Research Letters, 2012, 33, pp. 63–72. Available at http://dx.doi.org/10.2528/PIERL12052309

[5.4] Zhou, T.F., Wang, Z.G., Huan, W., Xu, R.M.: 'Design of microwave wave gain equalizer using microstrip shorted SIR', International Conference on Microwave and Millimeter Wave Technology, Shenzhen, China, May 2012, pp. 1-4. Available at http://dx.doi.org/10.1109/ICMMT.2012.6230399

[5.5] Zhao, Y., Zhou, D.F., Niu, Z.X.: 'Design of a microwave equalizer using a microstrip open-loop rectangular ring substructure', 3rd IEEE International Symposium on Microwave, Antenna, Propagation and EMC Technologies for Wireless Communications, Beijing, China, October 2009, pp. 1043-1046. Available at http://dx.doi.org/10.1109/MAPE.2009.5355872

[5.6] Wang, Z., Yan, B., Xu, R.: 'A millimetre-wave gain equalizer using E-plane microstrip-line probe and waveguide resonator', Journal of Electromagnetic Waves and Applications, 2015, 29, (4), pp. 465–473. Available at http://dx.doi.org/10.1080/09205071.2014.1002629

[5.7] Gupta, K.C., Garg, R., Bahl, I. and Bhartia, P.: 'Microstrip lines and slotlines' (Artech House, Norwood, MA, USA, 1996, second edition)

CHAPTER VI: FGI RECEIVER TEST BENCH

Most of the designed circuits in this work are included in the Forty Gigahertz Instrument (FGI) of the QUIJOTE Experiment [6.1]. The main goal of QUIJOTE is to measure and characterize the polarization of the Cosmic Microwaves Background (CMB). This instrument is a polarimeter receiver operating in the 35-47 GHz frequency band.

6.1. Receiver Scheme

The FGI receiver is a polarimeter to obtain the Stokes parameters (I, Q, and U). The CMB is supposed to have a very weak linear polarization. The designed receiver measures the Q, U, I Stokes parameters simultaneously. The remainder parameter V is null because the CMB does not have circular polarization. The sketch in Fig. 6.1 shows the configuration of the full receiver. The Stokes parameters are calculated directly from the incoming signals.

The full FGI instrument has 29 pixels. Each chain is composed of a Front-end Module (FEM) cooled down to a physical temperature of 20 K inside a cryostat, and a Back-end Module (BEM) working at room temperature (298 K). The cryogenic part, the FEM, is made up of a feed horn, a polarizer, an OMT and two cryogenic low-noise amplifiers (Cryo-LNA). Outside the cryostat, two gain, filtering and equalization modules, phase switches module and the correlation and detection module operate at room temperature, in which the microwave signal is amplified, filtered, correlated and, finally, converted into DC voltages using square-law detectors. These signals are collected by a data acquisition system (DAS). The phase switches modules comprise 0/180º and 0/90º phases which provide sixteen different phase states. Their performance minimize the 1/f noise and different systematic errors in the receiver. Moreover, the gain module in the BEM provides amplitude equalisation for the full receiver to flatten the response inside the receiver frequency band.

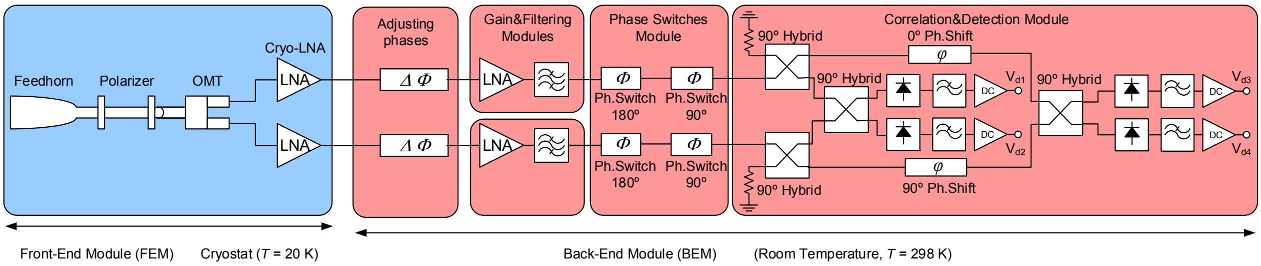

Fig. 6.1. Block diagram of a pixel of the FGI receiver.

In front of the BEM there are adjusting phases to balance the insertion phase between both branches. This adjustment must be done experimentally for each pixel in the integration and verification phase. The connection from the FEM output to the BEM input is done by a pair of 2.4 mm coaxial cables of the same length. Waveguide WR22 to coaxial adapters are used to interconnect the cables with the external wall of the FEM cryostat.

6.2. Principle of operation

Stokes parameters are calculated from the incoming signal field components. Using a circular basis of coordinates for the electromagnetic fields (*l*, *r*). In general the total electric field received by the feed horn is a combination of left hand and right hand circular electric fields (6.1)

$$\bar{E} = E_l \cdot \hat{l} + E_r \cdot \hat{r} \tag{6.1}$$

The circular coordinate unitary vectors can be related with rectangular coordinate unitary vectors as follows (6.2) (6.3),

$$\hat{l} = \frac{\hat{x} + j \cdot \hat{y}}{\sqrt{2}} \tag{6.2}$$

$$\hat{r} = \frac{\hat{x} - j \cdot \hat{y}}{\sqrt{2}} \tag{6.3}$$

The expression of the electric field in rectangular (Cartesian) coordinates is:

$$\bar{E} = E_x \cdot \hat{x} + j \cdot E_y \cdot \hat{y} \tag{6.4}$$

$$E_x = \frac{E_l + E_r}{\sqrt{2}} \tag{6.5}$$

$$E_y = \frac{E_l - E_r}{\sqrt{2}} \tag{6.6}$$

The Stokes parameters Q, U, and I can be obtained from left hand and right hand circular polarized components of the electric field as,

$$\begin{bmatrix} I \\ Q \\ U \end{bmatrix} = \begin{bmatrix} |E_\ell|^2 + |E_r|^2 \\ 2 \cdot Re(E_\ell^* \cdot E_r) \\ -2 \cdot Im(E_\ell^* \cdot E_r) \end{bmatrix} \tag{6.7}$$

The combination of a 90º polarizer and the OMT give two signals at the output. Each signal is proportional to the electric field components E_l and E_r of the total electric field received by the feed horn antenna.

To simplify the notation of the signals at the OMT output, signal A is proportional to left hand circular electric field and signal B is proportional to right hand circular electric field component.

$$E_l \rightarrow V_l = A \tag{6.8}$$

$$E_r \rightarrow V_r = B \tag{6.9}$$

A simplified block diagram of the FGI receiver is shown in Fig. 6.2. Front-end and Back-end amplifiers, filters and diode detectors are not included in this diagram.

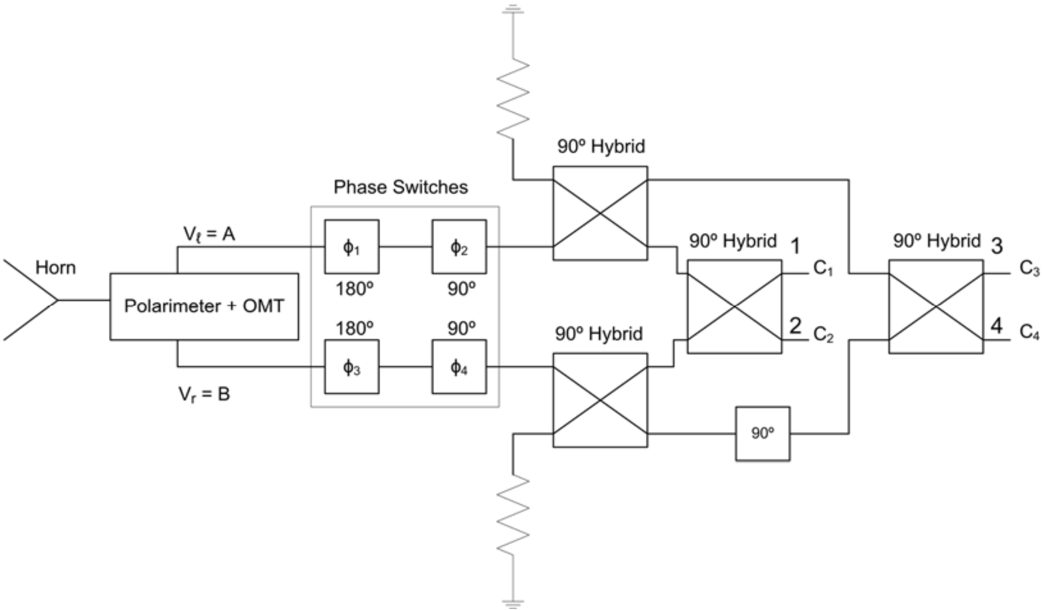

Fig. 6.2. Simplified block diagram of the FGI receiver.

The correlation is based on 90º hybrid couplers. According to the scheme shown in Fig. 6.3, the 90º hybrid Scattering parameter matrix is defined as follows,

$$[S] = \frac{-1}{\sqrt{2}} \cdot \begin{bmatrix} 0 & 0 & j & 1 \\ 0 & 0 & 1 & j \\ j & 1 & 0 & 0 \\ 1 & j & 0 & 0 \end{bmatrix} \tag{6.10}$$

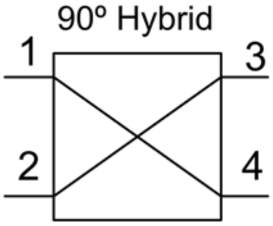

Fig. 6.3. Scheme of a 90º hybrid.

6.2.1. Detected signals in the receiver outputs without Phase Switches

Assuming as initial a null phase in the Phase Switches (6.11) the detected signal at the output of the receiver can be easily calculated.

$$\phi_1 = \phi_2 = \phi_3 = \phi_4 = 0^0 \tag{6.11}$$

The input waves to the Correlation and Detection Module are denoted by A and B. Solving the equations involving the Scattering parameters, the final results for the waves at the output in Fig. 6.2 are:

$$c_1 = -\frac{1}{2} \cdot (A - j \cdot B) \tag{6.12}$$

$$c_2 = \frac{j}{2} \cdot (A + j \cdot B) \tag{6.13}$$

$$c_3 = \frac{j}{2} \cdot (A - B) \tag{6.14}$$

$$c_4 = \frac{1}{2} \cdot (A + B) \tag{6.15}$$

These signals are detected by Schottky diode detectors, square-law detectors, and amplified by DC amplifiers. The signals at the BEM output are proportional to the square amplitudes in equations (6.12) – (6.15). Discarding the ½ factor, the voltage at the BEM outputs (see Fig. 6.1) are defined by,

$$V_{d1} = |A - j \cdot B|^2 \tag{6.16}$$

$$V_{d2} = |A + j \cdot B|^2 \tag{6.17}$$

$$V_{d3} = |A - B|^2 \tag{6.18}$$

$$V_{d4} = |A + B|^2 \tag{6.19}$$

From the expression in (6.7) the three Stokes parameters (I, Q, U) can be calculated substituting the circular electric fields as:

$$E_\ell = A \tag{6.20}$$

$$E_r = B \tag{6.21}$$

The Stokes parameters values are obtained in two ways as (6.22)-(6.24). Note that the Stokes parameters are usually normalised values ranging from -1 to +1. The intensity *I* is always equal to +1, so these values should be normalized accordingly.

$$\begin{aligned} I &\equiv |E_\ell|^2 + |E_r|^2 = |A|^2 + |B|^2 \\ I &\equiv V_{d1} + V_{d2} \equiv V_{d3} + V_{d4} = |A - j \cdot B|^2 + |A + j \cdot B|^2 \\ &= |A - B|^2 + |A + B|^2 \end{aligned} \tag{6.22}$$

$$\begin{aligned} Q &\equiv 2 \cdot Re(E_\ell^* \cdot E_r) = 2 \cdot Re(A^* \cdot B) \\ Q &\equiv V_{d4} - V_{d3} = |A + B|^2 - |A - B|^2 \end{aligned} \tag{6.23}$$

$$\begin{aligned} U &\equiv -2 \cdot Im(E_\ell^* \cdot E_r) = -2 \cdot Im(A^* \cdot B) \\ U &\equiv V_{d2} - V_{d1} = |A + j \cdot B|^2 - |A - j \cdot B|^2 \end{aligned} \tag{6.24}$$

6.2.2. Detected signals in the receiver outputs with Phase Switches

Introducing the phase states and assuming only the upper branch (see Fig. 6.2) changes its phase, then:

$$\phi_T = \phi_1 + \phi_2 \tag{6.25}$$

$$\phi_3 + \phi_4 = 0^0 \tag{6.26}$$

The total phase between the two branches is Φ_T. The calculus of the output voltages for the four different phase states (0^0, 90^0, 180^0 and 270^0) are summarized in Table 6.1.

Table 6.1. Output voltages for different Phase Switches states.

Φ_T	0^0	90^0	180^0	270^0
V_{d1}	$\|A - j \cdot B\|^2$	$\|A - B\|^2$	$\|A + j \cdot B\|^2$	$\|A + B\|^2$
V_{d2}	$\|A + j \cdot B\|^2$	$\|A + B\|^2$	$\|A - j \cdot B\|^2$	$\|A - B\|^2$
V_{d3}	$\|A - B\|^2$	$\|A + j \cdot B\|^2$	$\|A + B\|^2$	$\|A - j \cdot B\|^2$
V_{d4}	$\|A + B\|^2$	$\|A - j \cdot B\|^2$	$\|A - B\|^2$	$\|A + j \cdot B\|^2$

Finally, the Stokes parameters are directly calculated from expressions (6.22)-(6.24). The results are shown in Table 6.2.

Table 6.2. Stokes parameters for different Phase Switches states.

Φ_T	I	Q	U
0^0	$V_{d1}+V_{d2}=V_{d3}+V_{d4}$	$V_{d4}-V_{d3}$	$V_{d2}-V_{d1}$
90^0	$V_{d1}+V_{d2}=V_{d3}+V_{d4}$	$V_{d2}-V_{d1}$	$V_{d3}-V_{d4}$
180^0	$V_{d1}+V_{d2}=V_{d3}+V_{d4}$	$V_{d3}-V_{d4}$	$V_{d1}-V_{d2}$
270^0	$V_{d1}+V_{d2}=V_{d3}+V_{d4}$	$V_{d1}-V_{d2}$	$V_{d4}-V_{d3}$

6.3. Checking the radiometer operation

From equations (6.4)-(6.6) the circular components of the electrical field can be expressed in terms of rectangular components.

$$E_\ell = \frac{E_x + E_y}{\sqrt{2}} \tag{6.27}$$

$$E_r = \frac{E_x - E_y}{\sqrt{2}} \tag{6.28}$$

The Stokes parameters, not normalised, for different input polarized waves arriving at the input of the receiver are calculated in Table 6.3 according the expressions obtained in previous Table 6.1 and Table 6.2.

Table 6.3. Stokes parameters (not normalised) from different input waves in the receiver.

Polarisation (input wave)	E_ℓ	E_r	I	Q	U
Linear Horizontal (H)	$\frac{E_x}{\sqrt{2}}$	$\frac{E_x}{\sqrt{2}}$	$2\cdot\lvert E_x\rvert^2$	$2\cdot\lvert E_x\rvert^2$	0
Linear Vertical (V)	$\frac{E_y}{\sqrt{2}}$	$-\frac{E_y}{\sqrt{2}}$	$2\cdot\lvert E_y\rvert^2$	$-2\cdot\lvert E_y\rvert^2$	0
Circular Left (L)	E_ℓ	0	$2\cdot\lvert E_\ell\rvert^2$	$2\cdot\lvert E_\ell\rvert^2$	0
Circular Right (R)	0	E_r	$2\cdot\lvert E_r\rvert^2$	$2\cdot\lvert E_r\rvert^2$	0

The results in Table 6.3 confirm the theory of Stokes parameters. Table 6.4 summarises the normalised Stokes parameters.

Table 6.4. Theoretical normalised Stokes parameters from different waves.

Polarised wave	I	Q	U
Linear Horizontal (H)	1	1	0
Linear Vertical (V)	1	-1	0
Circular Left (L)	1	0	0
Circular Right (R)	1	0	0

6.4. Subsystems of the FGI receiver

The FGI receiver is composed of the Front-end Module (FEM) cooled down cryogenically to 20 K and the Back-end Module (BEM) operating at room temperature (300 K). The FEM is formed by the feed system, including the electromagnetic components (feed horn, polarizer and the OMT), and the first stage of amplification, two cryogenic low-noise amplifiers (cryo-LNA) placed at the outputs of the OMT. The BEM is composed of the second stage of amplification, which includes the filtering and equalization. The phase switches and the correlation and detection module complete the BEM.

6.4.1. FEM subsystems

An artist's view of the feed system including the cryo-LNA is depicted in Fig. 6.4.

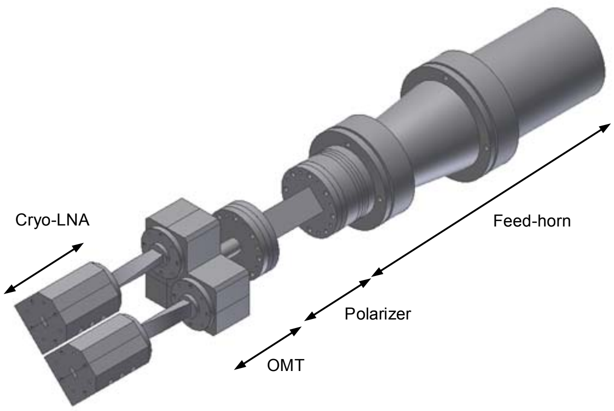

Fig. 6.4. Opto-mechanics 3D view of one pixel of the FGI receiver.

The feed horn is based on a corrugated feed with the output in circular waveguide. In Fig. 6.5 two identical manufactured units are shown.

Fig. 6.5. Feed horns of the FGI receiver.

The polarizer is a differential 90^0 phase shifter for the two orthogonal propagation modes (TE_{10} and TE_{01}) in the square waveguide. Two polarizers with its transitions from circular to square waveguide are presented in Fig. 6.6.

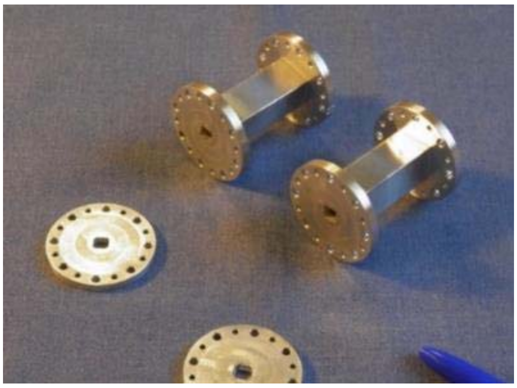

Fig. 6.6. Polarizers of the FGI receiver with its transitions from circular to square waveguide.

The constant phase difference between the two modes in the polarizer is achieved by internal stepped ridges placed inside the square waveguide. When the electric field at the input of the polarizer has a linear, horizontal or vertical, orientation, each orthogonal component propagates along the ridged square waveguide with different insertion phase. At the polarizer output the components have a 90^0 phase difference between them. A detail of the ridges placed inside the polarizer are shown in Fig. 6.7.

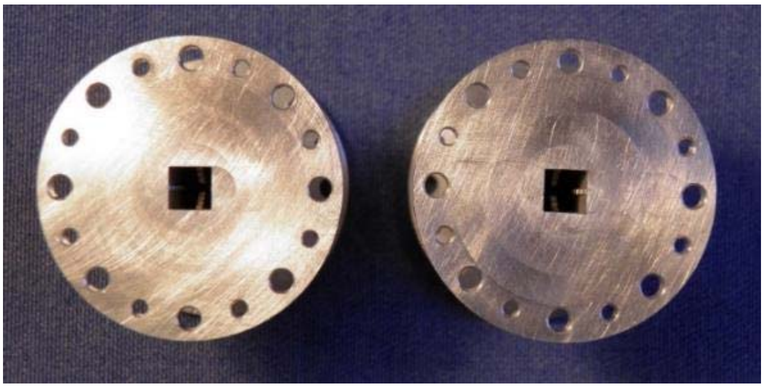

Fig. 6.7. Stepped ridges inside the square waveguide of the polarizer for the FGI receiver.

The assembly of the feed system of one pixel of the FGI receiver is shown in Fig. 6.8. It means the connection of the feed horn, the polarizer and the OMT. The rectangular waveguide outputs are labelled as H (horizontal) and V (vertical). The assembly has three physical ports. However, there are four electrical ports because the polarizer has two orthogonal modes at its input.

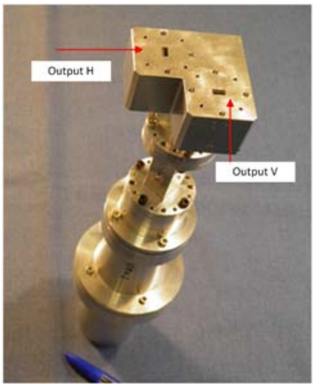

Fig. 6.8. Assembly of the feed system of the FGI receiver, feed horn +polarizer + OMT.

Naming the ports of the feed system (excluding the feed horn) assembly as follows, the Scattering parameters matrix can be defined as (6.29).

- Port 1: OMT output H.
- Port 2: OMT output V.
- Port 3: Polarizer input H.
- Port 4: Polarizer input V.

$$S = \frac{1}{\sqrt{2}} \cdot \begin{bmatrix} 0 & 0 & 1 & -j \\ 0 & 0 & -j & 1 \\ 1 & -j & 0 & 0 \\ -j & 1 & 0 & 0 \end{bmatrix} \qquad (6.29)$$

The 0^0 phase reference is taken from the transmission parameter related to the polarizer input H with the OMT output H. According to (6.29), when an input horizontal electric field comes into the Port 3, the two OMT output signals have the same amplitude but shifted 90^0. The same happens if an input vertical electric field comes into Port 4, then the two OMT output signals have the same amplitude shifted 90^0.

On the other hand, if a signal goes only on one rectangular waveguide port of the OMT (Port 1 or Port 2), then there is a circular polarised wave, right or left hand depending on the selected input port, at the output of the Polarizer.

Finally, the FEM ends in the cryo-LNA. Inside and outside views are shown in Fig. 6.9. The module is gold plated to keep a good thermal conductivity when it is cooled down at cryogenic temperature.

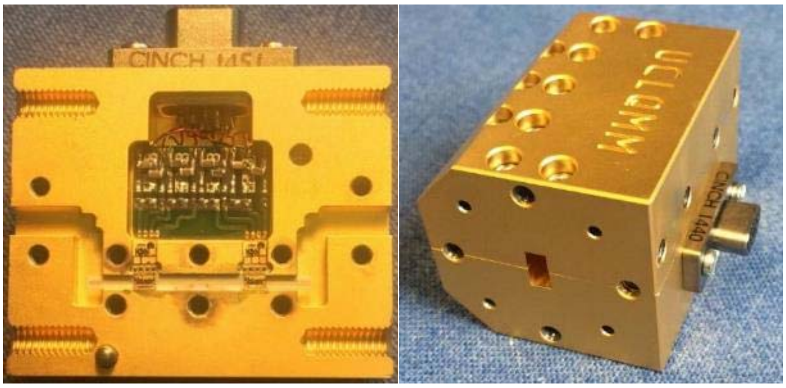

Fig. 6.9. View of the cryo-LNA for the FGI receiver.

The cryogenic performance of the LNA in terms of insertion gain and noise temperature is shown in Fig. 6.10. The physical temperature of the cryo-LNA is 15 K. Average values in the 35-47 GHz frequency band are summarized in Table 6.5.

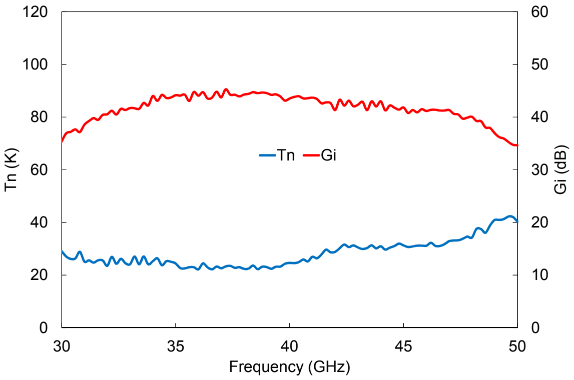

Fig. 6.10. Cryo-LNA noise temperature and associated gain at cryogenic temperature (15 K).

Table 6.5. Cryogenic performance of the LNA.

Frequency (GHz)	Te avg (K)	Te min (K)	Gi avg (dB)
35 – 47	27	22	43

The DC power is supplied though a DC connector (9 pins MDM). Total power consumption of the two MMIC chips of the cryo-LNA is detailed in Table 6.6.

Table 6.6. DC consumption of the cryo-LNA.

MMIC chip	Vd1 (V)	Id1 (mA)	Vd2 (V)	Id2 (mA)	Power (mW)
1st	0.6	6	1	10	13.6
2nd	0.6	6	1	10	13.6
TOTAL					27.2

6.4.2. BEM subsystems

The first module in each branch of the BEM is the second amplification stage. This module called BEM gain module includes other capabilities as equalisation (see chapter 5) and filtering in order to adapt the signal to the correlation and detection module input. A photo of the module is shown in Fig. 6.11. Scattering performance of first unit manufactured is presented in Fig. 6.12. The gain has a positive slope needed to compensate the negative slope in the transmission response of the connection cables and the negative gain slope of FEM module.

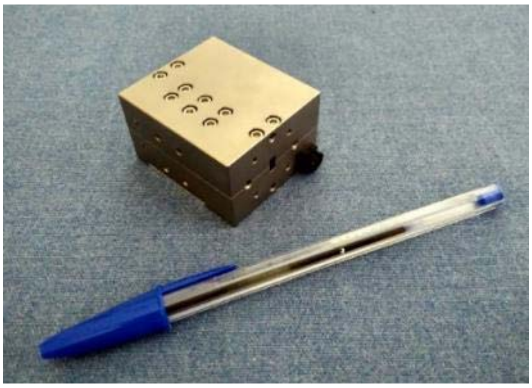

Fig. 6.11. Photo of the BEM gain module for the FGI receiver.

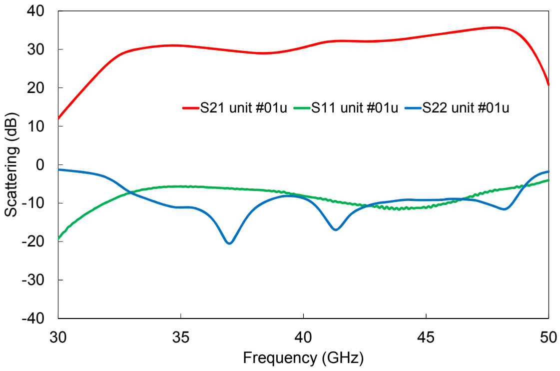

Fig. 6.12. Scattering performance of unit #01 BEM gain module for the FGI receiver.

Next module in BEM chain is the Phase Switch [6.2]. This module has two identical branches, which each one modulates the phase of the signal. Four different phase states, 0^0, 90^0, 180^0 and 270^0 are introduced by the two phase switches composing each branch of the module by using the appropriate TTL control signals. The Phase Switch module is based on microstrip hybrid technology, which combines microstrip lines with the use of a switching active device which enables the phase state variation. There are four different planar circuits integrated, a power divider, a 180^0 phase switch, a 90^0 differential phase shifter and a power combiner. The selected active switch device is a PIN diode from Avago Technologies. Two views, inside and outside, of the Phase Switch module assembled are shown in Fig 6.13 and Fig. 6.14.

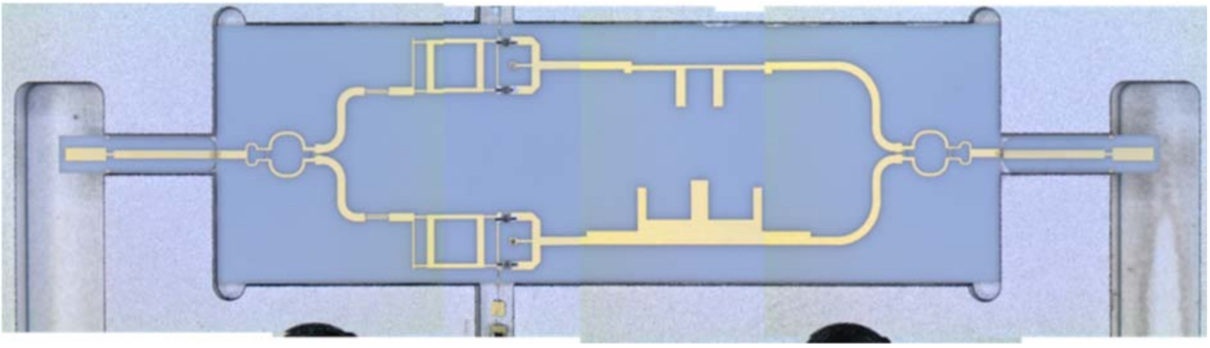

Fig. 6.13. Inside photo of the Phase Switch module for the FGI receiver.

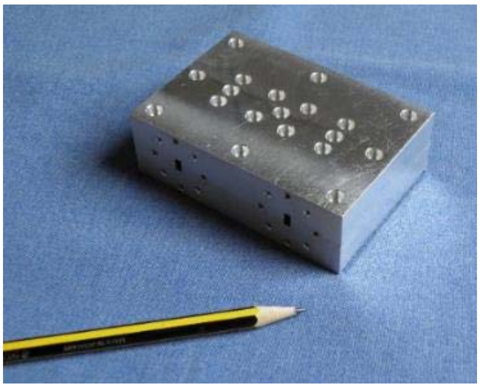

Fig. 6.14. Photo of the Phase Switch module chassis for the FGI receiver.

In Fig. 6.15 the performance of the Phase Switch module is presented. The phase response states referred to a 0^0 state are plotted in Fig. 6.15(a) and Fig. 6.15(b), for the upper and lower branches respectively. In Fig. 6.15(c) and Fig. 6.15(d) the amplitude imbalances of the two branches of the Phase Switch module are shown.

The last module in the BEM is the Correlation and Detection Module (CDM). This module carries out the correlation in waveguide technology [6.3] whereas the detection is performed by Schottky diode detectors [6.4] (Fig. 6.16). The subsequent DC amplifier provides adequate voltage levels at the four module outputs.

The module consists of four hybrids couplers, a 90^0 phase shifter and four Schottky diode detectors. The detected signals are amplified using video amplifiers.

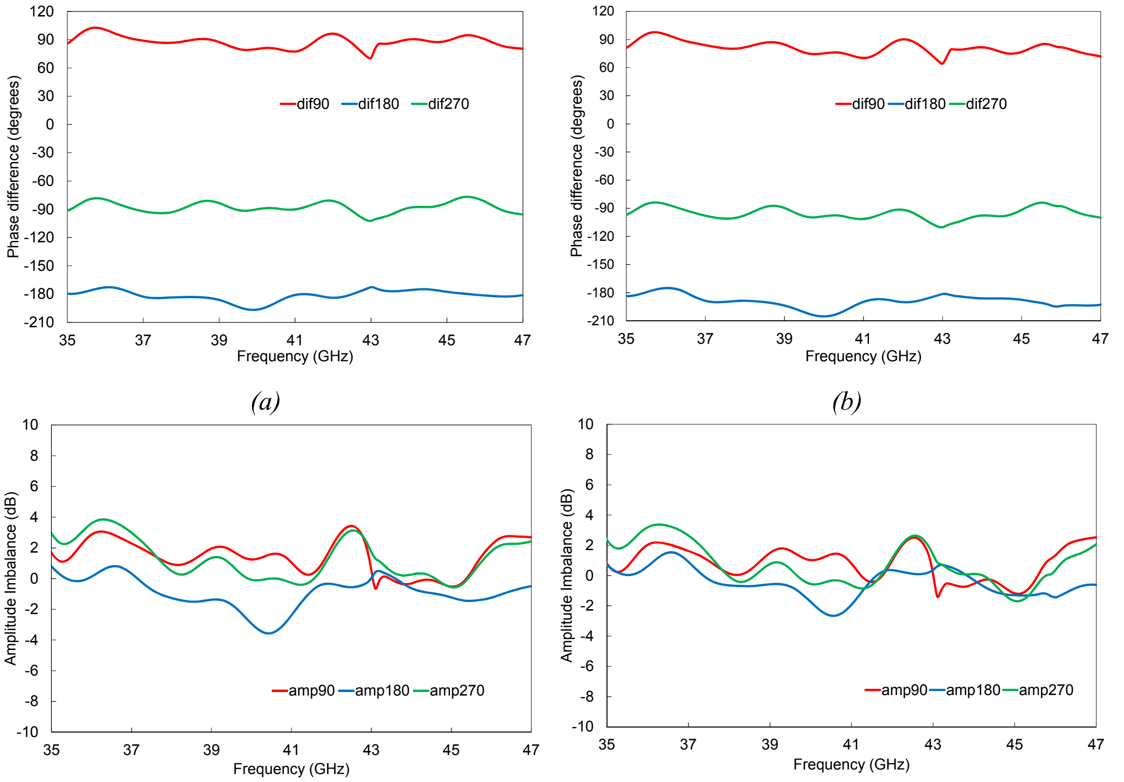

(a) *(b)*

(c) *(d)*

Fig. 6.15. Performance of the Phase Switch module for the FGI receiver. (a) Phase states of the upper branch. (b) Phase states of the lower branch. (c) Amplitude imbalance of the upper branch. (d) Amplitude imbalance of the lower branch.

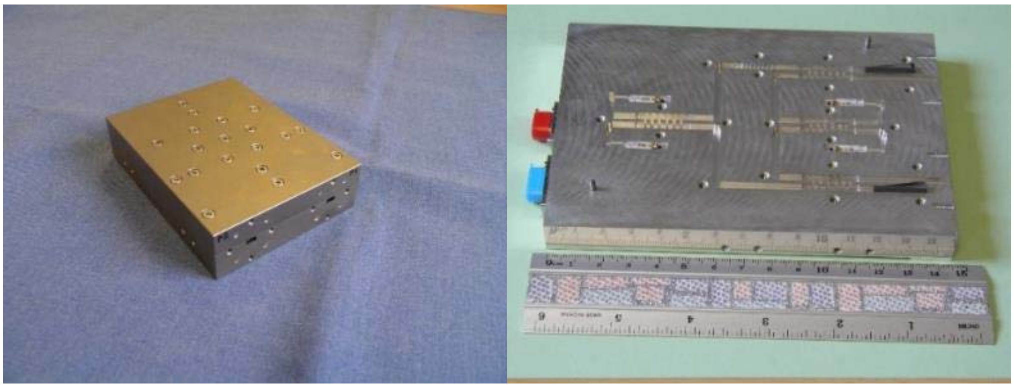

Fig. 6.16. Photos of the Correlation and Detection module for the FGI receiver.

The Scattering performance at the input ports of the CDM is presented in Fig. 6.17. Input return loss is better than 20 dB and the isolation between input ports is better than 15 dB.

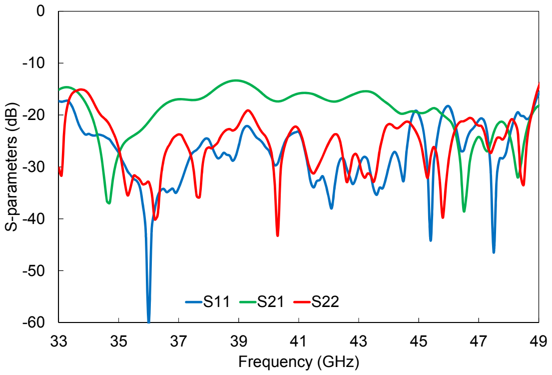

Fig. 6.17. Scattering parameters of the Correlation and Detection module for the FGI receiver.

The RF to DC characterization is done with the test set-up shown in Fig. 6.18. A hybrid coupler, similar to the one designed for the module, is placed in front of the module. This enables to produce two signals with equal power and 90^0 out of phase to be the inputs of the module. The incoming signal to the hybrid coupler is obtained from a signal generator.

Fig. 6.18. Test set-up for DC to RF characterization for the Correlation and Detection Module of the FGI receiver.

Fig. 6.19 plots the four detected DC signals versus frequency when the generator drives into the module a power of -15 dBm. One important issue in this module is the 1-dB compression point, it means, the detection window where the diode detector has a linear performance. In Fig. 6.20, a 1-dB compression point of -9.5 dBm is calculated. So the input signal of the CDM should go from -40 dBm to -9.5 dBm in order to achieve suitable detected output signals.

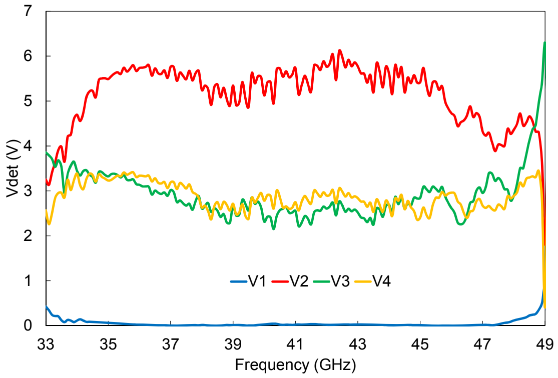

Fig. 6.19. Measured detected signal versus frequency.

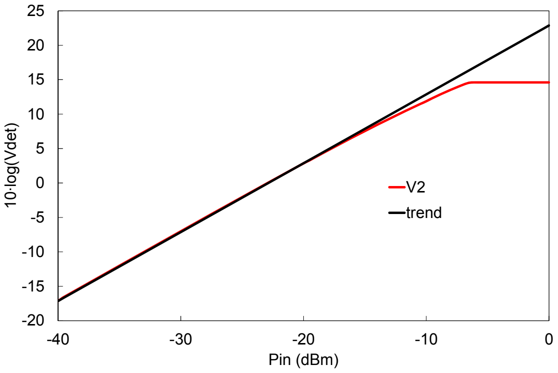

Fig. 6.20. Calculation of the compression point 1-dB from the measurements of the detected signals versus input power.

6.5. Test-bench

6.5.1. BEM test-bench

The test-bench proposed to verify the correct behaviour of the FGI receiver is composed by the BEM and the feed system including the feed horn (Fig. 6.21). A detail of the BEM integrated in a modular PCB support [6.5] is shown in Fig. 6.22. Rectangular waveguides interconnect the different modules of the BEM.

Fig. 6.21. Test-bench of the FGI receiver with the modular BEM.

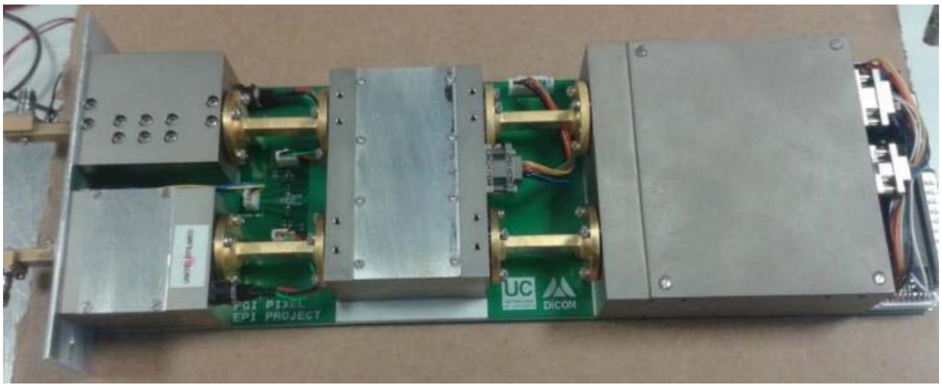

Fig. 6.22. BEM integration for the FGI receiver.

During the test of the FGI receiver, the detected signals are introduced in a data acquisition system (DAS) and saved. At the moment, two BEM modular cards has been integrated showing good results. Fig. 6.23 shows the detected signals for the two BEM in a period of time of one second while the phase switches are switching. The total amount of modular PCB support would be 29 in order to complete all the FGI instrument.

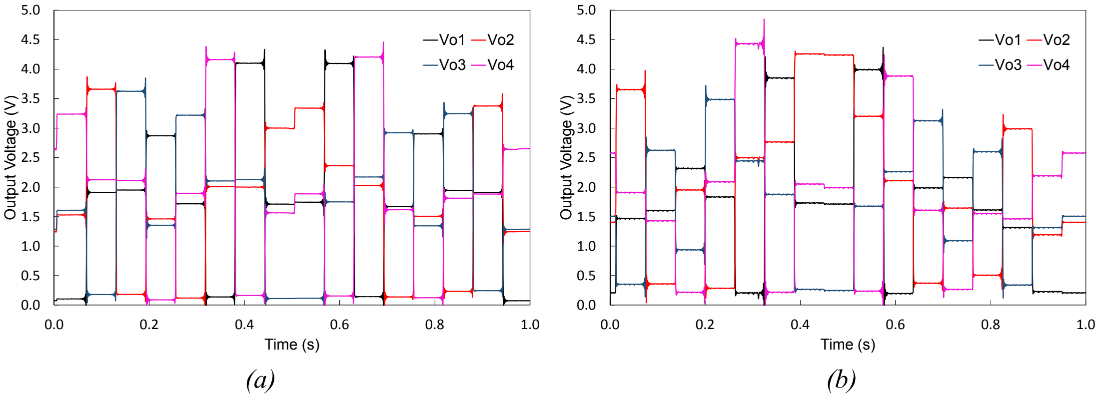

Fig 6.23. Detected signals in the data acquisition systems (DAS) for the modular BEM integration. Modular pixels (a) #01, (b) #02.

6.5.2. Gain chain test-bench

Since the amplification chain mainly sets the noise of the instrument (excluding the components in front of the FEM cryo-LNA), the noise performance of the FEM and BEM amplifiers is performed. The FEM cryo-LNA bias point is V_{d13}=0.6 V, I_{d13}=6 mA, V_{d24}=1 V, and I_{d24}=10 mA; while the BEM gain module bias point is V_d=±5 V and I_d=120 mA. A 7.5 dB attenuator is placed between the two gain modules, simulating the losses of the instrument (cryo-waveguides inside and coaxial cables outside the cryostat). Fig. 6.24 shows the FEM cryo-LNA inside the cryostat and the attenuator plus the BEM gain module outside (left-hand).

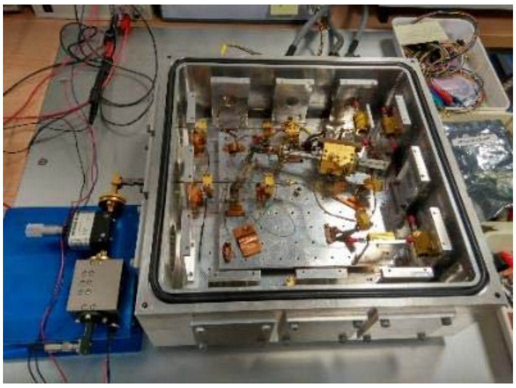

Fig. 6.24. Gain chain of FGI instrument.

6.5.2.1. Noise performance

First measurement was to cool down the FEM cryo-LNA to a cryogenic temperature of 14 K and measure the noise and gain using the hot-cold load termination method [6.6]. The load termination is connected to LNA input through a steel waveguide because the steel is a bad thermal conductor, so the LNA and the load are quasi-isolated in terms of temperature (Fig. 6.25). Two temperatures are used, 20 Kelvin as the cold load and 50 K as the hot one. The change in load temperature between 20 and 50 K means a physical temperature of the LNA from 14 to 16 K. This 2 K delta temperature appears due to the temperature flows thorugh the steel waveguide connecting the load and the LNA. In Fig. 6.26(a), the noise performance of the LNA using hot-cold load method is plotted. The average noise temperature in the 30-50 GHz frequency band is 28 K, meanwhile the associated gain in the 35-47 GHz frequency band is 43 dB. The hot-cold load method and the cold attenuator technique used to measure noise in a LNA are compared in Fig. 6.26(b). There is a good agreement in the gain for both methods, and the noise peroformance is more flat in the hot-cold load method because there are no missmatching between the noise source and the device under test (DUT).

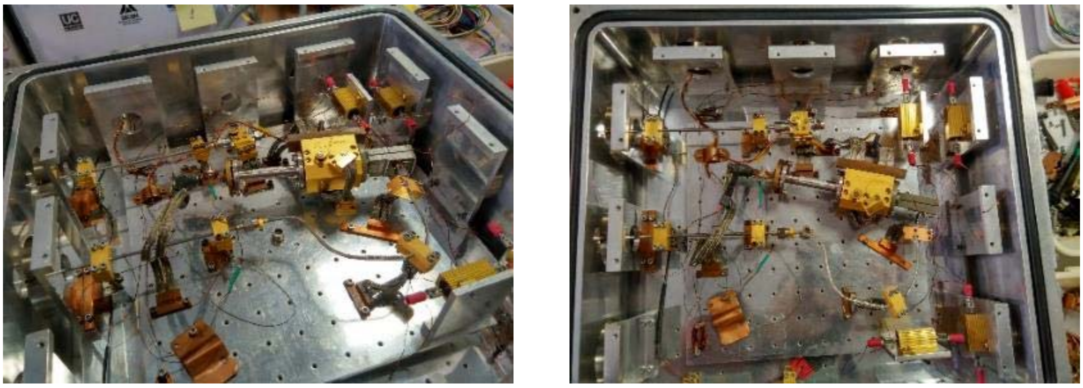

Fig. 6.25. FEM cryo- LNA placed in the cryostat just before a cooling cycle.

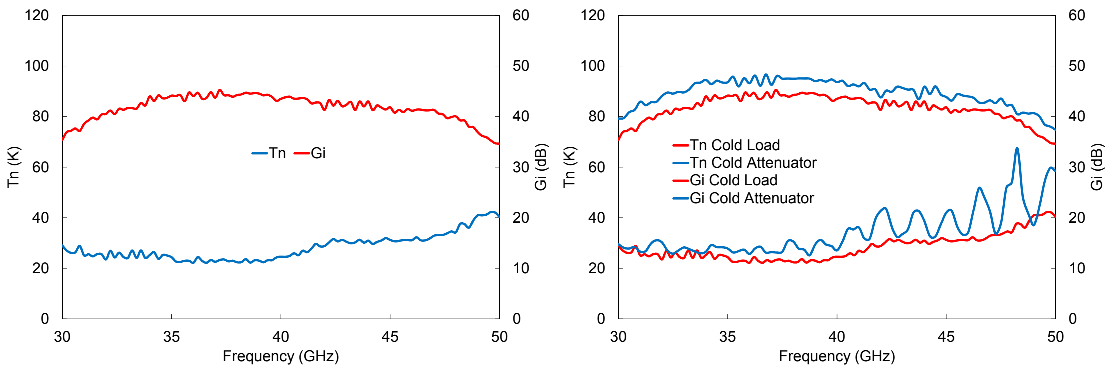

(a) *(b)*

Fig. 6.26. Noise performance of the FEM cryo-LNA cooled down to 15 K. (a) Measurement with hot-cold load termination method. In red the associated gain. In blue, the noise temperature. (b) Comparison of the cryo-LNA noise performance measured with hot-cold load termination method (red) and the cold attenuator technique (blue).

Then, the BEM module is connected at the output of the cryostat, with the 7.5 dB attenuator (Fig. 6.27). A photo of the set-up is presented in Fig. 6.28. The attenuation helps the BEM gain module not to compress because the high gain of the FEM LNA. A small gain compression implies a high noise increase.

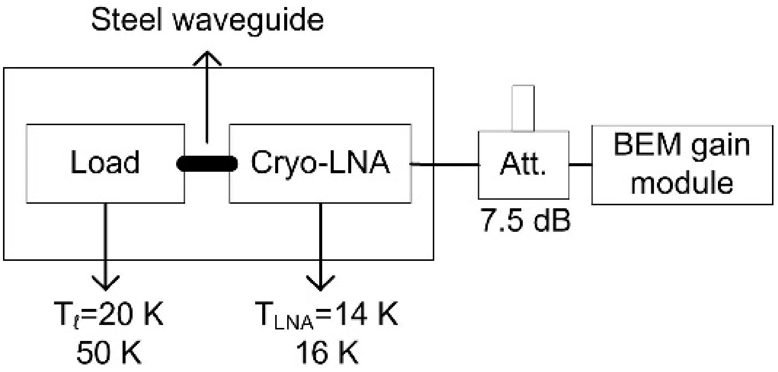

Fig. 6.27. Scheme of the noise measurement set-up for the gain chain of FGI instrument.

Fig. 6.28. Noise measurement set-up for the gain chain of FGI.

The full gain chain performance (Fig. 6.29(a)) achieves an associated gain of 65 dB in the 35-47 GHz frequency band and noise temperature of 25.3 K in the 30-50

GHz frequency band. After 42.5 dB of gain in the FEM the contribution of the BEM should be almost zero but the uncertainties of the measurement produces some discrepancies between the FEM measurement and the FEM plus BEM gain module measurement (Fig. 6.29(b)).

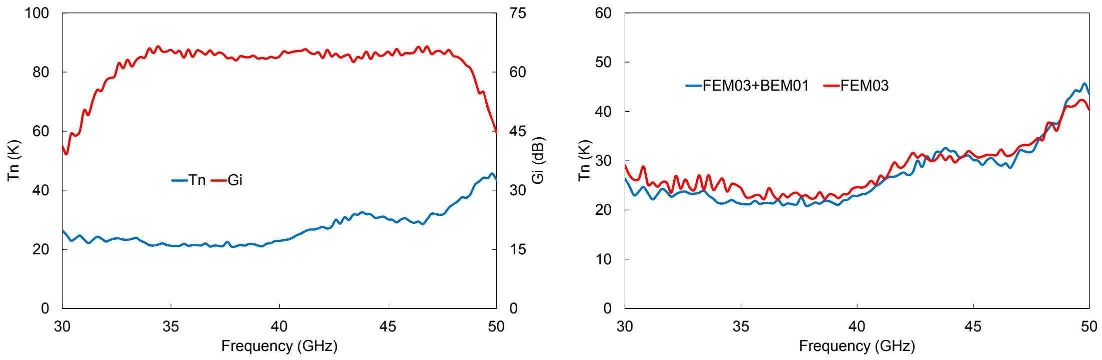

(a) *(b)*

Fig. 6.29. Noise performance of the gain chain for the FGI instrument. (a) Measurement with hot-cold load termination method. In red the associated gain. In blue, the noise temperature. (b) Comparison of the cryo-LNA noise performance (red) with the gain chain (blue) of the FGI instrument (cryo-LNA plus BEM gain module).

Tests done in the gain chain validate both the FEM cryo-LNA and BEM gain module working together. The high gain of the cryo-LNA minimizes (quasi-remove) the BEM gain module noise contribution. So the receiver noise is mainly set by the cryo-LNA in the FEM, and the BEM gain module only adds gain to the receiver.

6.5.2.2. Effective bandwidth

The bandwidth of a receiver is very important in a radio astronomy receiver because the broadband the receiver is, the bigger is the sensitivity. A high sensitivity receiver means high accuracy measurement and low time of observation to achieve a certain accuracy.

In order to measure the effective bandwidth a square-law detector (model HP8474E from Hewlett Packard) is used at the output of the receiver (Fig. 6.30). A vector signal analyser (model HP4395A from Hewlett Packard) measures the power spectral density, shown in Fig. 6.31, for the two temperatures of the cold load at the input of the chain (20 K and 50 K).

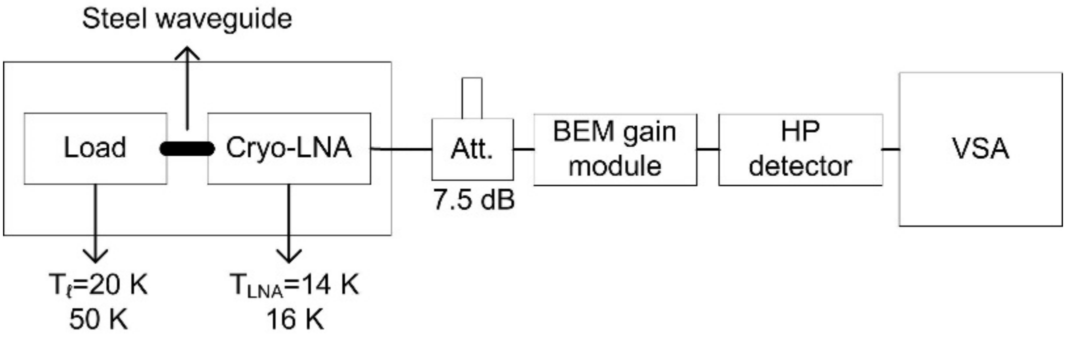

Fig. 6.30. Measurement set-up for the low-frequency spectra of the FGI gain chain.

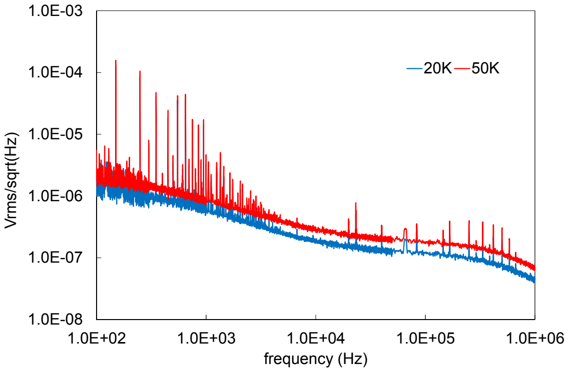

Fig. 6.31. Low-frequency spectra of the gain chain for the FGI instrument.

The effective bandwidth, B_{eff}, for the gain chain can be calculated as follows [6.7],

$$B_{eff} = \frac{2 \cdot V_{DC}^2}{\Delta V^2} \tag{6.30}$$

where V_{DC} is the DC voltage detected at the output of the receiver, and ΔV is the RMS voltage value when the power spectral density becomes flat.

In Table 6.7, the effective bandwidth for the two input temperatures, applying (6.30), is calculated. The value obtained for both load temperatures is around 14 GHz. The more accurate effective bandwidth is 14.75 GHz, for the 50 K load temperature, because the input power is higher. Although the frequency band of interest of the receiver is 12 GHz (35-47 GHz), the chain still has gain out of band and the overall bandwidth goes up 14 GHz.

Table 6.7. Effective bandwidth calculus of the gain chain for one pixel of the FGI instrument.

Load temperature (K)	V_{DC} (V)	ΔV (V_{RMS}/sqrt(Hz))	B_{eff} (GHz)
20	9.65e-3	1.15e-7	14.08
50	15.46e-3	1.8e-7	14.75

6.5.3. Instrument operation with the FEM at cryogenics

To complete the instrument characterisation, the FEM is cooled down inside a cryostat and connected to the BEM at room temperature. Due to the reduced size of the cryostat chamber, the feed system is removed and instead of it, a 3 dB coupler divides the input noise signal of a waveguide load into the two branches of the receiver. The hot-cold load at the input of the coupler provides a noise input power (Fig. 6.32(b)). The full test-bench is shown in Fig. 6.32(a), from left to right hand, the DAS, the BEM card, and the cryostat.


(a) *(b)*

Fig. 6.32. FGI test-bench with the FEM cryo-LNA working at cryogenics. (a) General view of the BEM connected to the cryostat. The DAS is at the left-hand. (b) The two FEM LNA placed inside the cryostat and put together to the input load through and 3-dB coupler.

Two type of measurements are performed. First, a short time measurement of the detected signals is used to calculate the noise temperature of the receiver, and to correct the offset of the detected signals due to the equivalent noise temperature of the receiver. Then, a long time measurement with and without switching the phase switches is used to obtain the frequency spectrum of the detected signals.

For the short time measurement, the detected signals are measured during 1 second with a sample rate of 1000 samples per second for four different input load temperatures, while the phase switches commute at a switching rate of 16 Hz. The input load is cooled down to a minimum of 15 Kelvin, after that a heater in the input load sets its temperature to 50, 70 and, 88 K respectively. Input load at higher temperatures than 88 K the receiver is saturated and the detected signals are overshoot up to 12 volts. In Fig. 6.33 the detected signals for the four input load temperatures are presented. When the input signal temperature is below or close to the equivalent noise temperature of the receiver, it means around 30 K, the detected levels are mainly proportional to the equivalent noise temperature and the input load noise temperature is not distinguishable for the phase switches states (Fig. 6.33 (a)).

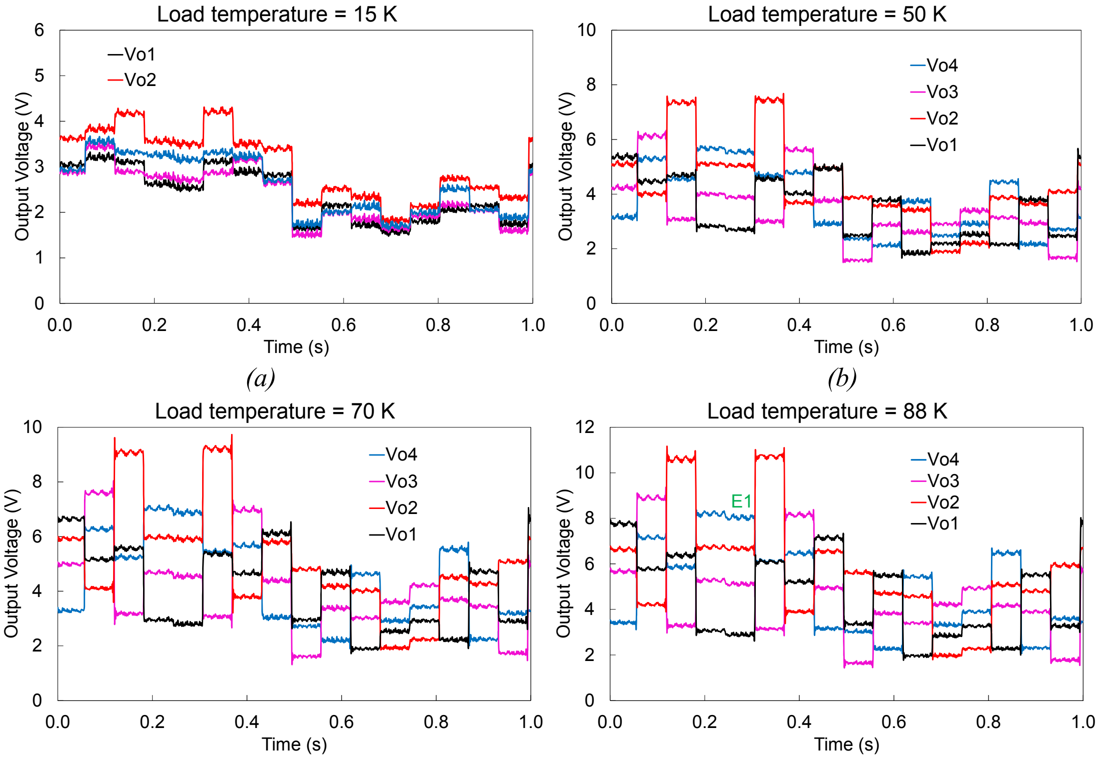

(a) *(b)* *(c)* *(d)*

Fig. 6.33. Detected signals in the FGI test-bench for different input cold loads. Load temperature (a) 15 K, (b) 50 K, (c) 70 K, and (d) 88 K.

The phase states sequence is listed in Table 6.8. Φ_T is the phase difference between branches of the phase switches module, Φ_{B1} is the upper branch in the phase switches module and, Φ_{B2} is the lower one (see Fig. 6.1). The initial of the sequence, state 1, is marked with E_1 in green in Fig. 6.33(d).

Table 6.8. Phase states sequence.

State	**Φ_T (deg.)**	**Φ_{B2} (deg.)**	**Φ_{B1} (deg.)**
E1	0	0	0
E2	90	90	0
E3	270	270	0
E4	180	180	0
E5	270	0	90
E6	0	90	90
E7	180	270	90
E8	90	180	90
E9	180	0	180
E10	270	90	180
E11	90	270	180
E12	0	180	180
E13	90	0	270
E14	180	90	270
E15	0	270	270
E16	270	180	270

Ideally, the four detected signals in each phase state are proportional to the receiver equivalent noise temperature, T_e, and the input load noise temperature, T_i, as follows:

$$V_{max} = A \cdot \left(\frac{T_e}{2} + \frac{T_i}{2}\right) \tag{6.31}$$

$$V_{min} = A \cdot \left(\frac{T_e}{2}\right) \tag{6.32}$$

$$V_{med1} = V_{med2} = A \cdot \left(\frac{T_e}{2} + \frac{T_i}{4}\right) \tag{6.33}$$

$$A = \alpha \cdot k \cdot G \cdot B_{eff} \tag{6.34}$$

where G is the RF gain of the receiver, B_{eff} is the equivalent bandwidth, k the Boltzmann constant, and α is the sensibility of the square law detector. The two input noise temperatures used for the calculus of T_e are T_c=50 and T_h=88 K. The highest input load temperature measured without saturating the receiver is 88 K and 50 K is the temperature similar to the T_e expected. These two input temperatures provide a suitable excess noise ratio (ENR) to calculate T_e.

Adding the four detected signals in each time sample and taking into account the noise contributions (6.31)-(6.34), a measurement proportional to the input noise T_h and twice T_e is obtained. Then, the system equivalent noise temperature, T_e, can be calculated as follows,

$$T_e = \frac{1}{2} \cdot \frac{T_h - Y \cdot T_c}{Y - 1} \tag{6.35}$$

where the two input temperatures, T_h and T_c, are 88 and 50 K respectively. The Y factor is the ratio of noise power at T_h divided by noise power at T_c. In Fig. 6.34, the obtained T_e for all the detected states is plotted. The average T_e is 35.4 K.

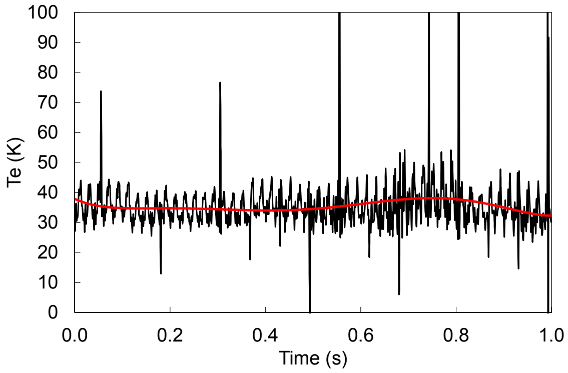

Fig. 6.34. System equivalent noise temperature, T_e, in each time sample for the addition of the four detected signals.

There are phase states in which the detected signal is weak due to the phase switch losses and there are some dispersion (see the time range 0.6 to 0.8 seconds in Fig. 6.33 and Fig. 6.34) in the calculus of T_e over the average value (red trace in Fig. 6.34).

Knowing T_e, a global responsivity, including the sensitivity of the detectors and the overall gain of the receiver, can be calculated (6.36).

$$\Re_g = \frac{\sum V_d}{k \cdot B_{eff} \cdot (2 \cdot T_e + T_i)} \tag{6.36}$$

Where ΣV_d is the addition of the four average detected voltage in each phase state, k the Boltzmann constant, B_{eff} the effective bandwidth (6.30), T_i is the input load temperature, and T_e the equivalent noise temperature.

The obtained responsivity $\boldsymbol{\Re}$ for each phase state versus the input load temperature is shown in Fig. 6.35. Attending the flat traces it is clear the responsivity does not depend of the input load temperature. The difference of responsivity level between states is due to the losses of the phase switches involved in each phase state.

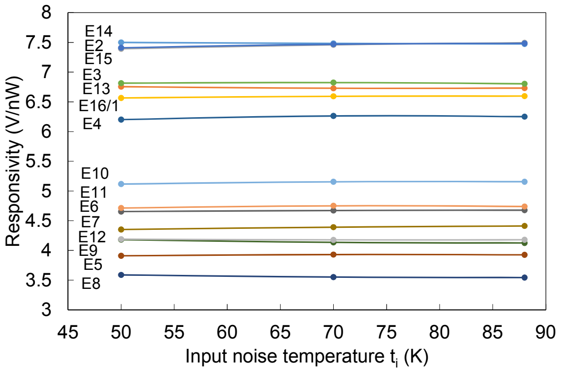

Fig. 6.35. Responsivity $\boldsymbol{\Re}$ versus input load temperature for the sixteen phase states.

In order to evaluate the goodness of the instrument performance, a new figure of merit, I, is defined. This will show how far are the obtained detected signals for each phase state from the ideal performance without leakage between outputs. It indicates an isolation between detected signals or receiver outputs when an input load temperature is applied. Three isolations are defined taking into account the maximum, minimum, and medium detected signals (6.37)-(6.39). These figures are calculated with detected voltages due only to the input load temperature. They are corrected removing the detected voltage due to the receiver noise temperature T_e.

$$I_1 = \frac{V_{\max corr} + V_{\min corr}}{V_{\max corr} - V_{\min corr}} \tag{6.37}$$

$$I_2 = \frac{V_{\max corr} - V_{\min corr}}{V_{med1\ corr} - V_{med2\ corr}} \tag{6.38}$$

$$I_3 = \frac{V_{med1\ corr} + V_{med2\ corr}}{V_{med1\ corr} - V_{med2\ corr}} \tag{6.39}$$

In an ideal case, I_1 equals 1 because the minimum detected signal, V_{min}, is zero. I_2 and I_3 is infinite because the medium values V_{med1} and V_{med2} are equal. And calculating the logarithm of these isolations ($10 \cdot \log_{10}(I)$), I_1 is zero and I_2, I_3 are infinite in the ideal case.

The offset due to the equivalent noise temperature of the receiver (T_e) is corrected in the detected signals. The detected signals due to the 15 K input temperature are considered to correct that offset. At 15 K input noise temperature the detected voltages are essentially proportional to the receiver noise temperature, but it has also the contribution of the input load noise. Then, the offset for each output is obtained with the coefficients C_{max}, C_{min}, C_{med}, and the output voltages at 15 K. So the corrected output signals follow,

$$V_{\max corr} = V_{max} - V_{max}(15\ K) \cdot C_{max} \tag{6.40}$$

$$V_{\min corr} = V_{min} - V_{min}(15\ K) \cdot C_{min} \tag{6.41}$$

$$V_{\mathrm{med}\, corr} = V_{med} - V_{med}(15\ K) \cdot C_{med} \tag{6.42}$$

where C_{max}, C_{min}, and C_{med} are the correction coefficients defined by,

$$C_{max} = \left(\frac{T_e}{2}\right) \cdot \frac{1}{\left(\frac{T_e}{2} + \frac{T_h}{2}\right)} \tag{6.43}$$

$$C_{min} = 1 \tag{6.44}$$

$$C_{med} = \left(\frac{T_e}{2}\right) \cdot \frac{1}{\left(\frac{T_e}{2} + \frac{T_h}{4}\right)} \tag{6.45}$$

The minimum correction coefficient is equal to 1 (6.44) because the minimum voltage output is ideally only proportional to T_e.

The detected signals corrected for three different input load temperatures are plotted in Fig. 6.36. The minimum values are not zero because the unbalances in the receiver.

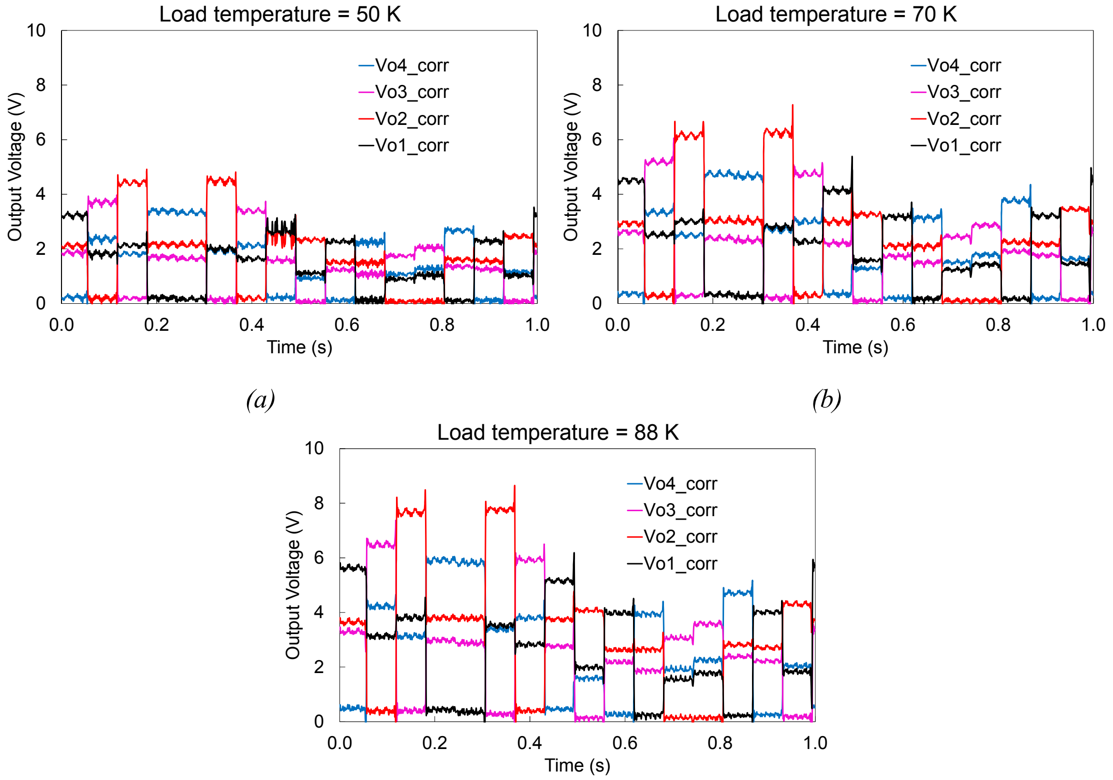

(a) *(b)*

(c)

Fig. 6.36. Detected signals after offset correction for different input load temperatures; (a) 50 K, (b) 70 K and (c) 88 K.

After the correction of the detected signals, the isolations (6.37)-(6.39) are calculated. In Fig. 6.37, the isolation values (dB) for each phase state and input load temperature of 88 K are plotted. The isolation between maximum and minimum output voltages (Fig. 6.37(a)) is lower than 1 dB.

The sensitivity of the detected signals for E_1 phase switch state versus the input load temperature is evaluated before and after de offset correction. In Fig. 6.38, the solid traces represent the original output detected voltages and, in dash line, the corrected detected signals for the first phase state E_1. Table 6.9 summarises the sensitivity values that correspond with the slope of the traces in Fig. 6.38 in both cases, original and corrected signals. The sensitivity values are independent of the offset correction. The sensitivity for the maximum signal (V_{o4}) of the phase state E_1 is 66 mV/K.

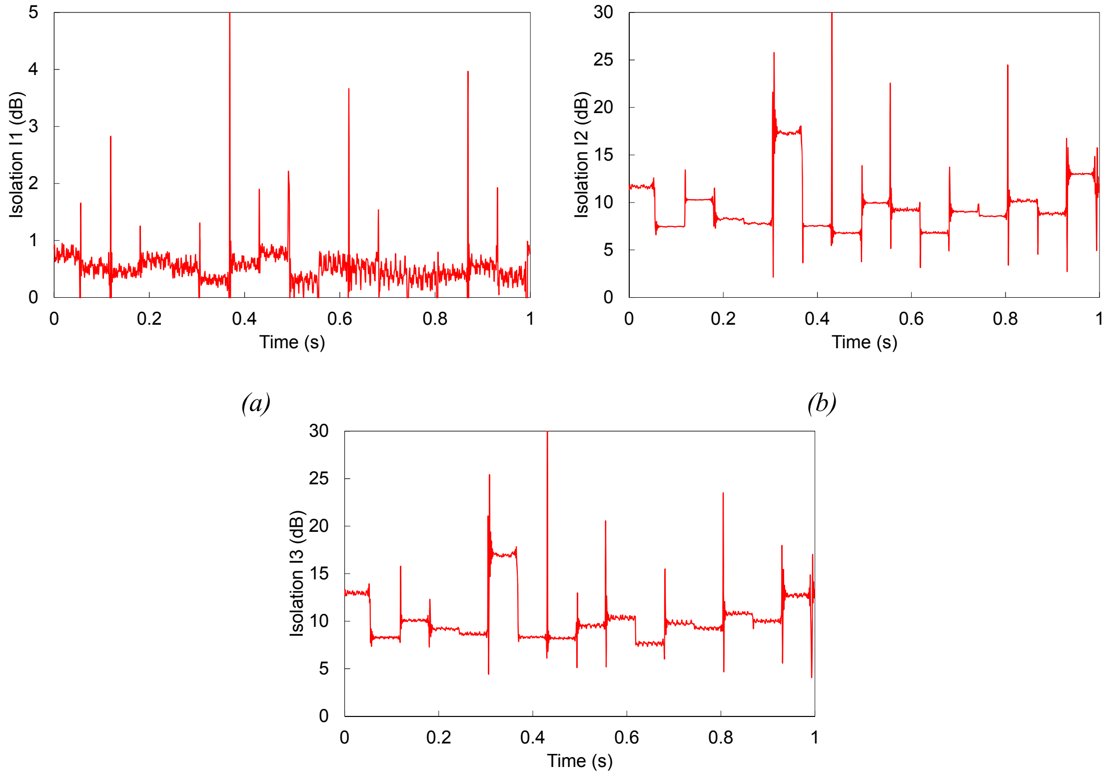

(a)

(b)

(c)

Fig. 6.37. Isolation after detected signal correction for 88 K input load temperature. (a) I_1, maximum with minimum output voltages. (b) I_2, maximum and minimum with medium output voltages. (c) I_3, between medium voltages.

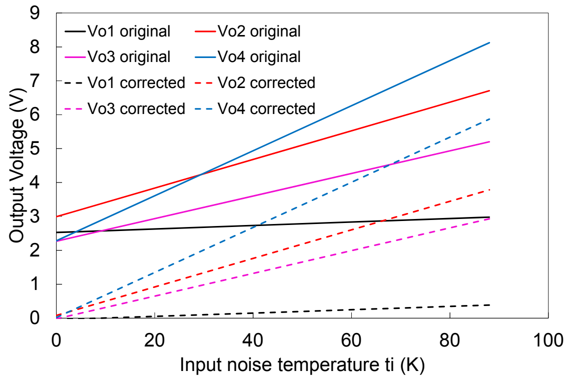

Fig. 6.38. Output detected voltages foe E_1 phase switch state versus input load temperature. $V_{o4} = V_{max}$. $V_{o1} = V_{min}$. V_{o2}, $V_{o3} = V_{med}$.

Table 6.9. Sensitivity values for the detected signals of the FGI receiver.

Output signal	**Sensitivity (mV/K)**
V_{o1}	5
V_{o2}	42
V_{o3}	33
V_{o4}	66

6.5.3.1. Low-frequency spectrum

Two different long time measurements were performed to extract the low-frequency spectrum of the detected signals. Each measurement was 5 minutes long with a sample rate of 3200 samples per second. The sample rate fixes the maximum frequency in the spectrum, it means 1600 Hz because the sample rate is twice these frequency [6.8]. The duration of the measurement sets the lowest frequency in the spectrum (1/5minutes = 3.3 mHz).

6.5.3.1.1. No switching

Applying the Fast Fourier Transform (FFT) to the detected output signal for an input load temperature of 88 K, the low-frequency spectrum is obtained (Fig. 6.39). The f_{knee} of the receiver without switching is around 10 Hz.

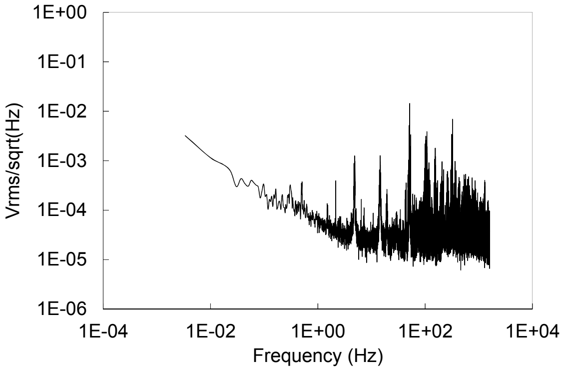

Fig. 6.39. Low-frequency spectrum of V_{max} when the receiver works without switching in a phase state E_7 for T_i=88 K.

The DC voltage (V_{signal}) for the maximum output detected signal is,

$$V_{signal} = A \cdot \left(\frac{T_{sys}}{2} + \frac{\Delta T}{2}\right) \tag{6.46}$$

where A is defined in (6.34), T_{sys} the equivalent noise of the system, and ΔT is the temperature variation. The DC power signal derived from (6.46) is,

$$P_{signal} = \left[A \cdot \left(\frac{T_{sys}}{2} + \frac{\Delta T}{2}\right)\right]^2 \tag{6.47}$$

The AC Noise Power Spectral Density (S_n) in the same output is defined by,

$$S_n = 2 \cdot \left[A \cdot \left(\frac{T_{sys}}{2} + \frac{\Delta T}{2}\right)\right]^2 \cdot \frac{1}{B_{eff}} \tag{6.48}$$

The AC Noise Power signal in the low-frequency bandwidth derived from (6.48) is,

$$P_n = 2 \cdot \left[A \cdot \left(\frac{T_{sys}}{2} + \frac{\Delta T}{2}\right)\right]^2 \cdot \frac{B_{LF}}{B_{eff}} \tag{6.49}$$

where B_{LF} is the equivalent noise bandwidth of the low-pass filter in the detection section. The minimum detectable signal ΔT_{min} can be calculated when the signal power is equal to the noise power. It means the term of ΔT in equation (6.47) is equal to the terms of T_{sys} in equation (6.49) resulting (6.50),

$$\left(A \cdot \frac{\Delta T}{2}\right)^2 = 2 \cdot \left(A \cdot \frac{T_{sys}}{2}\right)^2 \cdot \frac{B_{LF}}{B_{eff}} \tag{6.50}$$

Solving (6.50) for ΔT and considering $B_{LF} = 1/2\tau$ with τ the equivalent time integration results in (6.51),

$$\Delta T_{min} = \frac{T_{sys}}{\sqrt{B_{eff} \cdot \tau}} \tag{6.51}$$

Considering the DC voltage, V_{DC}, of the output signal and the white noise level ΔV ($V_{RMS}/\sqrt{Hz}$) in the low-frequency spectrum, the equality in (6.51) can be written to calculate the effective bandwidth of the receiver, B_{eff}.

$$\frac{\Delta T_{min}}{T_{sys}} = \frac{\Delta V}{V_{DC}} = \frac{1}{\sqrt{B_{eff} \cdot \tau}} \tag{6.52}$$

If the integration time, τ, is ½ [6.7], then B_{eff} can be rewritten as follows,

$$B_{eff} = 2 \cdot \frac{V_{DC}^2}{\Delta V^2} \tag{6.53}$$

Taking the maximum signal for the measurement of 88 K input load and the phase switch state E_7 in the no switching operation mode of the receiver, V_{DC} is 4.7 V and ΔV is 6e-5 $V_{RMS}/\sqrt{Hz}$. B_{eff} results 12.3 GHz. The effective bandwidth of the whole receiver is lower than the obtained for the gain modules, B_{eff} (6.30), because the combination of return loss, the insertion loss and bandwidth of the phase switches and correlation modules.

The minimum detectable temperature variation, ΔT_{min}, defined by (6.50) has a value of 1.57 mK when the radiometer without switching for a input load temperature of 88 K. In the case of the radiometer measuring the sky at 50 GHz, the input noise temperature will be 15 K and the ΔT_{min} is 643 μK.

6.5.3.1.2. Switching operation

When the radiometer is used switching the phase states, the values of each state appears every 1/16 seconds (16 different states per second). For an acquisition of 5 minutes, the overall time of each state is 5/16 minutes, it means 18.75 seconds of the total measurement time. So the minimum frequency in the spectrum is 53 mHz (1/18.75).

In order to obtain the low-frequency spectrum, the slot time of each state every 1/16 seconds is accumulated in a unique time series. So the detected signal is composed of 16 time series corresponding to the 16 phase states, each time series with the four detected voltages. The complementary state of the phase state E_7 (that one measured when no switching) is the one in which there is a 180° phase change. In this case the phase state E_6 is the complementary to E_7. A time series (*TS*) with these two phase states is built as follows,

$$TS = (V_{min}|_{E7} + V_{max}|_{E6}) - (V_{min}|_{E6} + V_{max}|_{E7}) \qquad (6.54)$$

The resultant spectrum of *TS* is shown in Fig. 6.40. The f_{knee} of the receiver with phase switching decreases to around 2 Hz approximately. The f_{knee} improvement is due to the cancellation of gain fluctuation coming from the correlation and detection module, the subsystem subsequent to the phase switches module. The f_{knee} change, when switching the phases, is not very noticeable because the major contribution to the correlated noise comes from the amplifiers in front of the switching module. And this contribution cannot be removed.

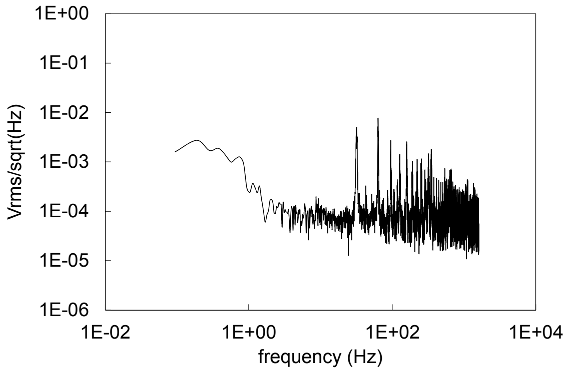

Fig. 6.40. Low-frequency spectrum of TS (6.54) when the receiver works switching the phase states.

The equivalent noise temperature, T_e, and the equivalent bandwidth, B_{eff}, are unique for the receiver. So the minimum temperature variation, ΔT_{min}, is the same when switching the phase states.

6.6. Conclusions

In this chapter, the characterization of the radio astronomy receiver has been performed. All the components involved in the module have been briefly presented. The characterization starts with a mathematical and theoretical analysis of the expected output signals. Then, all the components has been assembled in a test-bench in order to test the behaviour of the receiver, validating it as a radiometer polarimeter aimed for radio astronomy applications measuri

6.7. References

[6.1] www.epi-consolider.es/

[6.2] E. Villa, J. Cagigas, B. Aja, L. de la Fuente, and E. Artal, “Q-band 4-state phase shifter in planar technology: Circuit design and performance analysis”, Review of Scientific Instruments **87**, 094705 (2016); doi:10.1063/1.4963322

[6.3] A. R. Perez, J. L. Cano, E. Villa, A. Mediavilla, E. Artal, “Módulo de Correlación y Detección de Banda Ancha y Banda Q en Guía de Onda”, XXIX Simposium Nacional de la Unión Científica Internacional de Radio, URSI 2014, Valencia, 3-6 Septiembre, 2014.

[6.4] E. Villa, B. Aja, L. de la Fuente, E. Artal, “Detector basado en diodo Schottky en la banda de 35 a 47 GHz”, XXVII Simposium Nacional de la Unión Científica Internacional de Radio, URSI 2012, Elche, 12-14 Septiembre, 2012.

[6.5] Juan L. Cano, Enrique Villa, José V. Terán, Ana R. Perez, Luisa de la Fuente, Angel Mediavilla, Eduardo Artal, “Módulo Posterior para la Integración de Polarímetros Multi-Pixel a 40 GHz en Radioastronomía”, Simposium Nacional de la Unión Científica Internacional de Radio, URSI 2016, Madrid, 5-7 Septiembre, 2016.

[6.6] E. Maxwell and B. J. Leon, “Absolute Measurement of Receiver Noise Figure at UHF”, IRE Transactions on Microwave Theory and Techniques, vol. 4, no.2, April 1986, pp. 81-85

[6.7] M. E. Tiuri, “Radio Astronomy Receivers”, IEEE Transactions on Military Electronics, July-October 1964, pp. 264-272

[6.8] A. Bruce Carlson, Communication Systems, McGraw Hill International Editions, 3rd ed., 1986

CHAPTER VII: RADIOMETER AT W-BAND

7.1. Introduction

In W-band there are mainly two areas of interest for the radiometric systems: one is scientific, including Earth's observations, radio astronomy [7.1]-[7.2] and the spectroscopy; the other is security applications or low visibility conditions through the composition of images in millimetre waves [7.3]. Some experiments in the radio astronomy field pretend to study the Cosmic Microwave Background (CMB), in which the foregrounds (unwanted signals) contaminate the CMB radiation. The W-band frequency band, 75-110 GHz, offers a terrestrial observation window in which some of the foregrounds are highly attenuated.

The RF filter plays an important role in radio astronomy receivers in which the incoming signal is converted to intermediate frequency. First, the filter should be broadband to keep a high sensitivity in the receiver, and second because there should have a high image band rejection in relation to the frequency band of interest to avoid unwanted signals and its noise contribution.

Traditionally, the technologies used to realise microwave filters have been based on planar microstrip lines or rectangular waveguides. Even though, broadband filters can be implemented with microstrip lines achieving high image band rejection levels, the transmission losses increase quickly with frequency. On the other hand, the rectangular waveguide presents very low losses with high frequency selectivity, and high image band rejection values can be achieved outside the frequency band of interest. Another issue is the manufacturing, at high frequencies the dimensions of microstrip lines are too small and its implementation is not easy. However, the machining of a rectangular waveguide is more accurate and easy to manufacture.

In this chapter, the design and characterisation of a W-band (81-99 GHz) filter with high image band (57-75 GHz) rejection is detailed [7.4]. The filter will be introduced in the scheme of a W-band receiver aimed for radio astronomy applications [7.5]. The characterisation of the receiver as a total power and Dicke radiometer will be useful to evaluate the feasibility of the proposed scheme [7.6].

7.2. Radiometer sensitivity principles

The very low-noise receivers used in radio astronomy are radiometers which require high stability and sensitivity. They can measure the electromagnetic emission of a body, differentiating low power signal levels [7.7]-[7.9]. The sensitivity of the radiometer is set by the temperature of the lowest detected source, which is mainly determined by the noise fluctuations at the output of the receiver. For a thermal noise source, special techniques are implemented to reduce noise and gain fluctuations produced in itself circuits of the receiver. So they are distinguished from the interest signals.

A total power radiometer provides an average voltage value proportional to a square-law detector, and in turn proportional to the noise power of the receiver including the antenna.

The radiometric sensitivity in terms of temperature (7.1), ΔT (Kelvin), or the minimum detectable temperature change in the antenna (T_A) at the output of the radiometer depends on the thermal noise, on the radio frequency effective bandwidth (B, Hz), and on the noise equivalent bandwidth of the low pass filter or integrator circuit (B_{LF}) with an integration time constant τ (seconds),

$$\Delta T = \frac{T_{sys}}{\sqrt{B \cdot \tau}} \tag{7.1}$$

$$\tau = \frac{1}{2 \cdot B_{LF}} \tag{7.2}$$

where T_{sys} is the noise temperature of the whole radiometer. This sensitivity is degraded due to gain and noise fluctuations of the receiver. Dicke receiver configuration, or synchronous detection [7.10], avoids the decrease of sensitivity due to this fluctuations. It is based on commuting periodically between the power received in the antenna and a reference temperature. Since the interest signal is received half time of the period, the sensitivity is half the one obtained in a total power radiometer,

$$\Delta T = \frac{2 \cdot T_{sys}}{\sqrt{B \cdot \tau}} \tag{7.3}$$

7.3. Goals of the designed filter

The waveguide filter belongs to the RADOM project, in which a radiometer polarimeter working in the 81-99 GHz frequency band is developed. RADOM continues the QUIJOTE project main goal, the study of the polarisation of the CMB. The 90 GHz observation window completes the frequency bands of QUIJOTE, 10, 20, 30, and 40 GHz instruments (see Fig. 7.1).

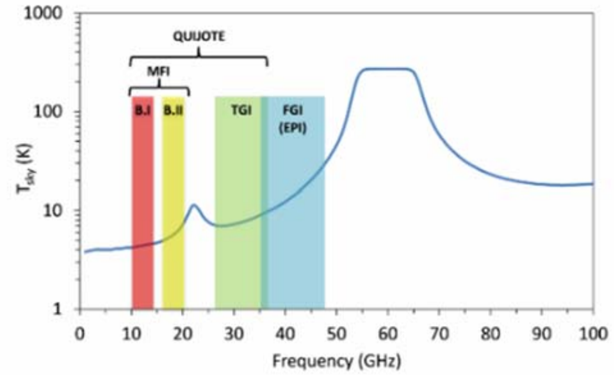

Fig. 7.1. Sky temperature versus frequency.

In rough outlines, the radiometer down-convert the input RF signal (81-99 GHz) to an intermediate frequency (IF) of 3-21 GHz (Fig. 7.2). This IF signal is detected at the end. The RF filter placed at the input of the sub-harmonic mixer confines de RF signal and minimizes the image bands that introduce noise. The minimum image rejection at the end of the image band, 75 GHz, should be higher than 30 dB versus the frequency band of interest.

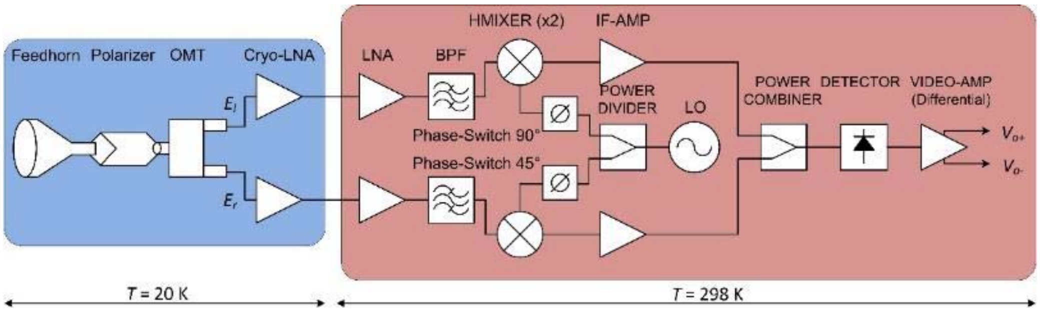

Fig. 7.2. RADOM scheme.

7.4. Filter implementation

The design process of the filter is divided into three steps: first the design equations are applied, then an adjustment and, finally the manufacture.

7.4.1. Filter design

The design starts from the equivalent low-pass prototype [7.11]. The relative bandwidth is calculated from (7.4),

$$W = \frac{f_2 - f_1}{f_0} = \frac{f_2 - f_1}{\sqrt{f_2 \cdot f_1}} \tag{7.4}$$

where f_2=99 GHz, and f_1=81 GHz. Central frequency, f_0, results 89.55 GHz, and the relative bandwidth is W=20.1 %.

Next step is the frequency translation from low-pass to band-pass [7.11]. Based on the rejection frequency, f_a=75 GHz, the normalised frequency is calculated as follows,

$$\omega_a' = \frac{1}{W} \cdot \left(\frac{f_a}{f_0} - \frac{f_0}{f_a}\right) = -1.77 \tag{7.5}$$

To obtain the Chebyshev filter order, expression (7.5) is rewritten as (7.6),

$$|\omega_a'| - 1 = 0.77 \tag{7.6}$$

A filter order of n=5 is obtained from Chebyshev plots with a ripple in band of ℓ_{ar}=0.5 dB [7.11]. The coefficients of the filter are collected in Table 7.1:

Table 7.1. Coefficients of a Chebyshev filter with order n=5.

g_0=g_6=1	g_2=g_4=1.2296
g_1=g_5=1.7058	g_3=2.5408

Right after, the impedance inverters [7.12] are calculated as,

$$\overline{K_{01}} = \sqrt{\frac{\pi \cdot W}{2 \cdot g_1}} \tag{7.7}$$

$$\overline{K_{J,J+1}} = \frac{\pi \cdot W}{2 \cdot \sqrt{g_j \cdot g_{j+1}}} \quad j \neq 0 \tag{7.8}$$

$$\left|\overline{B_{J,J+1}}\right| = \frac{1 - \overline{K_{J,J+1}}^2}{\overline{K_{J,J+1}}} \tag{7.9}$$

The dimensions of resonant cavities of the waveguide filter (see Fig. 7.3) are calculated from the values of B (7.9). The rectangular waveguide standard used is the

WR-10, with 2.54 mm of width and 1.27 mm of height (half width). The diaphragm apertures d [7.13] are given by,

$$d = \frac{2\cdot a}{\pi}\cdot tg^{-1}\left(\sqrt{\frac{\lambda_g}{|\bar{B}|\cdot a}}\right) \tag{7.10}$$

$$\lambda_g = \frac{\lambda_0}{\sqrt{1-\left(\frac{\lambda_0}{2\cdot a}\right)^2}} = 4.456\,mm \tag{7.11}$$

$$\lambda_0 = \frac{300}{f_0\ (GHz)} = 3.35\,mm \tag{7.12}$$

Finally, the electrical lengths of the resonant cavities ℓ [7.14] are defined as,

$$\Phi_j = \pi + \frac{1}{2}\cdot\left(tan^{-1}\left(\frac{2}{\bar{B}_{j-1,j}}\right) + tan^{-1}\left(\frac{2}{\bar{B}_{j,j+1}}\right)\right) \tag{7.13}$$

$$\ell = \frac{\lambda_g}{2\cdot\pi}\cdot\Phi_j \tag{7.14}$$

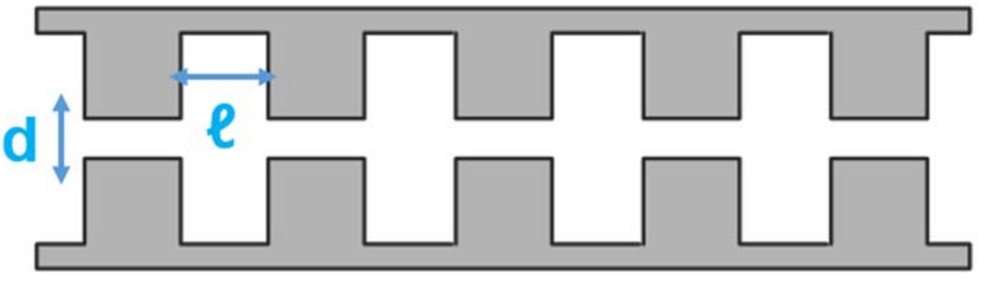

Fig. 7.3. Scheme of resonant cavities of the H-plane waveguide filter.

All the dimensions of the waveguide filter (d and ℓ) and the necessary intermediate values of the calculus (K and B) are listed in Table 7.2.

Table 7.2. Dimensions in mm $^{(*)}$ of the waveguide filter with order n=5.

K_{01}=0.43	B_{01}=1.895	$d_{01}=d_{56}=1.239^{(*)}$	$\ell_1=\ell_5=1.789^{(*)}$
K_{12}=0.218	B_{12}=4.369	$d_{12}=d_{45}=0.913^{(*)}$	$\ell_2=\ell_4=1.95^{(*)}$
K_{23}=0.179	B_{23}=5.408	$d_{23}=d_{34}=0.837^{(*)}$	$\ell_3=1.977^{(*)}$

The filter is simulated with the electromagnetic 3D tool CST [7.15] considering a diaphragm thickness, T, of 0.025 mm (Fig. 7.4). The central frequency results f_0=90.2 GHz and the relative bandwidth W=9.8 % (Fig. 7.5(a)). In fact, the laminates of the diaphragms cannot be so thin. So the thickness is increase to T=0.5 mm and the filter is re-simulated. In this case, the central frequency is f_0=90.9 GHz and the bandwidth W=1.98 % (Fig. 7.5(b)).

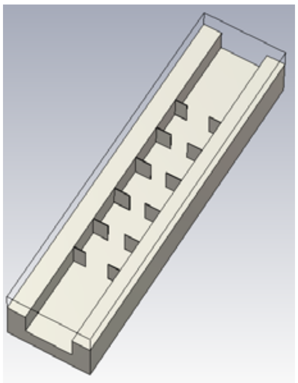

Fig. 7.4. Artist view of the fifth order waveguide filter with 0.025 mm diaphragm thickness.

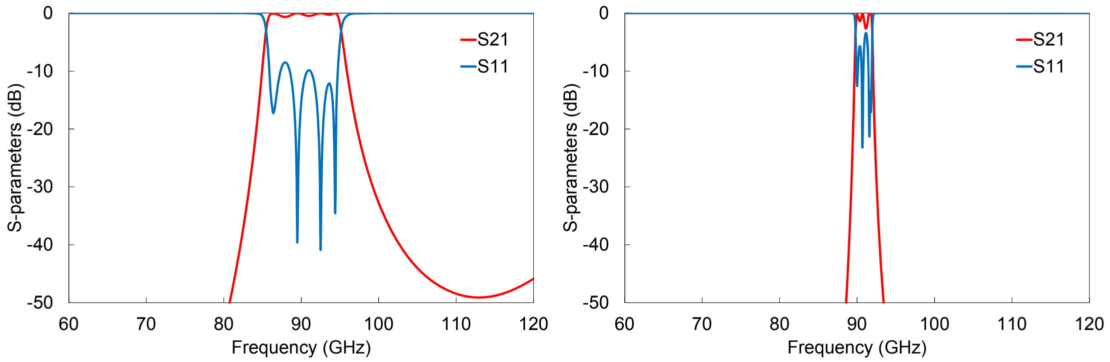

(a) *(b)*

Fig. 7.5. Scattering parameters performance simulation of the fifth order waveguide filter. In red, S_{21}; in blue, S_{11}. With (a) 0.025 mm and (b) 0.5 mm diaphragm thickness.

The achieved bandwidth is extremely poor so the bandwidth goal of the filter is widened in a range of ±10 GHz. Then, f_1=71 GHz, f_2=109 GHz. According to (7.4), f_0=87.97 GHz, and W=43.2 %. Now the rejection image frequency downs to f_a=65 GHz, and applying the transformation in (7.5)-(7.6) the filter order is n=7. The new coefficients are summarised in Table 7.3. Meanwhile, the Table 7.4 show the new dimensions of the filter (Fig. 7.6).

Table 7.3. Coefficients of a Chebyshev filter with order n=7.

$g_0=g_7=1.7372$	$g_3=g_5=2.6381$
$g_2=g_6=1.2583$	$g_4=1.3444$

Table 7.4. Dimensions of the waveguide filter with order n=7, in mm (*).

$K_{01}=0.625$	$B_{01}=0.975$	$d_{01}=d_{78}=1.516$ (*)	$\ell_1=\ell_7=1.576$ (*)
$K_{12}=0.459$	$B_{12}=1.720$	$d_{12}=d_{67}=1.191$ (*)	$\ell_2=\ell_6=1.724$ (*)
$K_{23}=0.372$	$B_{23}=2.316$	$d_{23}=d_{56}=1.171$ (*)	$\ell_3=\ell_5=1.786$ (*)
$K_{34}=0.360$	$B_{34}=2.418$	$d_{34}=d_{45}=1.154$ (*)	$\ell_4=1.794$ (*)

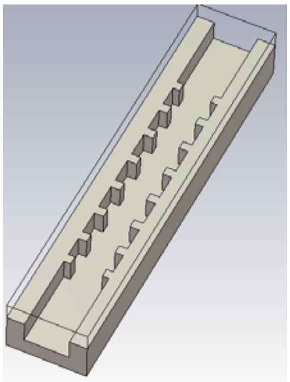

Fig. 7.6. Artist view of the seventh order waveguide filter with 0.5 mm diaphragm thickness.

The electromagnetic simulation of the filter with a thickness of 0.025 mm (Fig. 7.7(a)) results in f_0=89.7 GHz (f_1=80.3 and f_2=100.3 GHz) and W=22.3 %. With 0.5 mm of thickness, the simulation (Fig. 7.7(b)) achieves f_0=90.1 GHz (f_1=86.4 and f_2=94 GHz) and W=8.4 %. Due to manufacture considerations the diaphragm laminates are fixed to 0.5 mm and the final order of the filter is n=7.

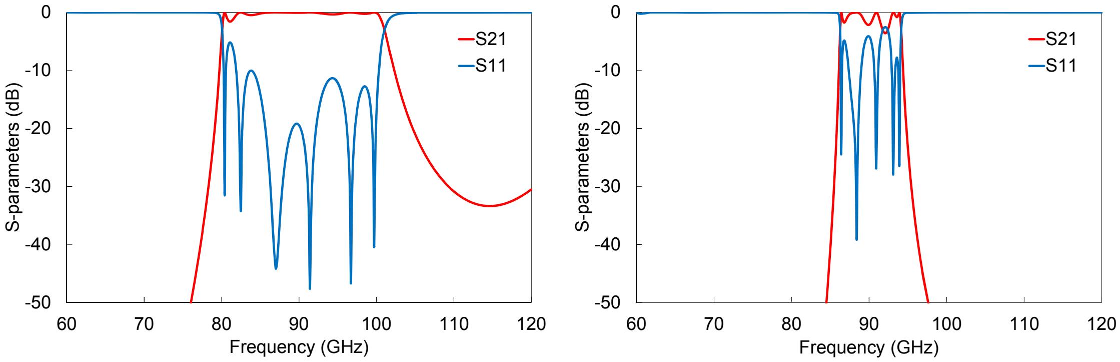

(a) *(b)*

Fig. 7.7. Simulated Scattering parameters performance of the seventh order waveguide filter. In red, S_{21}; in blue, S_{11}. With (a) 0.025 mm and (b) 0.5 mm diaphragm thickness.

7.4.2. Adjustment

It is necessary to adjust the diaphragm apertures (d) and resonator lengths (ℓ) in order to increase the bandwidth. The diaphragm thickness is kept to 0.5 mm. This adjustment is done through the Scattering parameters performance, the Scattering parameters [7.14].

First each diaphragm aperture (Fig. 7.8) is adjusted matching the Scattering parameters performance (7.15)-(7.16) to the theoretical response at the central frequency of 90 GHz.

$$|S_{11}|^2 = \frac{|\bar{B}|^2}{4+|\bar{B}|^2} \tag{7.15}$$

$$|S_{21}|^2 = \frac{4}{4 + |\bar{B}|^2} \tag{7.16}$$

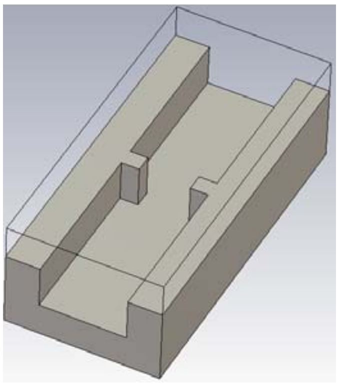

Fig. 7.8. Basic diaphragm cell of the W-band waveguide filter.

After the diaphragm adjustment, all the apertures have been increased as shown in Table 7.5.

Table 7.5. Adjusted filter diaphragm apertures for a 0.5 mm thickness.

diaphragm	Design (mm)	Adjustment (mm)
d_{01}=d_{78}	1.516	1.794
d_{12}=d_{67}	1.291	1.605
d_{23}=d_{56}	1.171	1.502
d_{34}=d_{45}	1.154	1.49

The resonators are adjusted following the basic cell in Fig. 7.9, in which two identical diaphragms (previously adjusted) are separated a distance ℓ. For each of the four different resonators, its resonant frequency (f_R) is simulated for a 0.025 thickness. Then, the diaphragm thickness is set to 0.5 mm and cavity length, ℓ, is tuned to equal the resonant frequency in both thickness cases.

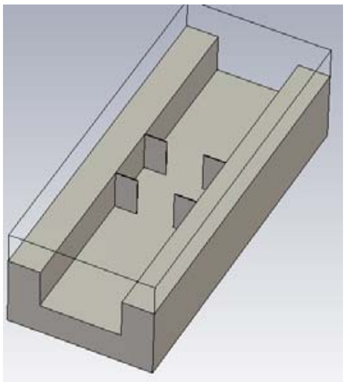

Fig. 7.9. Basic resonant cavity of the W-band waveguide filter.

The new ℓ values for the resonant cavities and the associated resonant frequency are summarised in Table 7.6. The distances have been reduced in opposition to the increase of the apertures.

Table 7.6. Adjusted filter resonant cavity lengths for a 0.5 mm thickness.

cavity	f_R (GHz)	Design (mm)	Adjustment (mm)
$\ell_1=\ell_7$	85.1	1.576	1.191
$\ell_2=\ell_6$	86.3	1.724	1.378
$\ell_3=\ell_5$	87.5	1.786	1.465
ℓ_4	87.7	1.794	1.468

The simulation of the filter (Fig. 7.10) after the adjustments for a 0.5 mm diaphragm thickness results in f_0=89.3 GHz (f_1=80.3 and f_2=99.2 GHz) and W=21.2 %.

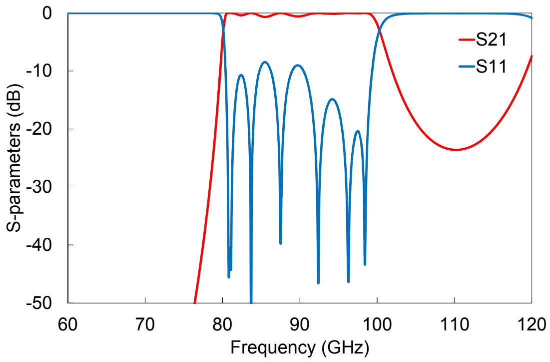

Fig. 7.10. Simulated Scattering parameters performance of the seventh order waveguide filter after the adjustment. In red, S_{21}; in blue, S_{11}.

7.4.3. Manufacture considerations

Mechanical considerations have to be taken into account besides the diaphragm thickness. The filter mechanic is done with a 1 mm bit. So, the diaphragm laminate corners will be round and the dimensions of the filter are re-optimized (Fig. 7.11).

This optimisation is performed with MICIAN tool [7.16]. The goal of 20 dB return losses in the frequency band of interest is included in the optimisation due to previous simulations only achieved 10 dB, and it is not enough because the filter will be connected to a LNA, whose output return losses are also 10 dB. New dimensions show diaphragms more opened (d increases) and smaller cavities (ℓ decreases). In Table 7.7 all the dimensions of the final W-band waveguide filter are summarised.

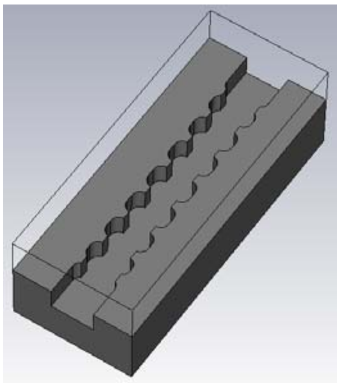

Fig. 7.11. Artist view of the final W-band waveguide filter.

Table 7.7. Dimensions of the final designed waveguide filter. All dimensions in mm.

d_{01}=d_{78}=1.974	ℓ_1= ℓ_7=1.128
d_{12}=d_{67}=1.651	ℓ_2= ℓ_6=1.327
d_{23}=d_{56}=1.543	ℓ_3= ℓ_5=1.423
d_{34}=d_{45}=1.509	ℓ_4=1.448

The last simulation in CST achieves the next results: f_0=90.1 GHz (f_1=81 GHz and f_2=100.3 GHz) and W=21.4 %. Return losses are better than 20 dB in the frequency band of interest, and the image rejection is better than 50 dB at 75 GHz (Fig. 7.12).

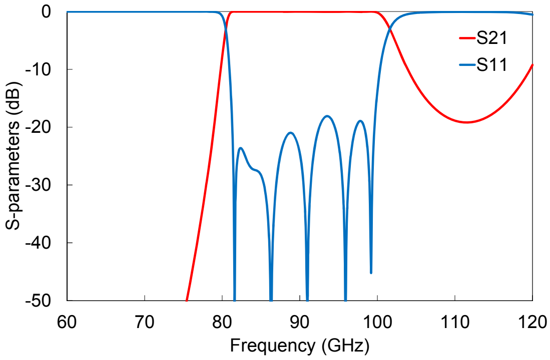

Fig. 7.12. Simulated Scattering parameters performance of the final W-band waveguide filter. In red, S_{21}; in blue, S_{11}.

7.5. Filter characterisation

Once the design is validated, the waveguide filter is fabricated. Two units have been manufactured in Aluminium 6082. Some meetings with the mechanic team were necessary in order to have the lowest tolerance with the design specifications; note that a 50 µm shift in a dimension implies a frequency shift of 500 MHz (Fig. 7.13-7.14).

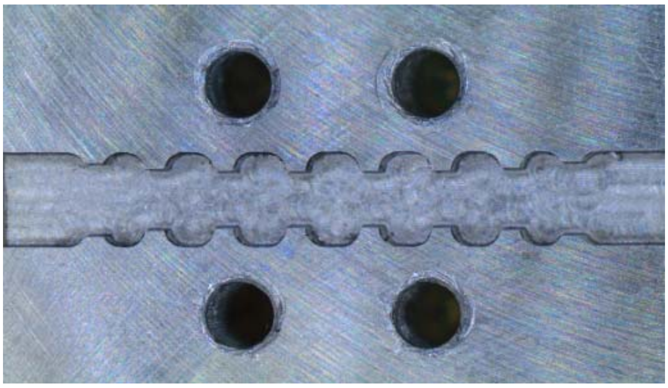

Fig. 7.13. Internal photo of the manufactured waveguide filter.

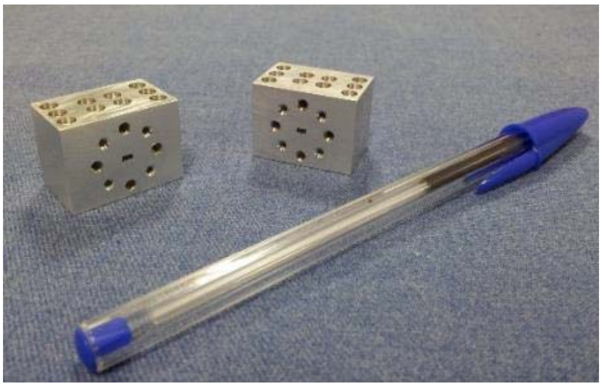

Fig. 7.14. Photo of the two waveguide filter units manufactured.

The Scattering parameters characterisation is performed in the network analyser PNA-X N5242A from Keysight Technologies (Fig. 7.15). There is also a controller (N5261A from Keysight Technologies) to master the conversion heads up to W-band. These mixer heads are from OML, Inc, and multiply the local oscillator signal (OL) by 8, and the radio frequency signal (RF) by 6. The measurement process starts with a RF power calibration, then a Scattering TRL (thru-reflect-line) calibration in the 75-100 GHz frequency band. Next the Scattering parameters measurement is done with an input power of -5 dBm.

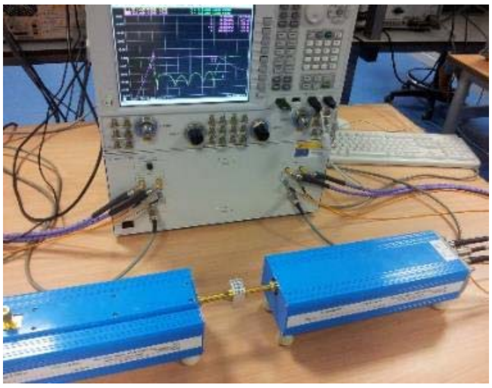

Fig. 7.15. W-band set-up to measure the waveguide filter.

The bandpass frequency measurements obtained for the two filters are collected in Table 7.8. The bandwidth achieved in both units is *W*=21 %.

Table 7.8. Frequency measurements for the two waveguide filters manufactured.

Unit	f_1 **(GHz)**	f_2 **(GHz)**	f_0 **(GHz)**	W **(%)**
#01	80.1	99.6	89.3	21.8
#02	80.4	99.1	89.3	20.9

In Fig. 7.16, the Scattering parameters performance for the two waveguide filters manufactured is plotted. The transmission response (red traces in Fig. 7.16) is flat over the whole bandwidth with 0.4 dB of insertion losses. The estimated losses were 0.1 dB but the simulation does not take into account the roughness of the material (Aluminium) and the variation of the electrical conductivity with frequency. The image rejection is 40 dB at 75 GHz and the return losses are better than 20 dB.

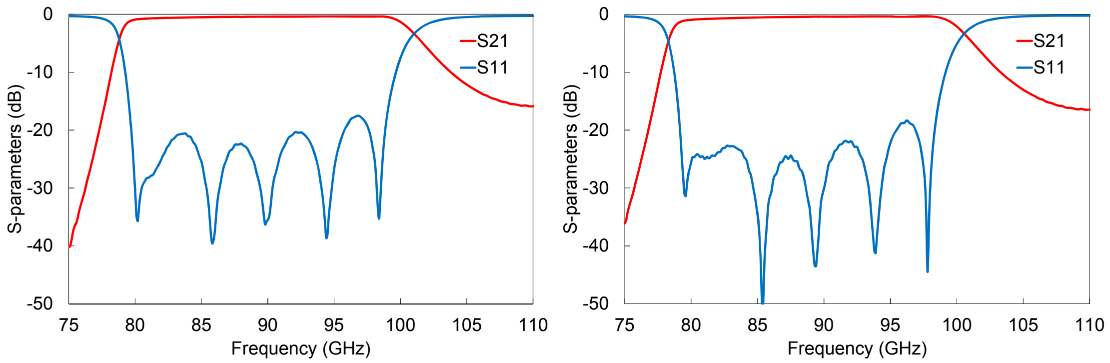

(a) *(b)*

Fig. 7.16. Measured Scattering parameters performance of the two W-band waveguide filters. In red, S_{21}; in blue, S_{11}. (a) Unit #01. (b) Unit #02.

7.6. W-band radiometer scheme

The total power radiometer developed is divided into three parts: a RF section with amplification in W-band, an intermediate frequency (IF) section, and at the end a square-law detector. A scheme of the block diagram of the radiometer is presented in Fig. 7.17.

The gain stage is formed by two low-noise amplifiers interconnected with a low-losses isolator. Then the signal is filtered with the band-pass waveguide filter previously designed in this chapter, and converted to IF using a sub-harmonic mixer. The IF signal is amplified with a broadband amplifier and detected in DC with a square-law detector. Next lines describe each subsystem of the radiometer.

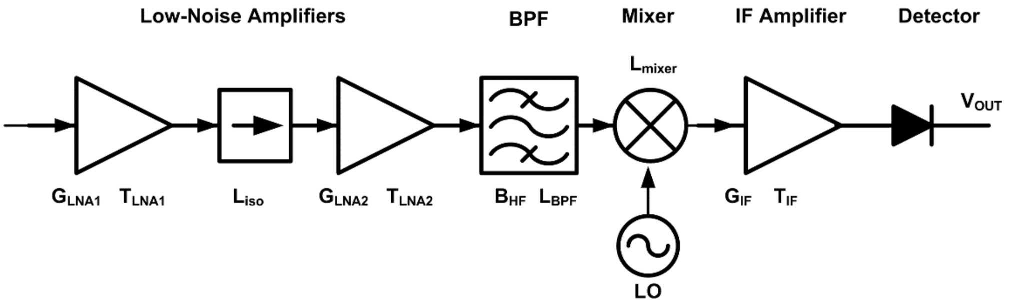

Fig. 7.17. Scheme of the W-band radiometer.

7.6.1. W-band low-noise amplifiers

The low-noise amplifiers (LNA) used in W-band are commercial monolithic circuits (MMIC) mounted in dedicated chassis with transitions from microstrip to WR-10 waveguide.

First amplifier is from OMMIC foundry (France), reference CGY2190UH/C2 (Fig. 7.18). It is a MMIC in 70 nm metamorphic technology (mHEMT). Mounted in the chassis, it achieves more than 25 dB in the 75-110 GHz frequency band, and a noise figure of 3.5 dB. The bias point is V_{d1}=1.2 V, I_{d1}=8.5 mA, V_{d2}=1.4 V and I_{d2}=21 mA. See red trace in Fig. 7.20.

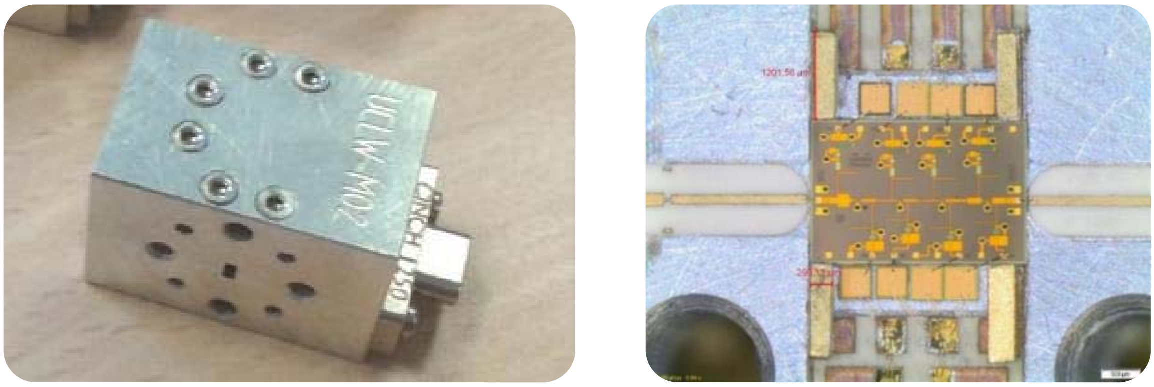

Fig. 7.18. MMIC LNA CGY2190UH/C2 from OMMIC foundry mounted in chassis.

Second amplifier is a MMIC LNA from NGC foundry, reference ALP283 (Fig. 7.19). This amplifier is built in 0.1 μm Indium Phosphide (InP) HEMT technology. Mounted in chassis, the gain is greater than 20 dB, and has 5 dB of noise figure in the 75-110 GHz. The bias point is V_d=1.3 V, and I_d=10 mA.

The noise and gain measurement is performed with the noise analyser (NFA8975A from Keysight Technologies) and a mixer QHSW3FBDO from Quinstar.

The IF is set to 100 MHz, and the noise source is the QNSFB12LW reference from Quinstar, with an excess noise ratio (ENR) of 15 dB,

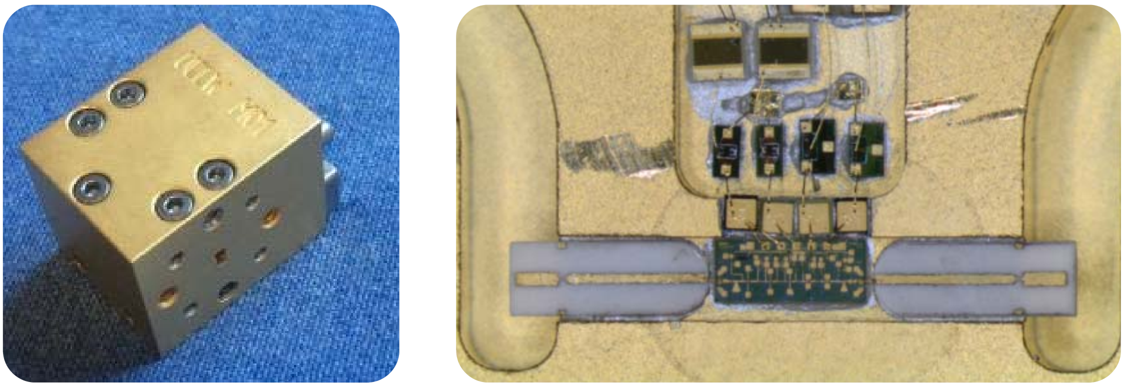

Fig. 7.19. LNA external view and MMIC LNA ALP283 from NGC foundry mounted inside.

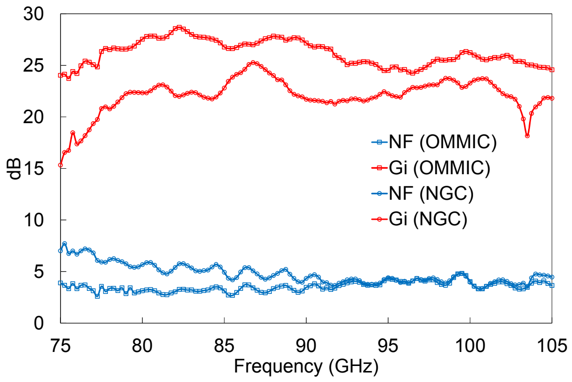

Fig. 7.20. Measured noise figure and associated gain for the two W-band MMIC LNA. In red, CGY2190UH/C2 from OMMIC, V_{d1}=1.2 V, I_{d1}=8.5 mA, V_{d2}=1.4 V and I_{d2}=21 mA; in blue, ALP283 from NGC, V_d=1.3 V, and I_d=10 mA.

The NGC amplifier could not be biased in its minimum noise bias point because instabilities appeared. So the NGC LNA is placed as the second amplifier in the chain due to its higher noise compared with the OMMIC LNA. The two LNA are interconnected by an isolator (WR365A from HP) with 1.5 dB of insertion losses.

7.6.2. W-band band-pass filter

The W-band band-pass filter (*BPF*) used is the one described in this chapter (see 7.4 and 7.5 sections). In particular, unit #01 has been used, which frequency band is 80.1-99.6 GHz (*W*=21.8 %), the insertion losses are 0.4 dB, and the image rejection is 40 dB at 75 GHz.

7.6.3. Sub-harmonic mixer

The mixer chosen to down-convert the RF to IF signal is a sub-harmonic mixer from Quinstar, reference QHSW3FBDO (Fig. 7.21). The mixture is with the third harmonic of the local oscillator (LO), and has low insertion losses. Moreover, it provides a broadband IF because it works with the full W-band (75-110 GHz) RF signal at the input. Since the LO frequency is low, this mixer makes easier the implementation of set-up in laboratory measurements. The RF input is a WR-10 waveguide, meanwhile a diplexer drives the LO input and the IF output.

Fig. 7.21. Sub-harmonic mixer from Quinstar, reference QHSW3FBDO.

The mixer configuration for the radiometer is LO input signal with 27.1 GHz frequency (f_{LO}), and 8 dBm of power (P_{LO}). The insertion losses are 15 dB. The frequency range at the IF output is 0.1-15 GHz. Fig. 7.22 shows the estimated conversion losses of the mixer versus RF frequency, obtained from a gain measurement of the two W-band LNA, the isolator, the BPF, and the mixer, known the gain of amplifiers and losses of the isolator and filter.

The noise contribution of the mixer is smaller in the total noise of the radiometer, because it is placed after the two LNA which have a gain higher than 40 dB.

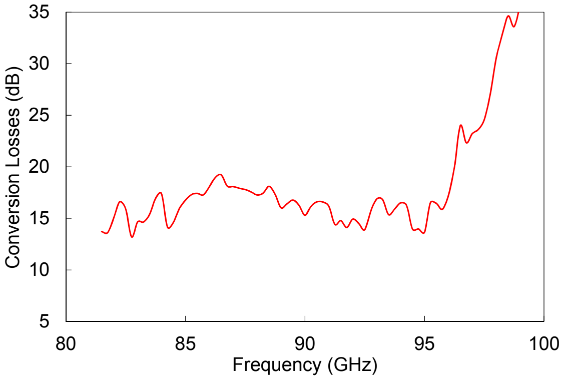

Fig. 7.22. Measured conversion losses pf the sub-harmonic mixer from Quinstar, reference QHSW3FBDO. f_{LO}=27.1 GHz and P_{LO}=8 dBm.

7.6.4. IF amplifier

The IF amplifier is a distributed MMIC from Triquint, reference TGA2513 (Fig. 7.23). It is built in a 0.15 μm pseudomorphic (pHEMT) of Gallium Arsenide (GaAs) technology. The working frequency band goes from 0.5 to 23 GHz with a 15 dB gain and noise figure lower than 4 dB (Fig. 7.24(a)). The 1-dB compression point is always better than 10 dBm (Fig. 7.24(b)). The bias point for this behaviour is V_d=±5 V, and I_d=90 mA.

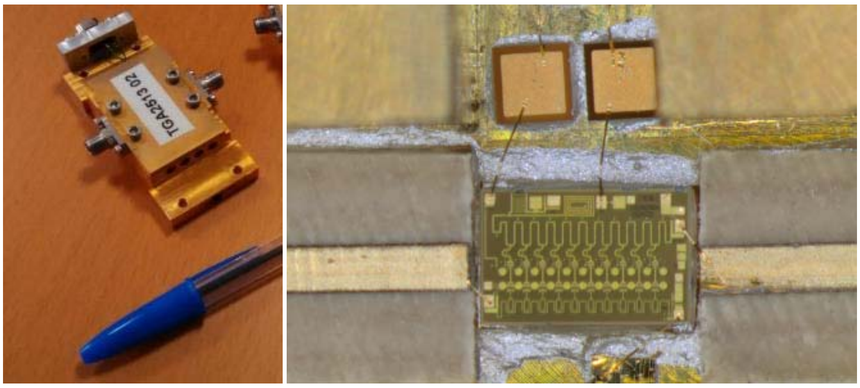

Fig. 7.23. IF amplifier from Triquint, reference TGA2513.

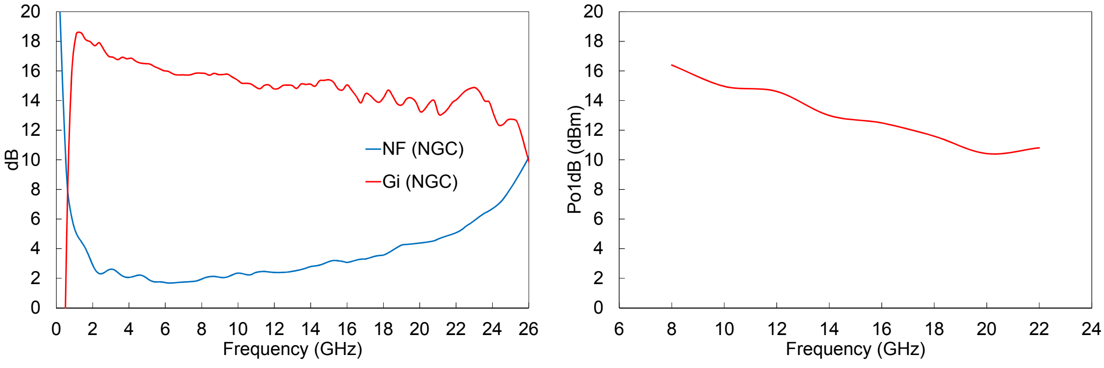

(a) *(b)*

Fig. 7.24. Measured Scattering parameters of the IF amplifier from Triquint, reference TGA2513. (a) Noise and associated gain. (b) 1-dB compression point.

7.6.5. Detector and video amplifier

The square-law detector (Fig. 7.25(a)) is a commercial one from Hewlett Packard, reference HP8474E. It works from 10 MHz to 50 GHz with a 500 mV/mW sensitivity.

The video amplifier is a low-noise pre-amplifier from Standford Research Systems, reference SR560 (Fig. 7.25(b)). It amplifies the DC signal and provides low-pass filtering options.

(a) *(b)*

Fig. 7.25. Photos of the detector and video amplifier. (a) Detector from Hewlett Packard, reference HP8474E. (b) Low-noise pre-amplifier from Standford Research Systems, reference SR560.

7.7. Radiometer characterisation

The complete receiver is characterised in terms of noise and gain from the input of the first W-band amplifier to the IF amplifier output. Measurement is performed with the noise figure analyser NFA8975A calibrating at IF with the noise source HP346B. The noise source QNSFB12LW plus a variable attenuator from Hitachi (W1513) are used in the measurement. The attenuator reduces in 9 dB the ENR of the noise source to avoid compression of the second W-band LNA (NGC LNA). The results for an upper side band measurement are plotted in Fig. 7.26. The average gain in the 82-96 frequency band is 48 dB, and the noise temperature is 425 K (3.9 dB of NF).

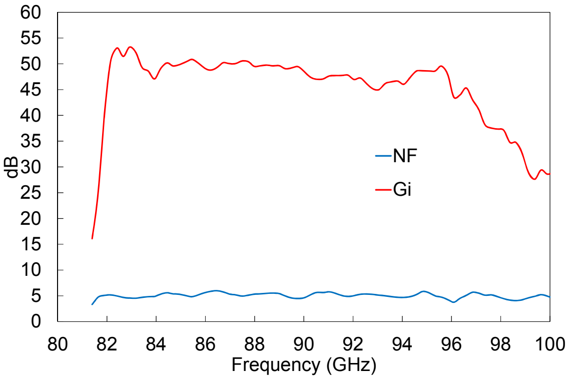

Fig. 7.26. Noise figure and gain performance of the W-band radiometer.

From noise and gain measurements, the effective bandwidth (*B_{HF}*) of the radiometer is calculated as (7.17). The obtained value is 10.7 GHz integrating the 81-99 GHz frequency band.

$$B_{HF} = \frac{\left[\int_0^\infty G^2(f)df\right]^2}{\int_0^\infty G^2(f)df} \tag{7.17}$$

In the case of an ideal radiometer, without any gain fluctuations, the sensitivity can be calculated from (7.1) or (7.3) depending the operation mode. For a 10.7 GHz effective bandwidth, a noise temperature of 425 K and assuming an integration time of 30 ms, the sensitivities obtained are 24 mK and 48 mK, in total power and Dicke operation mode respectively.

Two measurements are performed in order to test the behaviour of the radiometer, one working as a total power radiometer and the other in Dicke configuration. A W-band horn antenna, from Quinstar reference QSH27F20, is connected at the input of the radiometer with 20 dBi of gain. The transmitter is formed by the W-band noise source QNSFB12LW, the attenuator W1513 and other antenna QSH27F20.

7.7.1. Total power radiometer

The radiometer test set-up scheme working in total power configuration is presented in Fig. 7.27. In order to obtained the detected signal, a square-law detector HP8474E and a video amplifier SR560 with 1 dB gain and 0.1 Hz low-pass filter configuration are placed at the output of the radiometer. The DC output voltage is measured with a digital multi-meter from Keysight Technologies reference 34401A. Fig. 7.28 shows the radiometer working as total power operation mode. The distance between horn antennas is 2.7 cm approximately.

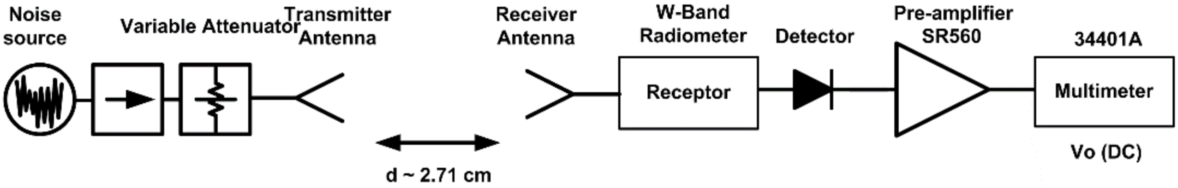

Fig. 7.27. Scheme of the W-band radiometer in Total-Power configuration.

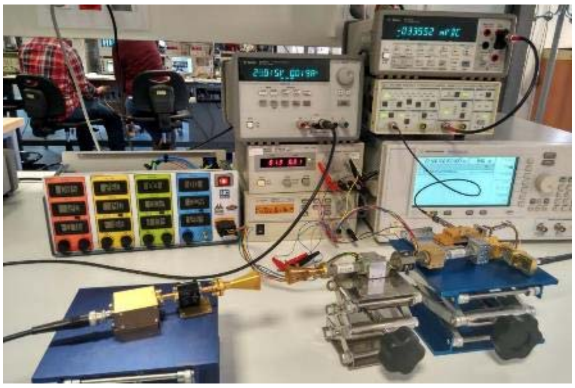

Fig. 7.28. W-band radiometer working in total power configuration.

With the noise source in ON state the input RF power in the radiometer is varied with the variable attenuator. The source ENR is 15 dB and the attenuation goes from 3.5

to 9 dB. Detected signal is proportional to the transmitted noise (T_h) plus the noise temperature of the receiver (T_R) as (7.18),

$$V_O = C_1 \cdot G \cdot k \cdot (T_h + T_R) \cdot B_{HF} \quad (7.18)$$

where C_1 is a constant (mV/mW), G is the receiver gain, k the Boltzmann constant, and B_{HF} the effective bandwidth of the receiver. Fig. 7.29 plots the detected signal versus the equivalent noise temperature for different attenuation levels in the input RF signal.

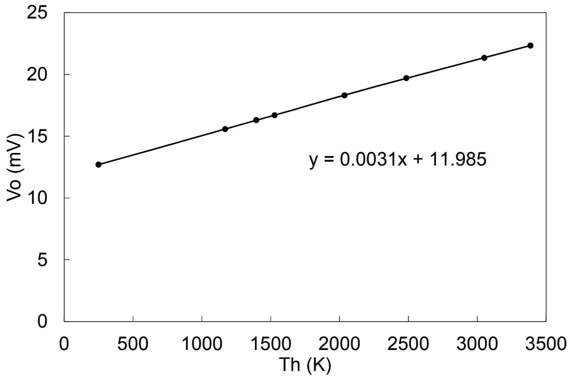

Fig. 7.29. Detected signal V_O (mV) versus the equivalent transmitted noise temperature (T_h (K)) for the total power radiometer configuration.

The lineal equation extracted from measurements has a slope of 3.1 µV/K with 11.98 mV of offset. This offset corresponds to the detected signal when the transmitted noise temperature is equal to ambient temperature of 290 K.

7.7.2. Dicke radiometer

In the Dicke configuration of the radiometer an optical chopper from Standford Research Systems (reference SR540) is placed between the two antennas (see scheme in Fig. 7.30). The chopper (Fig. 7.31) allows a modulation of the input RF signal with a square signal. The frequency of the reference signal of the chopper can be set from 4 Hz to 3.7 kHz, and a value of 120 Hz is chosen to perform the measurements.

The detected signal, after the video amplifier, is introduced in a lock-in amplifier (reference SR830 DSP from Standford Research Systems) synchronised with the chopper through the reference signal (Fig. 7.30). A photo of the measurement set-up when the radiometer works in Dicke configuration is shown in Fig. 7.32.

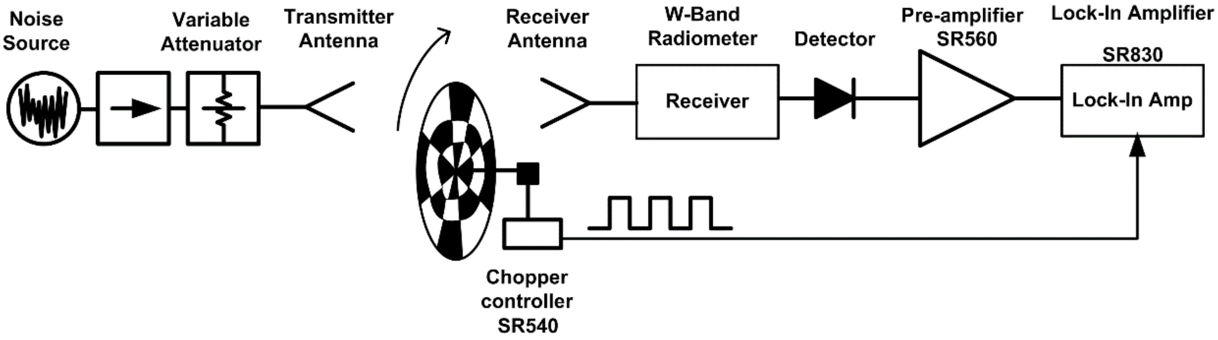

Fig. 7.30. Scheme of the W-band radiometer in Dicke configuration.

Fig. 7.31. Photo of the chopper used to modulate the RF input signal in the Dicke radiometer.

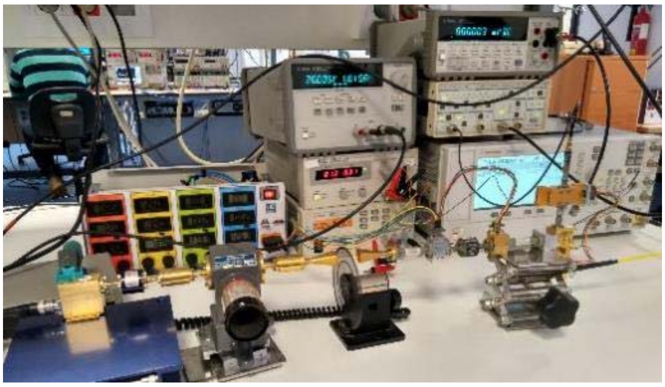

Fig. 7.32. Set-up to characterise the W-band radiometer in Dicke configuration.

So there is a square signal at the output, whose low level is proportional to a black body at room temperature (T_c) measured when the chopper covers the transmitter antenna (7.19). Meanwhile the high level is proportional to the equivalent noise temperature (T_h) of the input signal (7.20).

$$V_c = C_1 \cdot G \cdot k \cdot (T_c + T_R) \cdot B_{HF} \tag{7.19}$$

$$V_h = C_1 \cdot G \cdot k \cdot (T_h + T_R) \cdot B_{HF} \tag{7.20}$$

The lock-in amplifier multiplies the detected signal with chopper reference signal and filters in a way that the noise of the measurement is strongly attenuated. Filter time constant is 300 ms and the parameter R is obtained directly in the lock-in amplifier. R (7.21) is the root mean square (RMS) voltage proportional to the difference of the two levels of the detected signal.

$$R = C_2 \cdot G \cdot (V_h - V_c) \tag{7.21}$$

In Fig. 7.33 the parameter R is plotted versus the equivalent noise temperature for different attenuation levels in the input RF signal. The lineal equation provides a RMS voltage slope of 1.2 μVrms/K with -62.5 μVrms of offset. When T_h is equal to ambient temperature T_c the parameter R results zero because it is the difference between the two temperatures.

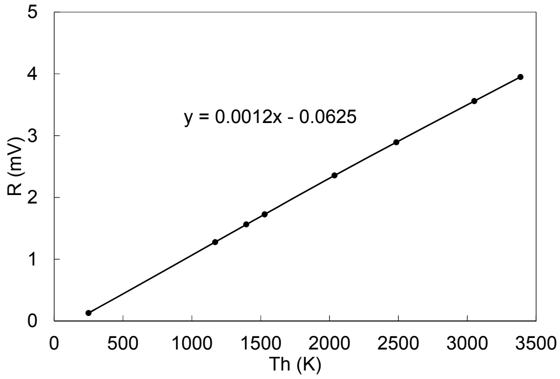

Fig. 7.33. R parameter (mV) versus the equivalent transmitted noise temperature (T_h (K)) for the Dicke radiometer configuration.

7.8. Conclusions

A radiometer composed by commercial subsystems is presented. The performance of the subsystems has been detailed individually. The radiometer has a total gain around 50 dB with a noise figure of 4.5 dB. The effective bandwidth is 10 GHz. Moreover, the behaviour of the radiometer working in total power and Dicke configurations has been demonstrated.

As a part of the radiometer, a W-band waveguide filter with high image rejection aimed to a radiometer for radio astronomy applications has been designed and characterised. A 21 % of bandwidth is achieved in the 80-99 GHz frequency band with 40 dB of image rejection at 75 GHz.

7.9. References

[7.1] M.W. Pospieszalski, et al., “Design and Performance of Wideband, Low-Noise, Millimeter-Wave Amplifiers for Microwave Anisotropy Probe Radiometers”, in IEEE Radio Frequency Integrated Circuits Symposium, Boston, USA, 2000, pp. 217-220.

[7.2] J.M. Lamarre, et. al. “The Planck High Frequency Instrument, a third generation CMB experiment, and a full sky submillimeter survey“, New Astronomy Reviews, Vol. 47, Issues 11-12, pp. 1017-1024, Dec. 2003.

[7.3] L. Yujiri, M. Shoucri, P. Moffa, “Passive millimeter wave imaging,” *IEEE Microwave Magazine*, vol. 4, no. 3, pp. 39-50, sept. 2003.

[7.4] Vicente Terán Collantes, David Vegas, Eduardo Artal, “Filtro en banda W con alto rechazo en banda imagen”, in XXX Simposium Nacional de la Unión Científica Internacional de Radio, Pamplona. Spain, 2015.

[7.5] J.L. Cano, E. Villa, V. Terán, E. González, L. de la Fuente, E. Artal, A. Mediavilla, “Polarímetro en Banda W para Aplicaciones de Radioastronomía: Diseño y Simulación”, in XXX Simposium Nacional de la Unión Científica Internacional de Radio, Pamplona. Spain, 2015.

[7.6] J. Vicente Terán Collantes, Beatriz Aja, Juan L. Cano, Enrique Villa, Luisa de la Fuente, Juan Pablo Pascual, Eduardo Artal, “Radiómetro en Banda W para Aplicaciones de Radioastronomía”, Simposium Nacional de la Unión Científica Internacional de Radio, URSI 2016, Madrid, 5-7 Septiembre, 2016.

[7.7] John D. Kraus, “Radio Astronomy”, Cygnus-Quasar Books, 2nd Edition, 1986.

[7.8] M.E. Tiuri, “Radio Astronomy Receivers”, *IEEE Transactions on Antennas and Propagation*, vol. 12, no. 7, pp.930-938, December 1964.

[7.9] F. T. Ulaby, R. K. Moore, A. K. Fung, "Microwave Remote sensing - Active and Passive" Volume I, Artech House Inc. 1981.

[7.10] R.H. Dicke, "The measurements of thermal radiation at microwave frequencies" *Rev. Sci. Instrum.*, vol.17, pp.268-275, July 1946.

[7.11] George D. Vendelin, Anthony M. Pavio, Ulrich L. Rode, *Microwave Circuit Design Using Linear and Nonlinear Techniques,* Section 6.3.3. John Wiley and sons, Inc., second edition 2005.

[7.12] G. Matthaei, L. Young, E.M.T. Jones, *Microwave Filters, Impedance-Matching Networks and Coupling Structures,* Section 8.03. Artech House, Inc., 1980.

[7.13] Simon Ramo, John R. Whinnery, Theodore Van Duzer, *Fields and Waves in Communication Electronics,* Section 11.15. John Wiley and sons, Inc., third edition 1994.

[7.14] Javier Bará Temes, *Circuitos de microondas con líneas de transmisión,* Edicions UPC 1994.

[7.15] CST Studio Suite 2009.

[7.16] MICIAN µwave wizard 7.9.

CHAPTER VIII: CONCLUSIONS

The study of a radio astronomy receiver starting with its importance in the performance of CMB experiments, following by the design and development of subsystems of a receiver such the cryogenic low-noise cryogenic amplifiers, and finishing in the characterisation of the full radiometer aimed to the study of the polarisation of the CMB have been the main goals of this thesis.

Right after the results of this work are summarised.

8.1. Thesis results

A MMIC LNA in the Q-band has been designed and characterised. The technology used is a mHEMT process with 70 nm gate length; reference D007IH from OMMIC foundry (France). The design has been supported by a full European technology.

The amplifier exhibits a gain of 28 dB and a noise temperature of 145 K in the 33-50 GHz frequency band for on wafer measurements at room temperature. When the amplifier is cooled down to 15 K, the gain is 27.3 dB and the noise temperature is 18.4 K. Apart from the very low noise, the DC power consumption is a main positive feature in the MMIC LNA, only 4.1 mW at cryogenic temperatures. The impact of the MMIC behaviour in terms of operation temperature in a radiometer has been also studied.

The hybrid technology has been used to design and develop a MIC low-noise amplifier in the 26-36 GHz frequency band. The amplifier exhibits 22.4 dB of gain and 175 K of noise temperature in the 26-36 GHz frequency band for measurements at room temperature. When the amplifier is cooled down 13 K, the gain achieved is 23.8 dB and the average noise temperature is 26 K. The DC power consumption at cryogenic temperatures is extremely low, only 5.7 mW.

The components of the MIC LNA such the transistor and capacitors have been modelled in order to have an accurate design. The technology for the transistor is mHEMT process from the Fraunhofer Institute for Applied Solid State Physics (Freiburg, Germany).

The distributed topology has been chosen to increase the power delivered in the gain modules of a radiometer. A methodology for the improvement of noise performance in a DA at low frequencies has been investigated making use of an active feedback termination of the gate line. To this goal, the influence of temperature changes in DA line termination has been analysed, demonstrating the major influence of gate line termination noise temperature as compared to the drain one. A mathematical formulation of noise temperature for an active load has been also presented. Noise figure expressions in a DA based on the active device small signal and noise parameters have been derived.

In order to verify experimentally the analysis, a hybrid two-stage distributed amplifier has been designed and fabricated both with resistive and active loads. Measured data result in broadband amplifier performance from 1 to 5.2 GHz with 10.9 dB flat gain. A 0.6 dB noise figure improvement below 2 GHz has been achieved when the active load is adopted as the gate line termination.

In order to improve the sensitivity in a radiometer, the effective bandwidth has been increased equalising the linear performance of the low noise amplifiers. The design methodology of an equaliser composed of a lossy pi-network that provides positive slope response over a frequency range has been described.

Several equalisers covering the 35-47 GHz frequency band have been manufactured and integrated in two gain modules of a radiometer; three equalisers working at room temperature with different attenuation levels and a 6.5 dB gain slope, and a cryogenic equaliser providing a 4.7 dB gain slope.

The full-characterisation of a radiometer in Q-band has been performed when the front-end module is cooled down to cryogenic temperature; describing all the components from the receiver antenna to the detection module, measuring the output DC detected signals, and measuring the noise temperature of the gain receiver chain. The main characteristics of the radiometer have been obtained from the detected signals, such the equivalent system noise temperature, the low-frequency spectra, the effective bandwidth and the sensitivity.

Finally, a new proposal of a radiometer in the W-band has been introduced. W-band is an observation window for the CMB that complements the measurements of other experiments in twenty, thirty, and forty Gigahertz bands. The proposed radiometer is made up commercial products, except a W-band filter designed in waveguide technology. The filter fixes the 80-99 GHz frequency band and exhibits a high image rejection, 40 dB at 75 GHz.

The W-band radiometer has a total gain around 50 dB with a noise figure of 4.5 dB. The effective bandwidth is 10 GHz. Moreover, the behaviour of the radiometer working in total power and Dicke configurations has been demonstrated.

8.2. Future lines

The work done in this Thesis continues in many open lines, the design of new chassis to host the LNA, upgrading the frequency band of the distributed topology, and new measurements of the radiometer front-ends.

The work in the LNA consists in the design of a new waveguide chassis in order to reduce the mismatching in the soldering of the coaxial connectors and microstrip access lines. The waveguide chassis is designed in WR-28 standard for the Ka-band MIC and in WR-22 standard for the Q-band MMIC. The improvement in return losses relieves the negative gain slope of the amplifier, especially at the high part of the frequency band.

Since the reduction of low-frequency noise in the DA in the 1-5 GHz has been demonstrated, the design would be upgraded to the Q-band in order to be assembled with the LNA. The new DA would be designed in monolithic technology in order to have identical basic DA cells, and cascade them to increase the gain in an optimum way if needed in the radiometer gain module.

Regarding the W-band radiometer proposal, the front-end module should be cooled down in order to minimize the noise and increase the sensitivity.

8.3. Publications

8.3.1. Magazines

J. Vicente Terán, M^a Luisa de la Fuente, Ernesto Limiti, Beatriz Aja, Eduardo Artal, "Noise Analysis in Distributed Amplifiers with Feedback-Active Load", IET Microwaves, Antennas and Propagation, pp. 1-9. June, 2016, ISSN 1751-8725

Enrique Villa, Juan Luis Cano, Jaime Cagigas, David Ortiz, Francisco Javier Casas, Ana Rosa Pérez, Beatriz Aja, J. Vicente Terán Collantes, Luisa de la Fuente, Eduardo Artal, Roger Hoyland, Angel Mediavilla, "The thirty gigahertz instrument receiver for the Q-U-I Joint Tenerife experiment: Concept and experimental results" Review of Scientific Instruments, 86 – 2, pp. 24702.

8.3.2. International Symposiums

J. Vicente Terán Collantes, Luisa de la Fuente, Beatriz Aja, Eduardo Artal, "Cryogenic Broadband Q-Band MMIC Low-Noise Amplifier", European Microwave Week, October 2016, London (UK).

Juan Luis Cano, Enrique Villa, Jaime Cagigas, Beatriz Aja, J. Vicente Terán Collantes, Ana Rosa Pérez, Luisa de la Fuente, Eduardo Artal, Angel Mediavilla, Roger Hoyland, "Multi-Pixel Ka-Band Radiometer for the QUIJOTE Experiment (Phase II)", Proceedings of the 42nd European Microwave Conference, October 2012, Amsterdam (Netherlands).

8.3.3. National Symposiums

J. Vicente Terán Collantes, Beatriz Aja, Juan L. Cano, Enrique Villa, Luisa de la Fuente, Juan Pablo Pascual, Eduardo Artal, "Radiómetro en Banda W para Aplicaciones de Radioastronomía", Simposium Nacional de la Unión Científica Internacional de Radio, URSI 2016, Madrid, 5-7 Septiembre, 2016.

J. Vicente Terán Collantes, Luisa de la Fuente, Beatriz Aja, Eduardo Artal, "Amplificador Criogénico MMIC de Bajo Ruido en Banda Q para Aplicaciones de Radioastronomía", Simposium Nacional de la Unión Científica Internacional de Radio, URSI 2016, Madrid, 5-7 Septiembre, 2016.

Eduardo Artal, Beatriz Aja, Juan Luis Cano, Luisa de la Fuente, Angel Mediavilla, J. Vicente Terán Collantes, Enrique Villa, “Radiómetros en ondas milimétricas del experimento QUIJOTE”, Simposium Nacional de la Unión Científica Internacional de Radio, URSI 2016, Madrid, 5-7 Septiembre, 2016.

Juan Luis Cano, Enrique Villa, J. Vicente Terán Collantes, Ana Rosa Pérez, Luisa de la Fuente, Angel Mediavilla, Eduardo Artal, “Módulo Posterior para la Integración de Polarímetros Multi-Pixel a 40 GHz en Radioastronomía”, Simposium Nacional de la Unión Científica Internacional de Radio, URSI 2016, Madrid, 5-7 Septiembre, 2016.

Vicente Terán Collantes, David Vegas, Eduardo Artal, “Filtro en banda W con alto rechazo en banda imagen”, in XXX Simposium Nacional de la Unión Científica Internacional de Radio, Pamplona. Spain, 2015.

Eduardo Artal, Beatriz Aja, Juan Luis Cano, Luisa de la Fuente, J. Vicente Terán Collantes, Enrique Villa, “Amplificadores criogénicos de muy bajo ruido en microondas y ondas milimétricas”, in XXX Simposium Nacional de la Unión Científica Internacional de Radio, Pamplona. Spain, 2015.

Juan Luis Cano, Enrique Villa, J. Vicente Terán Collantes, Elena González, Luisa de la Fuente, Eduardo Artal, Angel Mediavilla, “Polarímetro en banda W para aplicaciones de radioastronomía: diseño y simulación”, in XXX Simposium Nacional de la Unión Científica Internacional de Radio, Pamplona. Spain, 2015.

Vicente Terán Collantes, Luisa de la Fuente, Juan Luis Cano, Eduardo Artal, “Ka-Band Full-Hybrid Cryogenic Low-Noise Amplifier”, XXIX Simposium Nacional de la Unión Científica Internacional de Radio, URSI 2014, Valencia, 3-6 Septiembre, 2014.

Eduardo Artal, Beatriz Aja, Jaime Cagigas, Juan Luis Cano, Luisa de la Fuente, Angel Mediavilla, J. Vicente Terán Collantes, Enrique Villa, Roger Hoyland, Francisco Javier Casas, David Ortiz, “Receptor de polarización a 31 GHz para radioastronomía”, XXVII Simposium Nacional de la Unión Científica Internacional de Radio, Elche. Spain, 2012.

J. Vicente Terán Collantes, Enrique Villa, Juan Luis Cano, Luisa de la Fuente, Eduardo Artal, “Análisis de los efectos dispersivos en baja frecuencia de transistores HEMT a través de medidas de capacidad y conductancia”, XXVII Simposium Nacional de la Unión Científica Internacional de Radio, Elche. Spain, 2012.

RESUMEN

El experimento QUIJOTE (Q-U-I JOint TEnerife) tiene como misión la medida y el estudio de las características del Fondo Cósmico de Microondas (CMB de sus siglas en inglés) tales como la intensidad y la polarización. El telescopio y la instrumentación de medida para llevar a cabo el experimento se instala en el Observatorio de Izaña (Teide, Islas Canarias). La instrumentación se compone de un instrumento multi frecuencia (MFI) que se encuentra funcionando en el Observatorio, un instrumento a 30 GHz (TGI) que se encuentra en fase de integración en el telescopio, y un instrumento a 40 GHz (FGI) que se encuentra en fase de producción.

El experimento QUIJOTE es un consorcio científico formado el por el Instituto de Astrofísica de Canarias (IAC), el Instituto de Física de Cantabria (IFCA), el Departamento de Ingeniería de Comunicaciones (DICOM), el Observatorio Jodrell Bank de Manchester (Reino Unido), el Laboratorio Cavendish de Cambridge (Reino Unido) y la compañía española de integración mecánica IDOM. El grupo del DICOM es el responsable del diseño y desarrollo de los instrumentos TGI y FGI. El FGI es un radiómetro que opera en la banda de frecuencia Q (40 GHz), y complementa las medidas del CMB tomadas por los instrumentos MFI y TGI del experimento QUIJOTE.

El objetivo de la presente tesis es el diseño, desarrollo, y caracterización de amplificadores criogénicos de muy bajo ruido (LNA de sus siglas en inglés) en tecnología mHEMT destinados a operar dentro del módulo frontal (front-end) de un radiómetro. Se utiliza la tecnología de circuitos integrados monolíticos (MMIC) para el diseño de un LNA en la banda de frecuencias Q (40 GHz). Y la tecnología de circuitos integrados híbrida (MIC) para el diseño de un LNA en banda Ka (30 GHz). La

topología distribuida (DA) para el diseño de amplificadores se estudia como una opción para obtener una potencia de salida más alta frente a las topologías clásicas de bajo ruido. Se construye un prototipo en la banda de 1 a 5 GHz incluyendo una carga activa como terminación de línea para minimizar el alto ruido de baja frecuencia típicamente presente en la topología distribuida.

La planaridad de un amplificador es muy importante dentro de un radiómetro sensible para obtener un ancho de banda mayor. Por ello se diseñan ecualizadores en tecnología planar destinados a amplificadores operando tanto a temperatura criogénica como temperatura ambiente. Los circuitos diseñados se integran en el prototipo de radiómetro para el instrumento FGI. Se realiza la caracterización del radiómetro completo midiendo su ancho de banda efectivo, temperatura de ruido de operación, y obteniendo las señales detectadas de salida.

Una nueva ventana de observación astronómica se abre en la banda de frecuencias W (90 GHz), para la cual se propone un esquema de radiómetro en banda W con conversión a frecuencia intermedia. El radiómetro consta de componentes comerciales, exceptuando el filtro en banda W que fija la banda de radio-frecuencia de interés, en este caso de 80 a 99 GHz.

La estructura de la presente tesis se divide en los siguientes puntos:

- Una introducción sobre el CMB y la instrumentación necesaria para medirlo.
- El diseño y caracterización de amplificadores criogénicos de muy bajo ruido en tecnología mHEMT sobre GaAs. Se presentan un MMIC y un MIC.
- Estudio y mejora de ruido de baja frecuencia en topología distribuida (DA).
- Diseño de ecualizadores en microstrip para compensar la pendiente negativa de ganancia en los amplificadores de bajo ruido, aumentando de este modo el ancho de banda efectivo.
- Caracterización de un radiómetro en términos de ancho de banda efectivo, temperatura de ruido y señales detectadas.
- Propuesta de un radiómetro en banda W para una nueva ventana de observación del CMB.

CONCLUSIONES

El principal objetivo de la presente tesis ha sido el estudio de un receptor de radio astronomía, comenzando por la importancia que tiene los experimentos del CMB, continuando por el diseño y desarrollo de subsistemas que componen el receptor, como los amplificadores criogénicos de bajo ruido, y finalizando con la caracterización completa del radiómetro.

Los resultados de este trabajo se recogen en las siguientes líneas.

Resultados de la tesis

Se ha diseñado y caracterizado un MMIC LNA en la banda de frecuencias Q. La tecnología usada es el proceso mHEMT con 70 nm de longitud de puerta de la fundición OMMIC (Francia), referencia D007IH. El diseño ha sido realizado con tecnología 100% europea. El amplificador presenta una ganancia de 28 dB y una temperatura ruido de 145 K en la banda de 33 – 50 GHz para las medidas en oblea a temperatura ambiente. Cuando el amplificador es enfriado a temperaturas criogénicas (15 K), la ganancia obtenida es 27.3 dB y la temperatura de ruido es 18.4 K. Un aspecto importante en el amplificador es el muy bajo consumo de potencia DC, solo 4.1 mW en temperatura criogénica. Se ha estudiado el impacto del funcionamiento del LNA dentro de un radiómetro en términos de temperatura de operación.

Se usa la tecnología híbrida para diseñar y desarrollar un amplificador de bajo ruido (MIC) en la banda de 26 - 36 GHz. El amplificador presenta una ganancia de 22.4 dB y una temperatura de ruido de 175 K en la banda de 26 – 36 GHz a temperatura ambiente. Cuando el amplificador se enfría a 13 K, la ganancia lograda es

23.8 dB y la temperatura media de ruido 26 K. El consumo de potencia DC a temperaturas criogénicas es muy bajo, solo 5.7 mW. Los componentes que conforman el MIC como son el transistor y los condensadores han sido modelados de modo que el diseño sea lo más preciso posible. La tecnología de los transistores pertenece a un proceso mHEMT de Instituto Fraunhofer (Friburgo, Alemania).

La topología distribuida se ha escogido como solución para aumentar la potencia suministrada por los módulos de ganancia de un radiómetro. Se ha investigado una metodología para mejorar el ruido en baja frecuencia de este tipo de topología usando una carga activa como terminación en la línea de puerta. Se ha analizado la influencia de la temperatura de ruido en las terminaciones de línea, demostrando la mayor influencia de la temperatura de ruido en la línea de puerta frente a la de drenador. Se presenta una formulación matemática para evaluar el ruido en una carga activa, derivándose las expresiones de figura de ruido en el amplificador distribuido (DA) a través del modelo pequeña señal de dispositivo activo, el transistor, y sus parámetros de ruido. Para verificar experimentalmente el análisis, se ha implementado un amplificador distribuido de dos etapas con dos configuraciones, carga activa y carga resistiva como terminación de línea. Los datos medidos resultan en una ganancia plana de 10.9 dB sobre un ancho de banda de 1 – 5 GHz. La mejora de ruido por debajo de 2 GHz es 0.6 dB cuando se adopta la solución de carga activa frente a la resistiva en la línea de terminación de puerta.

Para mejorar la sensibilidad de un radiómetro, se ha trabajado en el diseño de ecualizadores que mejoren la planaridad de los amplificadores de bajo ruido y aumente con ello el ancho de banda efectivo. La metodología de diseño del ecualizador se basa en una red pi con pérdidas que proporciona una respuesta con pendiente positiva compensando la pendiente negativa del amplificador. Se construyen varios ecualizadores cubriendo la banda de 35 – 47 GHz y se integran dentro de dos módulos de ganancia de un radiómetro, tres ecualizadores trabajando a temperatura ambiente con diferentes niveles de atenuación y una pendiente de ganancia de 6.5 dB, y un ecualizador criogénico con 4.7 dB de pendiente en ganancia.

Se caracteriza por completo el comportamiento de un radiómetro en banda Q cuando el módulo frontal se enfría a temperatura criogénica. Se describen todos los componentes del receptor, desde la antena hasta el módulo de detección, midiendo las señales detectadas en DC y la temperatura de ruido de la cadena amplificadora. Las principales características de un radiómetro se obtienen directamente de las señales detectadas, la temperatura equivalente de ruido del sistema, el espectro de baja frecuencia, el ancho de banda efectivo y la sensibilidad.

Finalmente, se introduce el esquema de un radiómetro en banda W debido a que esta banda de frecuencias abre una nueva ventana de observación del CMB y sirve para complementar las medidas de otros instrumentos en 20, 30 y 40 GHz. El radiómetro propuesto se compone de elementos comerciales, exceptuando el filtro en banda W, diseñado en tecnología guía de onda. El filtro fija la banda de frecuencia en 80 - 99 GHz y presenta un alto rechazo a la banda de frecuencia imagen, 40 dB a 75 GHz. El radiómetro en banda W tiene una ganancia total de 50 dB con una figura de ruido de 4.5 dB. El ancho de banda efectivo es de 10 GHz. Además se ha demostrado su funcionamiento como radiómetro de potencia total y radiómetro de Dicke.

Líneas futuras

El trabajo realizado en esta tesis continua en varios frentes abiertos, el diseño de nuevos chasis para albergar los LNA, escalando la banda de frecuencias en la topología distribuida, y realizando nuevas medidas en los módulos frontales del radiómetro.

El trabajo en los LNA consiste en el diseño de un chasis en guía de onda de modo que se reduzcan las desadaptaciones en la soldadura entre el conector coaxial y las líneas microstrip de acceso. El chasis en guía de onda se diseña en el estándar WR-28 para la banda de 30 GHz (banda Ka) y en WR-22 para la banda de 40 GHz (banda Q). la mejora en la pérdidas de retorno mitiga la pendiente negativa de ganancia en el amplificador, especialmente acusada en la parte alta de la banda.

Una vez demostrada la reducción de ruido de baja frecuencia en el amplificador distribuido (DA), se escala su diseño hasta la banda Q de manera que pueda ser integrado junto al LNA. El nuevo DA se diseñara en tecnología monolítica de manera que puedan obtenerse idénticas celdas básicas con topología distribuida y pueda concatenarse fácilmente para incrementar la ganancia dependiendo de los requisitos en el módulo de ganancia del radiómetro.

Respecto a radiómetro propuesto en banda W, el módulo frontal se enfriara a temperatura criogénica para minimizar el ruido en incrementar la sensibilidad.